THÈSE

En vue de l'obtention du

DOCTORAT DE L'UNIVERSITÉ DE TOULOUSE

Délivré par l'Université Toulouse 3 - Paul Sabatier

Présentée et soutenue par

Glenda Tsholofelo MOTSI

Le 10 décembre 2019

Spark Plasma Sintering de composites base titane renforcés par des carbures pour applications en tribocorrosion

---

Ecole doctorale : **SDM - SCIENCES DE LA MATIERE - Toulouse**

Spécialité : **Sciences et Génie des Matériaux**

Unité de recherche :
CIRIMAT - Centre Interuniversitaire de Recherche et d'Ingénierie des Matériaux

Thèse dirigée par
Claude ESTOURNES et Sophie GUILLEMET-FRITSCH

Jury

M. Yann LEPETITCORPS, Rapporteur
M. Frédéric SCHOENSTEIN, Rapporteur
Mme Florence PETINARI-STURMEL, Examinatrice
M. Claude ESTOURNES, Directeur de thèse
Mme Sophie GUILLEMET-FRITSCH, Co-directrice de thèse

‘‘it always seem impossible until it’s done’’

Nelson Mandela

Acknowlegdements

Foremost, I would like to express my sincere gratitude to the director of ‘‘Centre Inter-universitaire de Recherche et d’Ingénierie des Matériaux (CIRIMAT)’’, Prof. Christophe Laurent for his warm welcome and allowing me to do my PhD Thesis in the laboratory.

I would like to thank Prof. Yann Lepetitcorps and Prof. Frederic Schoenstein for accepting to be rapporteurs of this thesis. I also thank Prof. Florence Pettinari-Sturmel for being the president during my defense presentation.

I thank my mentor Prof. Peter A. Olubambi for his assistance and encouragement in obtaining AESOP+ scholarship to study in France.

Special thanks to the AESOP+ project for giving me an opportunity to pursue my doctorate programme abroad.

My sincere gratitude to my supervisors Dr. Sophie Guillemet-Fritsch and Dr. Claude Estournès for their warm welcome at CIRIMAT’’. Your continuous support, motivation, guidance and insightful comments throughout my PhD study are highly appreciated.

Many thanks to the staff of CIRIMAT Marie-Claire Barthelemy, Geoffroy Chevallier, Benjamin Duployer, Raphaël Laloo, Jean-Jacque Demain and Vincent Baylac for teaching me operate research equipment independently, the technical skills I have acquired are most valuable to me.

I thank Dr. Babatunde Obadele, Mr. Jeremiah Akinribide and Mr. Olukayode Akinwamide at the Center for Nanoengineering and Tribocorrosion in the University of Johannesburg for his assistance during the tribocorrosion experiments.

Special thanks to TIMET-Savoie for their generous assistance in analysing interstitial elements in my powders, Marion Technologie for trace elements analysis with ICP-OES, Alexandre Freulon for his assistance in etching samples, Claudie Josse and Maria-Teresa Hungria-Hernandez for SEM/FIB and TEM analysis of my samples.

I thank my fellow doctoral students, Precious Radingoana, Ugras Kus, Juliano Schorne-Pinto, Arnaud Fregeac, Andréas Flareau, Yannick Thebault and Clément Genet for your cooperation and of course friendship.

Last but not the least, I would like to thank my family: my mother Caroline Dikeledi Motsi for being there always and giving me support during my academic years, my husband and daughters Wola Ladipo, Kgalalelo and Onthatile Motsi for your love and patience, my sister and niece Annah and Ontlametse Motsi, my grandmother and late grandfather Annah and Cornelius Motsi, I appreciate you all.

Table of contents

Nomenclature

COF	Friction Coefficient
CP-Ti	Commercial Pure Titanium
E_{corr}	Corrosion potential
EDS	Energy Dispersive Spectrometry
EELS	EDX spectrometer and a loss of energy spectrometer
FFT	Fast Fourier Transform
FIB	Focus Ion beam
Gr	Graphite
HP	Hot Pressing
I_{corr}	Corrosion current density
ICP-OES	Inductively Coupled Plasma - Optical Emission Spectrometry
OCP	Open Circuit Potential
PDP	Potentiodynamic polarisation
PSD	Particle Sizes and Distribution
RIR	Reference Intensity Ratio
SEM	Scanning Electron Microscope
SPS	Spark Plasma Sintering
TEM	Transmission Electron Microscope
TMCs	Titanium Matrix Composites

General introduction

Titanium and its alloys are well-known throughout engineering applications for their combined desirable properties of high specific strength to weight ratio, low density, biocompatibility and relatively good corrosion resistance (Welsch *et al.*, 1993). The production of bulk titanium involves expensive complex Kroll's processes such as refining, distillation and dissolution (Lütjering *et al.*, 2007a). These processes are performed using specific devices in a vacuum environment to avoid contamination by gaseous phases, especially oxidation because of titanium high affinity to oxygen (Lütjering *et al.*, 2007a; Shon *et al.*, 2014a) . In addition, the high energy consumption, the initial high cost of titanium tetrachloride and that of reducing agents (pure magnesium and sodium) contribute titanium high cost and thus its limitation of use in other applications such as automobile (Shon *et al.*, 2014a; Welsch *et al.*, 1993). The latter product is in form of rolled plates which are further processed. Due to the high cost of production, these classes of materials are extensively used in high added value industries such as the aerospace, biomedical and marine applications (Zadra *et al.*, 2008).

In comparison to other commonly used engineering materials high purity titanium has a melting point of 1668°C, higher than the one of Fe (1538°C), Al (660°C) and Ni (1455°C) as illustrated in Table 1 (Lütjering *et al.*, 2007a). The much higher melting temperature of titanium (1670°C) as compared to aluminum (660°C), the main competitor in light weight structural applications, give titanium a definite advantage for application temperatures above 150°C (Lütjering *et al.*, 2007a). Pure titanium has tensile strength of 240MPa, toughness in the range 99-140MPa-$m^{1/2}$, Vickers hardness of 60HV, modulus of elasticity of 120GPa and high friction coefficient (0.68 - 0.8) (Donachie, 2000). As a result of their light-weight coupled with moderately high strength and outstanding corrosion resistance properties, these have made titanium and its alloys candidate material for other engineering applications such as automotive, offshore, aeronautics and energy industries (Cheng *et al.*, 2012). However, conventional Ti and its alloys exhibit inferior wear resistance and suffer considerable loss in mechanical strength (Balaji *et al.*, 2015). These limitations prevent titanium in many engineering applications were both corrosion and wear may be encountered (Toptan *et al.*, 2016).

Table 1. Material characteristics of titanium compared to other structural metallic materials based on Fe, Ni, and Al(Lütjering et al., 2007a)

	Ti	Fe	Ni	Al
Melting temperature (°C)	1670	1538	1455	660
Allotropic transformation (°C)	882 $\beta \rightarrow \alpha$	912 $\gamma \rightarrow \alpha$	-	-
Crystal structure	BCC→HCP	FCC→BCC	FCC	FCC
Room temperature E(GPa)	115	215	200	72
Yield stress level (MPa)	1000	1000	1000	500
Density (g/cm^3)	4.5	7.9	8.9	2.7
Comparative corrosion resistance	Very high	Low	Medium	High
Comparative reactivity with O_2	Very high	Low	Low	High
Comparative price of metal	Very high	Low	High	Medium

Incorporation of hard ceramic particles or fibers reinforcements into titanium based matrix can significantly improve its wear resistance by direct strengthening effect taking place due to the ability of the reinforcing phases to carry the load (Blau *et al.*, 2007; Prakash *et al.*, 2016). Also by indirect strengthening, taking place by alterations on the metallic matrix structure, such as induced dislocations, Orowan strengthening, or grain size refinement and modification of the matrix microstructure as a consequence of the addition of the reinforcing phase (Chawla *et al.*, 2006). The demand for the use of titanium matrix composites (TMCs) is attributed to the availability of the ever-evolving sources of relatively inexpensive reinforcements and the frequent development of the processing routes which results in reproducible microstructures and properties (Ajayan *et al.*, 2006). Powder metallurgy techniques have been found as one of energy efficient ways for production of TMCs or other materials. Several techniques exist to densify but the use of innovative Spark Plasma Sintering (SPS) method has been the most favourable. The SPS process combine the effect of uniaxial pressure and Joule effect produced from pulsed electric current passing through sintering tool and a conductive powder. Thus, faster heating rates can be achieved and powders can be rapidly densified within short period of time as reported in literature (Abedi *et al.*, 2016; Kus *et al.*, 2016; Locci *et al.*, 2006; Munir *et al.*, 2006; Orru *et al.*, 2009; Zadra *et al.*, 2013)

TMCs are traditionally fabricated by ex-situ methods, whereby pure TiB_2 and TiC particulates are separately prepared and later added to Ti matrix for production of Ti-TiB_2/TiB and Ti-TiC composites respectively (Ajayan *et al.*, 2006). With this method, undesirable second phases

may be formed in the matrix-reinforcement interphase and resulting in poor interfacial bonding (Ajayan *et al.*, 2006). The second phases may act as stress concentrators leading to deterioration of mechanical properties. Moreover, synthesis of TMCs using pure TiB_2 and TiC which have high melting points of 2970°C and 3054°C respectively, make the sintering difficult due to their low self-diffusion coefficients (Wang *et al.*, 2012). However, densification of 99% was achieved when the composition ratio was 85%TiB_2: 15%TiC, processed by high pressure (3GPa) sintering techniques at higher temperatures (2250-2500°C) (Vallauri *et al.*, 2008).

Alternatively TMCs have been commonly fabricated by in-situ methods, most favourably using SPS technique. This method involves simultaneous synthesis and densification in one step at relatively low temperatures (Dudina *et al.*, 2013). The reinforcing phases synthesized in-situ by exothermic reactions between titanium and a constituent element (B_4C) often result in clean interface and strong interfacial bonding (Ajayan *et al.*, 2006; Campbell, 2010). Synthesis of TiC, TiB_2 and TiB can be achieved when a complete chemical reaction is reached.

Although in-situ method tends to be favourable in terms of reduced fabrication cost, energy consumption and cheap B_4C powders, there are challenges encountered during fabrication process. These include the ability to control the size of the reinforcement phase because the reaction kinetics of the reactants is not the same throughout. Hence, great care must be taken on the selection of the reactant's particles size (considering the high cost), mixing conditions and sintering parameters. Such that, when reactants with micron size particles are used in SPS, prolonged sintering time and very high temperatures (1100 to 1400°C) are required to reduce the amount of unreacted particles, in contrast to sub-micron size particles (<1100°C). TMCs fabricated from micro-sized reinforcing phases were reported to be characterized by incomplete reaction consisting of B_4C, TiB_2, TiB, TiB clusters and porosity found around B_4C agglomerates (Ni *et al.*, 2006; Toptan *et al.*, 2016). These microstructural characteristics may have adverse effect on the composites properties. Porosity may act as stress concentrator, high corrosion rates may results from porosity, unreacted B_4C may de-attach from matrix during rubbing and act as third-body abrasive accelerating wear rates (Toptan *et al.*, 2016).

In contrast to sub-micron sized reactants, the increased of their surface area, compare to the micron ones, leads to increased reactions kinetics which requires less periods during sintering

and complete reaction may be achieved. In this regard, when proper fabrication variables are chosen, the resultant composites have good microstructural characteristics such as clean interface between the matrix and reinforcing phase, the intermediate phases are eliminated and also good dispersion of reinforcing phase is achieved.

Nevertheless, the synergy effect of TiC, TiB_2 and TiB on tensile strength, elongation and hardness from in-situ synthesized TMCs has been widely explored (Geng *et al.*, 2008; Li *et al.*, 2016; Rahoma *et al.*, 2015). The literature based on corrosion and especially tribocorrosion behaviour is however lacking. Owing to the emerging technological applications of TMCs in harsh environments, such as automotive, marine, chemical and petrochemical industries (Mathew *et al.*, 2009) where corrosion and tribocorrosion are encountered, it is important to contribute knowledge on the corrosion and tribocorrosion performance of TMCs based on TiC, TiB_2 and TiB to this research field.

This work is focused on the elaboration of titanium based composites reinforced with TiC, TiB_2 and TiB phases by reactive spark plasma sintering. Our work will be focused on the optimisation of the densification parameters, on the understanding of the reaction kinetics, microstructure evolution, mechanical and tribocorrosion behaviour.

Thus the objectives are multiple:

- To simultaneously synthesize and consolidate TMCs with homogenously distributed TiB and TiC phases in the titanium matrix
- Study a detailed analysis of the in-situ reaction mechanisms and kinetics
- To improve the tribocorrosion properties of Ti by TiB and TiC.

The thesis is organised as follows:

In the **first chapter,** literature based on sintering of titanium and its composites, obtained microstructures and properties is reviewed. The **second chapter** contain materials of study, characterisations, sintering by SPS and tribocorrosion experiments. The **third chapter** present the results obtained for SPS of pure titanium, the effect of sintering parameters and interstitial element are thoroughly discussed. The **fourth chapter** present the results and discussion for densification of titanium matrix composites and reaction kinetics involved using reactants with varying particles sizes. The **fifth chapter** present the results and

discussion obtained for corrosion and tribocorrosion experiments of titanium matrix composites.

CHAPTER 1: Literature review

Table of contents

1.0 Pure titanium

1.1. Crystal structure

The crystal structure of pure titanium from room and temperatures up to 882°C has a hexagonal closed packed (HCP) crystal structure also known as alpha (α) phase. Above 882°C, which defines the transus temperature (T_β), it transforms to a body centred cubic (BCC) crystal structure, the beta (β) phase. The atomic unit cell for the α-Ti and β-Ti with their closely packed crystal planes are shown in the Figure 1.1 (Leyens *et al.*, 2003). The parameters of α-Ti and β-Ti phases are listed in Table 2. As shown in Table 2 α-Ti and β-Ti have densities of 4.51g/cm^3 at 20°C and 4.35g/cm^3 at 885°C with atomic packing factors of 78% and 68% respectively (Callister *et al.*, 2007; Welsch *et al.*, 1993). As a result, during polymorphic transformation occurring at the transus temperature there is a slight volume expansion of 3.7% during heating and slight contraction of -3.34% during cooling (Qian *et al.*, 2015).

Table 2. Structure characteristics of pure Titanium (Leyens *et al.*, 2003; Welsch *et al.*, 1993).

Phase	Space group	Crystal structure	Atomic packing factor	Lattice parameters	Lattice angles	Density
α-Ti	P63/mmc	HCP	78%	a = b = 0.295nm c = 0.468nm c/a=1.58	α = β = 90° γ = 120°	4.51 g/cm^3@ 20°C
β-Ti	lm-3m	BCC	68%	a = b = c = 0.332	α = β = γ = 90°	4.35 g/cm^3 @ 885°C

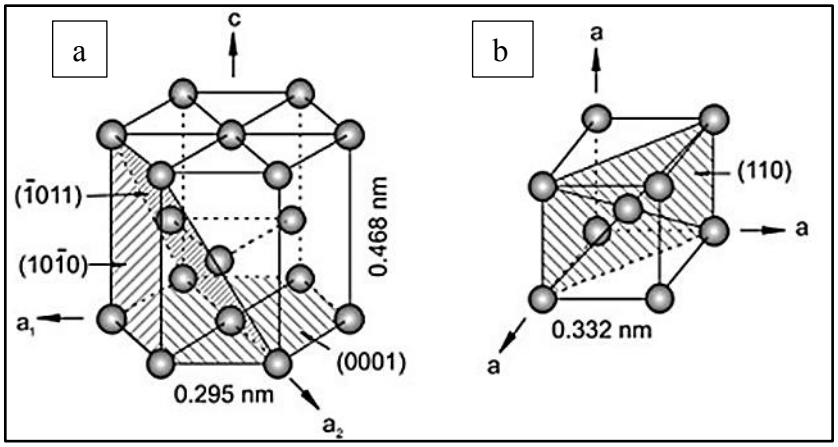

Figure 1.1. Crystallographic structures of titanium a) HCP (α-Ti) and b) BCC (β-Ti) (Leyens *et al.*, 2003)

1.1.1 Alloying elements for commercial pure titanium

In the HCP and BCC crystal structures of titanium, the alloying interstitial elements occupy tetrahedral and octahedral interstitial sites as shown in Figure 1.2 (Fukai, 2006). HCP crystal structure has 4 tetrahedral and 2 octahedral interstitial sites , while BCC crystal structure has 12 tetrahedral and 6 octahedral interstitial sties (Vasanthakumar *et al.*, 2018). The radius of the tetrahedral and octahedral site for the HCP crystal structure are 0.33Å and 0.61Å respectively, and for the BCC is 0.44Å for the tetrahedral site (Cordero *et al.*, 2008). Interstitial elements H, O, N and C in increasing order having atomic radii of 0.31, 0.66, 0.71 and 0.76Å occupy tetrahedral and octahedral interstitial sites respectively, while Fe atom with a larger atomic radius of 1.32Å atom may substitute titanium atoms (radius= 1.6Å) from the unit cell (Conrad, 1981; Cordero *et al.*, 2008). Among the alloying elements C, O, N and Fe are the α-Ti phase stabilisers and H is the β-Ti phase stabilizer. Oxygen has the highest solid solubility of 30at.% in α-Ti followed by 19at.% of nitrogen, 2at.% of carbon and 8at% hydrogen (Conrad, 1981) according to the binary phase diagrams in Figures (1.3, 1.4, 1.5 & 1.6).

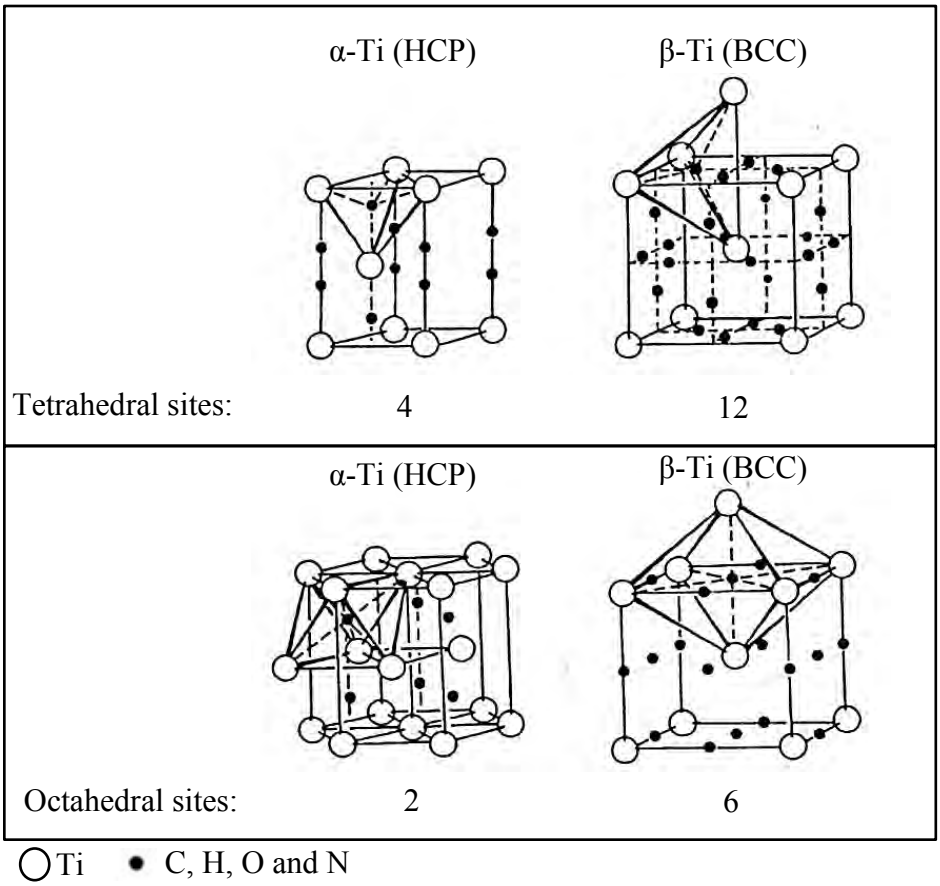

Figure 1.1. Tetrahedral and octahedral interstitial sites in HCP and BCC crystal structures. Adapted from (Fukai, 2006)

1.1.1.1 Oxygen

Titanium has a strong chemical affinity for oxygen and often forms an oxide layer on the surface of titanium and enhances corrosion resistance. This oxide layer forms at room temperature and thickness rapidly at elevated temperatures when heated in air. At temperatures exceeding 500°C the oxidation resistance of titanium decreases rapidly and the metal becomes highly susceptible to embrittlement by oxygen. In order to minimise oxygen contamination in titanium and its alloys the production has to be performed in a controlled atmosphere such as vacuum or inert gas atmosphere (Donachie, 2000).

Oxygen is an α-Ti stabilizer because of its high maximum solubility of 30at.% at temperature above 600°C (Kwasniak *et al.*, 2014) and it increases the α to β allotropic transformation temperature as shown in Figure 1.3 (Welsch *et al.*, 1993). It is important to consider oxygen content when analysing mechanical properties of α-Ti. Oxygen diffusion in α-Ti modifies lattice parameters and this has an effect on the mechanical properties. Baillieux *et al.* (2015) studied the effect of oxygen diffusion on the crystallographic evolution of α-Ti using

synchrotron X-ray diffraction at elevated temperature and varied dwell time. They analysed the lattice parameters on the cross section area from the oxide layer to the center of a sample They observed that the lattice parameters *c* and *a* , the ratio c/a and the hardness gradually increase as the distance from the oxide metal interface decreases for samples heat-treated in air. Moreover due to change in the lattice parameters there is also a slight unit cell volume expansion of about 0.00013nm^3 (Wasz *et al.*, 1996).

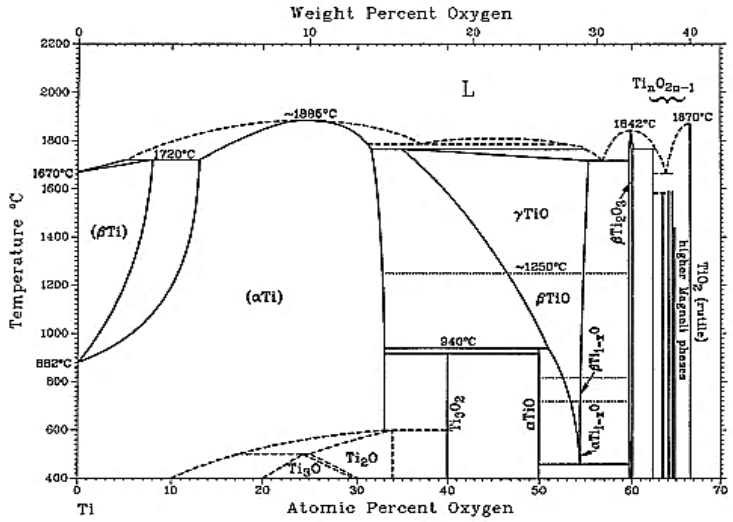

Figure 1.3. Ti-O binary diagram (Welsch et al., 1993)

1.1.1.2 Nitrogen

Similar effects have been obtained for α-Ti phase stabilisers nitrogen (Figure 1.4) (Galvanetto *et al.*, 2001; Vasanthakumar *et al.*, 2018). Interstitial nitrogen reacts much slower with titanium than oxygen but forms a very hard TiN or Ti_2N phases with good tribological properties. Thus, titanium nitriding is normally done to improve the surface properties of titanium for good surface hardness and tribology properties. But excessive nitrogen diffusion in titanium may cause embrittlement (Zhecheva *et al.*, 2005). Galvanetto *et al.* (2001) investigated the formation of nitride phases obtained by reactive plasma spraying of α-Ti powder in a nitrogen-containing plasma gas on 304L steel. The phases formed after coating consisted of α-Ti, TiN and Ti_2N layers and the lattice parameters calculated were compared with the JCPDS standards and from literature. The calculated lattice parameters *a* and *c* with reference to the α-Ti feedstock powders increased. For sample 1 which was sprayed with Ar/N_2 gas ratio of 3, at a distance of 100m the α-Ti phase lattice parameters were a = 0.2958nm and c = 0.4720nm, TiN phase a = 0.4225nm and Ti_2N phase a = 0.4952nm and c =

0.3032nm. In comparison with JCPDS α-Ti phase a = 0.2950nm and c = 0.4686nm, TiN phase a = 0.4241nm and Ti_2N phase a = 0.4945nm and c = 0.3034nm.

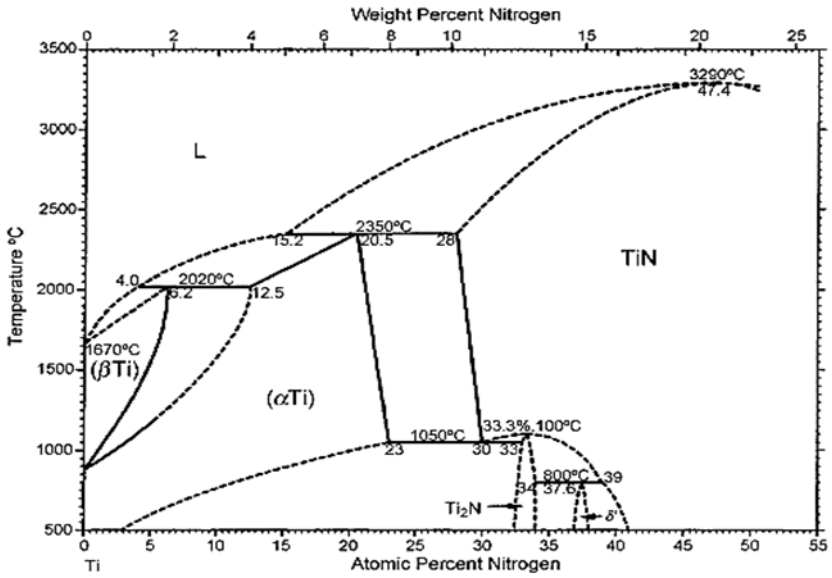

Figure 1.4. Ti-N binary phase diagram (Wriedt et al., 1987)

1.1.1.3 Carbon

Carbon impurity in commercial pure titanium are kept at low levels of 0.08wt% as shown in Figure 1.5 (Baker, 1992), to avoid formation of hard TiC phases. In comparison to oxygen and nitrogen, the solid solubility of carbon with a much larger atomic radius, is very low in both α-Ti and β-Ti. The solubility of carbon content in titanium can be less than 100ppm and still carbides can precipitates at grain boundaries during fabrication process such as casting and heat treatment and can lead to brittleness (Qian *et al.*, 2015; Solonina *et al.*, 1974; Welsch *et al.*, 1993). Vasanthakumar *et al.* (2018) studied the effect of C/Ti ratio on the lattice parameter, hardness and elastic modulus of TiCx prepared by reactive spark plasma sintering. The XRD patterns analysis of sintered TiCx compacts showed formation of a single TiC phase with increase of lattice parameters with increasing carbon content. Moreover, the calculated lattice parameter values in the study were in good agreement with the data found in literature (Frage *et al.*, 2002; Holt *et al.*, 1986; Yang *et al.*, 2013; Zarrinfar *et al.*, 2002).

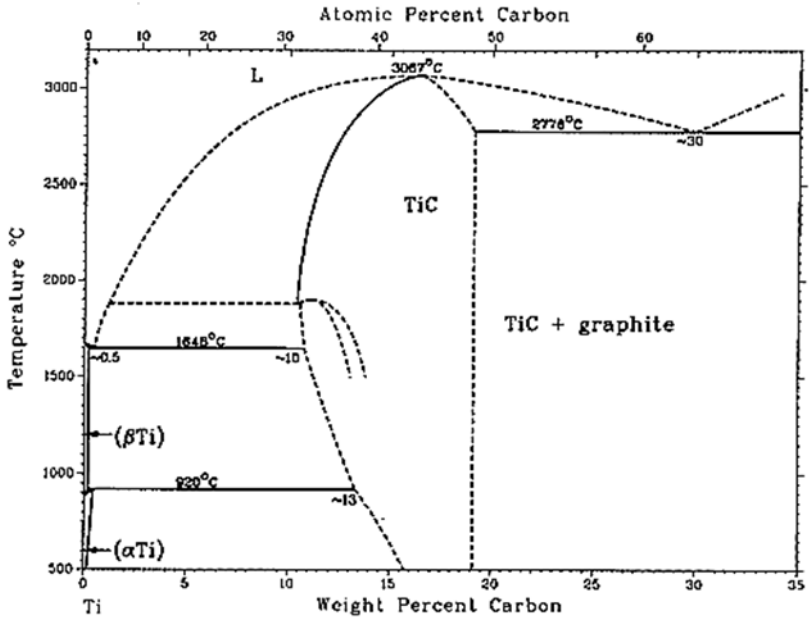

Figure 1.5. Ti-C binary phase diagram

1.1.1.4 Hydrogen

Hydrogen is well-known to cause hydrogen embrittlement in titanium and its alloys, hence its maximum content in kept at about 125-150ppm (Lütjering *et al.*, 2007a). So hydrogen contamination in α-Ti is undesirable when the concentration is above 200ppm, it has very high diffusion rates in β-Ti as well as in the α-Ti (Liang *et al.*, 2010). Hydrogen has an atomic radius of 0.53Å and occupies tetrahedral interstitial sites in the titanium crystal structures. The maximum solubility of hydrogen in α-Ti is about 7at.% at 300°C and it decreases rapidly with decreasing temperature. In the β-Ti the solid solubility of hydrogen is 50at.% at temperatures above 600°C without formation of hydrides. This is attributed by the open BCC crystal structure of β-Ti which consists of 12 tetrahedral and 6 octahedral interstitial sites, comparing with HCP crystal structure of α-Ti with only 4 tetrahedral and 2 octahedral interstitial sites (Tal-Gutelmacher *et al.*, 2005). Hence hydrogen is known to stabilize the β-Ti phase by lowering the α to β-phase transus temperature as shown in Figure 1.6.

Mechanical properties degradation in α-Ti and α + β-Ti alloys can still occur even when the H content is at safe levels (30 to 40ppm) below 125ppm (Wasz *et al.*, 1996; Welsch *et al.*, 1993), except annealed β-Ti alloys which are less sensitive to hydrogen embrittlement. β-Ti alloys have high tolerance to hydrogen mainly because the solid solubility of hydrogen is much higher the BCC crystal structure than the HCP (Lütjering *et al.*, 2007a). When hydrogen diffuses in α-Ti, it reacts with titanium to form a brittle hydride phase which has

different elastic properties compare to the α-Ti lattice (Wasz *et al.*, 1996). This hydride phase degrades mechanical properties of α-Ti by embrittlement and causes early fracture failure. Thus titanium often fails in hydrogen manifested aqueous or humid gaseous environments, especially under high static loads or fatigue loading (Lütjering *et al.*, 2007a).

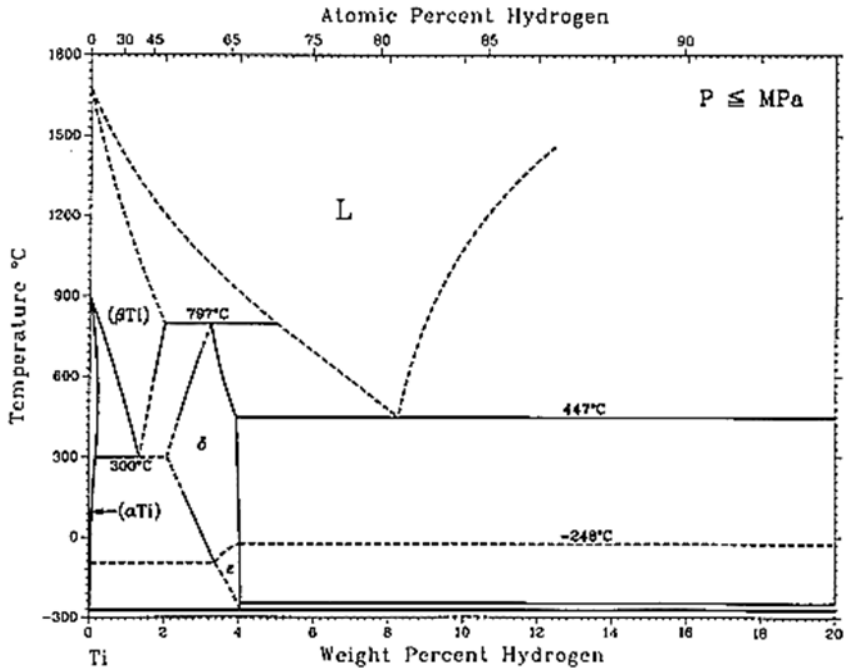

Figure 1.6. Ti-H phase diagram (Baker, 1992)

1.1.2 Microstructure of pure titanium

The microstructure of any material depends on its composition, processing steps, heat treatment and cooling rates (Wasz *et al.*, 1996). When CP-Ti is heated to the β-Ti phase region and cooled down to α-Ti phase, usually the β-Ti phase is not retained but transforms back to its room temperature α-Ti phase due to low quantity of beta stabilising elements. This transformation can be of martensitic type or can occur by diffusion controlled nucleation and growth process depending on cooling rate and composition (Lütjering *et al.*, 2007a). A martensitic microstructure (Figure 1.7) resulting from quenching is characterised by extremely fine acicular morphology which exhibits high strength and hardness but reduced ductility and toughness. Microstructure by diffusion controlled nucleation and growth is obtained by slower cooling rates producing a coarse Widmanstätten α plus α-prime or some retained β-phase (Figure 1.7). This microstructure has very low strength and hardness but the ductility and toughness is higher than the martensitic microstructure (Donachie, 2000).

Crystallographic orientation relationship between α and β is given by the Burgers relationship:

$$(110)\beta \parallel (0002)\alpha$$
$$[111]\beta \parallel [1120]\alpha$$

According to this relationship, a BCC crystal can transform to 12 hexagonal variants, having different orientations with regard to the parent β crystal (Lütjering *et al.*, 2007a).

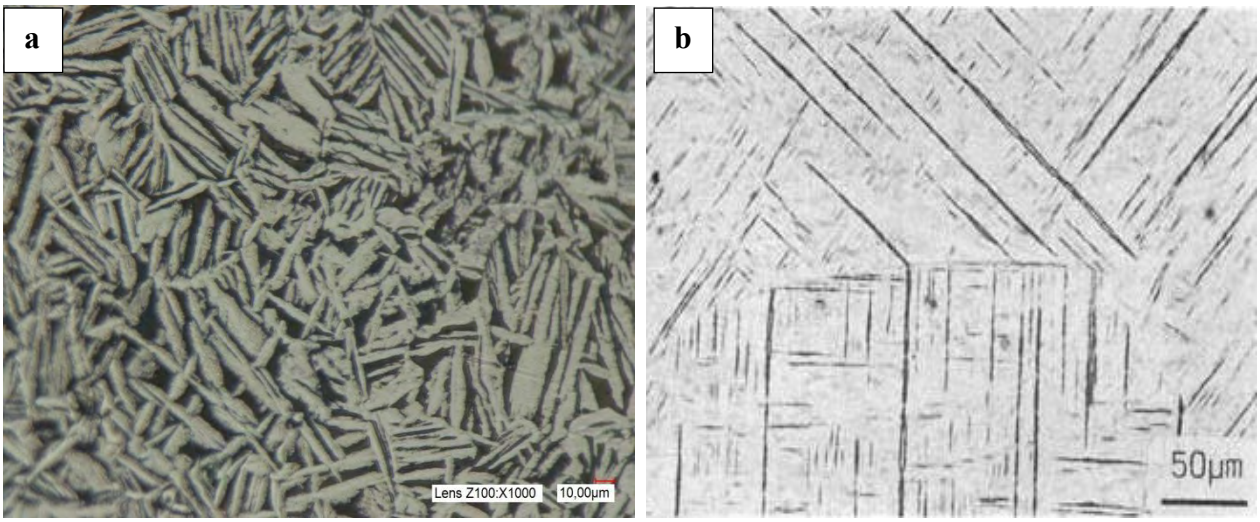

Figure 1.7. Microstructure example of a) Widmanstatten in pure titanium and b) Martensitic in Ti6Al4V

1.1.3 Alloying elements effect on CP-Ti mechanical properties

Commercially pure titanium (CP-Ti) grades produced according to the ASTM standards have compositions as shown in Table 3 (Welsch *et al.*, 1993). The concentration of carbon, nitrogen and hydrogen are typically very low and in order to compensate for the low strength oxygen is intentionally added to enhance the strength (Qian *et al.*, 2015; Welsch *et al.*, 1993). However, the addition of oxygen has to be controlled in order to minimise the reduction in fracture toughness and ductility. A summary of the influence of the alloying elements on the α to β transformation temperature , tensile strength and hardness is presented in Table 3 (Donachie, 2000; Welsch *et al.*, 1993). The β-transus denotes the α to β phase transformation temperature during heating, while the α-transus is the β to α phase transformation during cooling. High purity titanium grades with lower interstitial content have low strength and

hardness, and the α to β phase transformation temperature is lower, as compared to those with higher interstitial content which stabilizes the alpha phase (Lütjering *et al.*, 2003).

Table 3. ASTM standard grades of commercially pure titanium. Welsch et al. (1993).

Designation	Impurity limits (wt%)					β-transus (°C)	α-transus (°C)	Vickers hardness (HV)	Tensile strength (MPa)
	C	H	O	Fe	N				
ASTM grade 1	0.08	0.015	0.18	0.2	0.03	880	888	126	240
ASTM grade 2	0.08	0.015	0.25	0.3	0.04	890	913	210	340
ASTM grade 3	0.08	0.015	0.35	0.3	0.05	900	920	225	450
ASTM grade 4	0.08	0.015	0.40	0.5	0.05	905	950	265	550

1.1.4 Sintering methods

Powder metallurgy processes are more competitive than other fabrication methods like casting, stamping or machining, due to lower energy consumption, higher material utilisation and reduced numbers of processing steps thus reducing cost. The process allows fabrication of combination of material that would be conventionally difficult to fabricate such as those with higher melting points. Powder metallurgy is favourably method of choice because finer microstructures yielding superior properties can be obtained such as higher strength and wear resistance. Greater precision is obtained, eliminating most or all of the finish machining operations required for castings. It avoids casting defects such as blow holes, shrinkage and inclusions. Thus with powder metallurgy near net-shape components are directly produced from powders while simultaneously reducing material input and fabrication costs making it an attractive alternative for the production of most materials. However, powder metallurgy processes are economical only when production rates are higher, since the tooling cost is quite appreciable (Masikane, 2016; Upadhyaya, 1997).

There are several sintering techniques available these include spark plasma sintering (SPS), uniaxial hot-pressing (HP), hot isostatic pressing, (HIP) and pressing & sintering (P&S) (Bolzoni *et al.*, 2013). In HP, a conventional sintering method, the powder is loaded into a graphite mold and sintered, under uniaxial applied pressure, by indirect heating via resistive heating units (Shon *et al.*, 2014a). However, HP often requires very long time for sintering (several hours) and as a result high energy consumption. On the opposite, Spark Plasma

Sintering (SPS) allows rapid consolidation (several minutes) and controlled grain growth by the reduction of the sintering temperature and time (Chaim *et al.*, 2008; Chaim *et al.*, 2012; Munir *et al.*, 2006). Here also the powder is loaded in a graphite mold and a uniaxial pressure is applied but the heating is directly obtained by the use of DC pulsed current passing through the material and/or the mold (Munir *et al.*, 2006). The two methods are widely used by researchers, SPS technique is a promising technique due to aforementioned reasons (Yang *et al.*, 2015).

1.1.5 Sintering of titanium, densification and mechanical properties

Recent studies have shown that SPS technique can produce material with relatively improved properties**.** Ti6Al4V master alloy and TiAl intermetallic are among advanced materials that are widely used in high added value industries and thus most investigated by the economic SPS technique (Abedi *et al.*, 2016; Crosby *et al.*, 2014; Garbiec *et al.*, 2016; Hussainova, 2003; Kus *et al.*, 2016; Lampke *et al.*, 2006; Manière *et al.*, 2017; Martins *et al.*, 2017; Matsugi *et al.*, 1996; Mischler *et al.*, 2014; Prakash *et al.*, 2016; Trzaska *et al.*, 2016; Weston *et al.*, 2015) while only few investigations are focused on SPS of commercial pure titanium.

Sintering of CP-Ti by SPS has been reported by Zadra *et al.* (2008), Weston *et al.* (2015), Shon *et al.* (2014b) and Shon *et al.* (2014a). In their studies, these authors have shown that sintered CP-Ti components produced have similar Vickers hardness values close to ASTM grades (126-265HV) (Welsch *et al.*, 1993). Zadra *et al.* (2008) investigated the use of SPS on 45µm spherical CP-Ti grade 1 and irregular shaped CP-Ti grade 3. Sintering experiments were conducted in the temperature range 750 - 1100°C for 5min, under uniaxial pressure of 60MPa in vacuum followed by free cooling to produce SPS pellets with diameter and thickness of 30mm and 5mm respectively. Full densification for both grades was reached at 950°C but at 800°C the relative density was already 99%. However, the grain sizes of the two grades were different when sintered at 950°C. CP-Ti grade 1 grains were coarser (~30µm) compared to that of CP-Ti grade 3 (~16µm). These authors explained these differences by the amounts of dissolved oxygen which was measured on the sintered pellets and was relatively higher (~0.32wt%) in CP-Ti grade 3 compared to CP-Ti grade 1 (~0.075wt%). On the contrary, Weston *et al.* (2015) explained this phenomenon in terms of particles shapes. For spherical particles the grain growth was rapid because there were higher initial particle-to-particle contacts with smaller pores and thus underwent more densification. In contrary to areas with less particle interactions and larger pores as found in irregular shaped particles

leading to lower densification. However, it is known that, oxygen is very detrimental to the mechanical properties of CP-Ti and its alloys because it has an influence on the microstructure (Yan *et al.*, 2014). ASTM CP-Ti grades are classified according to the oxygen content dissolved and this has shown to have effect on the transus temperature and Vickers hardness. For instance ASTM grade 1 has low oxygen content of 0.18wt% (~126HV) leading to lower transus temperature (890°C) while grade 3 has high oxygen content of 0.35wt% (~280HV) thus increasing the transus temperature to 920°C (Lütjering *et al.*, 2007b; Welsch *et al.*, 1993). Zadra *et al.* (2008) found that Vickers hardness of CP-Ti grade 3 (~190-240HV) was higher than CP-Ti grade 1 (~120-150HV) whatever the sintering temperature. The difference in Vickers hardness was attributed to high amount (~0.3-0.34wt %) of oxygen dissolved in grade 3.

Eriksson *et al.* (2005), studied the influence of sintering pressure and temperature on the morphology of SPS partially consolidated CP-Ti powders. The compacts heated to 200°C and 500°C with 50MPa pressure did not present change in grain size and morphology but the latter sample at 600°C was ~90% dense. According to the authors, at 500°C, particles deformation features were observed at grain boundaries instead of micro-welding and local melting of particles. However, the authors seem not to discuss the effect of pressure on the sintering mechanisms occurring. Different sintering mechanisms influenced by compaction pressure have been reported for Ti6Al4V alloy during SPS (Garbiec *et al.*, 2016) . The authors explained that sintering mechanisms at 5MPa compaction pressure occurred by electric discharges between particles and were dominant during the whole sintering stage. At much higher compaction pressure, at 25MPa and above, the electric discharges were only dominant in the early stages of sintering and were suppressed thereafter. The presence of spark discharges which is a pathway for electron migration have been proposed by Tokita (1999). This phenomenon occurs in the initial stages of sintering and leads to neck formations between particles. Experimentally neck formations have been observed for Ti6Al4V alloy with and without applied pressure (Kus, 2017). In contrast, Trzaska *et al.* (2016) have suggested no detection of the electric arcs, plasma or local overheating in TiAl intermetallic, but plastic deformation as the main densification mechanism.

Garbiec *et al.* (2016) further suggest that increased compaction pressure assisted in densification during heating by more rapid formation of necks favoring Joule effect which in turn enhanced diffusion and thereafter grain growth resulted. The grain sizes of samples

sintered with heating rate of 300°C/min increased from 15.49±3.81µm at 5MPa to 143.6±46.8µm at 25MPa. However at 50MPa the grain sizes reduced to 86.94±19.28 µm, authors explain that Joule effect was inferior at this pressure compared with 25MPa. The same effect was observed for 200°C/min and 400°C/min heating rates. Wang *et al.* (2017) report plastic deformation as densification mechanism in TiAl intermetallics prepared by SPS, the authors related the effect of pressure on density. At sintering temperature of 1150°C, by increasing pressure from 10MPa to 50MPa, the density gradually increased from 3.947g/cm^3 to 3.967 g/cm^3. The authors explained that higher sintering pressure led to more severe plastic deformation and it accelerated the mass transport between the particles which promoted densification. Plastic deformation of particles was confirmed by Trzaska *et al.* (2016), TEM thin foils were extracted in between necks of sintered TiAl powder particles, high densities of dislocations and twins which are characteristics of plastic deformation were observed. Despite the reported studies on the densification and mechanisms governed by sintering pressure for Ti6Al4V alloy and TiAl intermetallic, there is however limited literature on pressure effect on densification of CP-Ti powders.

1.2. Metal Matrix Composites

Generally, metal matrix composites (MMCs) can be defined as materials consisting of at least two distinct phases with different chemical and physical properties, for example a ceramic reinforcement embedded in a metallic matrix (Chawla *et al.*, 2006; Kainer, 2006). Metallic matrix is a continuous phase which is ductile, chemically unstable and has good thermal conductivity and its properties are improvised when reinforcement is introduced. Metallic matrix which have been explored in the literature include Al, Mg, Ti, Co, Ni, Be and Ag (Jayalakshmi *et al.*, 2015; Kainer, 2006).

Ceramic reinforcement is a load bearing phase in the composite due to its high Young's modulus, high strength and high stiffness (Jayalakshmi *et al.*, 2015; Kainer, 2006). The morphology of ceramic phase may be long fibers, short fibers or particulates made of oxides, carbides, nitrides and borides (Jayalakshmi *et al.*, 2015). The ceramic phases include SiC, Al_2O_3, B_4C, TiB_2, TiB, TiC, TiN, TiCN and graphite (Choi *et al.*, 2013; Kelly *et al.*, 2000; Song *et al.*, 2013).

The selection of metal matrix and reinforcing ceramic phase entirely depend on foremost compatibility of the two phases, required properties, intended applications and cost efficiency (Nalwa, 1999). In this regard, when good compatibility is obtained between the two distinct

phases, the resultant MMCs have outstanding properties such as increased yield and tensile strength at room and elevated temperatures, increased young modulus of elasticity, improved corrosion and wear resistance over the individual phases and some conventional material (Balaji *et al.*, 2015; Chawla *et al.*, 2006; Choi *et al.*, 2013; Kim *et al.*, 2011).

MMCs are categorized according to the type of reinforcement morphology and there are three major groups namely; continuous reinforcement in the form of long fibers and discontinuous reinforcement in the form of short fibers or whiskers, and particulates as shown in Figure 1.8 (Clyne *et al.*, 1995). Subsequently, the selection of reinforcement morphology is determined by the required properties, the application and the fabrication cost (Clyne *et al.*, 1995; Kelly *et al.*, 2000). For instance, the continuously reinforced MMCs have anisotropic properties, thus properties are high in the direction of the fiber orientation and the fabrication cost is relatively high (González *et al.*, 2001). As a result, the discontinuously reinforced MMCs which have isotropic properties are favorable because they are easy to fabricate and fabrication cost is low (Batraev *et al.*, 2014; Kim *et al.*, 2011).

MMCs can be fabricated by several methods, the commonly used are listed here

a) Liquid processes: casting, pressure infiltration, spray co-deposition and in-situ
b) Solid processes: powder metallurgy, extrusion, forging, pressing and sintering, roll bonding and co-extrusion, diffusion bonding
c) Gaseous state: physical vapor deposition (Chawla *et al.*, 2006)

MMCs are mostly used in industrial application such as aerospace, automotive, structural, military, commercial, industrial products, electronic packaging and thermal management. (Rosso, 2006).The demand for the use of MMCs is attributed to the availability of the ever-evolving sources of relatively inexpensive reinforcements, and the frequent development of the processing routes which results in reproducible microstructures and properties (Ajayan *et al.*, 2006).

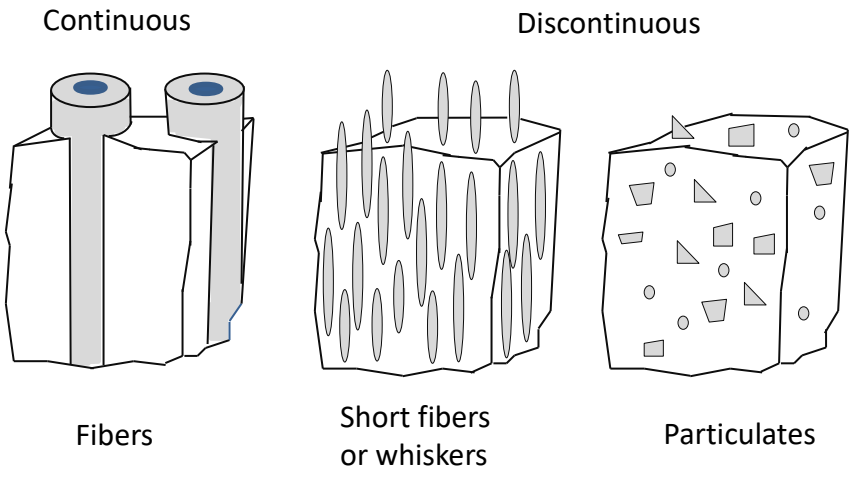

Figure 1.8. Three classes of reinforcement's morphology. Clyne et al. (1995)

1.2.1 Titanium Matrix Composites (TMC)

1.2.1.1 Continuously reinforced TMCs

SiC (SCS-6) fiber is the commonly used continuous reinforcing phase in TMCs normally with a larger diameter of about 100-140µm (Jayalakshmi *et al.*, 2015). SiC fibers are strong, stiff, have low density, have anisotropic properties and are widely used for high temperature (815°C) applications (Campbell, 2010). Main application for these classes of materials is in hot structures (hypersonic airframe structures) and in jet engines replacing some portions of super alloys. However due to their high cost, the fabrication process and assembly their use is limited (Campbell, 2010; González *et al.*, 2001). Moreover, interfacial reactions between titanium matrix and the fiber may occur during fabrication and also in later application at high~~er~~ temperatures (Campbell, 2010; Gundel *et al.*, 1991; Huang *et al.*, 2015). As a result second phase particles (Ti_3SiC_2, TiCx and $Ti_5Si_3(C)$) formed at the interface cause defects and significantly decrease mechanical properties of these composite (Kieschke *et al.*, 1991). Fukushima *et al.* (2000) studied the reaction kinetics between $Ti_{15}Al_3V$ and SiC fiber at heat treatment temperatures of 1153K and additional heat treatment at 1203K and 1253K. The reaction zone thickness increased linearly with the square root of the heat treatment time. The interfacial tensile strength of the composites decreased with the increase of reaction zone thickness. Therefore, focus has been made on selecting a compatible reinforcement with titanium matrix and also various SiC fiber coatings such as Mo, B_4C and C have been investigated to minimize or prevent the interfacial reactions (Luo *et al.*, 2012; Zhang *et al.*, 2014).

1.2.1.2 Discontinuously reinforced TMCs

TMCs reinforced with discontinuous fibers, whiskers or particles have isotropic properties and allow easy fabrication of near net shaped components and also secondary processing of the composites is possible (Campbell, 2010). A wide variety of discontinuous reinforcements including SiC, TiC, TiB_2, B_4C, TiN, and TiCN have received great attention because of their ability to improve mechanical properties of titanium (Choi *et al.*, 1994).These types of reinforcements are used in applications where the higher stiffness and strength properties of continuous reinforcements are not needed (Campbell, 2010).

Discontinuously reinforced TMCs (DTMCs) can be fabricated ex-situ and in-situ. For ex-situ fabrication (conventional processing), the reinforcing phase is prepared separately and later added to the metal matrix (Ajayan *et al.*, 2006; Casati *et al.*, 2014). Although DTMCs fabricated by ex-situ have demonstrated good properties making them suitable for variety of applications (Chen *et al.*, 2014; Prasad *et al.*, 2004), the composites interfacial bonding with the matrix is poor and sometimes the interface can be contaminated with second phases (Ajayan *et al.*, 2006). In case of the in-situ composites, the desired reinforcements are synthesized during fabrication step with exothermic chemical reactions between a compound and the titanium matrix (Campbell, 2010). The interface between titanium and reinforcing phase is normally without an interphase and a strong interfacial bond exists. Microstructure is characterized by a uniform dispersion of reinforcing phases in the matrix yielding optimized mechanical properties (Kainer, 2006). Due to different growth kinetics occurring with the individual reinforcing fibers, whiskers or particles, there is no specified orientation and also their sizes vary.

Among reinforcements, TiC and TiB_2 have shown to promote good wetting at the matrix/reinforcement interface, also they have showed to improve mechanical properties of Ti (Kim *et al.*, 2011). However due to their high melting temperatures (Table 4) and thus low diffusivity, TMC made of both pure TiC and TiB_2 phases are difficult to synthesize. However, the chemical instability of B_4C when reacted with Ti tends to be favorable as the products formed are TiC, TiB_2 and TiB. As a result simultaneous synthesis and consolidation of the TMCs by in situ method is accomplished. In the present study B_4C is chosen as a constituent element for in situ synthesis and consolidation of Ti - (TiB_2 + TiB + TiC) composites.

Table 4. Material properties of Ti, TiB_2 TiB, TiC (Chandran *et al.*, 2004) and B_4C (Domnich *et al.*, 2011; Sairam *et al.*, 2014)

Property	Ti	TiB_2	TiB	TiC	B_4C
Density (g/cm^3)	4.57	4.52	4.56	4.92	2.52
Elastic modulus (GPa)	110	540	371	450	570
Vickers hardness (HV)	150	2200	1800	3200	3793
Melting temperature (°C)	1668	2970	2200	3054	2763

1.2.1.3 Ti-TiB_2 composite

Titanium diboride (TiB_2) is a ceramic material known to have relatively high strength, durability and density of $4.52 g/cm^3$ close to that of pure titanium. It is characterized by high melting point of 2970°C, hardness of 2200HV, elastic modulus of 540GPa, strength to density ratio and excellent wear resistance (Ravi Chandran *et al.*, 2004). This material is used in engineering applications such as impact resistant armor, cutting tools, molten metal crucibles and heavy duty wear application (Basu *et al.*, 2006; Vallauri *et al.*, 2008). Its high melting point has restricted its broader application due economic factors. But with the current favorable developments in fabrication of components by powder metallurgy techniques, its production and thus vast application becomes possible (Munro, 2000). TiB_2 has unit cell consisting of eight Ti atoms at the vertices and two boron atoms at the center. The crystal structure of TiB_2 is shown in Figure 1.9, is a layered hexagonal structure with alternating closed-packed hexagonal layers of titanium and graphite-like boron layers. Similar to TiC and other ceramics, it has relatively low fracture toughness (~$5MPam^{½}$) and low self-diffusion coefficient making it difficult to sinter, thus a metallic binder is often needed in sintering (Morsi *et al.*, 2007).

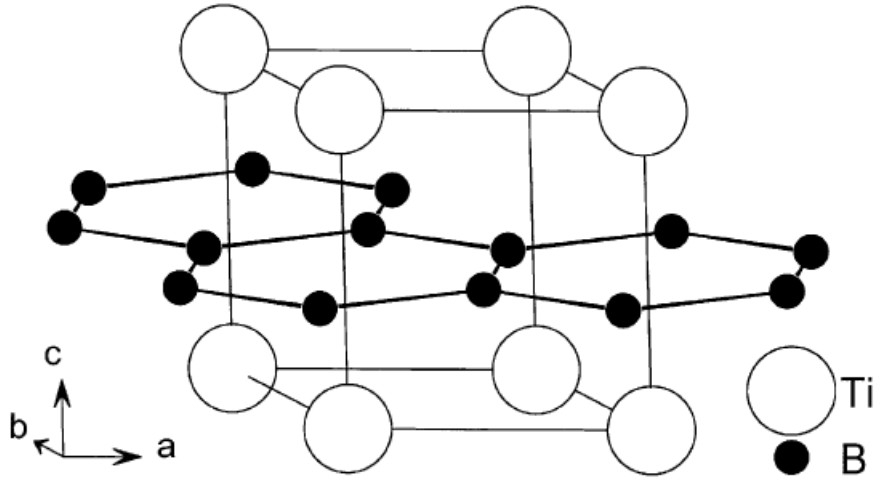

HCP : P6/mmm space group
Lattice parameters: a = 0.3026nm
c = 0.3226nm

Figure 1.9. TiB_2 crystal structure (Will, 2004)

In the production of Ti-TiB_2 composites, the Ti + 2B → TiB_2, reaction has more negative Gibbs free energy (ΔG). However, when mass fraction of Ti is higher than TiB_2, TiB_2 can further react with Ti to form TiB phase by this reaction, Ti + TiB_2 → 2TiB (Chandran *et al.*, 2004). The reaction has a slightly negative ΔG value (Figure 1.10) assuring that it can occur in Ti-TiB_2 composites. Moreover, because of low diffusion rates of B in Ti, the reaction rate is limited, so TiB_2 phase initially forms (from first reaction) and then followed by TiB phase (Morsi *et al.*, 2007).Eriksson *et al.* (2008) investigated densification and deformation of $Ti_x(TiB_2)_{1-x}$ composites by SPS from 1400 up to 1900°Cat holding times from 0 to 3min and pressure of 50MPa, using coarse grained Ti (45μm) and amorphous TiB_2 (1.4μm). Authors studied the effect of varying mass fraction (x=0.05, 0.1 & 0.2) of Ti on densification and phases formed. They found that at 1500°C, 3min and 50MPa densification was 100% for mass fraction x=0.05 and 0.1 when increased to x=0.2 the relative density decreased to 97%. Phases present for the three compositions after sintering was TiB_2 with Ti but for composite with x=0.2 TiB phase in minor amount was also detected.

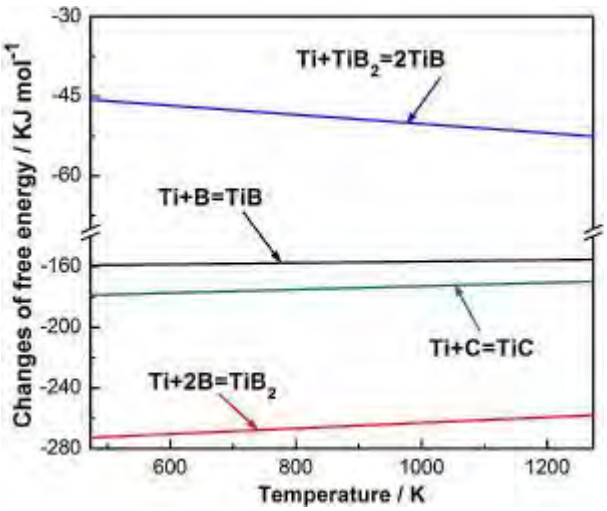

Figure 1.10. The values of ΔG for some reactions forming TiC, TiB_2 and TiB as a function of temperature (Mao et al., 2015)

1.2.1.4 Ti-TiB composites

Titanium monoboride, TiB, can be synthesized from a reaction between titanium and powder sources such as TiB_2, pure B, CrB and MoB (Balaji *et al.*, 2014; Feng *et al.*, 2006). Various synthesizing techniques such as combustion synthesis, rapid solidification and powder metallurgy have been employed to synthesize Ti-TiB composites (Cao *et al.*, 2015; Feng *et al.*, 2006). In cases whereby the powder source is TiB_2, TiB whisker is normally an intermediate phase between Ti and TiB_2 when incomplete reaction occurs. TiB has excellent chemical stability and the interfacial bonding between Ti and TiB is clean without interphase and this has shown to result in improved mechanical properties (Feng *et al.*, 2006). TiB has density of 4.56g/cm^3, high hardness of 1800HV, elastic modulus of 371GPa modulus thermal expansion coefficient of $8.6x10^{-6}$, thermal conductivity of 7.2 x $10^{-6}K^{-1}$. Its similar density to Ti make TiB even more attractive reinforcement because there is less modification in density, while mechanical properties of Ti are improved (Cao *et al.*, 2015; Ravi Chandran *et al.*, 2004; Sahay *et al.*, 1999).

In the crystal structure of TiB the principal building block is trigonal prism, whereby six Ti atoms are positioned at the corners and the B atom is at the center. The trigonal prisms stack up transversely in columnar arrays forming orthorhombic unit cell in its stable form of B27 structure (FeB type). From this, the B atoms arrangement pattern is characterised by zigzag chains which are parallel to the [010] direction as shown in Figure 1.11(a) (Feng *et al.*, 2006; Panda *et al.*, 2006; Ravi Chandran *et al.*, 2004). The growth mechanism of the TiB is the

stacking up of the (100) plane and the cross section of the TiB is normally a hexagonal structure with (100), (101) and $(10\bar{1})$ planes as show in Figure 1.11(b). Moreover the growth rate of the transverse direction is slower than the longitudinal direction (Feng *et al.*, 2006; Ravi Chandran *et al.*, 2004). Therefore, morphology of TiB is normally characterised by a needle like structure, namely whiskers (Feng *et al.*, 2006).

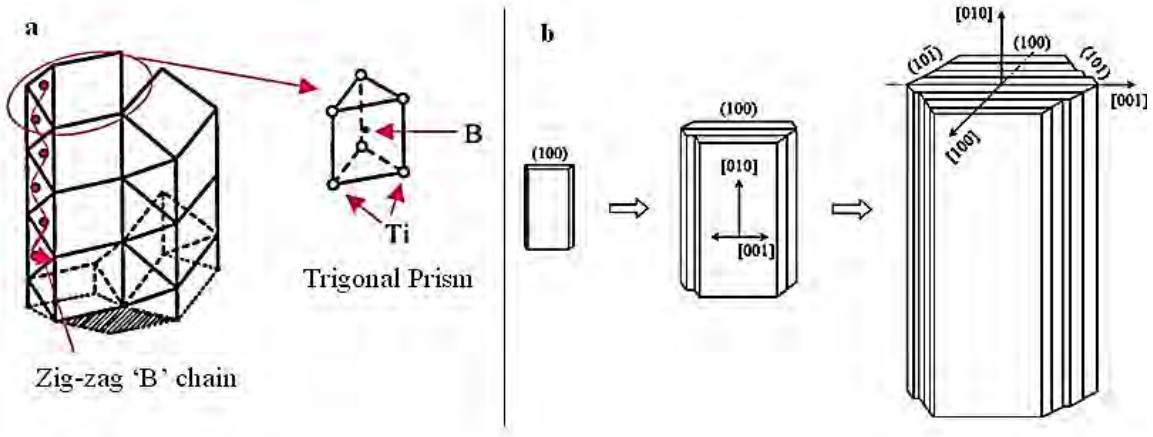

Orthorhombic: 62(Pnma) space group
Lattice parameters: a = 0.612nm, b = 0.306nm, c = 0.456nm

Figure 1.11. Crystal structure of TiB: a) Stacking up trigonal prisms with B zigzag chain (Panda et al., 2006), b) TiB whisker growth (Feng *et al.*, 2006).

Shen *et al.* (2011), in situ synthesized TiB reinforced TMCs from Ti and TiB_2 powders with average particles sizes of 30 μm and 4.5μm fabricated by SPS method respectively, with a composition of 15wt% TiB_2 and 85wt% Ti powder. The structure of the sintered composites showed that TiB was formed at 950°C and the microstructure revealed a uniform distribution of needle and rod shape TiB whiskers with a high aspect ratio growing rapidly with sintering temperature. The rapid growth of the TiB whiskers leads to coarsening and agglomeration of the whiskers leading to cross-sectional diameters from 0.2μm to 2 μm at 950°C and 1150°C respectively. According to the authors the TiB whiskers which are fine grow along the grain boundaries while others grow towards inner grains of titanium. Sahay *et al.* (1999) reported three different morphology of TiB formed at low and high volume fraction of the reinforcement fabricated by hot pressing. The first morphology at low volume fractions of 0.3 was characterised by long and needle-shaped TiB whiskers which are isolated and randomly oriented in the Ti matrix. The second morphology at volume fractions of 0.55 to 0.86, colonies of refined and densely packed short TiB whiskers which seemed to be interconnected

were observed. Chandran *et al.* (2004) explain the interconnection morphology of TiB whiskers to be due to spatial diffusion limitations of boron atoms from the parent TiB_2 particle and resulted in interceptions between TiB whiskers forming from that parent TiB_2. The third morphology at the highest volume fractions of 0.92, the TiB whiskers were coarse and elongated with a few needle-shaped whiskers. Further illustration of the different morphologies developments at low and high volume fraction of starting TiB_2 powders is shown in Figure 1.12. The dominant reinforcing phase was TiB however at higher volume fractions of 0.86 and 0.92, a significant amount of unreacted TiB_2 was still present (Sahay *et al.*, 1999). Table 5 presents some of the relative densities and hardness values of sintered Ti-TiB composites found in literature.

Table **5**. Relative densities and hardness values of Ti-TiB_2/TiB sintered composites

Reference	Process & parameters	Material	Relative density (%)	Hardness (HV)
(Diouf *et al.*, 2017)	**SPS**			
	1000°C, 50MPa, 5min	Ti2.5wt%TiB_2	98.9	~ 360
		Ti5wt%TiB_2	97.8	~ 380
(Namini *et al.*, 2017)	**SPS**			
	1050°C, 50MPa, 5min	Ti – 0.6wt%TiB_2	98	328±08
		Ti – 1.2wt%TiB_2	98	344±06
		Ti – 2.4wt%TiB_2	99	363±09
		Ti – 4.8wt%TiB_2	99	477±13
		Ti – 9.6wt%TiB_2	100	586±17
(Chaudhari *et al.*, 2013)	**SPS**			
	1300°C, 50MPa & 10min	Ti – 10wt%TiB	98	416
(Shen *et al.*, 2011)	**SPS**			
	950°C, 50MPa & 5min	Ti – 26vol%TiB	94	Phase 1 = 418
				Phase 2 = 449
	1250°C, 50MPa & 5min	Ti – 26vol%TiB	100	Phase 1 = 479
				Phase 2 = 673
(Kumar *et al.*, 2012)	**SPS**			
	1100°C, 20MPa & 5min	Ti – 24vol%TiB	99	710
		Ti – 38.5vol%TiB	96	890
	Hot isostatic pressing			
	1200°C, 120MPa & 5h	Ti – 20.6vol%TiB	99	658
		Ti – 38.3vol%TiB	99	823
	Vacuum sintering			
	1200°C & 5h	Ti – 17.6vol%TiB	85	424
		Ti – 37.9vol%TiB	95	618
(Gorsse *et al.*, 2003)	**Reactive hot pressing**			
	900°C, 80MPa & 2h	Ti – 20vol%TiB	-	550
(Alman *et al.*, 1999)	**Cold isostatic pressing**			
	1400°C, 275MPa, 2h	Ti2.5vol%TiB_2	88.8	265
		Ti5vol%TiB_2	93.3	234
		Ti10vol%TiB_2	96.0	413
		Ti20vol%TiB_2	98.8	610
		Ti40vol%TiB_2	76.5	352

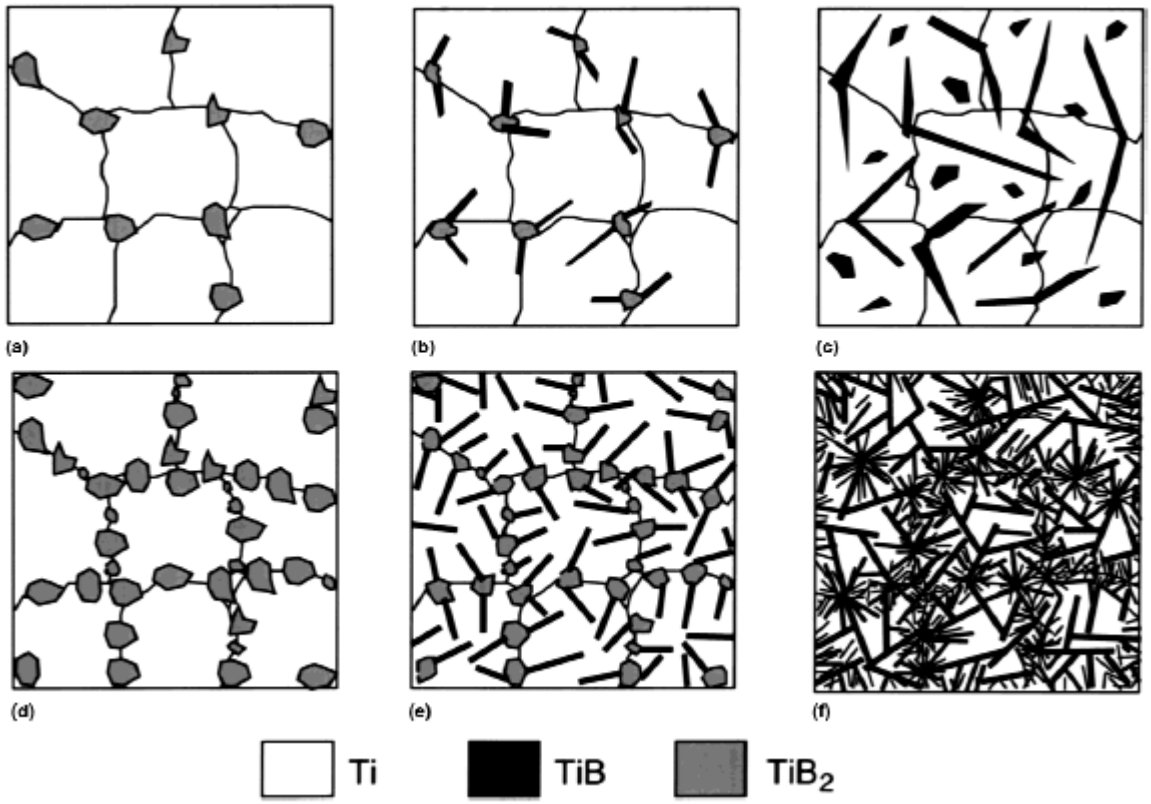

Figure 1.12. Schematics of TiB whisker morphologies development in Ti-TiB composites at starting volume fraction of TiB_2: (a, b & c) low volume fraction of 10vol% TiB_2, (d, e & f) high volume fraction of 29vol% TiB_2 (Sahay *et al.*, 1999).

1.2.1.5 Ti-TiC composites

Titanium carbide (TiC) belongs to a class of interstitial carbides and its crystal structure is face centered cubic (FCC) (Fu et al, 2017). The building unit cell consists of six titanium atoms positioned in the corners and surface centers of the FCC with interstitial carbon atom positioned in center of each corners and the cubic as shown in Figure 1.13 (Jin *et al.*, 2002; Nie *et al.*, 2012). Two types of bond exist in TiC that is metallic Ti-Ti bond and a much stronger covalent Ti-C bond (Djellouli *et al.*, 2001; Johansson, 1995). TiC has high electrical and thermal conductivity of 30 x 10^6 S/m and 28.9 $Wm^{-1}K^{-1}$ respectively. It has low density of 4.92g/cm^3, high hardness greater than 3200HV, elastic modulus of 450GPa, low friction coefficient, high solvency with other carbides and high melting temperature of 3054°C due to its strong covalent bonds (Fu *et al.*, 2017; Ravi Chandran *et al.*, 2004). These properties make TiC an abrasive material that is resistant to high temperature oxidation and in chemically corrosive environments (Vallauri *et al.*, 2008). It is widely used in abrasive wear applications

such as cutting tools, gears, bearings and shafts it is also useful in erosion, corrosion and creep (engine) applications (Covino Jr *et al.*, 2002; Gu *et al.*, 2012; Mohanty *et al.*, 1995)

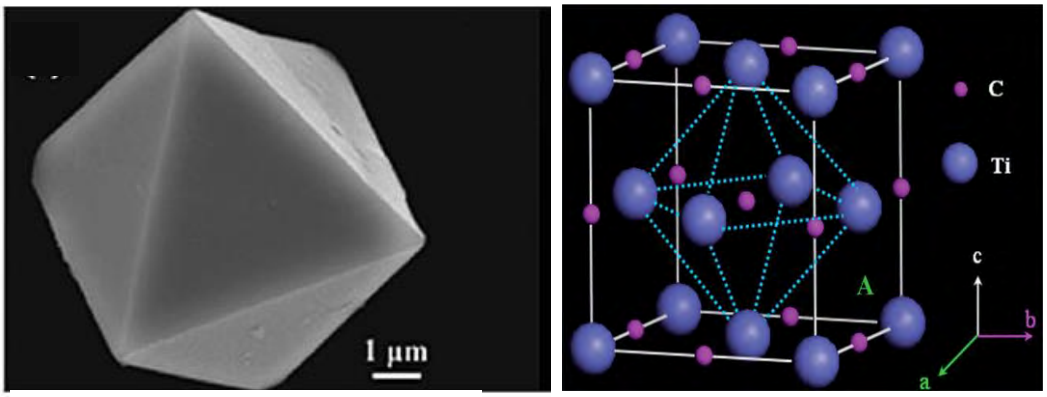

FCC: Fm-3m space group
Lattice parameters: a = 0.4328nm

Figure 1.13. TiC crystal structure (Nie *et al.*, 2012)

TiC is brittle in nature, as such metallic binders are normally incorporated to provide ductility and toughness in the bulk material. In terms of sintering, the binder phase also aid in consolidation to full density by controlling bonding with the ceramic phase (Hussainova, 2003). This is due to TiC poor sinterability resulting from its low self-diffusion coefficient which is unfavorable for mass transfer. At high temperature it experiences rapid grain growth leading to pores entrapment in grains and also oxide impurity in the powder inhibits densification (Gu *et al.*, 2017). However, with addition of binding phase to TiC the hardness and corrosion/oxidation resistance properties are reduced. Nevertheless, economical sintering of TiC still partly requires liquid phase for full densification during sintering because of its higher melting temperature (Teber *et al.*, 2012). Previous studies have shown that high sintering temperature was required for TiC consolidation as shown in Table 6. Relative densities obtained by presureless sintering in Fu *et al.* (2017) and Gu *et al.* (2017) at temperatures of 1700°C and 2300°C was 95.7% and 96.67% with grain sizes of 5.5±0.9µm and 7.5µm respectively. For hot pressing and spark plasma sintering in the study of Xue *et al.* (2016) and Cheng *et al.* (2012) at 2000°C and 1600°C densification was 98.15% and 99% with grain sizes of 19.62µm and 3.21µm respectively. These results clearly indicate the need for a binding phase to lower the sintering temperature while achieving full densification. Several metallic binding phases such as Co, Cr, Ni, Mo, Al, Ti and Fe have been explored and have shown excellent hardness, fracture toughness and wear resistance (Degnan *et al.*, 2002; Fu *et al.*, 2016; Kübarsepp *et al.*, 2001; Lagos *et al.*, 2016; Li *et al.*, 2009; Teber *et al.*,

2012; Wu *et al.*, 2011). TiC composites based on Ti and Ti6Al4V as matrix are the most common combination explored mainly because of their chemical compatibility (Georgiou *et al.*, 2017; Konitzer *et al.*, 1989; Lagos *et al.*, 2016).

Table 6. Relative densities and hardness values of Ti-TiC sintered composites

Reference	Process & parameters	Material	Relative density (%)	Hardness (HV)
(Vasanthakumar *et al.*, 2017)	**SPS**			
	800°C, 50MPa, 5min	Ti25wt%TiC	97%	1121±103
	1000°C, 50MPa, 5min		99%	1232±128
	1200°C, 50MPa, 5min		102%	1595±136
	800°C, 50MPa, 5min	Ti50wt%TiC	87%	475±40
	1000°C, 50MPa, 5min		88%	402±70
	1200°C, 50MPa, 5min		102%	871±102
(Zhang *et al.*, 2017)	**SPS**			
	1200°C, 5min, 50MPa	Ti3vol%TiC	4.550g.cm^{-3}	458
		Ti7vol%TiC	4.564g.cm^{-3}	514
(Diouf *et al.*, 2017)	**SPS**	Ti2.5wt%TiC	99.3%	~350
	1000°C, 50MPa, 5min	Ti5wt%TiC	99.3%	~375
(Cheng *et al.*, 2012)	**SPS**	TiC	99%	3091
	1600°C, 50MPa, 5min			
(Fu *et al.*, 2017)	**Presureless sintering**	TiC	95.7%	2070
	1800°C, 1h			
(Gu *et al.*, 2017)	**Presureless sintering**	TiC	96.67%	2243
	2300°C, 1h			
(Xue *et al.*, 2016)	**Hot pressing**	TiC	98.15%	-
	2000°C, 30MPa, 60min			
(Alman *et al.*, 1999)	**Cold isostatic pressing**	Ti2.5vol%TiC	89.1%	245
	1400°C, 275MPa, 2h	Ti5vol%TiC	94.2%	296
		Ti10vol%TiC	93.8%	304
		Ti20vol%TiC	96.0%	354
		Ti40vol%TiC	95.1%	354
(Gülsoy *et al.*, 2014)	**Powder injection moulding**	Ti1.5wt%TiC	~97%	~106*
		Ti3wt%TiC	~95.5%	~110*

***HRB**

According to the binary phase diagram of Ti-C in Figure 1.5, the interaction between Ti based matrix and TiC leads to formation of wide range of (x=0.5-1.0) sub-stoichiometric carbides according to reaction 1 (Baker, 1992).

$$(1\text{-}x)TiC + xTi = TiC_{1\text{-}x} \qquad [Eq.1]$$

Quinn *et al.* (1984) investigated solid state reaction of single-crystal diffusion couples of Ti and TiC forming sub-stoichiometric carbides during sintering and hot pressing from 1350 up

to 1525°C. According to the authors, the reaction between reactants proceeds by carbon diffusion at the interface of reactants forming sub-stoichiometric carbides in the sequence $TiC_{0.89}$, $TiC_{0.53}$ and $TiC_{0.01}$ from the centre of TiC particle into the Ti matrix.. Microstructural analysis of reaction couple revealed growth of second phase platelets into the original TiC crystal. The morphology of the platelets resembled that of Widmanstatten pattern. Authors suggest that carbon diffuse across the Ti-TiC interface and react to form $TiC_{0.5,}$ the product nucleates at the interface and grow with the advancing phase boundary and also back into the original carbide crystal. The Ti_2C phase provides a faster diffusion path for carbon atoms in new carbide phase (Ti_2C) and also in the original carbide crystal.

Wanjara *et al.* (2000) also reported the presence Ti_2C phase at interface of Ti6Al4V alloy and TiC compacts processed by graphite-element vacuum furnace at 1200 and 1500°C. Microstructural analysis by low voltage FEG-SEM showed a distinct phase at the boundary of TiC particles. EDS quantitative elemental analysis revealed a low amount of carbon at boundary and it increased towards the center of the TiC particle. Further analysis by neutron diffraction revealed that lattice parameters of the matrix increased with the holding time at the various isothermal temperatures, suggesting that carbon diffuse from the TiC to the Ti6Al4V alloy matrix. However, the authors do not report any Widmanstatten pattern morphology for Ti_2C in the TiC particles as observed by Quinn 1984. They reported a rapid growth of interface layer with processing temperature at 1500°C until the entire TiC particle has fully reacted. However, with in-situ synthesized Ti based TiC composites using various carbon sources such as graphite (Yu *et al.*, 2017), carbon fiber (Hao *et al.*, 2015), graphene (Zhang *et al.*, 2017), the interface between matrix and reinforcing phase is normally clean without interphase and have strong metallurgical bonds (Kainer, 2006). On the contrary, Vasanthakumar *et al.* (2017) reported formation of non-stoichiometric TiC_x when CNT was the carbon source. In fact, the carbon addition was obtained from decomposition of toluene during milling for 10h this was confirmed with XRD and Raman spectroscopy analysis and not from the CNT.

1.2.1.6 Ti - B_4C composites

Boron carbide (B_4C), is one of the hardest engineering materials with hardness value of 3793HV, a high elastic modulus of 570GPa, low density of 2.52 g/cm^3, melting temperature of 2763°C and high electrical resistivity at elevated temperatures (Domnich *et al.*, 2011; Sairam *et al.*, 2014). Because of its high melting point and thermal stability it is used in

refractory applications. Its extreme abrasion resistance make it useful as abrasive powder and coating. Also it is commonly used in nuclear applications as neutron radiation absorbent. Moreover, boron carbide is a high temperature semiconductor that can potentially be used for novel electronic applications. The primary structural units of boron carbide are the 12-atom icosahedra located at the vertices of a rhombohedral lattice of trigonal symmetry (R3m space group), and the 3-atom linear chains that link the icosahedra along the (111) rhombohedral axis, as shown in Figure 1.14 (Domnich *et al.*, 2011). B_4C has received much attention in the fabrication of in situ titanium based TiC, TiB_2, TiB composites, more especially in fabrication by powder metallurgy techniques. This is due to its lower melting temperature of 2763°C compared to that of the single phases TiC (3054°C) and TiB_2 (2970°C).

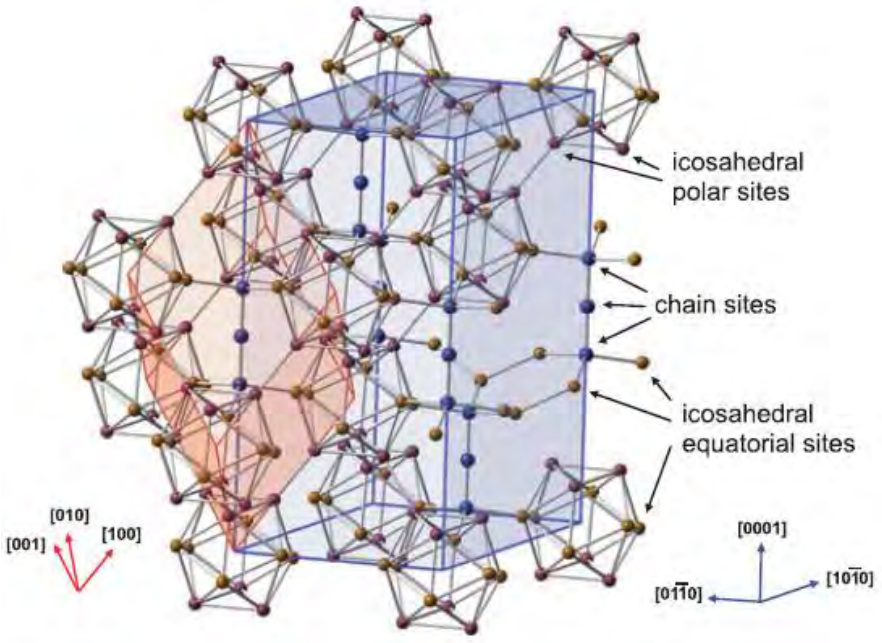

Figure 1.14. Crystal lattice of B_4C illustrating the correlation between the rhombohedral in read and the hexagonal in blue unit cells (Domnich et al., 2011).

The relative densities of with the mechanical properties of Ti-B_4C are summarised in Table 7. Balaji *et al.* (2014) investigated the densification behaviour and microstructural evolution of Ti (100µm) and B_4C (50 µm) powder mixture by SPS. Sintering was performed at 1400°C with pressure 40MPa and varying dwell time of 5 to 30min. On the densification behaviour at 30min dwell time, the relative density decreased with increasing amount of B_4C from 99.06±0.224% to 98.04±0.236% for Ti5wt%B_4C and Ti15wt%B_4C respectively. While on the sintering parameters effect, Ariza Galván *et al.* (2017) reported that increase of temperature from 1000°C to 1100°C increased density from 3.83g/cm^3 to 3.87 g/cm^3 for Ti30vol%B_4C at

50MPa. Also by increasing dwell time from 1 to 5min the density was improved from 3.77 g/cm^3 to 3.83 g/cm^3 at 950°C and 80MPa, similar results when dwell time was increased from 5min to 30min have been reported (Balaji *et al.*, 2013). However, the increase of pressure from 50MPa to 80MPa at 1000°C had an insignificant effect on the density which remained constant (Ariza Galván *et al.*, 2017). While Shufeng *et al.* (2015) further hot extruded vacuum sintered composites billet to improve the density and microstructure.

Table **7**. Relative densities and hardness values of Ti-B_4C sintered composite

Reference	Process & parameters	Material	Relative density (%)	Hardness (HV)
(Ni *et al.*, 2006)	**Hot Pressing**			
Ti : 10µm	1200°C, 30min, 20MPa	Ti10vol%B_4C(0.5µm)	-	581
B_4C: 0.5µm		Ti10vol%B_4C(3.5µm)	-	452
B_4C: 3.5µm				
(Balaji *et al.*, 2014)	**SPS**			
Ti : 100µm	1400°C, 30min, 40MPa	Ti5wt%B_4C	99.06±0.224	-
B_4C : 50µm		Ti10wt%B_4C	98.46± 0.223	-
		Ti15wt%B_4C	98.04±0.236	-
(Ariza Galván *et al.*, 2017)	**Inductive hot pressing**			
Ti: 20-45µm	950°C, 80MPa, 1min		3.77*	317
B_4C:45-75µm	950°C, 80MPa, 5min		3.82*	333
	1000°C, 50MPa, 5min	Ti30vol%B_4C	3.83*	324
	1000°C, 80MPa, 5min		3.83*	383
	1100°C, 50MPa, 5min		3.82*	397
	1100°C, 80MPa, 1min		3.87*	367
(Jimoh *et al.*, 2012)	**Presureless sintering**			
TiH_2: 4.5µm	1400°C	Ti		270 ± 30
B_4C: 4.6µm		Ti10vol%B_4C	100	705 ± 20
		Ti20vol%B_4C	99.12	850 ± 40
		Ti40vol%B_4C	93.44	860 ± 25
	Hot pressing	Ti20vol%B_4C	100	942 ± 5
	1400°C, 30MPa	Ti40vol%B_4C	100	1085 ± 35
		Ti60vol%B_4C	100	1455 ± 50
		Ti80vol%B_4C	100	1600 ± 20
	Presureless sintering			
	1100°C	Ti		270±31
		Ti10vol%B_4C	97.36	727±10
		Ti20vol%B_4C	92.09	695±21
		Ti40vol%B_4C	80.53	500±11
	Hot pressing	Ti20vol%B_4C	98.46	921±33
	1100°C,	Ti40vol%B_4C	99.34	1061±14
	30MPa,120min,	Ti60vol%B_4C	93.04	1194±66
	10°C/min	Ti80vol%B_4C	67.32	232±12

It is crucial to understand reaction kinetics and thermodynamics of the interfacial reactions in TMCs, as they aid when improving the mechanical properties of the composite. The data found in literature based on the reaction kinetics and the thermodynamics of interfacial reactions is mostly focused on continuous SiC based TMC (Campbell, 2010; Fukushima *et*

al., 2000; Gundel *et al.*, 1991; Huang *et al.*, 2015; Jayalakshmi *et al.*, 2015; Kieschke *et al.*, 1991; Luo *et al.*, 2012; Zhang *et al.*, 2014) and TiB_2 based coatings on Ti/Ti alloys (Ataibis *et al.*, 2015; Fan *et al.*, 1997; Fenghua *et al.*, 2010; Kartal *et al.*, 2013; Keddam *et al.*, 2017; Keddam *et al.*, 2016; Makuch *et al.*, 2017), and limited for TMCs prepared by powder metallurgy techniques.

Recently, attempt has been made to study the effect of temperature and processing time in the kinetics of TMCs for such techniques. Jia *et al.* (2016) investigated solid state reaction mechanisms of SPS Ti-B_4C system (1000°C, 60min and 30MPa) using experimental investigations and theoretical calculations. Observations made by laser scanning confocal microscope revealed decomposition of B_4C into B and C diffusing on the Ti side to form fine TiB whiskers and TiC particles and the sharp corners of the B_4C became smoother. Interdiffusion competition between B, C and Ti atoms in either Ti and B_4C rich side was proposed to be the reaction mechanisms occurring at the interface of the reactants as shown in Figure 1.15. Similar observations were made for mechanically alloyed Ti-B_4C (Rafiei *et al.*, 2014). However, when it came to which phase formed first between TiB and TiC, comparing the theoretical and experimental analysis there seemed to be a contradiction (Jia *et al.*, 2016; Ni *et al.*, 2008b; Rafiei *et al.*, 2014).

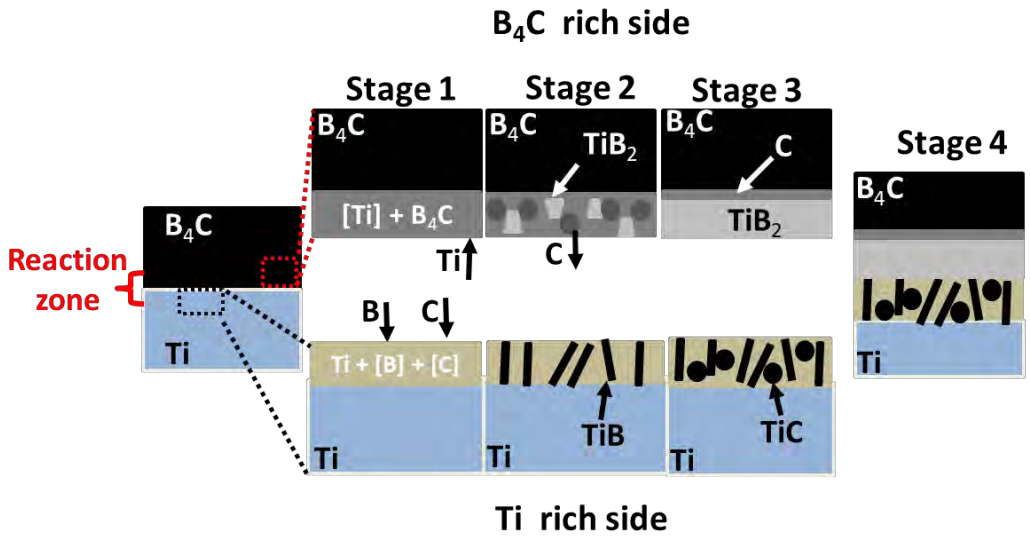

Figure 1.15. Chemical reactions mechanisms in Ti-B_4C couple system. Adapted from (Jia et al., 2016)

Theoretically, the threshold activities for formation of TiB_2 (5.96×10^{-7}) and TiB (3.97×10^{-7}) are higher than that of TiC (1.05×10^{-7}), so TiC was expected to primarily form followed

by TiB rather than TiB_2 (Jia *et al.*, 2016). However, experimentally the DTA analysis and XRD patterns for mechanically alloyed Ti-B_4C Rafiei *et al.* (2014) proposed that TiB_2 phase forms first then TiC followed. While Jia *et al.* (2016) suggest that although the theoretical threshold activity for formation of TiC (1.05×10^{-7}) is lower than that of TiB (3.97×10^{-7}), according to concentration level of B and C determined around the Ti/B_4C interface, TiB formed first prior to TiC in agreement with (Rafiei *et al.*, 2014). This suggestion was based on the lower and high diffusion velocity of B and C in Ti matrix respectively (Brodkin *et al.*, 1996; Rafiei *et al.*, 2014).So, C diffuse further into Ti matrix and later form TiC particles while, B diffuse closer to Ti/B_4C interface to form TiB whiskers. Hence, this resulted in higher concentration of B at the Ti/B_4C interface than C atoms (Jia *et al.*, 2016).

The proposed sequence of atoms inter-diffusion mechanisms in SPS Ti-B_4C layers by (Jia *et al.*, 2016) is as follows. In the initial stage, B_4C decomposes, B and C atoms diffuse into Ti matrix, and chemical reactions [Eq. 3, 4 and 5] which solely depends on B and C atoms take place. Simultaneously in B_4C rich side Ti diffuse into vacancies left by B and C atoms, reactions in [Eq. 6 - 9] which depend on Ti atoms they take. In the second stage TiB whiskers form in Ti rich side and while dispersed TiB_2 particles form in B_4C rich side due to limited amount of Ti atoms and also some C was formed. The C then diffuses into the Ti rich side and increases the C carbon content to form TiC particles in stage 3 of reaction. Further processing of the in situ reaction in stage 4 results in formation of a monolithic layer of TiB_2, which inhibits C diffusing out and results in C layer which form between unreacted B_4C and monolithic layer of TiB_2. At this stage reaction between Ti and B_4C stops because B and C can hardly diffuse across monolithic layer of TiB_2.

$$Ti + 2B \rightarrow TiB_2 \quad \text{[Eq. 2]}$$

$$Ti + B \rightarrow TiB \quad \text{[Eq. 3]}$$

$$Ti + C \rightarrow TiC \quad \text{[Eq. 4]}$$

$$Ti + B_4C \rightarrow TiC + 4B \quad \text{[Eq. 5]}$$

$$2Ti + B_4C \rightarrow TiB_2 + C \quad \text{[Eq. 6]}$$

$$3Ti + B_4C \rightarrow TiB_2 + TiC \quad \text{[Eq. 7]}$$

$$4Ti + B_4C \rightarrow 4TiB + C \quad \text{[Eq. 8]}$$

$$5Ti + B_4C \rightarrow 4TiB + TiC \quad \text{[Eq. 9]}$$

On the microstructure evolution Jia *et al.* (2016) investigated two layers composed of sintered B_4C and Ti powder. The sintered B_4C (0.5µm) was placed onto inferior punch of SPS mold then filled up with pure Ti powder. To study the microstructure evolution the sintered cold compacts were heat treated at varying temperature from 700°C to 900°C for 5 min as well at 1000°C with varied dwelling time of 5 min to 60 min. On the effect of temperature, at lower temperature (700°C) the reaction between Ti and B_4C did not take place due to poor compaction. Increasing temperature to 800°C for 5min, led to improved contact and formation of large amount of fine TiB whiskers on the Ti side and the interface was observed. Further increase in temperature to 900°C for 5min a thick TiB_2 layer formed with fine TiB whiskers growing from it. The TiB_2 layer became denser while the TiB whiskers. Balaji *et al.* (2014) reported the reduction of ''spherical'' B_4C particles size to needle like TiB and equiaxed TiC particulates forming a homogeneous microstructure. When dwell time was increased from 5 to 30min at higher temperatures of 1400°C as shown in Figure 1.16. However, Jia *et al.* (2016) found that at lower temperature of 1000°C dwelling time had insignificant effect on the growth TiB whiskers while the layer of TiB_2 became thicker (4µm). The microstructure at 1000°C for 10min was the same as for 30min and 60min (Jia *et al.*, 2016).

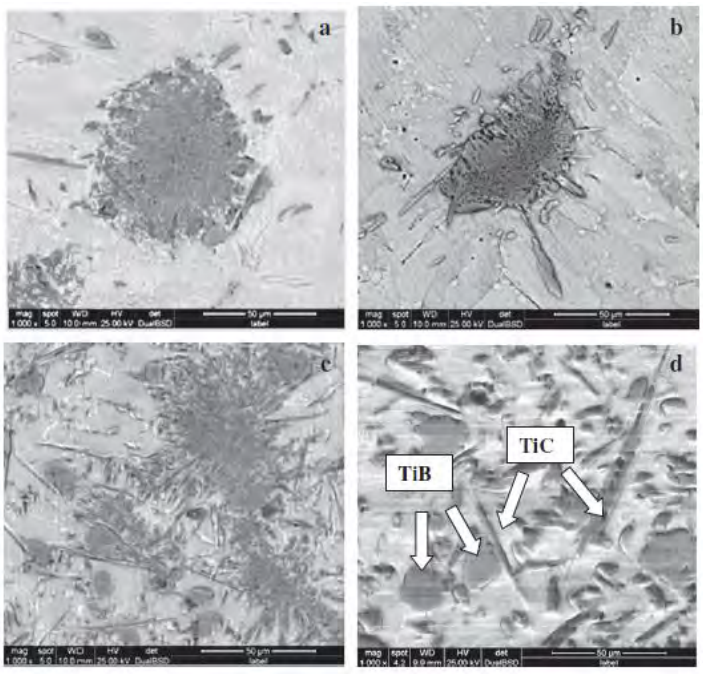

Figure 1.16 . Microstructure evolution of Ti-B_4C sintered at a) 5min, b) 10min, c) 15min and d) 30min (Balaji et al., 2014).

Particles size of B_4C also has effect on the formation of TiB and TiC reinforcing phases. It was found that hot pressed (1200°C and 20MPa for 30min) Ti-B_4C composites fabricated using 3.5µm B_4C formed particles clusters while those with 0.5µm B_4C powder particles clusters were absent (Ni *et al.*, 2006). The size of the TiB clusters was similar to the original size of the B_4C particles and were characterised with many small TiC particulates with a diameter of 0.5µm surrounded by densely packed fine TiB whiskers. The TiB whiskers grew in all directions from centers initially occupied by B_4C particles before reaction occurred, after the complete reaction B_4C was consumed, but inhomogeneous microstructure was obtained. These TiB clusters have adverse effect on mechanical properties, the could act as crack initiators at much lower strains, limiting the strength and ductility of the composite (Gorsse *et al.*, 2003). Only by either further heat treatment (1200-1300°C), hot extrusion (1100°C) or prolonged processing time (6-100h) the particles clusters were eliminated at the expense of excessive matrix grain growth (Gorsse *et al.*, 2003; Ni *et al.*, 2006). Mechanical properties of the extruded composites and composites with finer B_4C (0.5µm) powders were evaluated and compared. The tensile strength of the extruded composites was 817MPa with ductility of 0.55% lower than that without particles clusters (950MPa and 0.64%) (Ni *et al.*, 2006).

When the correct processing conditions (temperature, time, pressure) are utilized the final microstructure of the Ti-B_4C composites is expected to be characterized homogeneously distributed TiB and TiC. In addition, a symbiosis structure as shown in Figure 1.17 of TiB and TiC has been reported to exist for Ti-B_4C system prepared by reactive hot-pressing (1200°C, 20MPa and 30min) of blended Ti and B_4C powders. Whereby, the TiC particle appeared to be relatively fixed into the TiB whisker. Observations made by TEM showed the TiC particles with crystal planes $(\bar{1}0\bar{1})$ and $(11\bar{1})$, grew on the TiB whisker in (101) and $(10\bar{1})$ crystal planes and seldom on the (100) crystal plane (Ni *et al.*, 2008b). Available literature based on solid state fabrication support this structure formation (Li *et al.*, 1993; Tang *et al.*, 2000; Vallauri *et al.*, 2008). This phenomenon results from large number of stacking faults in the (100) TiB plane causing steps in the $(\bar{1}0\bar{1})$ and $(11\bar{1})$ TiB planes. The steps cause a roughening on the crystal planes which promotes the growth of TiC in them (Li *et al.*, 1993). In addition, interconnections of TiB whiskers formed from Ti-TiB_2 system have also been reported, the morphology is favoured because the growth of TiB is by decomposition of TiB_2, TiB whiskers grow from centres occupied by TiB_2 particles (Huang *et al.*, 2009; Sahay *et al.*, 1999).

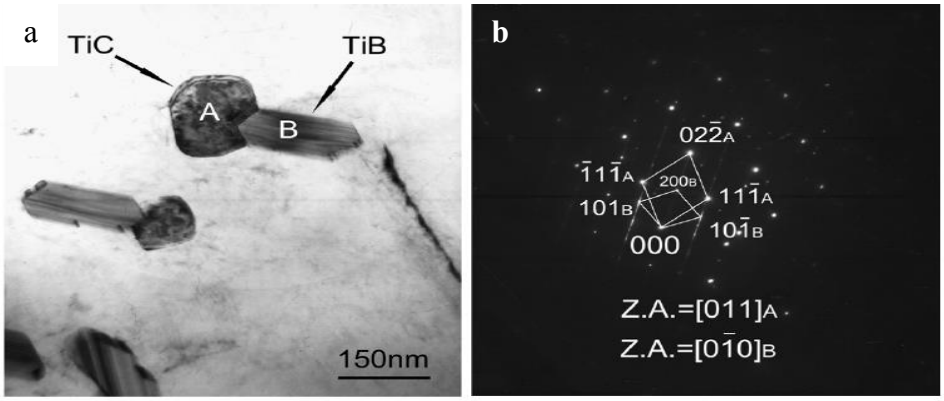

Figure 1.17. TEM micrographs of composites symbiosis structure (a) bright field images and (b) electron diffraction patterns corresponding

On the mechanical properties evaluation of Ti-B_4C composites fabricated by powder metallurgy routes, the available literature is focused on the strengthening effect of TiC and Ti at room and elevated temperature strength of Ti matrix, the effect of B_4C particles size and composition effect (Barsoum *et al.*, 1993; Bhaumik *et al.*, 2000; Brodkin *et al.*, 1996; Geng *et al.*, 2008; Jia *et al.*, 2014a; Jia *et al.*, 2014b; Ni *et al.*, 2006, 2008a; Ogwu *et al.*, 1996; Shufeng *et al.*, 2015; Tjong *et al.*, 2008; Wen *et al.*, 2001). Shufeng *et al.* (2015) carried out room temperature tensile tests a strain rate of 5 x 10^{-1} s^{-1} of TMCs consisting of TiB whiskers with low volume fraction of fine TiC particles. The yield and tensile strength increased gradually when the B_4C content volume fraction was increased from 0, 1.76, 2.85 and 5.0vol%. Ti-5vol%B_4C TMCs showed improved yield and tensile strength of 916MPa and 1138MPa, compared with pure Ti 484MPa and 654MPa respectively. However, elongation was compromised and reduced significantly from 32.4% to 2.3% for the Ti-5vol%B_4C TMC.

With the effect of increasing the temperature from 25 to 700°C the tensile strength decreased from ~1200 to 100MPa and ~700 to 40MPa for the Ti-1.61wt%B_4C TMCs and Ti, respectively. The decrease of strength was attributed to softening of Ti matrix at elevated temperatures (Jia *et al.*, 2014a).

On the particle sizes effect Ni *et al.* (2006) found that the tensile and yield strength were improved when the B_4C particles sizes was reduced from 3.5µm to 0.5µm for hot pressed (1200°C, 20MPa and 30min) Ti-10vol%B_4C TMCs. The extruded (1100°C) Ti-10vol%B_4C

TMCs with 3.5µm B_4C tensile strength was 817MPa with ductility of 0.55%, and the finer Ti-10vol%B_4C TMCs with 0.5µm B_4C yielded improved strength of 950MPa without reduction in ductility of 0.64%. In contrast, Ti-1.61wt%B_4C TMCs prepared by SPS (1000°C, 30MPa and 60min) and extrusion (1000°C), with 40µm (11.73%), 11µm (9.26%) and 0.5µm (6.9%) B_4C particles size showed reduced ductility for the finer TMCs, but the ultimate tensile strength was improved (709.98, 873.56 and 1117.76MPa) respectively (Jia *et al.*, 2014b).

Load transfer strengthening mechanism from the soft Ti matrix onto the hard TiB and TiC reinforcements take place in the TMCs. Long TiB whiskers are however reported to be prone to stress concentration and fracture due to their large aspect ratio. Although the TiC particles cannot take up loads as efficient as TiB whiskers, they prevent cracks from being formed and retard the crack propagation more effectively than TiB whiskers due their equiaxed shape (Ni *et al.*, 2008a). Moreover, by substituting some part of TiB whiskers by TiC particles effectively retarded crack propagation as there were no cracks found in the fractured surfaces of TMCs (Ni *et al.*, 2008a). Jia *et al.* (2014a) studied the fractured surfaces on composites surface were observed at room temperature and 400°C. When temperature was increased, small and large dimples emanated from spaces occupied by TiB whiskers and TiC particles respectively. By further increasing the temperature the larger dimples gradually increased while the smaller dimples reduced due to severe necking closing the smaller dimples. Due to good bonding strength between Ti with TiB whiskers or TiC particles there was no evidence of reinforcement pulling out observed, similar to Ni *et al.* (2008a) .

1.2.2 Summary

Densification of Ti-B_4C TMCs requires high sintering temperatures when high contents of B_4C are used. Increased temperature and dwell time significantly improves the relative densities, while pressure has less effect. On the interfacial reaction mechanisms, atoms inter-diffusion has been proposed to occur during the production of TiB whiskers and TiC particles by powder metallurgy route. B and C diffuse into Ti matrix while Ti diffuses into the vacancies left by B and C in B_4C. It has been found experimentally that TiB/TiB_2 phases primarily form then followed by TiC based on diffusion velocities of B and C atoms in Ti matrix. In the reaction sequence, when TiB_2 monolithic layer was formed it prevented diffusion of C into the Ti matrix and the reaction was stopped.

On the microstructure evolution, chemical reaction between Ti and B_4C in powder metallurgy fabrication route depends on the contact of the reactants and temperature. At lower temperature due to poor compaction the reaction does not take place, irrespective of the dwell time. Higher temperature improves compaction and activates the reaction, with varied dwell time B_4C particles transform into coarser TiB whiskers and TiC particles. Reducing particles size yields improved tensile strength while hot extrusion of the composites seems to reduce ductility. When coarser B_4C particles are used TiB/particles clusters are formed, to remove them either hot extrusion can be employed or dwelling time can be increased. However, the TiB/particles clusters were not completely removed by hot extrusion. These clusters adversely affect mechanical properties by acting as stress concentrators.

Strengthening in TMC occur by load transfer from the soft Ti matrix to harder TiB and TiC reinforcing phases. TiB whiskers are more effective in carrying load while TiC particles retard crack propagation due to their equiaxed shape. Due to the strong interfacial bonds between either TiB or TiC with Ti matrix, decohesion was not observed on the fracture surface.

Based on the literature reviewed to prevent TiB/particles clusters and be more energy efficient, B_4C with finer particles size has to be used. There is still a wide gap in the data reported on the reaction kinetics in relation to the microstructure evolution for powder metallurgy fabrication route. Further investigations with the use of TEM could be helpful. Furthermore, reactions activation energies during fabrication by the SPS could also be determined.

1.3 Tribology

Tribology is the science of friction, wear and lubrication of interacting surfaces in relative motion. Wear is the major cause of material wastage and loss of mechanical performance and any reduction in wear can result in considerable savings. Friction is a principal cause of wear and energy dissipation. Considerable savings can be made by improved friction control. It is estimated that one-third of the world's energy resources in present use is needed to overcome friction in one form or another. Lubrication is an effective means of controlling wear and reducing friction. Tribology is a field of science which applies an operational analysis to problems of great economic significance such as reliability, maintenance and wear of

technical equipment ranging from household appliances to spacecraft (Stachowiak *et al.*, 2006).

1.3.1 Wear behaviour of Ti-TiB_2/TiB, Ti-TiC and Ti - B_4C composites

Titanium and its alloys exhibit inferior wear resistance and suffer considerable loss in mechanical strength (Balaji *et al.*, 2015). These limitations prevent these class of material in many engineering applications (marine, chemical, automotive and petrochemical industries) were both corrosion and wear may be encountered (Mathew *et al.*, 2009; Toptan *et al.*, 2016). Notwithstanding, addition of hard ceramic particle or short fiber reinforcements such as TiB_2, TiB and TiC (Choi *et al.*, 2013) into titanium based matrix to produce TMCs, can significantly improve its wear resistance.

A summary of available literature on the specific wear rates and average COF values is presented in Table 8. IZUI *et al.* (2018) studied dry sliding wear behaviour of Ti-TiC and Ti-TiB composites prepared by SPS (900°C, 70MPa and 10min), using a Ø10mm high carbon chromium steel counter ball on a three ball-on-disk machine. Sliding velocity of 100mm/s and a sliding distance of 500m at a constant load of 23N were used. They observed that the wear depth reduced with increasing amount of TiC, that of Ti-15vol%TiC was about 30µm and Ti-25vol%TiC depth was maintained at the same level as the unworn surface. Although the wear depth of Ti-TiB_2 composites reduced from about 40 to 20µm for 25 to 35vol%, the depth of Ti-35vol%TiB was still higher than that of Ti-25vol%TiC. So, Ti-20vol%TiC composites exhibited lower specific wear rates close to 0 m^2/N than Ti-TiB composites with 4 x 10^{-13} m^2/N (IZUI *et al.*, 2018). However, an opposite wear behaviour was observed for TiB and TiC reinforcements synthesized from Ti and B_4C reaction. However, in the case of TiB and TiC synthesized from Ti and B_4C a different behaviour was observed.

Table 8. Specific wear rate and average COF values of TMCs

TMC	Sliding wear conditions	Material	Relative density (%)	Hardness (HV)	Specific wear rate (m^2/N)	Average COF
SPS Ti: 45 µm TiC: 1-2 µm (IZUI *et al.*, 2018)	Ball on disk Dry sliding Ball: Ø10mm 100Cr6 Load: 23N Sliding velocity:100mm/s	Ti Ti 5vol% TiC Ti 15vol% TiC Ti 25vol% TiC	- - - -	- - - -	~ 6.2 ~ 6 ~ 4 ~ 0	- - - -
Selective laser melting Ti: 22.5 µm TiC: 50nm (Gu *et al.*, 2012)	Ball-on-disk Dry sliding wear 25°C Ball: Ø3mm GCr15 steel Load : 3N Sliding velocity: 560rpm Time: 30min	Ti Ti7.5wt%TiC Ti12.5wt%TiC Ti17.5wt%TiC Ti22.5wt% TiC	- 98.3% 97.2% 94.7%	- 577 - -	- [b] 2.6×10^{-16} [b] 2.3×10^{-16} [b] 3.55×10^{-16} [b] 6.5×10^{-16}	- 0.23 0.19 0.35 0.41
Cold isostatic pressing 1400°C, 275MPa, 2h (Alman *et al.*, 1999)	Pin-on-drum Dry sliding Pin: Sintered Ti-TiC and Ti-TiB_2 Pressure: 2.1MPa Sliding velocity: 0.36mm/s Time:-	Ti Ti2.5vol%TiC Ti5vol%TiC Ti10vol%TiC Ti20vol%TiC Ti40vol%TiC Ti2.5vol%TiB_2 Ti5vol%TiB_2 Ti10vol%TiB_2 Ti20vol%TiB_2 Ti40vol%TiB_2	99.1% 89.1% 94.2% 93.8% 96.0% 95.1% 88.8 93.3 96.0 98.8 76.5	297 245 296 304 354 354 265 234 413 610 352	[c] 41.0±0.6 [c] 46.0±1.4 [c] 43.7±1.5 [c] 41.5±1.3 [c] 34.2±0.6 [c] 7.6±0.6 [c] 49.1±0.6 [c] 38.2±0.4 [c] 29.5±0.5 [c] 12.6±0.4 [c] 1.7±0.1	- - - - - - - - - - -
SPS Ti: 45 µm TiB_2: 1-2 µm (IZUI *et al.*, 2018)	Ball on disk Dry sliding Ball: Ø10mm 100Cr6 Load: 23N Sliding velocity:100mm/s	Ti Ti 5vol% TiB_2 Ti 15vol%TiB_2 Ti 25vol%TiB_2 Ti 35vol%TiB_2	- - - - -	- - - - -	~ 6.2 ~ 6 ~ 6.1 ~ 4 ~ 1	- - - - -
Investment casting process B_4C: 150µm (Kim *et al.*, 2011)	Ball-on-disk Dry sliding Ball: 52100 bearing steel Load: 0.35N Sliding velocity:125mm/s Time: 30min	Ti Ti–0.94 wt%B_4C Ti–1.88 wt%B_4C Ti–3.76 wt%B_4C	- - - -	[a] 134 [a] 239 [a] 259 [a] 306	[d] 0.57 [d] 0.54 [d] 0.5 [d] 0.15	- - - -

[a] HRB

[b] $m^3\ N^{-1}\ m^{-1} lap^{-1}$ (wear rate)

[c] Δm, mg (average mass loss)

[d] mm^3 (wear loss)

Qin *et al.* (2012) investigated the synergistic effect of TiB and TiC (Ti-B_4C) reinforcing phases on the wear behavior under dry sliding loads of 40-100N, they found that the wear resistance of the TMCs increased with increased TiB whiskers volume fraction. Thus, TiB whiskers were more effective in improving the wear resistance of TMCs than the TiC particles. Similar to Kim *et al.* (2011) and Balaji *et al.* (2015) TMC with higher TiB content, 16.18vol%TiB and 6.54vol%TiC, and Ti – 15vo%(TiB + TiC) exhibited lower wear loss respectively. It was reported that during sliding wear heat is generated from the friction between sliding ball and the sample, the heat in turn oxidizes TiB_2 into TiO_2 and B_2O_3. Thereafter, B_2O_3 reacts with water to form H_3BO_3, the two in turn act as solid lubricants and prevent excessive wear (Zhang *et al.*, 2002). Balaji *et al.* (2015) also mention that the presence of Fe-rich wear debris (rotating steel disc) acted as solid lubricant and reduced the friction coefficient of the Ti-B_4C TMCs. Moreover, the higher aspect ratio and load-bearing capacity of TiB during sliding wear was also reported to the reason for improved wear resistance (Qin *et al.*, 2012).

It has to be noted that TiB clusters were present at the interface between the Ti and TiB whiskers in the study by IZUI *et al.* (2018). Smaller TiB clusters fractured due to fatigue caused by the sliding load, while it was difficult to fracture the larger TiB clusters and remove them from the wear track. So the poor wear resistance of the Ti-TiB could have been due to the presence of TiB clusters. Regardless, both reinforcing phases TiB whiskers and TiC particles were not pulled out after siding, this was due to their strong interfacial bonding strength with the matrix (Qin *et al.*, 2012).

Worn surfaces analysis showed that adhesive wear mechanisms on titanium. While, the wear debris of Ti - (TiB + TiC) composites has been reported to consists of a mixture of titanium matrix, hard reinforcements and oxidation fine particles formed by abrasion, adhesion and oxidation as predominant wear mechanisms, which led to three-body abrasive wear (Balaji *et al.*, 2015; Kim *et al.*, 2011). A protective layer was formed and it prevented direct contact between the sliding surfaces and protects the composite from severe wear (Balaji *et al.*, 2015). The wear behavior of the metal matrix composites has been found to be influenced by the size, hardness, volume fraction of reinforcement, the distribution of reinforcement material, the nature of the reaction products between Ti and the reinforcement particles and thus the interfacial bond strength (IZUI *et al.*, 2018).

1.3.1.1 Summary

The wear behaviour of Ti-TiB and Ti-TiC TMCs is lacking, the available data showed higher wear loss for TiB based TMC which could have been due to the presence of TiB clusters. For TiB and TiC produced by reactive synthesis of Ti and B_4C, TiB whiskers were found to be more effective in improving the wear resistance of the TMC than TiC particles. The formation of protective solid lubricants such as B_2O_3 and H_3BO_3 formed during oxidation of TiB, and Fe-rich layer were responsible for the lower wear rates. The wear mechanisms in Ti were found to be by adhesion and for the TMCs abrasion, delamination and oxidation. Due to the strong interfacial bonding strength for TiB and TiC formed by reactive synthesis of Ti and B_4C, the reinforcing phases were not pulled during sliding wear.

1.4 Corrosion

Corrosion is the deterioration of materials as a result of reaction with its environment. For corrosion to take place, the formation of a corrosion cell is essential. A corrosion cell is essentially comprised of the following four components (Ahmad, 2006);

a. Anode: Oxidation takes place and electrons are released at the anode, which is the more reactive metal.
b. Cathode: Reduction takes place at the cathode and electrons are consumed.
c. Electrolyte: It is the electrically conductive solution that must be present for corrosion to occur.

Metallic path: The two electrodes (anode and cathode) are connected externally by a metallic conductor

Electrochemical corrosion techniques are sufficiently rapid and accurate thus examination of a variety of conditions in a short time (weeks) is achieved. In contrast to salt spray or immersion corrosion techniques this could take months. Thus potentiodynamic polarization is one of the most preferred techniques used to determine the active/passive characteristics of a given metal in solution: i the corrosion potential (E_{corr}), ii) corrosion current density (I_{corr}) and iii) the corrosion rate. The polarization diagram for a passive metal with the anodic and cathodic branches is presented in Figure 1.18. For the anodic curve, potential scan typically starts at E_{corr} and scanning in a positive direction, and usually to a potential positive enough to oxidize the test solution. The scan rate is typically 0.1 to 5 mV/s and depends on the system (Bas *et al.*, 2017).

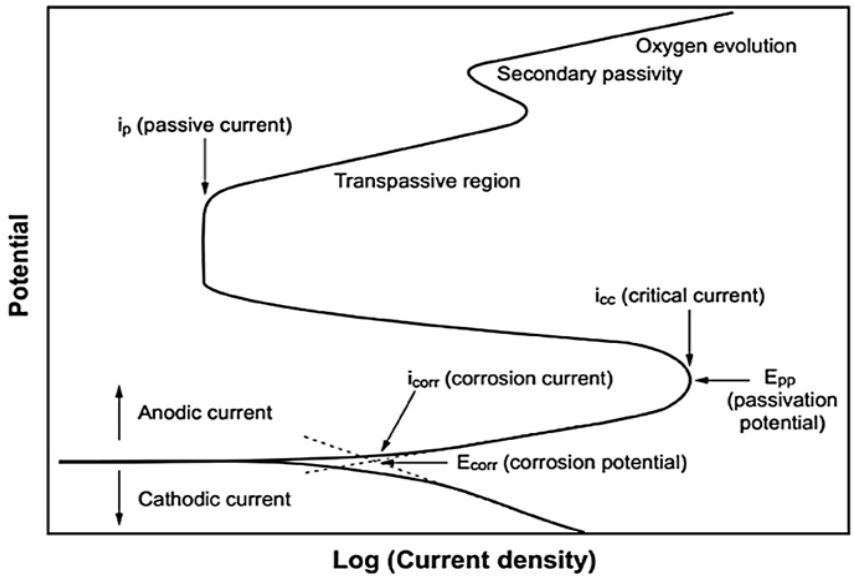

Figure 1.18. Hypothetical polarization diagram for a passive metal with anodic and cathodic branches (Bas et al., 2017)

1.4.1 Corrosion behaviour of Ti-TiB_2/TiB, Ti-TiC, TiC-TiB_2 and Ti-B_4C composites

The corrosion behaviour of TMCs can be significantly affected by the composition, reinforcement phases, micro-cracks, residual stresses, micro-crevices, porosity, secondary phase precipitates and interfacial products. The type of corrosion taking place in TMCs is reported to be galvanic coupling between the matrix and the reinforcement phase. This may result in selective corrosion at the matrix/reinforcement interface, chemical degradation of reinforcement phases and matrix defects (Doni *et al.*, 2014).

Onuoha *et al.* (2017) investigated corrosion response of a single phase TiC at room temperature in 3.5wt%NaCl, densified to 98% by SPS (1850°C, 5min and 50MPa). Open circuit potential (OCP) was measured for 2 hours in order to ensure steady-state conditions. The measured average OCP value was -0.209 ± 0.035V and the E_{corr} value was -0.173 ± 0.094 V, while Shvets *et al.* (2016) reported E_{corr} value of +0.05V for hot pressed TiC. In the potentiodynamic polarization curves there was a rapid dissolution then at 0V potential, the current density gradually decreased. This was due to passivation of TiC over a wide range of potential (0 to 1V) in NaCl solution (Onuoha *et al.*, 2017). Although work by Shvets *et al.* (2016) have reported small passivation region (0.25 to 0.45V) for hot pressed TiC, the current

density was sharply slowed down at these potentials then greatly increased, this indicated formation of a weak passive oxide film.

Verkhoturov *et al.* (1988) studied the corrosion behaviour of cold compacted and sintered TiC (87% and 55%) and TiB_2 (66%) in synthetic sea water. The measured E_{corr} values of TiC with density of 87% and 55% were -0.18V and -0.16V, while that of TiB_2 was more negative -0.42V showing higher susceptibility to corrosion, respectively. The presented literature in Table 8 support this, the E_{corr} values of TiC were more positively shifted (-0.18 to +0.2V) and that of TiB_2 were negatively shifted (-0.665 to -0.42V) (Ali *et al.*, 2011; Alkhateeb *et al.*, 2011; Beverskog *et al.*, 1990; Onuoha *et al.*, 2017; Shvets *et al.*, 2016; Verkhoturov *et al.*, 1988).

The measured I_{corr} values of the samples in Verkhoturov *et al.* (1988) were comparatively lower for TiC (2×10^{-7} A/cm^2) and higher for TiB_2 (1×10^{-5} A/cm^2), this could indicate that TiC has a lower dissolution rate compared to TiB_2 in synthetic sea water (3.5wt%NaCl). Similar results were reported in 40% H_2SO_4 acidic medium as shown in Figure 1.19, the corrosion rate decreased with increasing amount of TiC phase. Verkhoturov *et al.* (1988) suggest that higher corrosion resistance of TiC was due to two stage oxidation process, firstly formation of titanium oxycarbide layer followed by the natural protective layer phases of $TiO_2.H_2O$. In support of this, Andreev *et al.* (1997) also reports the formation of oxycarbide layer in TiC. In the case of TiB_2, boron anhydride B_2O_3 form on the surface during oxidation and the corresponding boric acid H_3BO_3 was then formed in the aqueous solution (Ali *et al.*, 2011; Verkhoturov *et al.*, 1988). This caused chemical heterogeneity on the surface of TiB_2 which led to higher corrosion rates.

Furthermore, even when TiC was incorporated in Ti matrix to produce TMCs, the composite still exhibited better corrosion resistance than Ti-TiB_2 composites in acidic medium at varying temperature (50 to 80°C) (Covino Jr *et al.*, 2002). Presented in Table 10 are the E_{corr} and I_{corr} values of TiC based composites. The E_{corr} values of pure Ti (-0.5 to -0.3V) were positively shifted with 20vol%TiC addition (±-0.2 to -0.1V) and comparably close to those of single phase TiC (-0.18 to +0.02V). In contrast, the E_{corr} values of 20vol%TiB_2 composites were negatively shifted (±-0.55V) thus lowering the corrosion resistance of pure Ti as shown in Table 9. However, it has to be noted that Ti and TiB_2 reacted to form TiB phase, so this phase also altered the surface chemistry of the composite resulting in mixed potentials. Thus, it is

not clear which phase was responsible for a negative E_{corr} shift as literature based on TiB composites still lacks. The Ti-TiB_2 composites yielded higher corrosion rates than Ti-TiC composites (Covino Jr *et al.*, 2002).

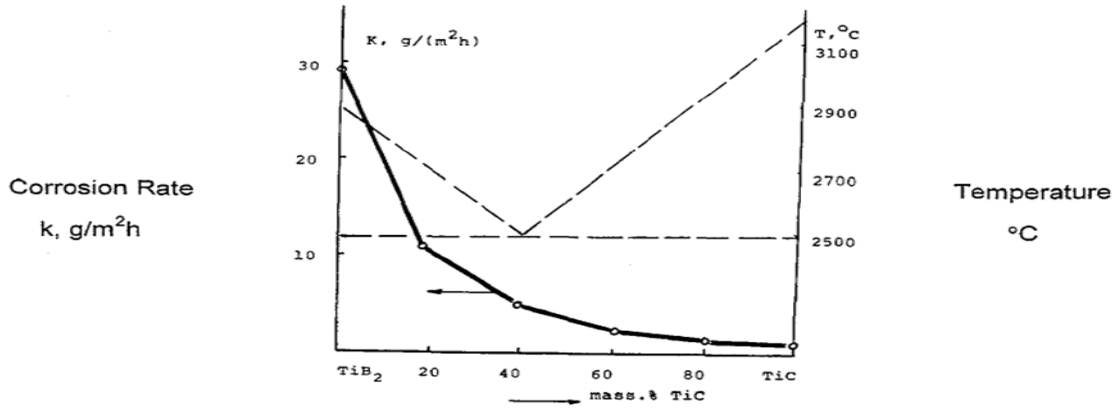

Figure 1.19. Corrosion rates of SHS TiC-TiB_2 CMCs in 40% H_2SO_4, dotted line presents simplified TiC-TiB_2 phase diagram (Andreev et al., 1997)

Similar results have been reported for TiC-TiB_2 ceramic matric composites prepared by self-propagating high temperature process. In which corroded samples showed a preferential dissolution of TiB_2 phase at the grain boundaries (Andreev *et al.*, 1997). The corroded morphology of the composites reported by (Covino Jr *et al.*, 2002) revealed galvanic corrosion took place thus no corrosion attack on the Ti matrix but on the reinforcing phases (TiB_2, TiB and TiC) was observed.

Table 9. Titanium E_{corr} and I_{corr} values

Material, Fabrication and Reference	Corrosion conditions	Relative density(%)	Passive range (V)	E_{corr} (V)	I_{corr} ($A.cm^{-2}$)
Ti **Hot pressing @ 1100°C, 120h, 15°C/min & 40MPa** (Toptan *et al.*, 2016)	3.5wt% NaCl	-	-	-0.499 ± 6	-
Ti **Vacuum sintering @ 1400°C, 2h, 10°C/min & 275MPa** (Covino Jr *et al.*, 2002)	Deaerated 2wt%HCl at 50, 70, and 90°C	99.1	-0.3 to 2	± -0.5 to -0.3	-
Ti film **Activated reactive evaporation** (Beverskog *et al.*, 1990) 1990	1M HCl	99.97	-0.260 to 6	-0.610	6×10^{-6}
Ti **Vacuum sintering @ 1400°C, 2h, 10°C/min & 275MPa** (Covino Jr *et al.*, 2002)	Deaerated 2wt%HCl @ 50°C	99.1	-	± -0.500	

Table 10. TiC based composites E_{corr} and I_{corr} values

Material, Fabrication and Reference	Corrosion conditions	Relative density(%)	Passive range (V)	E_{corr} (V)	I_{corr} ($A.cm^{-2}$)
TiC **Cold compact and sintered** (Verkhoturov *et al.*, 1988)	Synthetic sea water	87 55	- -	-0.180 -0.160	2×10^{-7} 2×10^{-7}
TiC **Hot pressing** (Shvets *et al.*, 2016)	3wt%NaCl	-	0.25 to 0.45	+0.050	-
TiC **SPS @ 1850°C, 5min & 50MPa** (Onuoha *et al.*, 2017)	3.5 wt%NaCl	98	0 to 1	-0.173 ± 0.094	1.28×10^{-6}
TiC films **Activated reactive evaporation** (Beverskog *et al.*, 1990)	1M HCl	-	0.09 to 6	+0.200	0.15×10^{-6}
Ti-20vol%TiC **Vacuum sintering @ 1400°C** (Covino Jr *et al.*, 2002)	Deaerated 2wt%HCl at 50, 70, and 90°C	89 to 96	± 0.5 to 2	50°C: ± -0.1 70 and 80 °C: ± -0.2	-

Table 11. TiB_2 based composites E_{corr} and I_{corr} values

Material, Fabrication and Reference	Corrosion conditions	Relative density (%)	Passive range (V)	E_{corr} (V)	I_{corr} ($A.cm^{-2}$)
TiB_2 **Cold compact and sintered** (Verkhoturov *et al.*, 1988)	Synthetic sea water	66	-	-0.420	1×10^{-5}
TiB_2 film **Chemical vapour deposition coated steel substrate** (Alkhateeb *et al.*, 2011)	0.5M NaCl	-	0.25 to 1	-0.457 @ 0h -0.409 @ 6h	-
TiB_2 film **Chemical vapour deposition coated steel substrate** (Ali *et al.*, 2011)	Simulated soil solution	-	-	-0.665	1.43×10^{-6}
TiB_2 **Self propagating high temperature synthesis** (Andreev *et al.*, 1997)	40% H_2SO_4	-	-	-	3.67×10^{-2}
Ti-20vol%TiB_2 **Vacuum sintering @ 1400°C** (Covino Jr *et al.*, 2002)	Deaerated 2wt%HCl at 50, 70, and 90°C	89 to 99	± -0.3 to 2	50 to 80 °C: ± -0.55	-

1.4.2 Summary

The literature reviewed here is based on the corrosion behaviour of TiB_2 and TiC based composites in acidic and neutral media. Although the sample preparations were different (coatings and sintering) and also yielded varying relative densities, the E_{corr} values were

comparably in the same range. It can be deduced that TiC based composites has better corrosion resistance than TiB_2 based composites. Formation of oxycarbide film together with TiO_2 passive film on TiC based composites were suggested to be responsible for improved corrosion resistance. In the case of TiB_2 based composites, TiB_2 dissolved to form B_2O_3 film which further reacted to form boric acid thus increasing the corrosion rates. However, the presented literature is still insufficient to make a clear conclusion on the influence of TiB and TiC reinforcing phases on the corrosion behaviour. Thus, the present study aims to investigate the synergy effect of the two phases on the corrosion behaviour of the composites.

1.5 Tribocorrosion

Between the late 1970s and early 1980s, the effect of wear on corrosion was studied by several researchers in different industrial application systems such as abrasion-corrosion, erosion-corrosion, or sliding-corrosion (López-Ortega *et al.*, 2018). Several terms commonly used in 1980s to describe this mechanism include oxidation wear, corrosive wear, corrosion wear and wear-corrosion. The term tribocorrosion was recently adopted in sliding systems and the individual mechanisms taking place have been systematically studied since the 1990s (Munoz *et al.*, 2011).

1.5.1 Definition of tribocorrosion

Tribocorrosion can be defined as materials deterioration or irreversible transformation resulting from simultaneous action of wear (mechanical degradation) and corrosion (chemical degradation) in a corrosive medium (López-Ortega *et al.*, 2018; Mischler, 2008). It involves two major scientific areas namely; tribology and corrosion. Tribology is defined as the study of friction, wear and lubrication while corrosion involves chemical aspects of materials degradation (Ahmad, 2006; Stachowiak *et al.*, 2006).

It is encountered in many areas where it causes damage to installations, machines, and devices and there are other industrial applications, where this phenomenon is put to good use, for example, electromechanical machining (Mathew *et al.*, 2009). A wide range of industrial sectors affected by tribocorrosion include; material processing, energy conversion, transportation, oil and gas exploration, medical and dental implants, surgical devices (Fazal *et al.*, 2014; Fedrizzi *et al.*, 2002; Landolt *et al.*, 2001; Stack, 2002; Wood, 2017).

Evaluation of electrochemically controlled tribocorrosion systems depends on many factors, among them four important parameters are presented in Figure 1.20, namely a) mechanical influences related to equipment design and operation, b) electrochemical conditions, c) the solution properties and, d) the materials and their surface properties (Landolt *et al.*, 2001).

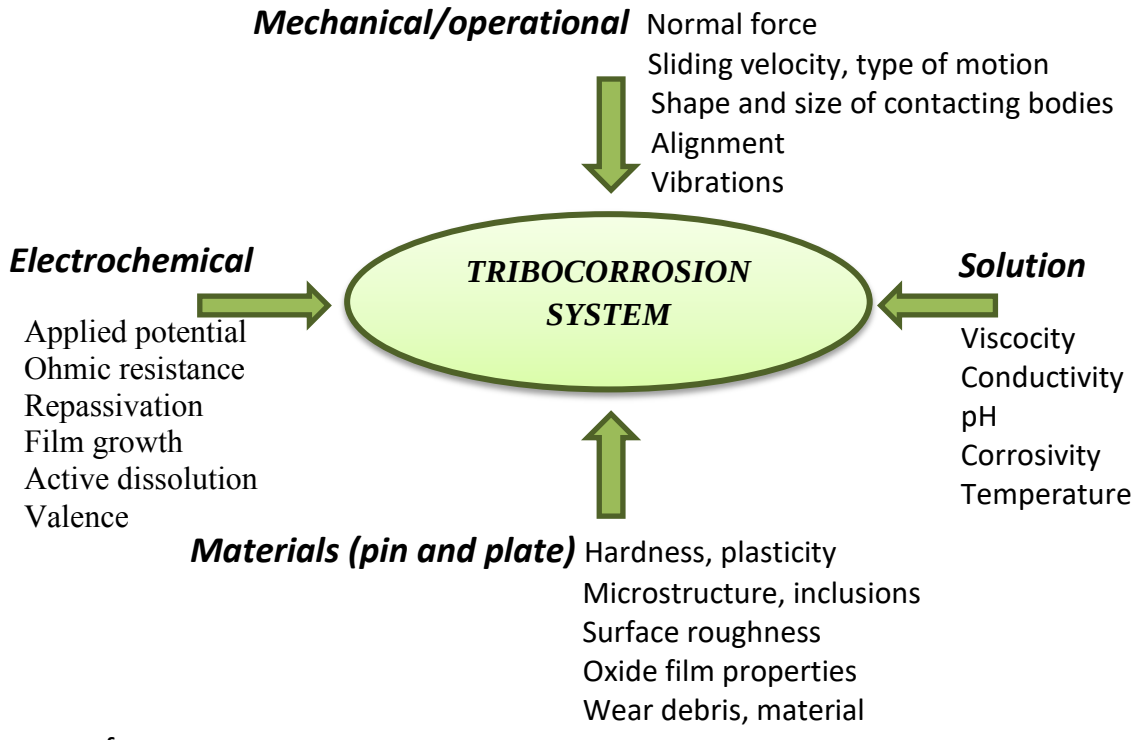

Figure 1.20. Types of parameters affecting tribocorrosion behaviour of a sliding contact under electrochemical control

1.5.2 Tribocorrosion model for degradation phenomena

The tribocorrosion model showing chemically and mechanically inert ball sliding on a passive metal, immersed in corrosive solution is presented in Figure 1.21. The three areas are of concern during wear-corrosion (Mischler *et al.*, 2014).

Area a, unworn area, it relates to metal surface unaffected by mechanical degradation and is only affected with corrosion. Despite of absence of direct interaction with the ball, the rubbing still affect corrosion in **area a**. Under typical tribocorrosion conditions, galvanic coupling is established between **area a** (passive "noble" metal) and **area c** (de-passivated "non-noble" metal). Resulting in electrode potential cathodic shift in **area a** and anodic shift in **area c** (Toptan *et al.*, 2016), with a consequent change in corrosion rate. Depending on the

specific situation, the corrosion rate of **area a** can differ substantially in absence of rubbing. (Mischler *et al.*, 2014)

Area b, contact area, is subject to mechanical loading (compression, friction) and is subjected to a number of phenomena such as frictional heating, elastic and plastic deformation, breakdown of the passive film and ejection of metal wear particles. Chemical reactions can profoundly affect the mechanical response in **area b** (Mischler *et al.*, 2014).

Area c, worn area, has undergone some depassivation (removal of the passive film and exposure of bare metal to the solution) resulting either from cracking of friable passive films, plastic deformation of the metal or from the detachment of metallic wear particles. As a result, **area a** is subject to enhanced corrosion (wear accelerated corrosion) that can exceed by order of magnitudes the typical corrosion rates observed on passive metals (Mischler *et al.*, 2014).

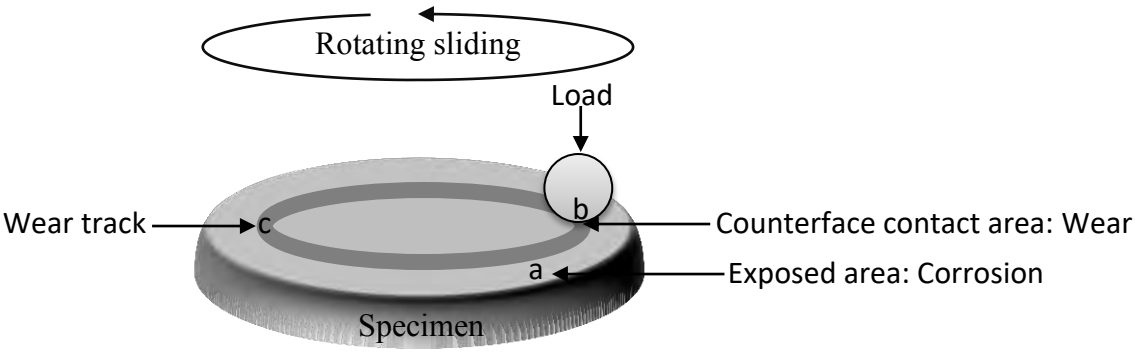

Figure 1.21. Tribocorrosion model for passive specimen

1.5.3 Tribocorrosion behaviour of TMCs

Degradation of materials by corrosion and tribocorrosion is encountered in various harsh technological applications (Fazal *et al.*, 2014; Fedrizzi *et al.*, 2002; Landolt *et al.*, 2001; Mathew *et al.*, 2009; Stack, 2002; Wood, 2017). The literature on the corrosion and tribocorrosion behaviour of TMCs is limited (Toptan *et al.*, 2017) and available literature involves a variety of newly developed, surface treated and coated Ti-alloys used in biomedical implants (Revathi *et al.*, 2016). With the emerging use of TMCs parts in harsh applications, their corrosion and tribocorrosion behaviour is yet to be clearly understood.

Toptan *et al.* (2016) investigated the tribocorrosion behaviour of hot pressed (1100°C, 120min and 40MPa) Ti-B_4C TMC in 9g/L NaCl. The final TMC was characterised with partially reacted B_4C particles. The E_{corr} value obtained from static polarisation curves of Ti were -499

± 6mV and for Ti-B_4C composites were -297 ± 8mV respectively. The positive E_{corr} value shift when B_4C was added in Ti was due to the diminished metallic surface area. Similar behaviour of E_{corr} positive shift has been reported for Ti6Al4V-B_4C composites in static corrosion test in 3.5wt%NaCl by (Prakash *et al.*, 2016). Hence, the corrosion resistance was improved by the inert physical barrier role of the reinforcement particles (Han *et al.*, 2015). Available literature report that addition of ceramic particles may shift the OCP or E_{corr} value to more noble values this effect may increase the corrosion resistance by the inert physical barrier role of the particles (Doni *et al.*, 2014; García *et al.*, 2003; Han *et al.*, 2015; Lampke *et al.*, 2006).

Nevertheless, the I_{corr} value of Ti-B_4C ((1.26 ± 0.14) x 10^{-6} A.cm^{-2}) composites measured in Toptan *et al.* (2016) was relatively higher than that of Ti ((1.26 ± 0.14) x 10^{-6} A.cm^{-2}). In addition, the corrosion resistance values of samples measured by impedance technique for Ti was higher than Ti-B_4C composites, it was around 10^6 Ωcm^2 and 10^4 Ωcm^2 respectively. The lower corrosion resistance value obtained for Ti-B_4C composite was due to localized corrosion in pore sites particularly near B_4C particles agglomerates sites, but for the well dispersed B_4C in the Ti matrix their interface was free of porosity. Moreover, Han *et al.* (2015) reported that by increasing the B_4C content in the composite may results in discontinuities of the protective oxide film making the composites more exposed to the chloride ions and thus generating a less noble potential. While Song *et al.* (2005), suggest that the presence of corrosive chloride ions in the solution also contribute to the higher current densities. Chloride ions destabilises the passive film by changing the composition, microstructure or thickness of the passive film resulting in the higher dissolution rate of the passive film.

Seah *et al.* (1998) stated that mechanical properties of material can be weakened by the presence of pore. In electrochemistry this effect common since pores are permeable thus they provide a passage for electrolyte infiltration in the material. Hence, the exposed larger surface area in porous material will be prone to corrosion than in full dense material. Moreover, higher current densities will be produced in porous material (Oksiuta *et al.*, 2009). In addition, crevices in the material are found to also influence corrosion rates which are not proportional to the surface area. Corrosion by crevice effect depends or geometry of pores while pitting corrosion depends on the composition. Electrolytes filled in crevices can become acidic or

oxygen deficient resulting in an autocatalytic process which accelerates corrosion (Oksiuta *et al.*, 2009; Seah *et al.*, 1998).

Electrochemical state of material under sliding can be evaluated by open circuit potential (OCP) since no potential is applied. The OCP values are monitored in three stages, first without applied load, secondly the load is initiated and the OCP values are reduced, then lastly the applied sliding load is removed then the OCP values are stabilized (López-Ortega *et al.*, 2018). OCP values measured in sliding conditions in a mixture of potentials from the unworn area and worn area (wear track) and galvanic coupling between the two areas may take place (López-Ortega *et al.*, 2018; Mischler, 2008). Ponthiaux *et al.* (2004) mention four factors which affect corrosion potential during sliding.

- OCP of the material in worn and unworn areas are in different electrochemical states. On the worn area the surface is damaged, the passive film is removed, material debris and corrosion products are absorbed on the surface by mechanical straining resulting sliding contact.
- Worn and unworn areas ratio, if the worn area increases the OCP of the material will shift. Depending on the controlling electrochemical process, being either the dissolution of the metal (anodic) or the reduction of hydrogen or dissolved oxygen (cathodic).
- The relative position of worn and unworn areas, since galvanic coupling occurs, current flows between anodic and cathodic areas. As a result non-uniform distribution of potential and current density over material surface may be induced by ohmic drop. Thus the measured OCP is actually an average value depending on that distribution.
- Anodic and cathodic reactions mechanism and kinetics in the worn and unworn area.

Using tribocorrosion techniques, friction coefficients (COF) values is simultaneously measured with the OCP values (López-Ortega *et al.*, 2018; Mischler, 2008; Toptan *et al.*, 2016). COF values measured during OCP and polarisation in Toptan *et al.* (2016), were relatively higher in Ti-B_4C composites. It was suggest that as the imparted 10N load continued stresses, breaking and/or pulling-out of some B_4C reinforcing particles may have led to third-body abrasion being responsible for the relatively higher COF and causing more material damage. In support of this, SEM analysis on worn area revealed fatigue stresses created around unreacted B_4C particles and de-attachment occurred due to poor bonding with Ti matrix. However, under dry sliding wear conditions with loads in the range of 40 - 100N

TiB whiskers and TiC particles were not pulled out due to their strong interfacial bonding strength with the matrix (Qin *et al.*, 2012). These results could clearly indicate the potential use of TiB and TiC based TMCs in wear-corrosion conditions, in contrast to those with partially reacted B_4C particles

The E_{corr} values of Ti-24vol%B_4C composites were shifted from -297±6 to -398±6mV, similar with unreinforced Ti from -499±6 to -623±24mV. Regardless the negative shift of E_{corr} values of the composite, the values was still more positive than that of unreinforced titanium. The potential difference of the worn and unworn surface resulted in accelerated corrosion under sliding, the I_{corr} values increased to two decades for Ti, $(10.8 \pm 3.4) \times 10^{-6}$ $A.cm^{-2}$ and almost two times for composites $(2.4 \pm 0.9) \times 10^{-6}$ $A.cm^{-2}$ (Toptan *et al.*, 2016).

1.5.4 Summary

The tribocorrosion properties of Ti can be significantly improved with addition of ceramic B_4C by shifting the E_{corr} values positively. However, with coarser and high volume fraction of B_4C particles agglomerates sites may be created and result in porosity. Porosity can reduce the corrosion resistance of the composites by increasing I_{corr} values thus corrosion rates would be accelerated. Moreover, the stresses can be concentrated around the partially B_4C particles causing de-attachment from the matrix when sliding wear continues. The particles will act as third-body abrasives and result in higher COF values, thus severe damage will be induced. Nevertheless, the E_{corr} values of the TMCs were still more positive than that of Ti, showing the load carrying capacity by the B_4C. This indicated good tribocorrosion properties improvement when B_4C particles were added.

Regardless the literature based on the tribocorrosion behaviour of Ti-B_4C and Ti-(TiB_2/TiB + TiC) TMCs is still lacking in both acidic and neutral solutions. Owing to emerging technological applications of TMC's in harsh environments such as in automobile brake rotors where both corrosion and wear are encountered during road deicing with salts**. I**t is important to evaluate and understand their performance in such harsh conditions. Hence there is still lot of work to be done under this research topic. The present study aims to evaluate the tribocorrosion behaviour of Ti - (TiB + TiC) TMCs in saline conditions.

CHAPTER 2: Materials and Experimental procedures

Table of contents

2.1 Materials of study

As-received CP-Ti powders with -325 mesh sizes were supplied by PI-KEM Ltd., UK (Ti(25.9μm)) and CERAC incorporated, US (Ti(35.9μm)) both were prepared by Hydride dehydride (HDH) process producing powders with angular morphology respectively. The boron carbide powders were supplied by H.C. Starck with particles size of 0.3μm-0.6μm B_4C (1.67μm) and LTS research laboratories. Inc. with -400 mesh B_4C(1.79μm) and -325 mesh B_4C(17.9μm).

2.2 Elemental analysis by ICP-OES and Instrumental gas analysis

Trace elements analysis in CP-Ti powders were analysed by Inductively Coupled Plasma - Optical Emission Spectrometry ICP-OES (JY 2000 2) technique at Marion Technologie. The interstitial elements O, N, H and C were analysed with instrumental gas analysis technique at TIMET, Fr using LECO ONH836 and LECO CS844 respectively.

2.3 X-ray Diffraction

Phases present in pure powders, mixed powders and sintered samples were identified by using D4-Endeavor X-ray diffractometer by Bruker with monochromatic Cu Kα radiation at 40KV and 40mA. The diffraction patterns were initially recorded in 2-theta range 10 -100° at step size of 0.01569. It was then found that the interesting section in the patterns for CP-Ti and Ti-B_4C TMCs were in between 34 - 42° and 20 - 50° 2 - theta range, the diffraction was then registered at this range at a much lower step size of 0.00998 respectively. The phases present were identified by searching and matching of peak positions and intensities with those in JCPDS using EVA software. The Reference Intensity Ratio (RIR) method was then used to quantify the concentration of phases formed in 20mm TMCs.

2.4 Scanning electron microscope

Particles shape, morphology and size were examined by scanning electron microscope (SEM) JSM6510LV with tungsten filament at 20KV acceleration voltage. The SEM was equipped with energy dispersive spectrometry (EDS) and the elements presents were confirmed with this technique.

2.5 Particle sizes

The particle sizes and distribution (PSD) was determined using Mastersizer 3000 in dry conditions at Laboratoire de Genie chimique, Fr (LGC).

2.6 Turbula mixing

The as-received powders prepared in compositions of Ti1wt%B_4C, Ti2.5wt%B_4C and Ti5wt%B_4C and Ti10wt%B_4C for the varying B_4C particles sizes were turbula mixed in dry conditions for 1 hour. Alumina balls were used as mixing medium and powder to ball ratio of 1:1 was used.

2.7 Spark Plasma Sintering

CP-Ti and Ti-B_4C powders were spark plasma sintered using a Dr. Sinter 2080 unit, SPS Syntex Inc., Japan, (Figure 2.1) available at the Plateforme Nationale de Frittage Flash located at the Université Toulouse 3 Paul Sabatier, using Ø8mm and Ø20mm Graphite die (Gr die) lined with a 0.2 mm graphite paper (PERMA-FOIL®Toyo Tanso). Sintering was performed at varying temperatures in the range of 550-900°C and 800-1100°C for CP-Ti and Ti-B_4C powders at pressure range of 25MPa-75MPa respectively. Dwelling time was varied from 3min to 30min and a constant heating rate of 100°C/min was used. K-type thermocouple was inserted 3mm in depth on the outer diameter of the Gr die to monitor all temperature readings. To ensure a uniform initial compaction for all the powders, pre-compaction at 25MPa for 3 minutes was done prior to the start of the thermal cycle. In SPS the temperature distribution is known to differ. Especially the temperature within a conductive powder is normally higher than the one measured on the graphite die (Anselmi-Tamburini *et al.*, 2005). Therefore, sets of experiments were performed to measure the real temperature in the powder and to determine temperature difference between Gr die and CP-Ti powder using K-type thermocouples. Gr dies with Ø8 and Ø20 diameters were used, a hole was drilled through Gr die reaching maximum thickness (16.6 and 29.6 mm respectively) and then the thermocouple was inserted through reaching CP-Ti powder filled inside Gr die. The second thermocouple was inserted as normal (3mm in depth) on the Gr die as illustrated in Figure 2.2. The set-point temperature was 800°C and 25MPa pressure was used at constant heating rate of 100°C/min with a dwelling time of 3 min.

Figure 2.1. Dr. Sinter 2080 Spark Plasma Sintering unit

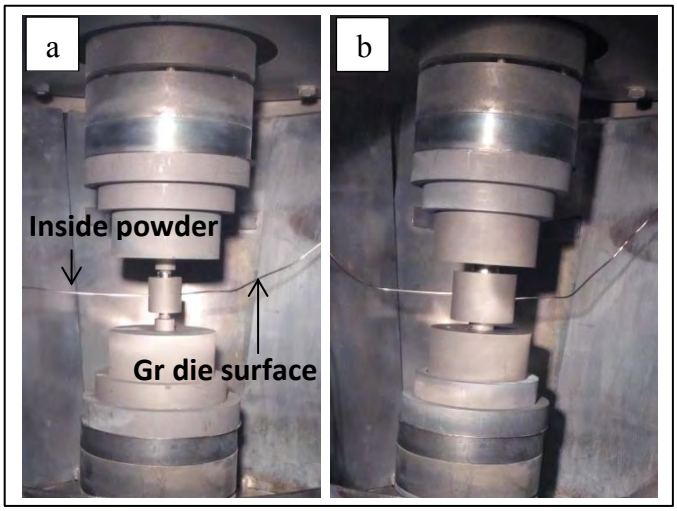

Figure 2.2. Thermocouples positions for temperature measurements
In (a) Ø8 mm and (b) Ø20 mm Gr dies

2.8 Relative density

The relative density of the sintered samples was measured by Archimedes principle using a hydrostatic balance (Sartorius MSE224S-YDK03). Before measurements, the graphite adhered to the sintered pellets was removed by grinding with P320 SiC paper. Measurements were done by weighing the sample in air and submerged in water, then with the use of [E.q 13] configured in the hydrostatic balance the density of the sample was calculated. With the use of theoretical densities the relative density was calculated. Samples were dried in oven at 150°C for 24 hours and measurements were repeated 3 to 4 times.

$$\rho = \frac{m_{air} \times \rho_{water}}{m_{air} - m_{water}} \quad [E.q\ 13]$$

When the relative density measured was or less than 92%, the relative density was measured geometrically. The sample was weighed and its dimensions (diameter and thickness) were measured using a micrometre to calculate the volume. The density was measured using [E.q 14] and using theoretical densities of CP-Ti and Ti-(TiB_2+TiB+TiC) composites the relative densities were determined. Whereby ρ is the density, m is the sample mass and v is the volume.

$$\rho = \frac{m}{V} \quad [E.q\ 14]$$

2.9 Hardness testing

The sintered samples were cold mounted using epoxy resin and the surface was grounded using a series of SiC papers P320, P600, P1200 and P2400. Then final polishing with colloidal silica on a neoprene cloth for a minimum of 10 min was performed to produce a scratch free surface. Vickers hardness was then determined using a HM-200 Mitutoyo hardness tester on the polished pellets at a load of 0.5kg and 10 indentations were made in different sections of the samples.

2.10 Microstructure analysis by SEM/FIB and TEM

Chemical etching was done for 15s to reveal the microstructure using Kroll's etchant consisting of 92ml distilled water, 6ml of nitric acid and 2ml hydrofluoric acid. The etched sintered samples were thoroughly rinsed with tap water to remove any traces of the etchant and then hot dried. The microstructure was observed and analysed using a SEM (JSM6510LV). To further understand phase transformations and products formed, lamellae were extracted from the reinforcements/matrix interface in Ti5wt%B_4C TMCs (8mm in diameter) sintered at 800°C and 1100°C using Focused Ion Beam (SEM/FIB FEI HELIOS 600i – EDS) equipment. Thereafter, the crystallography and elemental compositions were analysed using a Transmission Electron Microscope (TEM JEOL JEM-ARM200F Cold FEG) corrected probe coupled to EDX spectrometer and a loss of energy spectrometer (EELS). The FIB and TEM analysis were performed at UMS CASTAING in Toulouse. With the aid of CysTBox software the Fast Fourier Transform (FFT) patterns were obtained from the TEM crystallographic images to verify the phases formed. FFT patterns analyses lattice planes

coordinates and experimental d-spacing values matching the theoretical d-spacing values of the respective phases to be analysed (Klinger *et al.*, 2015).

2.11 Corrosion tests

Corrosion and tribocorrosion tests were performed at the Center for Nano-Engineering and Tribocorrosion at the University of Johannesburg in South Africa. Sintered samples at 1000 and 1100°C at 25MPa and 75MPa with a diameter of 20mm for electrochemical measurements were prepared by attaching copper wire using adhesive aluminium foil on one surface of the sample and cold mounted using epoxy resin for insulation. A surface area of 3.14cm^2 was left exposed to the electrolyte. Cold mounted samples were then grinded on Saphir 520 automatic polishing using SiC P320 paper, polished with Aka-allegran 3 using diamaxx 6µm poly as lubricant and final polishing with aka-chemal using alkaline 0.2µm fumed silica. After polishing the pellets were cleaned with ethanol to remove residual polishing medium. Princeton Applied Research Potentiostat (VersaSTAT 4) with versastudio electrochemical software (version 2.52.3) was used to perform corrosion tests at room temperature. The corrosion cell setup consisted of Ag/AgCl (3M KCl) reference electrode, graphite as counter electrode and sintered samples as working electrodes all immersed in 3.5wt%NaCl electrolyte. The open circuit potential (OCP) was conducted for 2 hours and potentiodynamic polarization (PDP) was conducted at set-point potentials of -500mV to +1000mV at a scanning rate of 2mV/s.

2.12 Tribocorrosion tests

Prior tribocorrosion testing the bare sintered pellets were metallorgraphycally prepared as in corrosion testing but without attaching copper wire. Tribocorrosion behaviour of the sintered pellets was investigated on Anton Paar pin-on-disk tribometer (TRB) integrated with a Versastat 4 potentiostat shown in Figure 2.3. Tests were conducted on rotating sliding under controlled load and linear speed of 2N and 0.55cm/s respectively. The counterface material was 6mm ZrO_2 ball and the wear track diameter was kept at 0.88mm. The exposed surface area of sintered pellets was 1.77cm^2. The test cell, sample holder and ball holder were made from an insulating material to prevent any electric conductive interference. The tribocorrosion cell was filled with 3.5wt%NaCl electrolyte containing Ag/AgCl (3M KCl) reference electrode, graphite counter electrode and sintered pellets as working electrodes. The open circuit potential (OCP) were done for 30 min without load, 60 min with applied load and

thereafter the load was removed and OCP let to stabilize for 30min. On freshly polished samples surface, the potentiodynamic polarization (PDP) tests were done at potentials of -500mV to +1000mV with a scan rate of 2mV/s

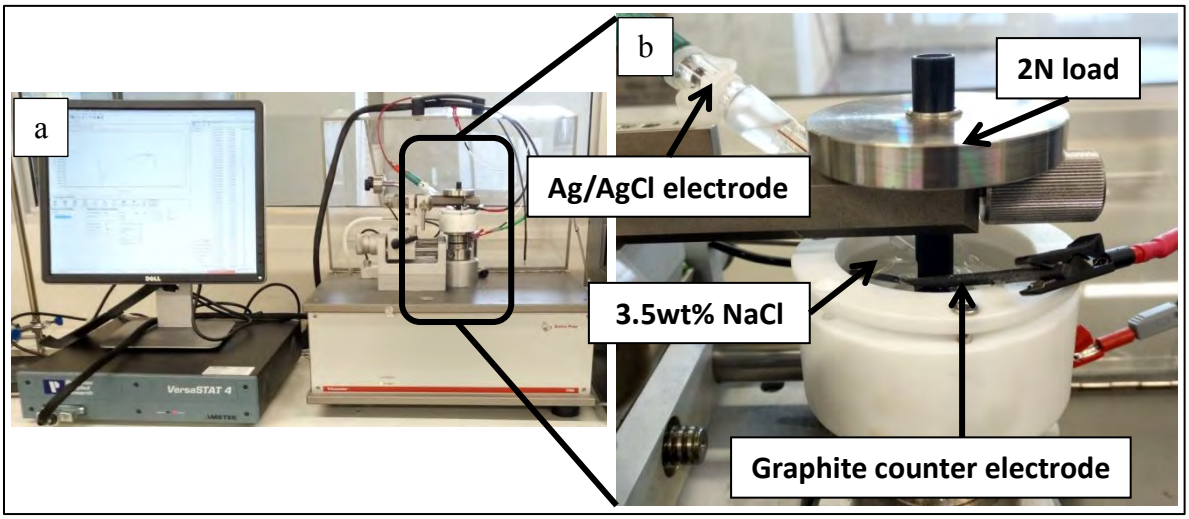

Figure 2.3. Tribocorrosion setup a) Anton Paar pin-on-disk tribometer (TRB) intergrated with Versastat, b) Cell-setup with electrodes

2.13 Characterisation of tribocorroded samples

The tribocorroded sintered pellets worn tracks surface were then analysed using optical microscope and SEM (JSM6510LV). The depth and width of the tracks was measured with Sensofar Interferometric and Confocal Microscope - S Neox. The volume loss (V_w) was calculated for a half-ellipse track using [Eq 10] respectively (Guiderdoni *et al.*, 2013).

$$V_w\,(mm^3) = \frac{1}{2}.\,\pi\,rd.\,2\,\pi\,L' \qquad [Eq.\,10]$$

CHAPTER 3: Sintering and characterization of CP-Ti powders

Table of contents

3.0 Introduction

The selection of metal matrix entirely depend on foremost compatibility with the reinforcing phase, required properties, intended applications and the cost efficiency (Nalwa, 1999). In this regard, when chemical compatibility is obtained between the two distinct phases, the resultant MMC have outstanding properties such as increased yield and tensile strength at room and elevated temperatures, increased young modulus of elasticity, improved corrosion and wear resistance over the individual phases (Balaji *et al.*, 2015; Chawla *et al.*, 2006; Choi *et al.*, 2013; Kim *et al.*, 2011).

In this study two CP-Ti powders with varying chemistry were sintered at varying temperature and pressure. In this chapter the powders were sintered using the economic SPS technique with pulsed electric current assisted with pressure(Tokita, 1999). The effect of sintering temperature and pressure on densification, microstructure and mechanical properties were thoroughly investigated on CP-Ti powders containing different amounts of interstitial elements.

3.1 Characterizations of CP-Ti powders

Particles morphology of the Ti powders is shown in Figure 3.1. It was observed from the SEM micrographs that the Ti powders particles exhibited different morphology. The Ti powder with D_{50} particles size of 25.9µm was irregular shaped and that with 35.9µm the periphery was smoother. The PSD analysis showed that CP-Ti(25.9µm) had a larger particles size distribution than Ti(35.9µm). The elemental analysis shown in Table 12 revealed significant difference in compositions. CP-Ti(25.9µm) had high oxygen content (7315ppm) but with low hydrogen content (546ppm), whereas CP-Ti(35.9µm) had high hydrogen content (2226 ppm) and low oxygen content (2451 ppm). A high iron content of 298ppm was analyzed in CP-Ti(25.9µm) while it was lower in CP-Ti(35.9µm) with 25ppm. In the XRD pattern shown in Figure 3.2, both Ti powders were identified by HCP α-Ti phase while TiH_2 lines were also detected for Ti(35.9µm). The presence of the hydride phase in the latter powder can result from an incomplete removal of hydrogen during processing, especially since hydrogen is present in high amount compared to Ti(25.9µm).

Table 12. Interstitial elements content (ppm), determined using instrumental gas analysis

	C	H	N	O	Fe*
CP-Ti(25.9µm)	205	546	175	7315	298
CP-Ti(35.9µm)	125	2226	326	2451	25

*ICP-OES

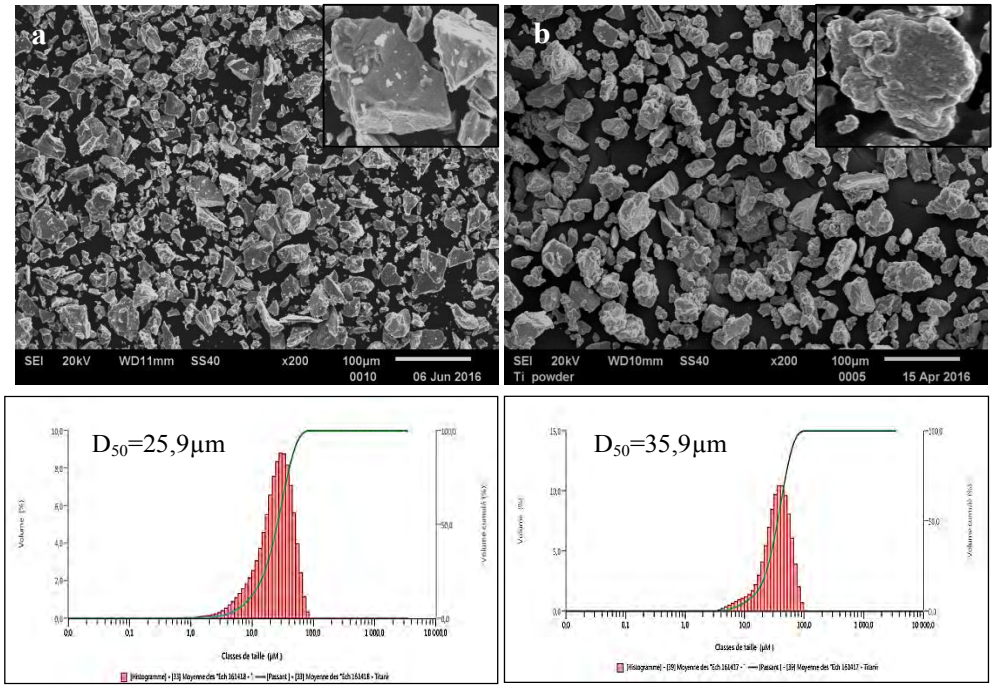

Figure 3.1. SEM micrographs of -325mesh Ti powders and their respective PSD analysis, a) PI-KEM Ltd., UK and b) CERAC incorporated, US

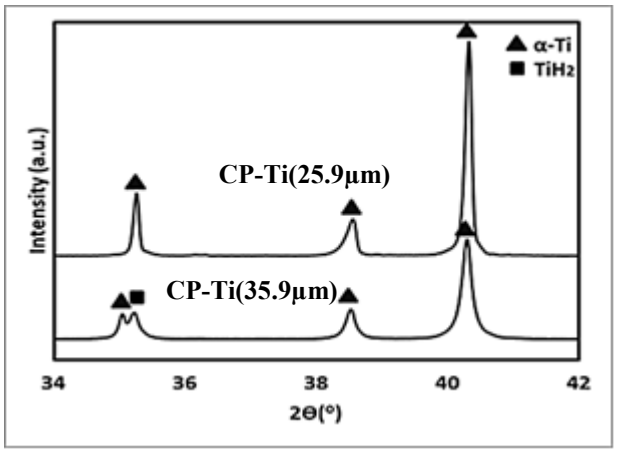

Figure 3.2. XRD pattern of as-received powders

3.2 Temperature variation during sintering

The temperature difference between Gr die and powder was measured in Ø8mm and Ø20mm. Figure 3.3 shows the temperature difference in the two measured locations. It was observed that the temperature increased linearly with time for the two locations. A variation in temperature was observed from 240s until final stages of the sintering cycle. The overall temperature measured in the powder was approximately 8% higher than in the Gr die. For Ø8mm Gr die in Figure 3.3(a), it was found that when ramping up to reach the set-point temperature of 800°C the temperature overshoot to 807°C then stabilized to 800°C at dwelling time. A similar behaviour was observed for Ti powder but higher temperatures were obtained in powder than in Gr die. Higher temperature of 874°C was reached before dwelling which thereafter lowered to 868°C just below 882°C α to β-Ti theoretical transus temperature. Hence, the temperature difference just before and after dwelling was 67°C and 68°C respectively. In comparison, for a Ø20mm Gr die, much higher temperatures of approximately 10% exceeding the theoretical transus temperature were reached. Temperature difference of 97°C and 89°C before and after dwelling were recorded (*see* Figure 3.3(b)). Figure 3.3(c) further shows that temperature of CP-Ti powder in Ø20mm Gr die was approximately 21°C higher than powder in Ø8mm Gr die. The temperature difference measured between CP-Ti (1041°C) and Gr die (1010°C) reported in Matsugi *et al.* (2003) was 31°C. Temperature measurements depend on the location of the thermocouple, in Matsugi *et al.* (2003) the thermocouple was positioned 2mm from the internal diameter and in this study it was positioned 3mm from the outer diameter. Hence with temperature gradient decreasing from the powder to the surface of the Gr die the temperature difference in Matsugi *et al.* (2003) was lower than in the present study.

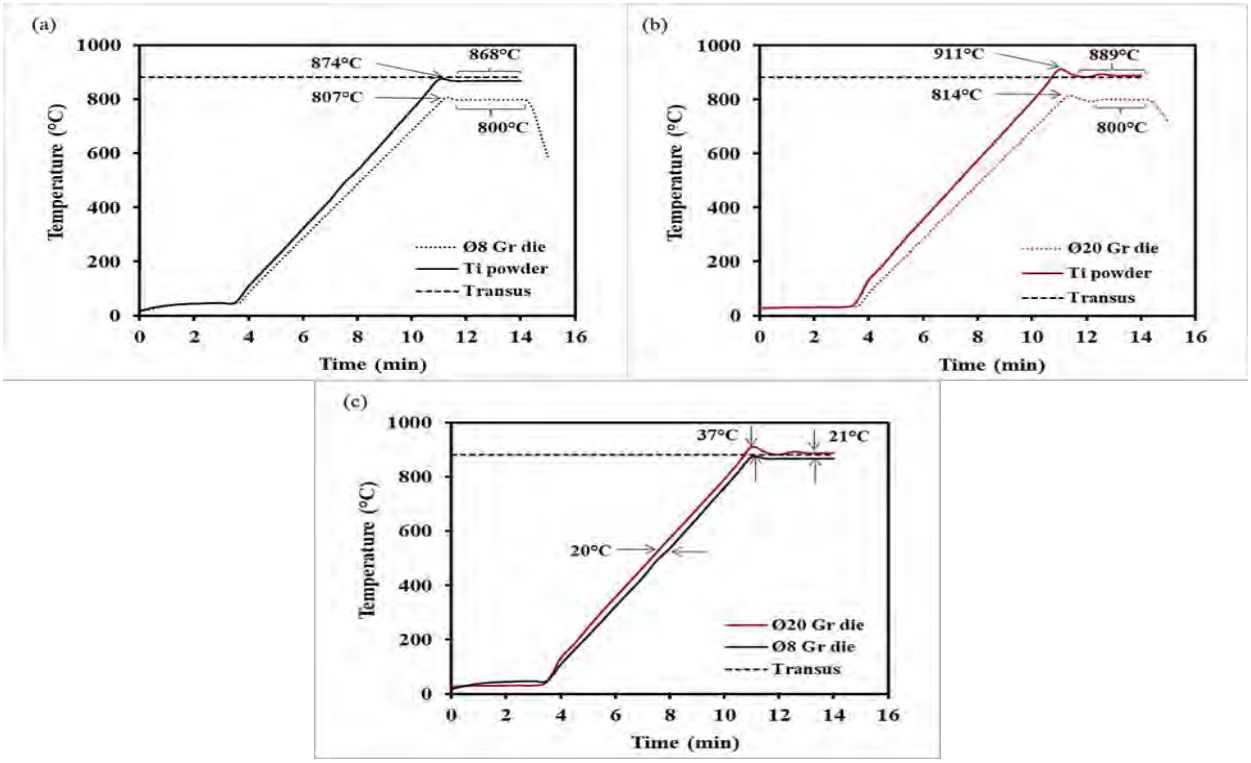

Figure 3.3. Temperature difference between Gr die and Ti powder, a) Ø8 Gr die, b) Ø20 Gr die and c) Temperature difference between Ø8 and Ø20 Gr dies

3.3 Effect of sintering temperature and pressure on densification

Figure 3.4 shows the variation of relative density for Ø8mm SPS pellets with the sintering temperatures for both CP-Ti(25.9µm) and CP-Ti(35.9µm). A density of 99% for CP-Ti(25.9µm) and CP-Ti(35.9µm) was reached at pressure of 25MPa at 800°C and 900°C respectively. Further, as expected densification above 95% is reached at much lower temperatures as the applied pressure (75MPa) is increased. Comparing to the alloy Ti6Al4V (Garbiec *et al.*, 2016) full densification was reached at 1000°C with higher heating rate of 300°C/min and that of intermetallic TiAl (Couret *et al.*, 2008) obtained at 950°C in similar SPS conditions. More surprising, at 550°C and 650°C for 25MPa the densification of CP-Ti(25.9µm) pellets was expected to be higher than CP-Ti(35.9µm) because of the small particles sizes. Spherical "like" particles tends to densify faster than irregular shaped ones. Grain growth is rapid for spherical particles because of higher initial particle-to-particle contacts with smaller pores. In contrast to irregular particles there is less particles interactions larger pores exist and lead to lower densification (Weston *et al.,* 2015). In addition, the early microstructural transformation of CP-Ti(35.9µm) due to high amount of hydrogen (lower oxygen content) lowering the transus temperature could be promoting diffusion of atoms resulted in faster densification. This effect was also noticed at the respective increasing

pressures at 550°C for CP-Ti(35.9µm). This indicated that for CP-Ti(25.9µm) with high amount of dissolved oxygen increased the transus temperature thus limiting atoms diffusion for enhancing densification at lower temperatures.

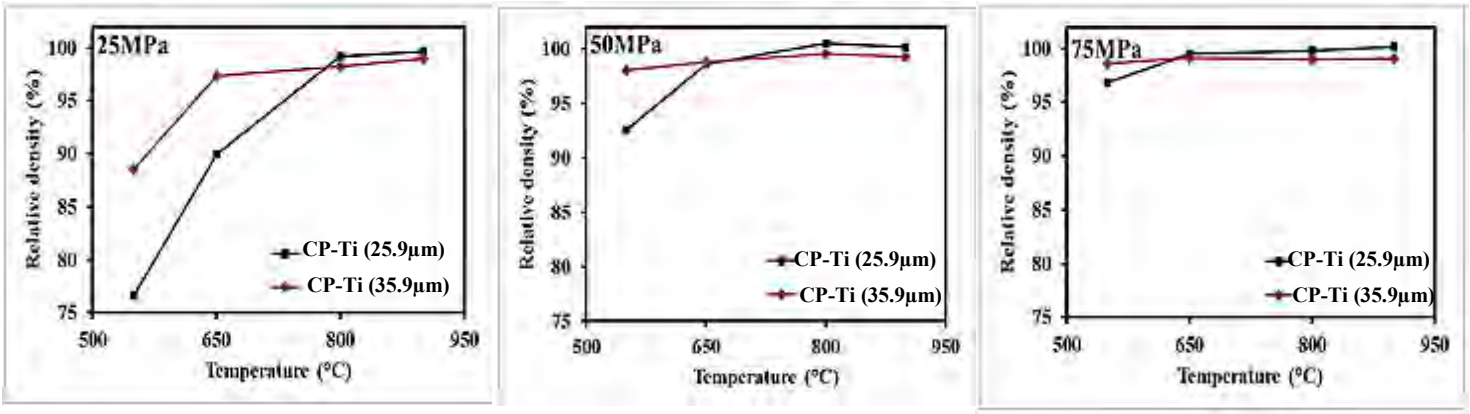

Figure 3.4. Evolution of the relative density versus set-point temperature for three applied pressure a)25, b)50 and c)75MPa for CP-Ti(25.9µm) and CP-Ti(35.9µm) SPS pellets

3.4 Effect of sintering temperature and pressure on the microstructure

XRD patterns of Ø8mm SPS pellets sintered at various temperatures is shown in Figure 3.5. No specific effect is observed since all the XRD patterns of the pellets are similar to those of the starting powders. Except the slight negative and positive 2-theta shift observed when temperature and pressure were increased respectively. In the CP-Ti(25.9µm) structure at 25MPa shown in Figure 3.5(a), the 2-theta angle slightly shifts to the left with increasing temperature, indicating that the lattice parameters are increasing and thus unit cell expansion. The negative 2-theta shift was however negligible at 50MPa and also for CP-Ti(35.9µm) in Figure 3.5 (c and d). Figure 3.6 shows the effect of applied pressure on the structure of the sintered pellets. In Figure 3.6(a) for CP-Ti(25.9µm) at lower temperature of 650°C with increased pressure there was a negligible positive shift of 2-theta angle, this behaviour was however not observed for CP-Ti(35.9µm) see Figure 3.6(c). For a temperature of 900°C in Figure 3.6(b), the positive shift of 2-theta angle was more pronounced for 50MPa than 75MPa, as for CP-Ti(35.9µm) in Figure 3.6(c and d) the shift was negligible. Comparing CP-Ti(25.9µm) and CP-Ti(35.9µm), the lattice parameters for CP-Ti(25.9µm) are reduced with the change in pressure at all temperatures but for CP-Ti(35.9µm) the change is negligible under the same conditions. Moreover the peak for hydrogen in CP-Ti(35.9µm) was detected on SPS samples showing no dehydrogenation took place.

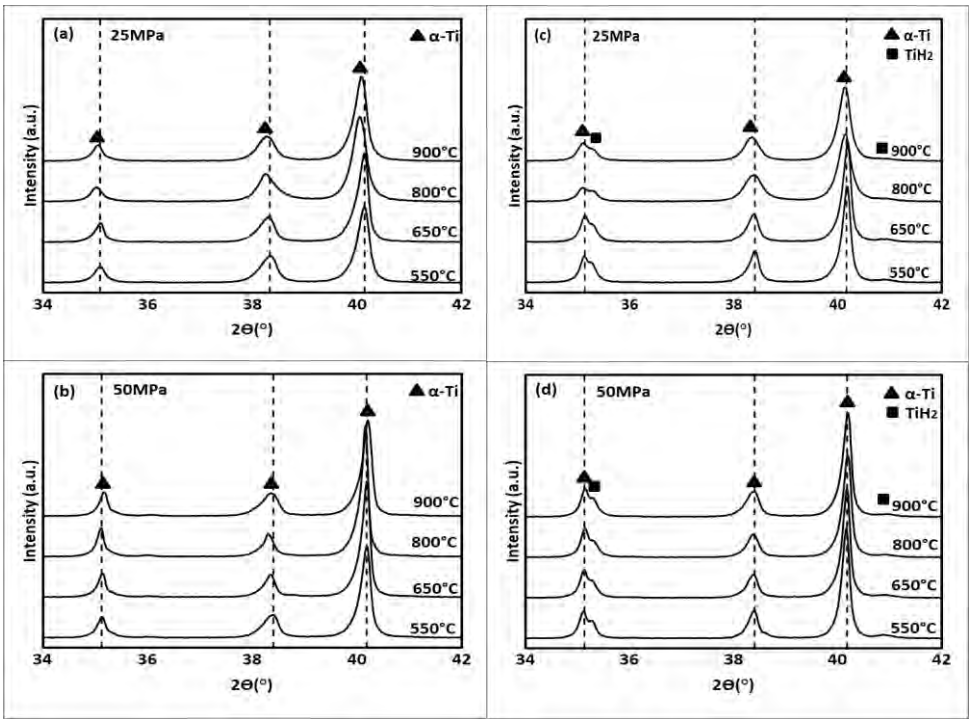

Figure 3.5. Effect of temperature on the structure of SPS pellets at 25MPa and 50MPa for CP- Ti(25.9µm) (a and b) and CP-Ti(35.9µm) (c and d)

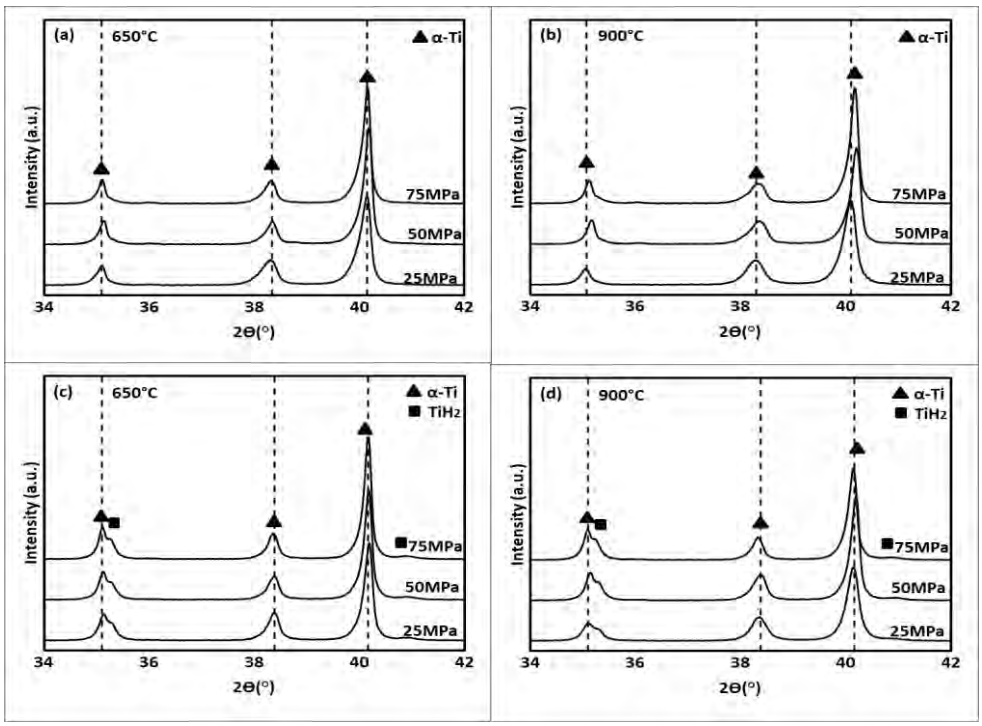

Figure 3.6. Effect of pressure on the structure of SPS pellets CP-Ti(25.9µm) a) 650°C, b) 900°C and CP-Ti(35.9µm) c) 650°C and d) 900°C

Microstructural evolution of CP-Ti(25.9µm) sintered pellets with increasing temperatures and pressure is presented in Figure 3.7. Porosity was observed at low temperatures of 550°C and 650°C, with the respective pressure and this was in good agreement relative density evolution reported in Figure 3.4.

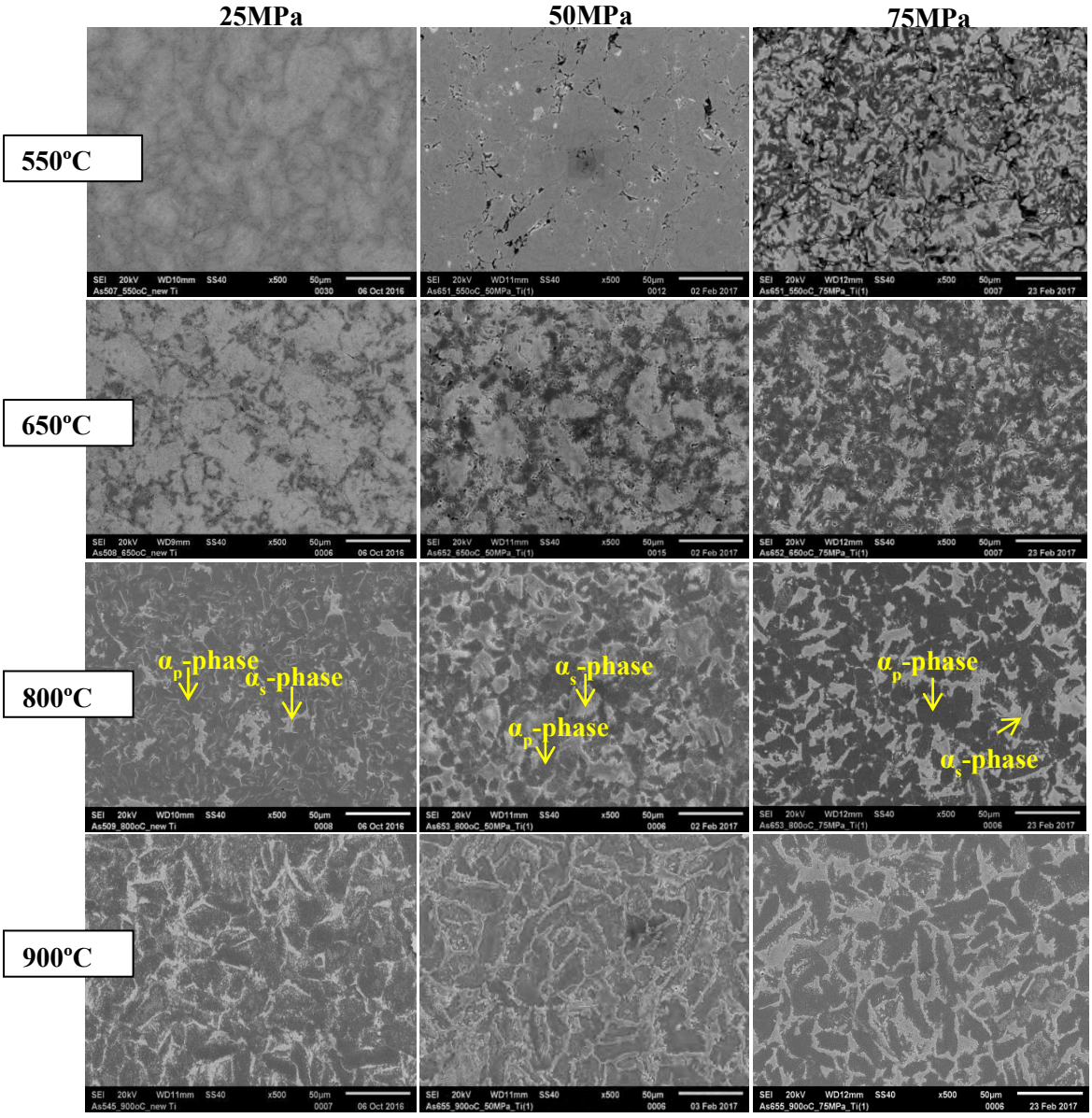

Figure 3.7. SEM micrographs of CP-Ti(25.9µm) SPS pellets

As previously discussed for varying temperature in the Gr die and powder, the actual temperature of the powder was higher than set-point temperature. In this discussion, we considered the actual temperature of the sample to be in excess of 68°C. Microstructural transformation of CP-Ti(25.9µm) at 800°C and 25MPa when cooling from above beta phase

transus temperature, show nucleation and growth of secondary α-phase (α_s) identified as the brighter phase at the grain boundaries of primary α-phase (α_p) which was identified as the darker phase (Lütjering *et al.*, 2007b). This could indicate that α_s-phase nucleation is initiated in the temperature range 718°C - 868°C, with few degrees below the α to β-Ti transus temperature for high purity titanium. When temperature was further increased to 900°C the microstructure transformed into equiaxed like structure, with increased volume fraction (21%) of α_s-phase. It was also observed that by increasing pressure to 50MPa at 800°C, an increase in the volume fraction (76%) of α_s-phase was noticed and decreased at 75MPa (19%). This was however not observed at 900°C, only the equiaxed like structure for α_s-phase became well defined.

Microstructural evolution of CP-Ti(35.9µm) is shown in Figure 3.8, when the temperature was increased to set-point of 800°C the microstructure completely transformed to lamellar structures with coarser α_s-phase, which was very visible as the pressure was increased to 50MPa. The pressure effect on the lamellar structure and α_s-phase volume fraction was minimal (insignificant phase shift as revealed by the diffraction patterns in Figure 3.6. Nucleation and growth of α_s-phase seem to have occurred at much lower temperatures of 618°C in the CP-Ti(35.9µm) as compared with CP-Ti(25.9µm)).

For the two powders investigated the dominant phases present were α_p and α_s-phases because there were few β-phase stabilising elements. When CP-Ti is heated to the β-Ti region and cooled down to α-Ti region, β-Ti phase is present only in small quantities or not retained and the structure transforms back to its room temperature α-Ti phase. Microstructure by diffusion controlled nucleation and growth is obtained by slower cooling rates producing a coarse Widmanstätten-α plus α-prime as observed for CP-Ti(35.9µm).

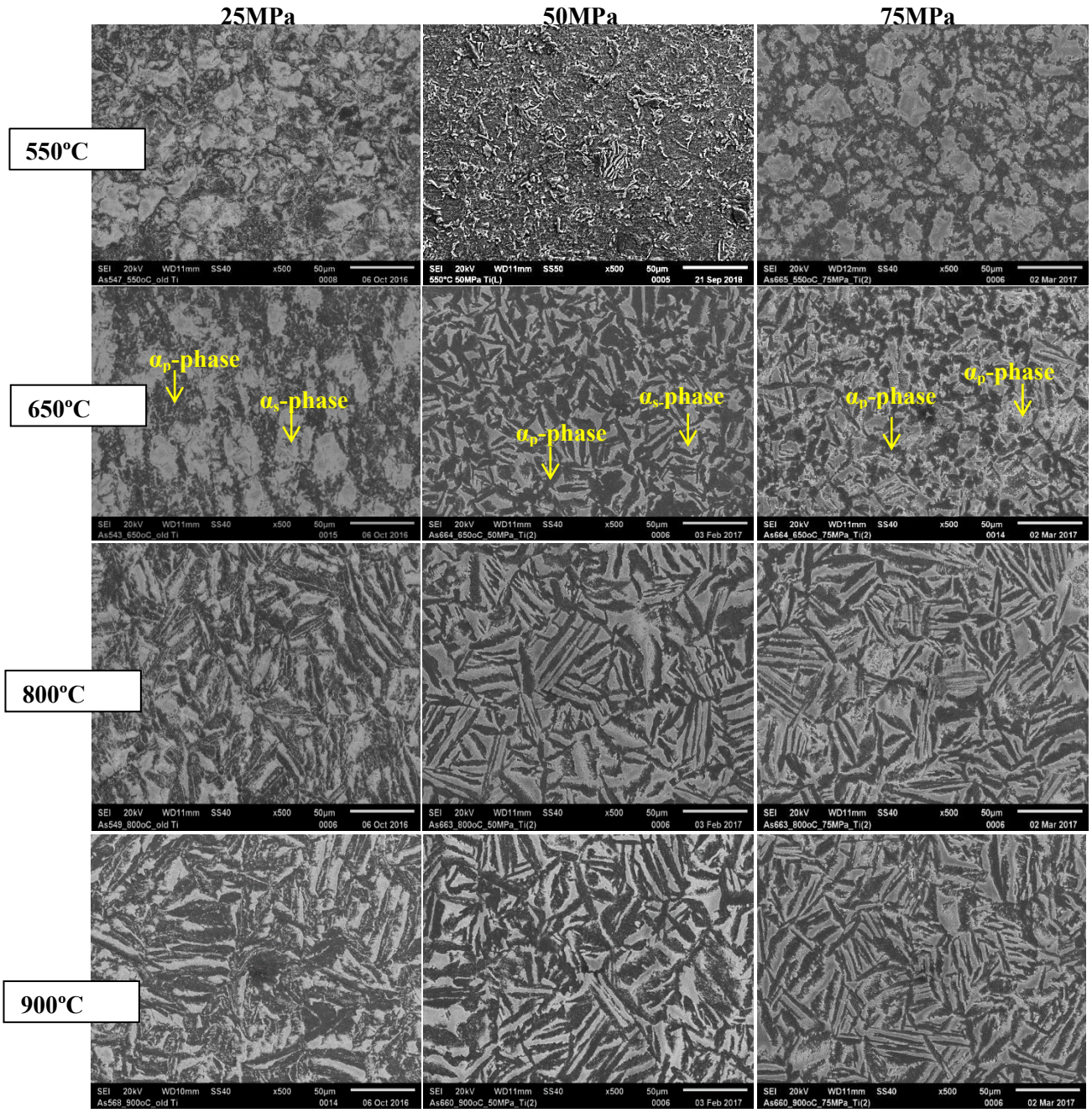

Figure 3.8. SEM micrographs of CP-Ti(35.9µm) SPS pellets

Microstructural transformation for CP-Ti(25.9µm) and CP-Ti(35.9µm) at 800°C at the various pressures is presented in Figure 3.9. The morphology of α_s-phase in the two samples was different at all pressures. At 25MPa, CP-Ti(25.9µm) has a combination of needle-like and irregular-shaped α_s-phase. When pressure was increased to 50MPa α_s-phase grain size increased then reduced at 75MPa. CP-Ti(35.9µm) at 25MPa has elongated needle-like and thickened α_s-phase showing the formation of lamellar structure. The lamellar structure is clearly visible at 50MPa and 75MPa for CP-Ti(35.9µm) where the grain sizes slightly

increased. These observations indicate that CP-Ti(25.9µm) microstructure transformation was delayed due to the high amount of dissolved oxygen (Table 12) which stabilized the α_p-phase. On the contrary, high amount of beta phase stabilizer hydrogen was measured in CP-Ti(35.9µm) (Table 12), promoting early microstructure transformation.

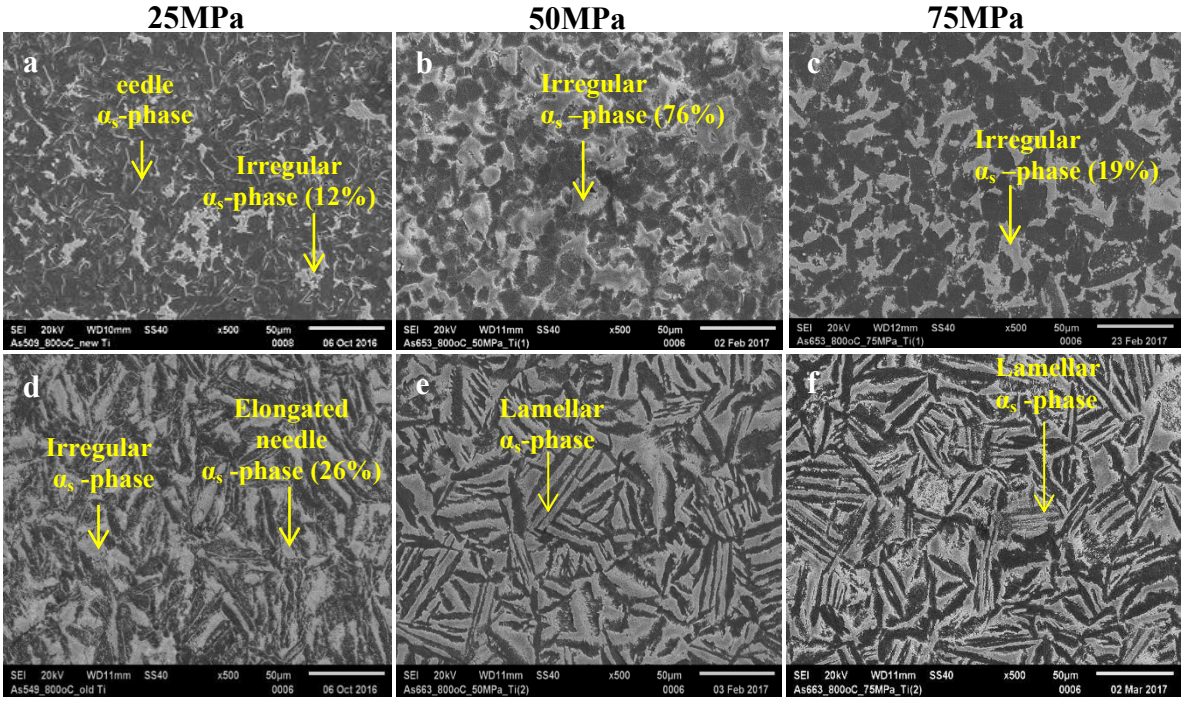

Figure 3.9. SEM micrographs for microstructure transformation at 800°C and varying pressures of 25-75MPa, CP-Ti(25.9µm) (a, b & c), CP-Ti(35.9µm) (d, e & f)

Moreover, on the grain growth with increase in pressure it appeared that different mechanisms occur during sintering and this phenomenon was more visible for CP-Ti(25.9µm). At low pressure of 25MPa the dominant mechanism could be due to electric discharging and neck formations between particles. This occurred by spark discharging between particles whereby high temperatures are reached causing vaporization and melting at the particles surface. This transient phenomenon resulted in necks formation around the contact area between the particles. The necks gradually developed and plastic deformation progressed during sintering until full densification was reached (Tokita, 1999). However, at high pressures these mechanisms were only dominant in the early stages of sintering. At high sintering pressure of 50MPa and 75MPa the possible mechanisms occurred were electric discharges dominant only in the beginning of sintering and were suppressed after. Particles rapidly plastically deformed and rapid neck formation occurred in favor of the Joule effect which enhanced diffusion and

the consequent grain growth. Hence sintering occurred by mechanical mechanisms in contrast to low sintering pressure (Garbiec *et al.*, 2016).

3.5 Effect of sintering temperature and pressure on Vickers hardness

Hardness evolution with increasing temperature and pressure for CP-Ti(25.9µm) and CP-Ti(35.9µm) is shown in Figure 3.10. The hardness of CP-Ti(25.9µm) at 25MPa increased as the temperature was increased from 550°C to 800°C then decreased after at higher temperatures. This could be due to the 21% volume fraction of α_s-phase formed at 900°C, in contrast to 12% at 800°C. The same behaviour is observed at 75MPa. Whereas CP-Ti(35.9µm) hardness increases with increasing temperature and pressure. It seems that CP-Ti(35.9µm) present the same hardness, whatever the applied pressure. The plateau was reached at lower temperature as the pressure was increased. There was a significant difference in hardness values for CP-Ti(25.9µm) and CP-Ti(35.9µm) SPS pellets, the values are in between 102-340HV and 160-260HV respectively, in agreement with values of the literature (Shon *et al.*, 2014b; Welsch *et al.*, 1993). The highest hardness of 340HV was obtained at 25MPa and 800°C for CP-Ti(25.9µm) with a "needle-like'' microstructure consisting of low volume fraction of α_s-phase as shown in Figure 3.9(a), and that of CP-Ti(35.9µm) with lamellar microstructure in Figure 3.9(f) was 262HV at 25MPa and 900°C.The high hardness of CP-Ti(25.9µm) was attributed by the smaller particle sizes (25.9µm) (according to Hall-Petch) (Callister *et al.*, 2011) and the high amount of oxygen dissolved in the matrix delaying the structural transformation into a lamellar structure with low mechanical properties. These results are similar to those reported by (Shon *et al.*, 2014b), who reported that CP-Ti with 25.06µm particles sizes with highest oxygen content yielded high hardness, tensile strength and reduced ductility, as opposed to 86.368µm powder. Zadra *et al.* (2008) investigated the dependence of mechanical properties on oxygen content by investigating CP-Ti powders of the same particles size of 45µm but different oxygen contents. Their results also demonstrated the same effect of oxygen on mechanical properties agreeing with the present study.

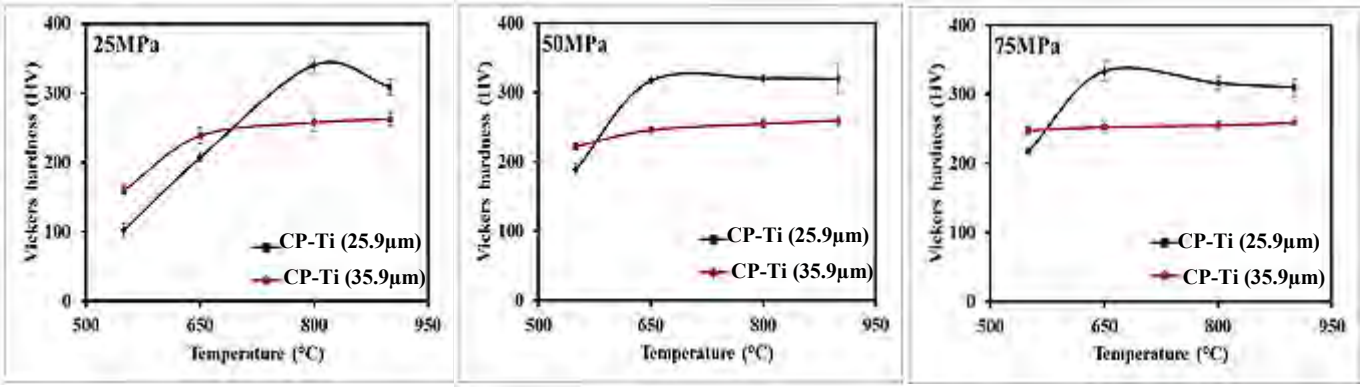

Figure 3.10. Vickers hardness vs temperature at 25MPa, 50MPa and 75MPa for CP-Ti(25.9µm) . and CP-Ti(35.9µm) SPS pellets

The Vickers hardness was plotted as a function of the relative density (Figure 3.11). SPS pellets with highest relative density have high hardness and vice versa (Miklaszewski *et al.*, 2018). The effect of pressure on densification is observed, the relative densities are in the range 77-100%, 93-100% and 97-100% for 25MPa, 50MPa and 75MPa respectively. However, the increased applied pressure shows to have minor effect on the hardness of the SPS pellets especially for those sintered at high temperatures (800-900°C) the values obtained are almost in the same range.

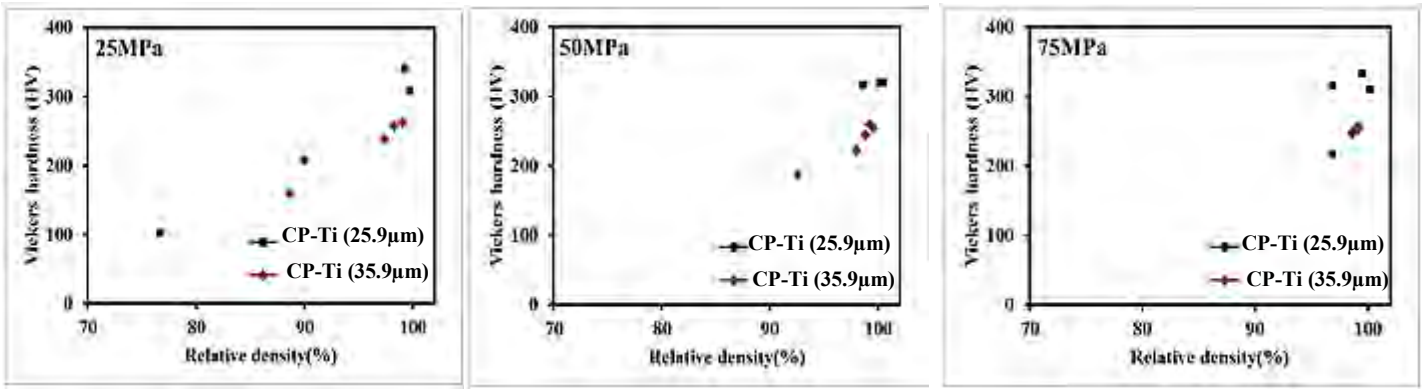

Figure 3.11. Vickers hardness vs relative density at 25MPa, 50MPa and 75MPa for CP-Ti(25.9µm) and CP-Ti(35.9µm) SPS pellets

Summary

Sintered CP-Ti samples were obtained at temperatures ranging from 550 to 900°C from CP-Ti powders of different composition. Full densification was obtained at 25MPa at temperatures of 800°C and 900°C for CP-Ti(25.9µm) and CP-Ti(35.9µm) respectively. The microstructure transformation for CP-Ti(25.9µm) with high amount of oxygen was delayed and only started

at higher temperatures. As for CP-Ti(35.9µm) with high amount of hydrogen the transformation was promoted at very low temperatures and increased pressure. As found in literature oxygen is α-phase stabiliser raising the α to β transus temperature while hydrogen is a β-phase stabiliser lowering the transus temperature. The different elemental composition of the fully dense samples resulted in different microstructures formation with CP-Ti(25.9µm) characterised by needle like structure and for CP-Ti(35.9µm) lamellar structure was obtained. Thus CP-Ti(25.9µm) exhibited higher Vickers hardness of 340HV compared to CP-Ti(35.9µm) with 262HV. In addition, smaller particles size resulting in retention of small grains for CP-Ti(25.9µm) also contributed to the high Vickers hardness value obtained in comparison to CP-Ti(35.9µm). It was found that increase of α_s-phase volume fraction with pressure could be related to electric discharges between particles and plastic deformation of particles at low and high pressure respectively. Increment of α_s-phase volume fraction was found to be influenced by increased pressure, temperature and high amount of hydrogen.

CHAPTER 4: Sintering, characterization and reaction mechanisms of Titanium Matrix Composites

Table of contents

4.0 Introduction

Fabrication of conventional TMCs based on pure TiB_2/TiB and TiC reinforcing phases with very high melting temperatures compared with B_4C, often requires much higher temperatures for full consolidation. Both the energy consumption and the related cost of the reinforcing phases are high (Vallauri *et al.*, 2008; Wang *et al.*, 2012). For economical reason, B_4C was chosen as source for the production of the reinforcing phases by reactive sintering with CP-Ti matrix. Moreover SPS technique, which is known to consolidate materials within short period due to the application of pulsed electric current and pressure reducing energy consumptions, was employed (Munir *et al.*, 2006; Orru *et al.*, 2009).

In this chapter, simultaneous synthesis and consolidation homogenously distributed TiB and TiC phases in the titanium matrix was investigated. The involved reaction kinetics between pure CP-Ti and B_4C powders of varying particles size and the influence of temperature, pressure and dwell time on the reaction was studied. Moreover, to effectively understand microstructure evolution, phase products formations, particularly TMCs consolidated from sub-micron B_4C powders, FIB and TEM analyses were carried out. Thereafter the weight percent of TiB and TiC on the fully consolidated TMCs were estimated with reference intensity ratio (RIR) method and the Vickers hardness values were quantified.

4.1Characterization as-received CP-Ti (25.9µm) and B_4C powders

A detailed characterization of as-received CP-Ti powder with D_{50} of 25.9µm obtained from PI-KEM Ltd., UK has already been discussed in Chapter 3. In this section three ceramic B_4C powders with varying particles size obtained from H.C. Starck (0.3 - 0.6µm) and LTS research laboratories. Inc. with (-400 and -325 mesh) were characterized. In addition, the powder mixtures of B_4C powders with CP-Ti(25.9µm) were also characterized. The SEM morphology and the particles size and distributions (PSD) of the as-received powder are presented in Figure 4.1: a) Ti with D_{50} size of 25.9µm and B_4C powders with varying D_{50} sizes of b) 1.67, c) 1.79 and d) 17.9µm.

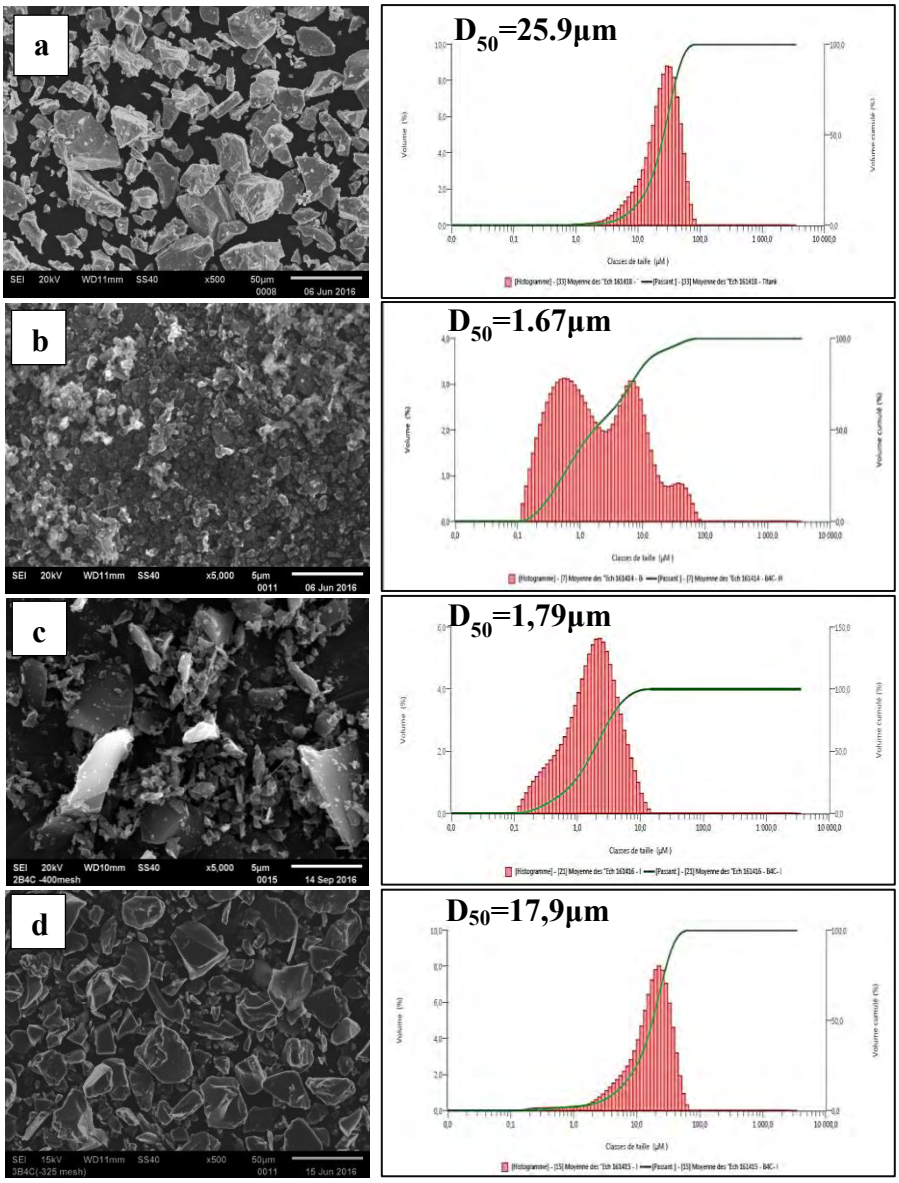

Figure 4.1. As received powders a) Ti(25.9µm) , b) B_4C (1.67µm), c) B_4C (1.79µm) and d) B_4C (17.9µm)

We can observe that both Ti and B_4C powders are irregular shaped and the PSD of the B_4C powders gets narrow with increasing D_{50} size. CP-Ti (25.9µm) with lower hydrogen content (546ppm) was chosen to reactively sinter with the B_4C powders to produce the desired TMCs. The XRD patterns of the pure powders are reported in Figure 4.2 CP-Ti(25.9µm) was characterized with alpha Ti phase and the B_4C powders contained elemental carbon and B_2O_3 phases. We can observe in the XRD patterns of B_4C the peaks become narrower with reducing particles size.

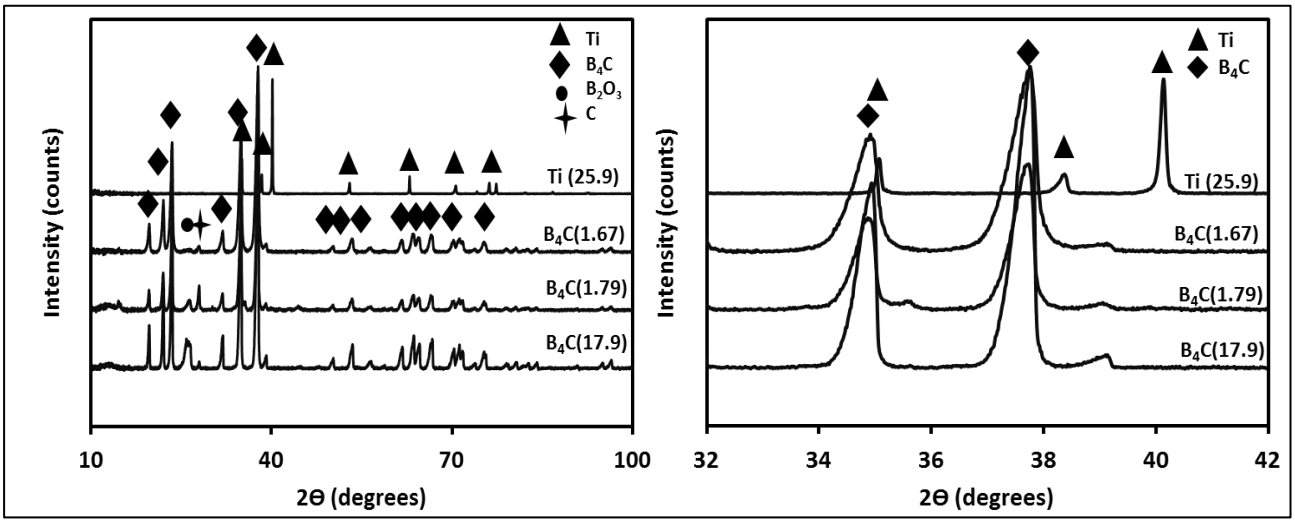

Figure 4.2. XRD pattern for Ti and B_4C as received powders

4.2 Characterization of mixed CP-Ti (25.9µm) and B_4C powders

To achieve a homogenous microstructure of sintered TMCs, the starting powders must be effectively homogenized by mixing. This method is important and can significantly affect the quality and properties of the final TMC. Ti (25.9µm) and B_4C powders were carefully mixed at weight percent ratios of 99:1, 97.5:2.5, 95:5, 90:10 to produce reinforcing phases (TiB and TiC) in volume percentages of 5vol%, 13vol%, 26vol% and 53vol%. The lower B_4C powder content of 1-10wt% was chosen in order to prevent agglomerates formation, high porosity, lower toughness and reduce high temperature required for complete reaction (Ariza Galván *et al.,* 2017, Balaji *et al.,* 2014, Ni *et al.,* 2006). The respective volume percentage of TiB and TiC phases in the TMCs are shown in Table 13 and detailed calculations for these volume percentages are shown in Appendix I.III. A homogeneous distribution of B_4C phase in Ti matrix will help further with uniform distribution of the desired reinforcing phases in the synthesized TMCs. Figure 4.3 shows SEM micrographs of powder mixtures for Ti5wt%B_4C and Ti10wt%B_4C. In the powder mixtures containing B_4C(1.67µm), smaller B_4C particles

adhered to the Ti particles this was more visible for Ti10wt%B_4C(1.67µm) (Figure 4.3 (d)). When powder mixtures contain larger B_4C particles, B_4C(1.79µm) and B_4C(17.9µm), the B_4C particles were homogeneously distributed with the CP-Ti(25.9µm) particles. The EDS analysis shown in Figure 4.4 further confirms that the bright and dark phases are Ti and B_4C particles respectively. The XRD phase analysis evidence a small B_4C peak in Ti10wt%B_4C powder mixtures as shown in Figure 4.5. The B_4C peak diminished with decreasing the content in powder mixtures of Ti1wt%B_4C, Ti2.5wt%B_4C and Ti5wt%B_4C. This is attributed to the B_4C lower density (2.52g.cm^3) and that XRD phase detection is limited to concentration of about 2-5wt% in powder mixtures. However, when the XRD scan was done for 2h at step size of 0.01 at reduced 2-theta range of 34°- 42° and 36° - 39.5° 2-theta ranges for Ti5wt%B_4C(1.67µm) the B_4C peak was visible as shown in Figure 4.6.

Table 13. Theoretical volume percentage of reinforcing phases in complete chemical reaction

	Ti	Ti1wt%B_4C	Ti2.5wt%B_4C	Ti5wt%B_4C	Ti10wt%B_4C
Ti (vol%)	100	95	87	74	47
TiB (vol%)	0	4	11	21	43
TiC (vol%)	0	1	2	5	10

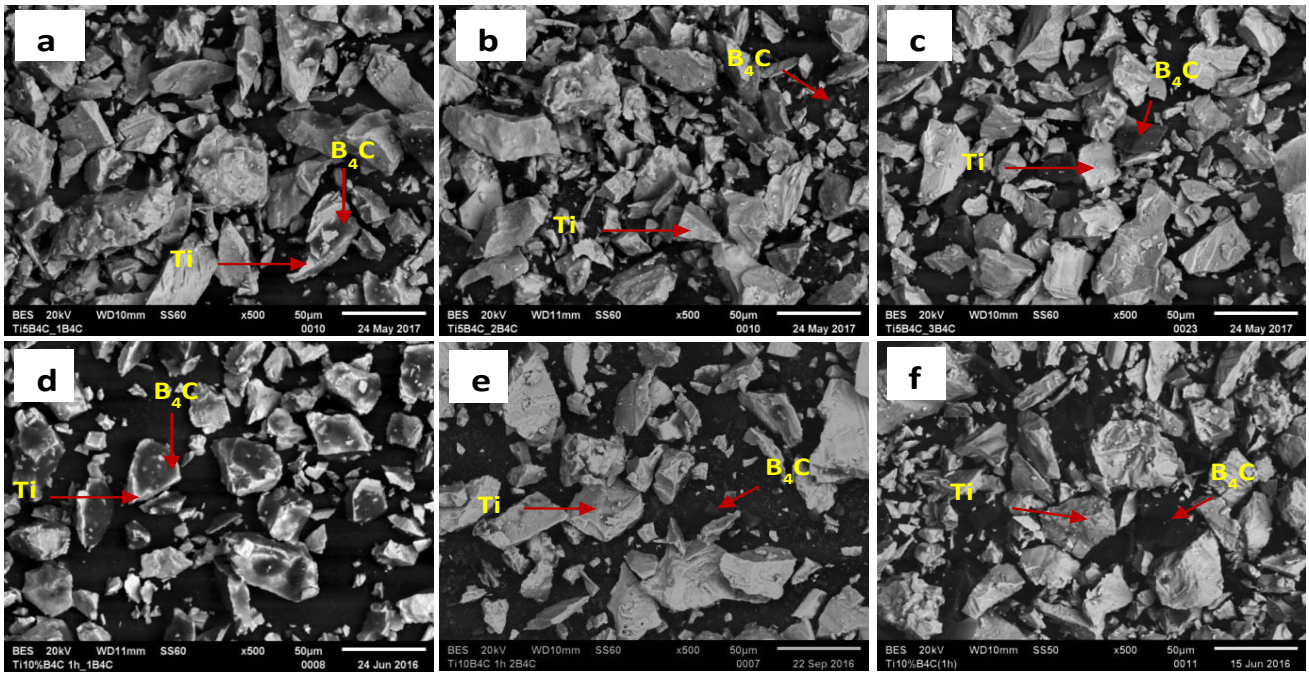

Figure 4.3. SEM micrographs of Turbula mixed powders Ti5wt%B_4C a) B_4C(1.67µm), b)B_4C(1.79µm) and c) B_4C(17.9µm)and for Ti10wt%B_4C d) B_4C(1.67µm), e) B_4C(1.79µm) and f) B_4C(17.9µm)

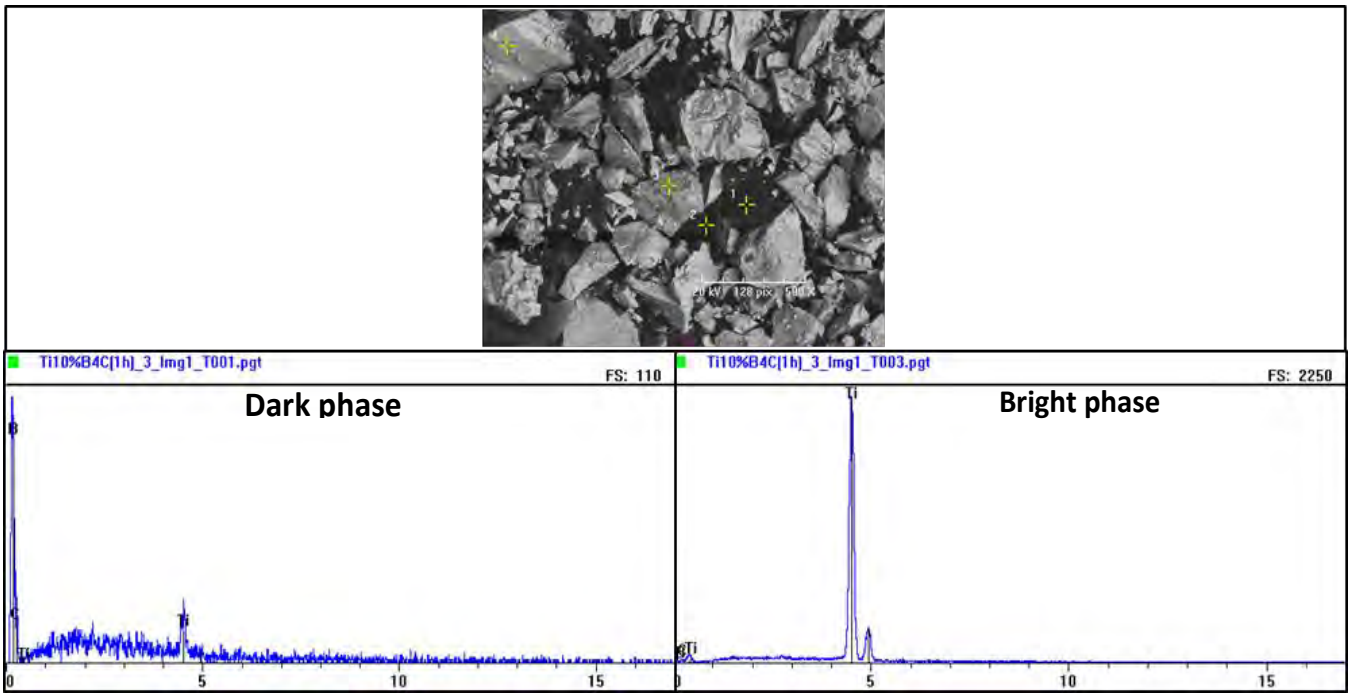

Figure 4.4. EDS analysis of mixed Ti10wt%B_4C(17.9µm) powder

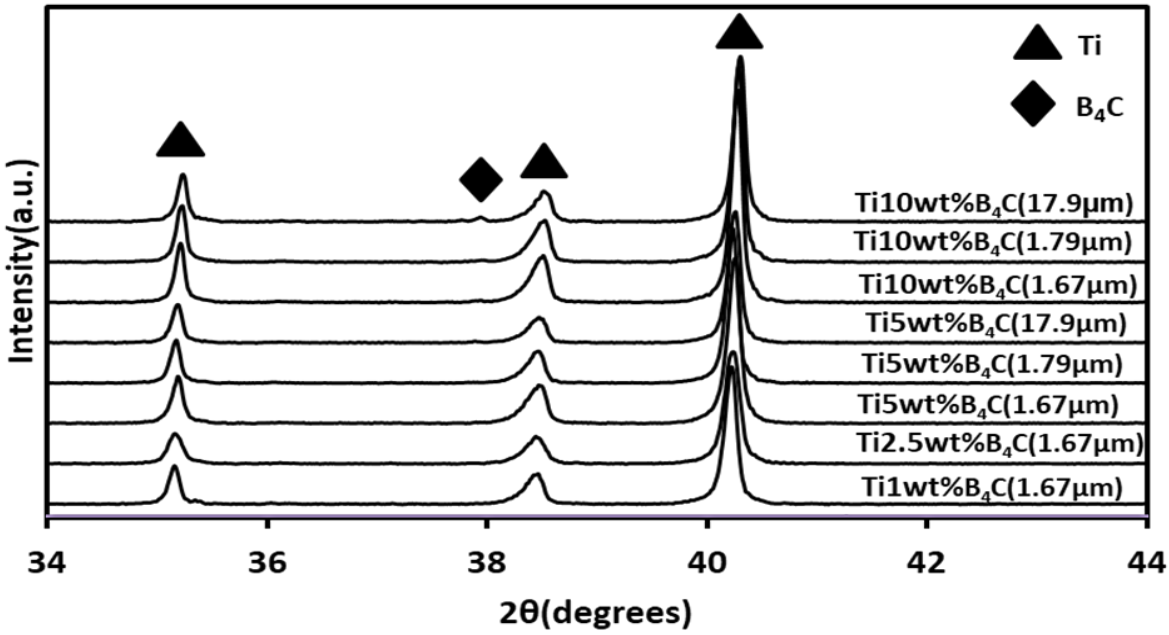

Figure 4.5. XRD patterns for mixed powders

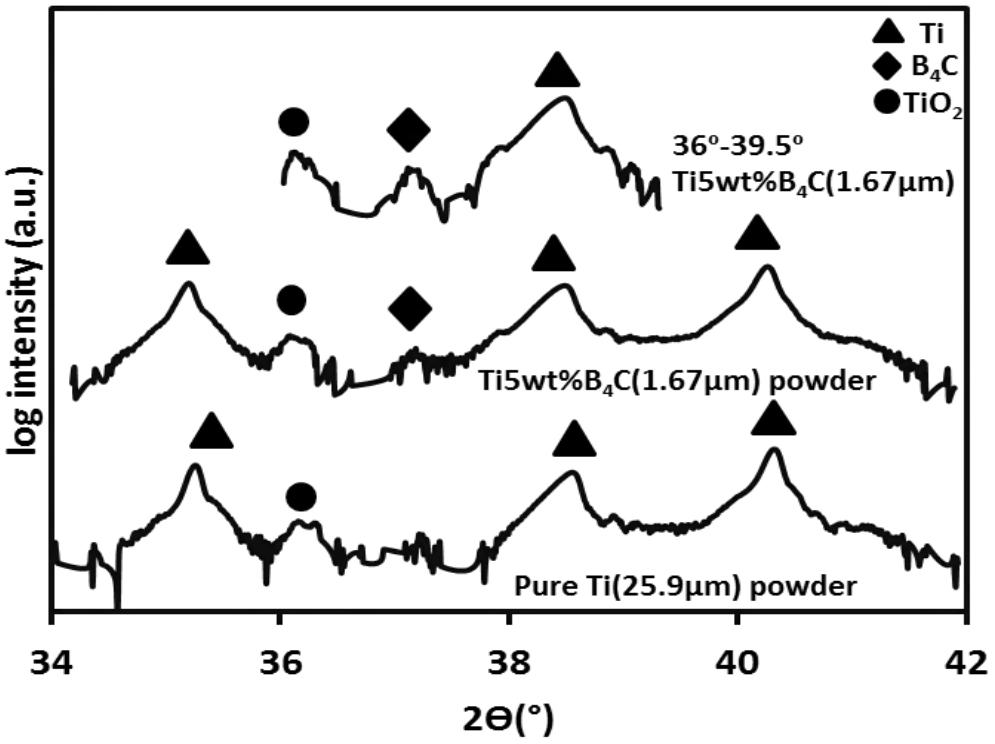

Figure 4.6. XRD patterns for CP-Ti(25.9 µm) and Ti5wt%B_4C(1.67 µm) powders at step size of 0.01 for 2h at 2-theta range of 34°- 42° and 36°- 39.5°.

4.3 Synthesis and densification of TMCs

Synthesis of TiB and TiC reinforcing phases considered in this study is based on exothermic chemical reactions between Ti and B_4C powders taking place during sintering at elevated temperatures (Campbell, 2010). In this method of fabrication, simultaneous synthesis of the desired reinforcing phases and consolidation of the TMC takes place in one step. This method promotes formation of a strong interfacial bond between Ti matrix and the reinforcing phases which could be a good microstructural characteristic for enhanced mechanical properties. Densification and microstructure characterization of CP-Ti(25.9µm) has already been discussed in chapter 3, in this chapter more focus will be put on characterization of TMCs.

Samples, 8mm in diameter and 2mm in thickness, were densified under vacuum (<10Pa) from Ti5wt%B_4C and Ti10wt%B_4C mixed powders of the respective varying B_4C particles size (1.67, 1.79 and 17.9µm) and CP-Ti(25.9µm). The evolutions of the relative densities are shown in Figure 4.7 as a function of temperature (800°C - 1100°C), for a dwell time of 3 min, for three applied pressures. It was observed that the relative densities at given applied pressure increase with increasing temperature for all the TMCs while CP-Ti(25.9µm) at

800°C already densified to 99%. Several factors affected the lower relative densities of the TMCs at lower temperature.

Firstly, it has to be noted that the relative densities were calculated by theoretically determining the amount of the reinforcing phases in the desired TMCs. Assuming that B_4C completely reacted to form TiB and TiC phases and with Ti as the remaining reactant (*see* Appendix I.II). So, the lower relative densities in Ti-B_4C (17.9 μm) TMCs were attributed to the higher theoretical densities of Ti (4.51 g/cm^3), TiB (4.56 g/cm^3) and TiC (4.93g/cm^3) phases, in comparison to B_4C (2.52 g/cm^3) with lower density. Secondly, sintering of finer particles (1.67 and 1.79μm) with a greater pore/solid interfacial area produces a greater driving force for sintering. The smaller particles promotes all types of diffusion transport in contrast to coarser particle (17.9 μm), which include greater surface area leading to more surface diffusion, small grain size promoting grain boundary diffusion and larger interparticle contact area to volume diffusion (Upadhyaya, 1997). Thirdly, densification of TMCs with D_{50} sizes of 1.67 and 1.79μm at lower temperatures could have also been enhanced by formation TiB whiskers at the grain boundaries which could have also aided in elimination of porosity

When the B_4C content was increased from 5wt% to 10wt% the relative densities lowered further. The difference in the relative densities could be due to inclusion of high amounts of unreacted B_4C particles, as previously explained for influence of theoretical density calculations, finer particles and reactions kinetics. Similar to Balaji *et al.* (2014), it was reported that densification of Ti-B_4C from room temperature (37%) to 573°C (35%) decreased (29%) with increasing B_4C content from 1.2wt%, 2.3wt% to 3.4wt% respectively. However, with temperature increase from 573°C to 900°C, 573°C to 950°C and 573°C to 1150°C densification (62%>64%>70%) increased with increasing B_4C content (1.2wt%>2.3wt%> 3.4wt%) Increasing the applied pressure slightly increase the relative densities especially at lower temperatures.

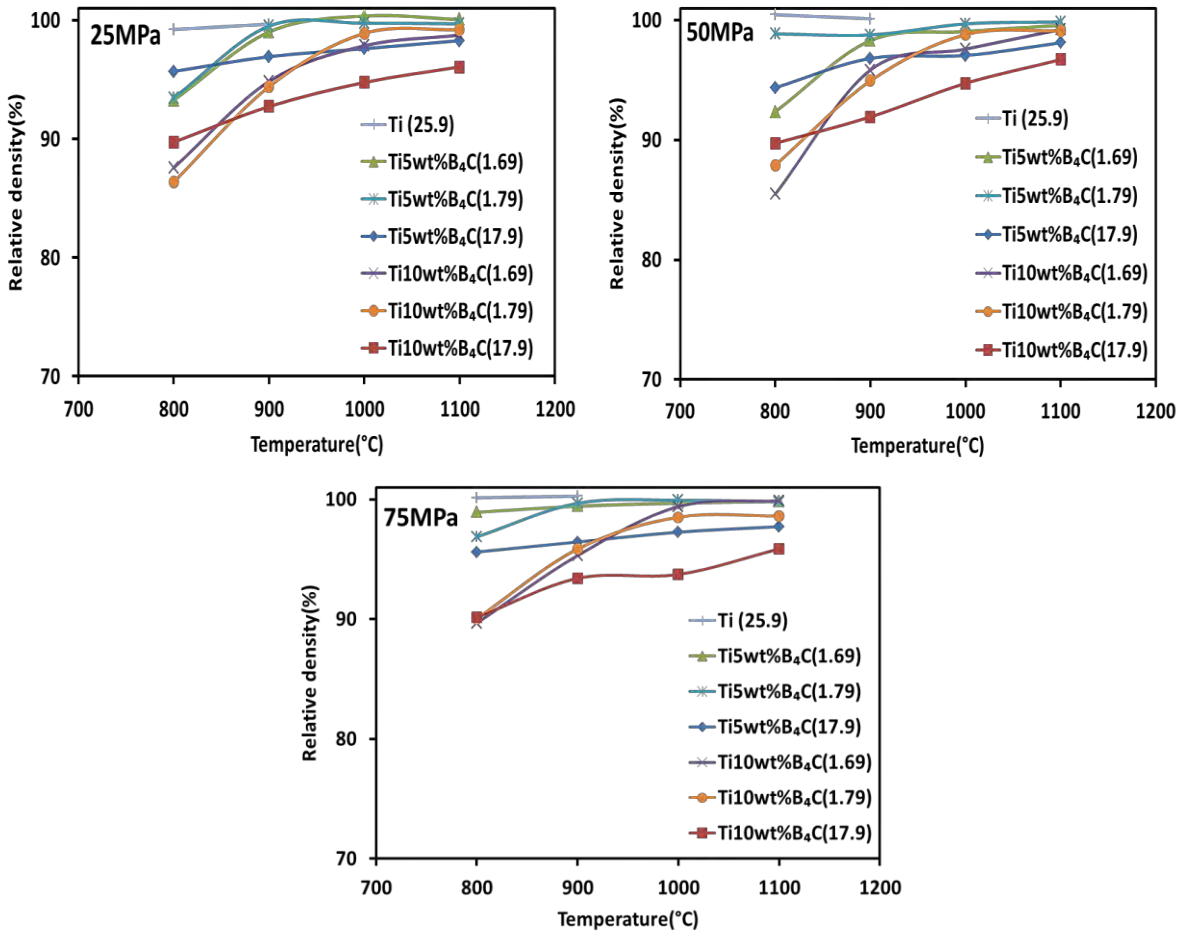

Figure 4.7. Relative density for CP-Ti, Ti5wt%B_4C and Ti10wt%B_4C TMCs at varying pressures of 25MPa, 50MPa and 75MPa

The XRD patterns of Ti-B_4C TMCs with varying B_4C particles (17.9µm, 1.79µm and 1.67µm) and B_4C content (5wt% and 10wt%) with 8mm diameter sintered at 800°C - 1100°C and 25MPa to 75MPa at 3min dwell time are shown Figure 4.8, 4.9 and 4.10 respectively. The reactivity of Ti and B_4C was reported take place at temperatures above 800°C (Lu *et al.*, 2008), while DTA analysis revealed wide a exothermic peak appearing at 1093°C (Liang *et al.*, 2008) and analysis by DSC revealed exothermic peaks before 1200°C (Ni *et al.*, 2008a). At 800°C and 25MPa in Figure 4.8(a) the reaction between Ti and coarser B_4C (17.9µm) particles was very slow despite the increase of temperature, pressure and B_4C content to 10wt%. From the XRD scan the B_4C peak was not detected due to limitation of phase detection at lower concentrations (5wt%). So, we cannot conclude that B_4C has completely reacted at 800°C for Ti-B_4C(17.9µm) TMCs. However, it was shown in Figure 4.6 for Ti5wt%B_4C powder with finer B_4C particles (1.67µm), the B_4C peak was only visible when

the scan was done for 2h at 36°- 39.5° 2-theta range. Also the evidence from the SEM micrographs in the next section 4.4 shows unreacted B_4C particles. So, we could say that B_4C with coarser particles (17,9µm) was not completely reacted for both at 800°C.

Increasing temperature from 900 to 1100°C at the respective pressures, TiB and TiC peaks were detected and the contents were higher in Ti10wt%B_4C(17.9µm) Figure 4.8 (d-f) in contrast to Ti5wt%B_4C(17.9µm) (Figure 4.8 (a-c)). Also, it is worth to note that TiB_2 phase as an expected transient phase for formation of TiB whiskers was not detected for all the TMCs at 10°-100° at 2-theta. This could indicate that TiB_2 phase was present only in trace amounts.

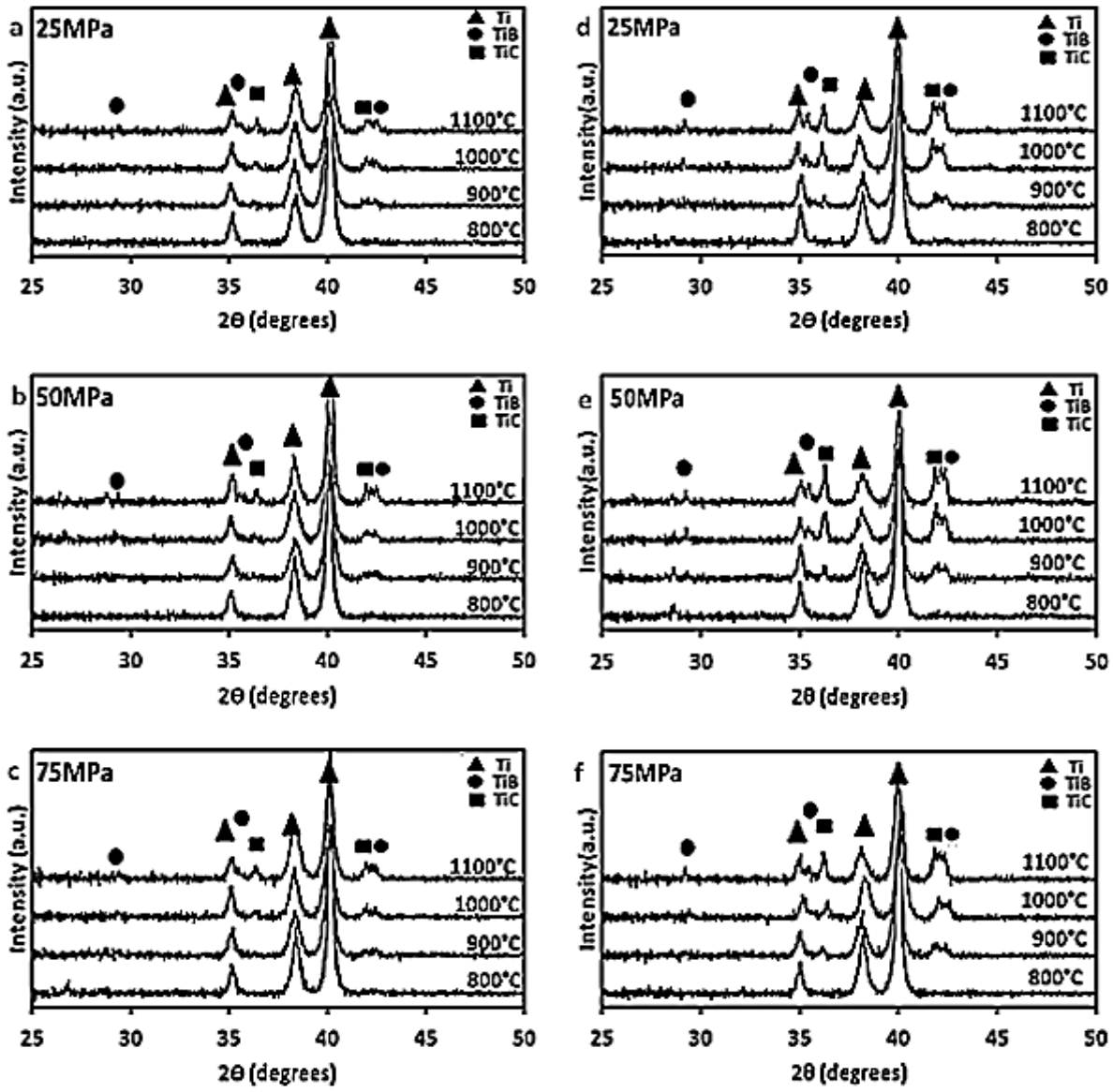

Figure 4.8. XRD patterns 8mm TMCs at sintered at varying temperature and pressure, (a-c)Ti5wt%B_4C(17.9µm) and (d-f) Ti10wt%B_4C(17.9µm)

When the B_4C particles size were reduced to 1.79 µm the TiB and TiC peaks at 800°C and 25MPa were partially visible for Ti5wt%B_4C(1.79µm) as shown in Figure 4.9(a-c). The peaks became relatively stronger especially with increase of pressure (50MPa and 75MPa) and B_4C content to 10wt% as shown in Figure 4.9(d-f). Figure 4.10 presents TMCs synthesized from finer B_4C particles (1.67µm), the TiB and TiC peaks were stronger at 800°C compared with other TMCs (1.79 and 17.9µm B_4C). It is expected for finer particles to have higher reaction spontaneity than coarser particles, because of their larger surface area.

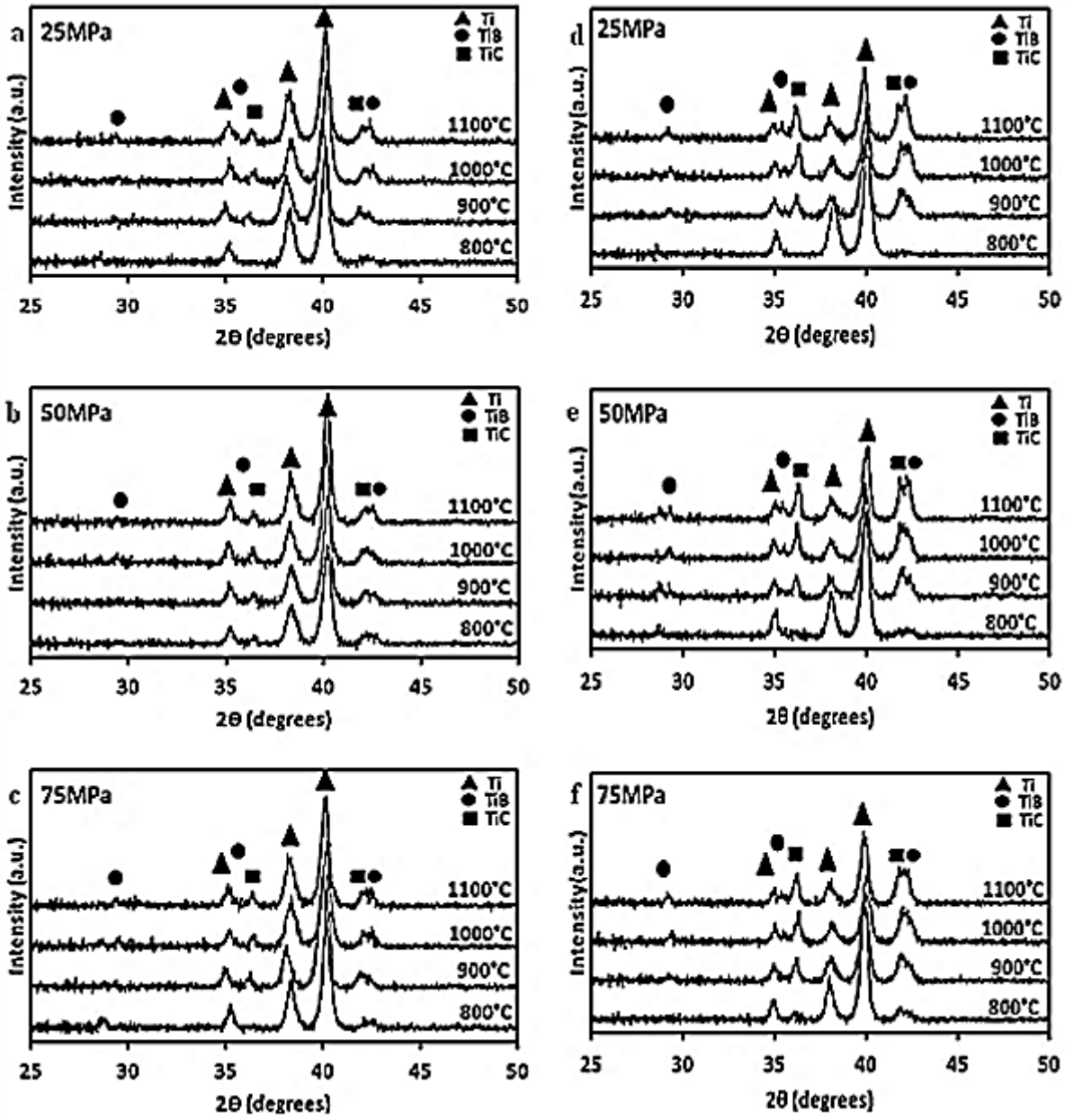

Figure 4.9. XRD patterns 8mm TMCs at sintered at varying temperature and pressure, (a-c) Ti5wt%B_4C(1.79µm) and (d-f) Ti10wt%B_4C(1.79µm)

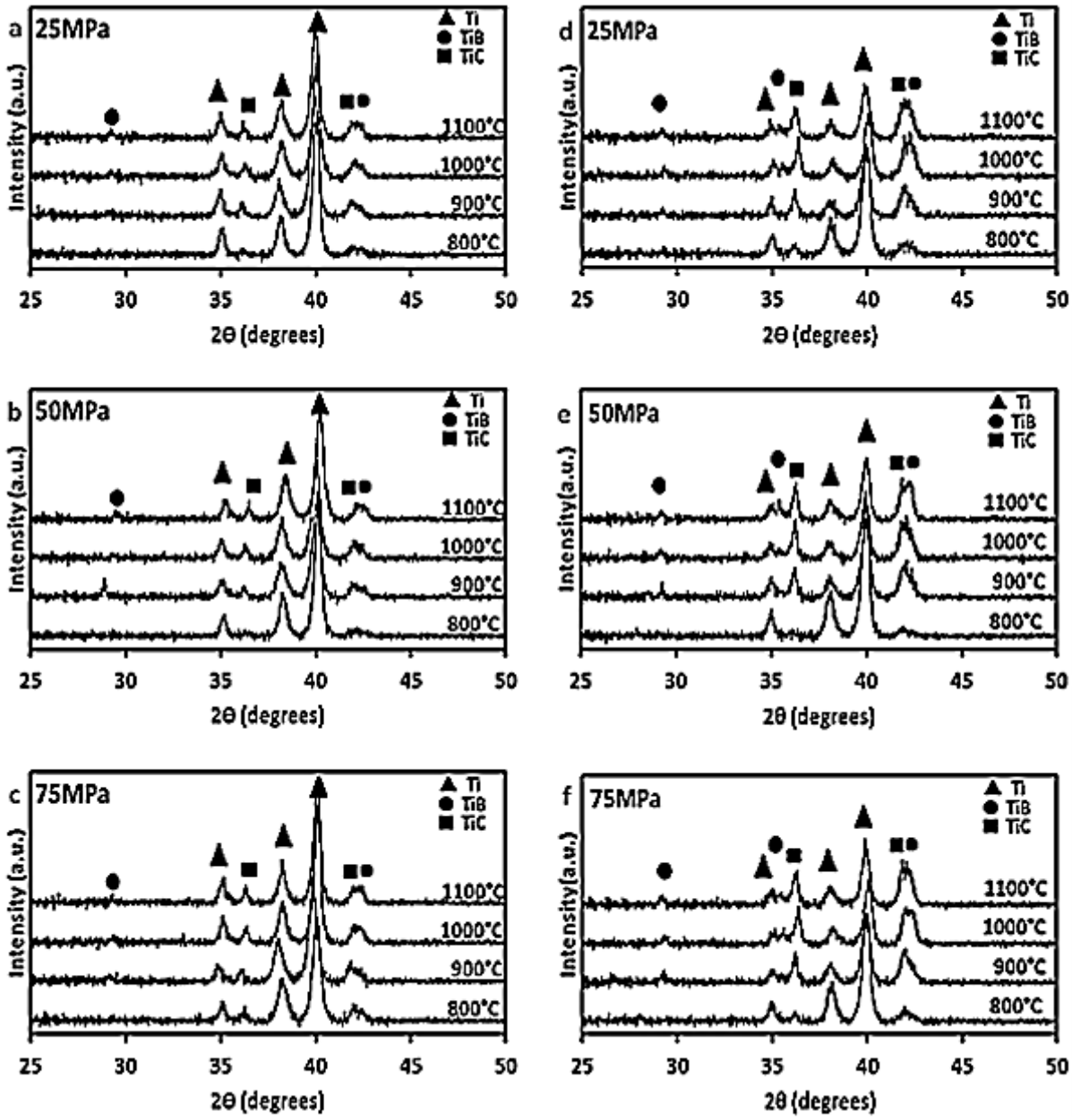

Figure 4.10 XRD patterns 8mm TMCs at sintered at varying temperature and pressure, (a-c)Ti5wt%B_4C(1.67µm) and (d-f) Ti10wt%B_4C(1.67µm)

Summary

Analysis of the XRD patterns for all the sintered TMCs shows that Ti, TiB and TiC are the major phases present. However, the B_4C and TiB_2 peaks were not detected due to low concentration. From the XRD patterns it was not clear which reinforcing phase formed first, it was reported that because of B low diffusion velocity in Ti matrix than C, B concentration would be high at the Ti/B_4C interface and TiB whiskers primarily form, while C diffuse

further into Ti matrix to form TiC particles (Brodkin *et al.*, 1996; Jia *et al.*, 2016; Rafiei *et al.*, 2014).

In order to quantify the reinforcing phase's volume fraction evolution with increasing temperature, pressure and B_4C content the RIR method could not be used due to the discrepancies related to the degree of the B_4C consumption during the reaction. Nevertheless, the increasing amount of reinforcing phases with sintering parameters and B_4C content showed that reaction between Ti and B_4C does take place. Moreover, it is worth to note that pressure increase has more effect on reinforcing phase's formation on TMCs with finer B_4C particles (1.67µm and 1.79µm) than those with coarser B_4C particles (17.9 µm) especially at lower temperature.

4.4 Microstructural evolution with temperature and pressure

The microstructure evolution of the sintered TMCs described in this section helps in understanding the reaction between Ti and B_4C with D_{50} particle sizes of 17.9µm, 1.79 µm and 1.67µm with varying content of 5wt% and 10wt%. This was carried out to investigate the desirable B_4C particle size to synthesize of TiB whiskers and TiC particulates. As observed in Figure 4.11(a) for Ti5wt%B_4C at 800°C and 25MPa there was porosity and the reaction between Ti and coarse B_4C(17.9 µm) already commenced as thin grey TiB_2 layer and fine TiB whiskers were evidenced. However, TiB_2 layer and TiB whiskers were not detected by XRD at 800°C and 25MPa, this indicate that volume percentage of these phases was below 2 - 5% detection limit for XRD technique. The TiB_2 layer on average grow from about 0.66µm to 8.13µm and the TiB whiskers from 1.97µm to 6.96µm for 800°C (Figure 4.11(a)) and 1100°C (Figure 4.11(d)) at 25MPa respectively. Moreover, at 1100°C the central portion of B_4C particle was unreacted and would require higher temperature or dwell time for a complete reaction (Balaji *et al.*, 2014). In agreement with the XRD (Figure 4.8), pressure had less effect on the formation of TiB and TiC synthesized from coarse B_4C, as the microstructures were almost similar. As the weight percent of B_4C increased to 10wt% the only difference was the increment of porosity and reinforcing phases as observed in Figure 4.12. The presence of the unreacted B_4C is undesirable in the final TMCs as they may have adverse effect on the mechanical properties (Tabrizi *et al.*, 2015).

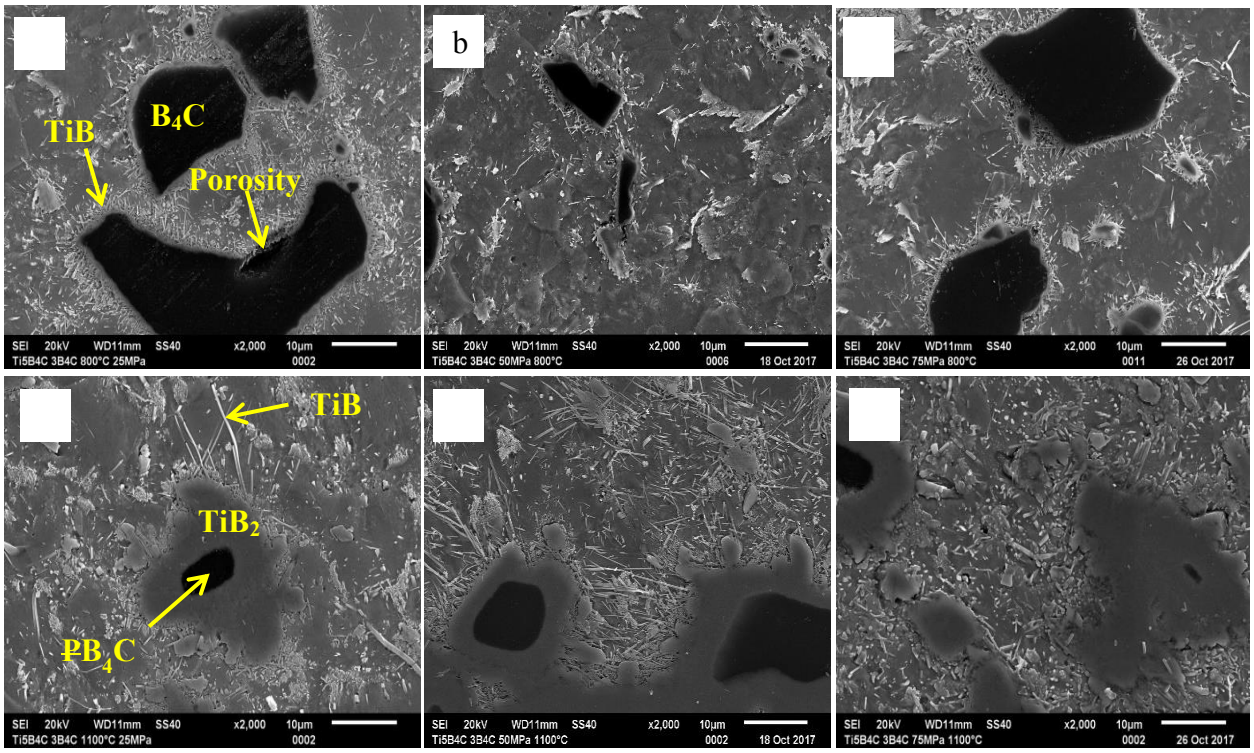

Figure 4.11. SEM micrographs for Ti5wt% B_4C for B_4C (17.9µm) powder at 25MPa, 50MPa and 75MPa for 800°C (a-c) and 1100°C (d-f)

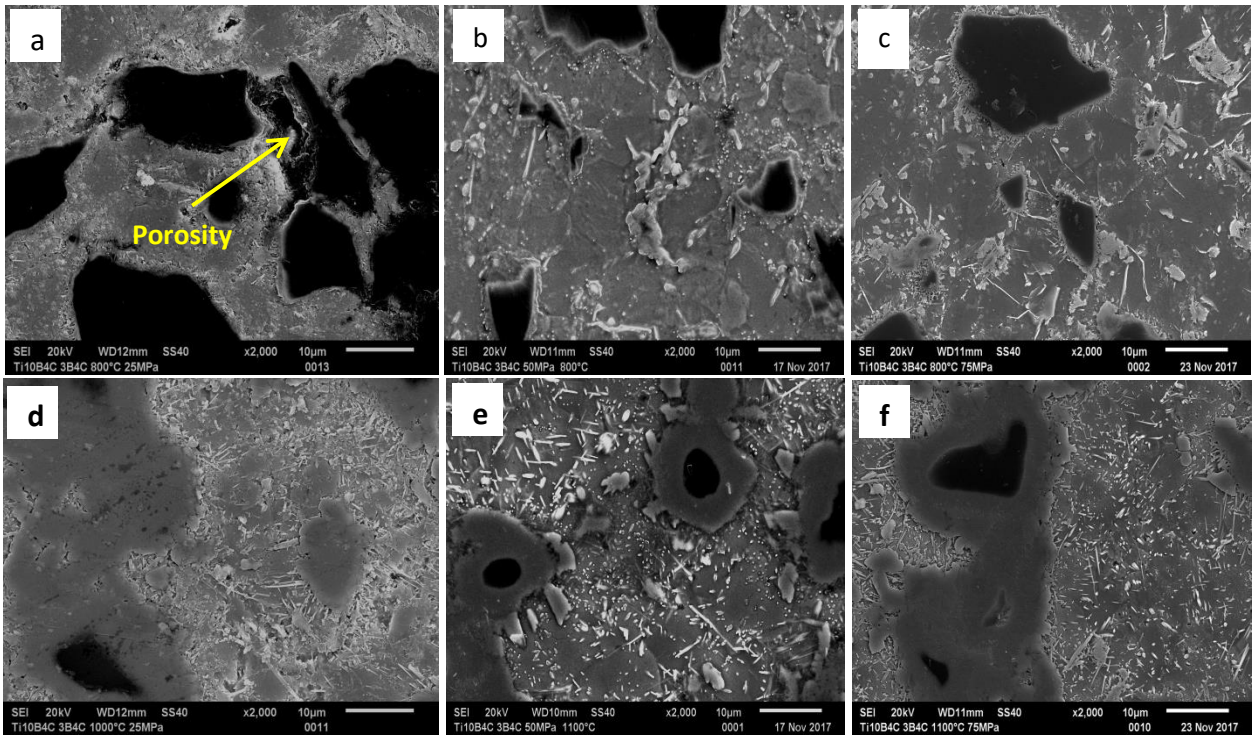

Figure 4.12. SEM micrographs for Ti10wt% B_4C(17.9µm) powder at 25MPa, 50MPa and 75MPa for 800°C (a-c) and 1100°C (d-f)

So the TMCs were further synthesized using finer B_4C with D_{50} particle sizes of 1.79µm and 1.69µm. In overview, finer B_4C particles (1.79µm and 1.69µm) segregated in Ti grain boundaries and reacted to form the grey phase as indicated in Figure 4.13-4.16 respectively. As observed in Figure 4.13(a) the TMCs synthesized from 1.79µm B_4C(5wt%) indicated high spontaneity of reaction with Ti at low temperature of 800°C at 25MPa in comparison to 17.9µm B_4C TMCs. The microstructure at the respective pressure shows the grey phase along Ti grain boundaries, TiB whiskers and TiC particles were not visible at 800°C also unreacted B_4C was not evidenced. At 1100°C the microstructure transformed to coarser TiB whiskers and TiC particles with some TiB clusters which further indicated that B_4C particles were fully reacted. The increase of B_4C content to 10wt% as shown in Figure 4.14, at 800°C and the varying pressures resulted in an increase of porosity level. Also the area of the TiB clusters doubled in size. Further reduction of B_4C particles size to 1.67µm for Ti5wt%B_4C TMCs favoured the formation of TiB whiskers and TiC particulates as noticed at 800°C and 25MPa in Figure 4.15(a) in contrast to TMCs synthesized from 1.79µm B_4C in Figure 4.13(a). Increasing pressure to 75MPa resulted in formation of coarser TiB whiskers as shown in Figure 4.15(c), in agreement with XRD analysis (Figure 44 (c & f)). Moreover, increasing the B_4C content to 10wt% in 1.67µm also led to increased porosity at 800°C (25MPa - 75MPa) as observed in Figure 4.16 (a-c).

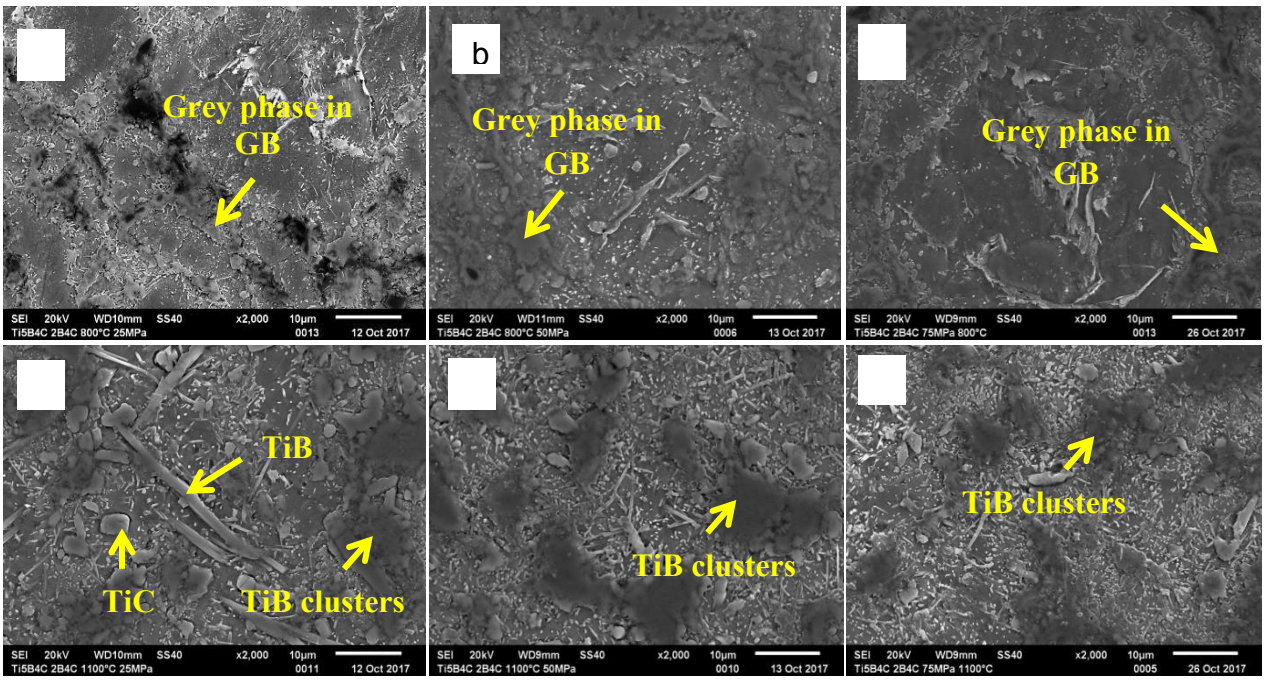

Figure 4.13. SEM micrographs for Ti5wt% B_4C for B_4C (1.79µm) powder at 25MPa, 50MPa and 75MPa for 800°C (a-c) and 1100°C (d-f)

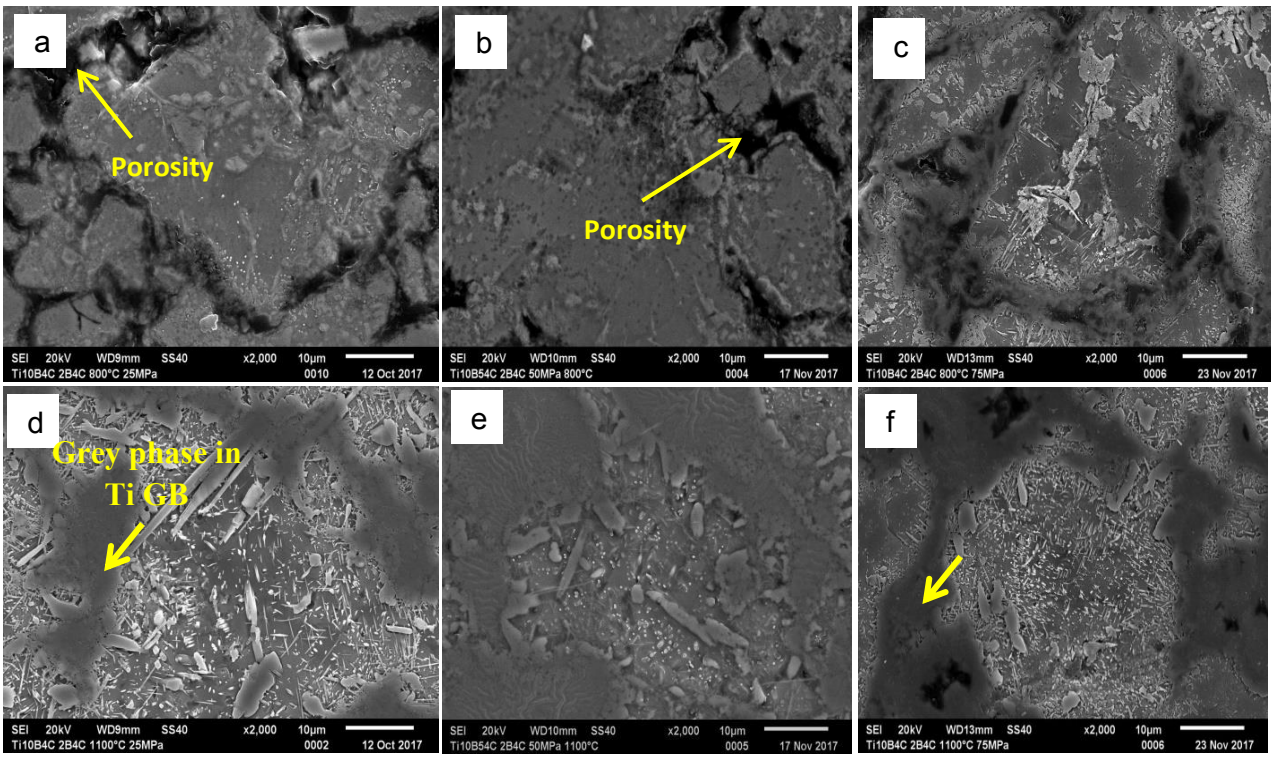

Figure 4.14. SEM micrographs for Ti10wt% B_4C(1.79µm) powder at 25MPa, 50MPa and 75MPa for 800°C (a-c) and 1100°C (d-f)

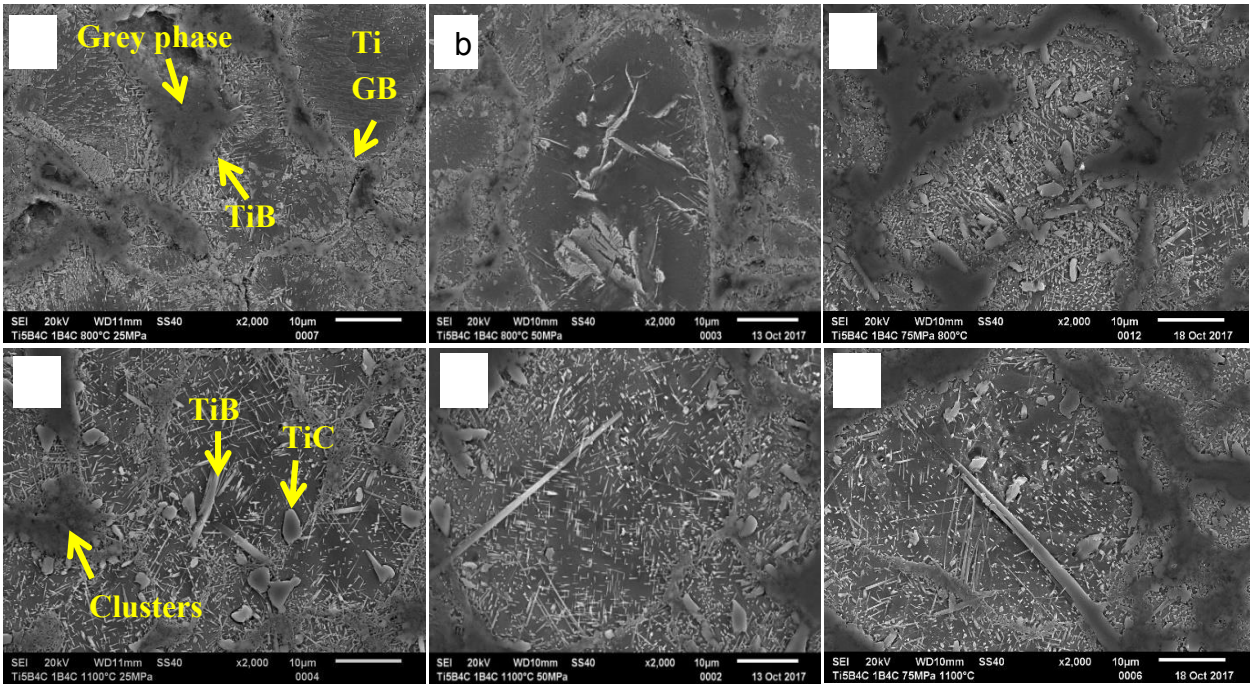

Figure 4.15. SEM micrographs for Ti5wt% B_4C(1.67µm) powder at 25MPa, 50MPa and 75MPa for 800°C (a-c) and 1100°C (d-f)

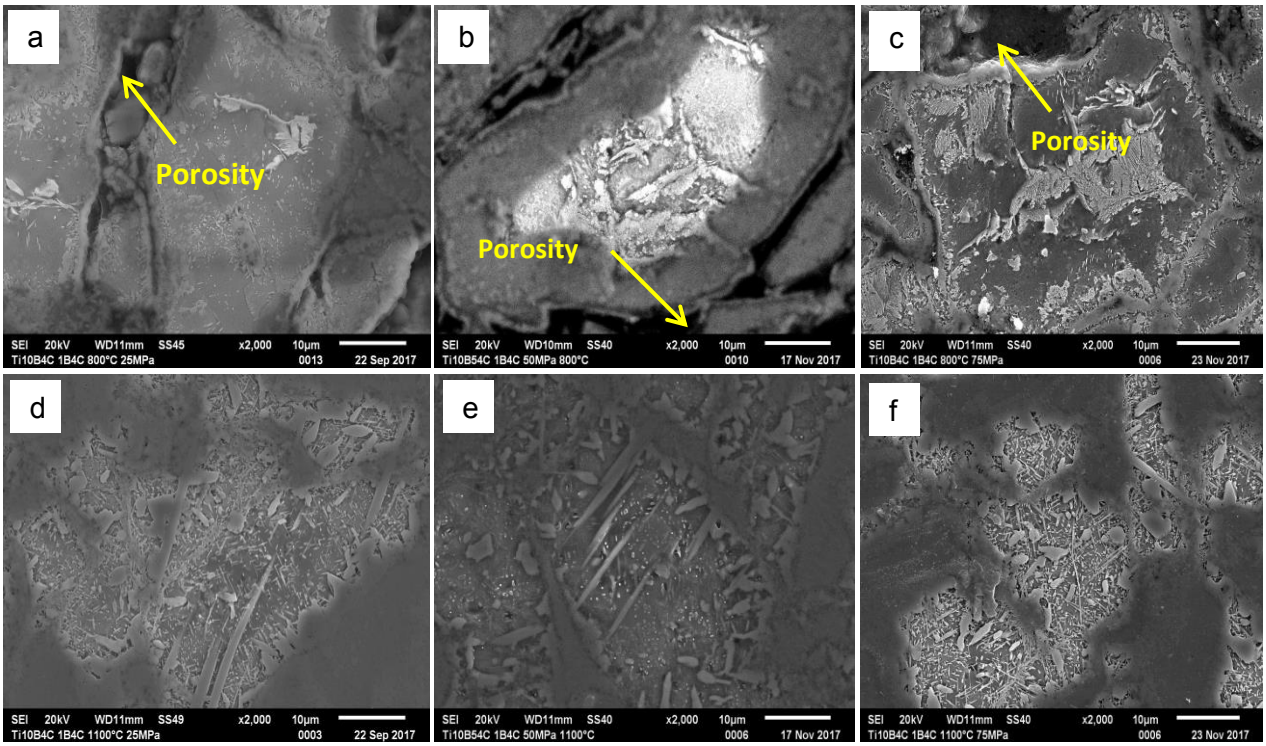

Figure 4.16. SEM micrographs for Ti10wt% B4C(1.67µm) powder at 25MPa, 50MPa and 75MPa for 800°C (a-c) and 1100°C (d-f)

Summary

Micrographs shown in Figure 4.11 & 4.12 essentially reveal that the reaction between Ti and coarser B_4C (17.9µm) require higher sintering temperature to form the reinforcing phases than those with finer B_4C (1.67µm and 1.79µm) in Figure 4.13 & 4.14 and Figure 4.15 & 4.16 respectively. The TiB clusters observed in the present study could be different from those reported in literature The TiB clusters were located in the grain boundaries of Ti and we know that the former B_4C particles were segregated in the grain boundaries. In this regard, we can say that TiB clusters emanated from clusters of sub-micron B_4C particles. In literature Ni *et al.* (2006) reported that for TMCs synthesized from 3.5µm B_4C particles, the clusters were similar to the original size of the B_4C particles and were characterized with many small TiC particulates with a diameter of 0.5µm surrounded by densely packed fine TiB whiskers. The fine TiB whiskers clusters grew in all directions, although the B_4C was completely reacted an inhomogeneous microstructure was obtained. It was reported that the TiB clusters could act as crack initiators at lower strains thus limiting the strength and ductility of the TMC (Gorsse *et al.*, 2003). The microstructure was homogenized by either heat treatment (1200-1300°C), hot extrusion (1100°C) or prolonged processing time (6-100h) by removing these TiB clusters (Gorsse *et al.*, 2003; Ni *et al.*, 2006). The TiB clusters in the present study will be further

characterized in the next section 4.5, whereby the FIB lamellae will be extracted from the TiB clusters region for analysis by TEM.

4.5 FIB and TEM characterization of TiB clusters in Ti5wt%B_4C (1.67µm) TMCs

Literature based on studying reaction mechanisms for Ti-B_4C TMCs by powder metallurgy techniques is limited. Focus has been on continuous SiC based TMCs and TiB_2 based coatings on Ti/Ti alloys (Campbell, 2010; Fukushima *et al.*, 2000; Gundel *et al.*, 1991; Huang *et al.*, 2015; Jayalakshmi *et al.*, 2015; Kieschke *et al.*, 1991; Luo *et al.*, 2012; Zhang *et al.*, 2014) (Ataibis *et al.*, 2015; Fan *et al.*, 1997; Fenghua *et al.*, 2010; Kartal *et al.*, 2013; Keddam *et al.*, 2017; Keddam *et al.*, 2016; Makuch *et al.*, 2017). Recently, an attempt was made to study the effect of temperature and processing time on the solid state reaction kinetics of SPS Ti-B_4C system (Jia *et al.*, 2016). Moreover, the available literature also reports TiB clusters morphology formed from using coarser B_4C particles (3.5µm) (Ni *et al.*, 2006). As such, in the present study phase transformations, products formed and the TiB clusters morphology resulting from exothermic reaction between Ti and sub-micron B_4C particles (1.67µm) are investigated by FIB and TEM characterization techniques.

Samples sintered at 800°C and 1100°C at 25MPa were metallorgraphycally polished and etched with kroll's etchant to reveal the microstructure. FIB lamellae were then extracted from the TiB clusters/Ti interface (grain boundary region) in Ti5wt%B_4C TMCs with 8mm in diameter sintered at 800°C and 1100°C at 25MPa as shown in Figure 4.17 and 4.18. Thereafter, the crystallography and elemental compositions were analyzed using a TEM coupled to EDX spectrometer and EELS. With the aid of CysTBox software, Fast Fourier Transform (FFT) patterns were obtained from the TEM crystallographic images to verify the phases formed. FFT patterns analyses lattice planes and experimental d-spacing values matching the theoretical d-spacing values of the respective phases to be analyzed (Ti, B_4C TiB, TiB_2, Ti_2B_3, etc.) (Klinger *et al.*, 2015).

Illustrated in Figure 4.17(a) and 4.18(a) is the TiB clusters/Ti interface where the FIB lamellae were extracted from the TMCs. The lamellae include an interface portion of the reinforcing phases and Ti phase. On the surface of the sample the grey phase appeared to be a continuous TiB_2 layer with TiB whiskers growing from it, but further analysis by TEM revealed various phases.

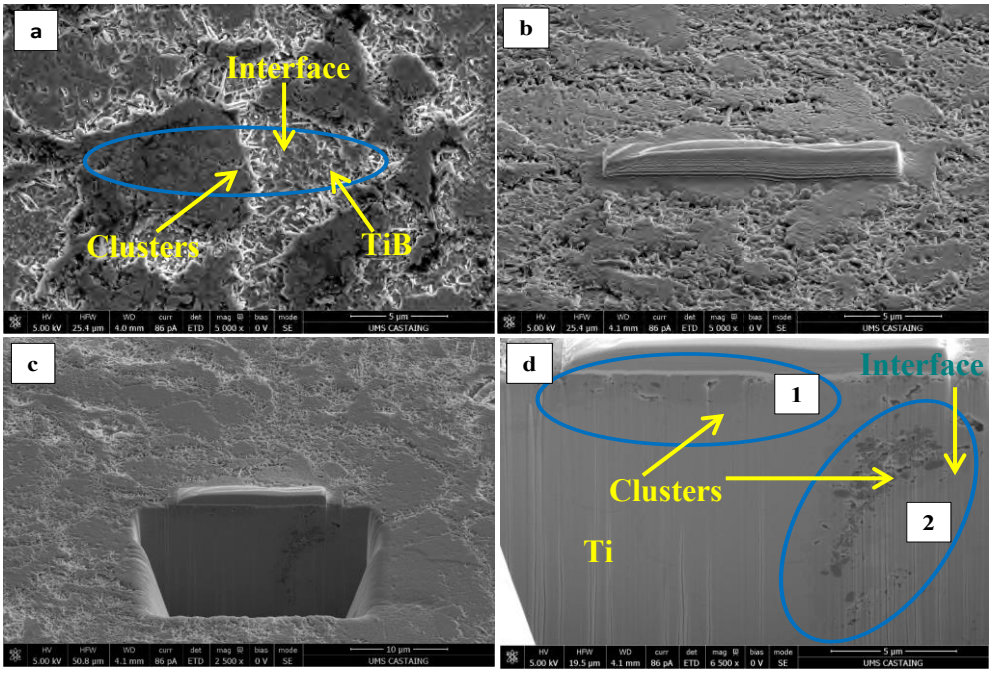

Figure 4.17. FiB lamellae for Ti5wt%B_4C(1.67µm) sintered at 800°C, 3min and 25MPa

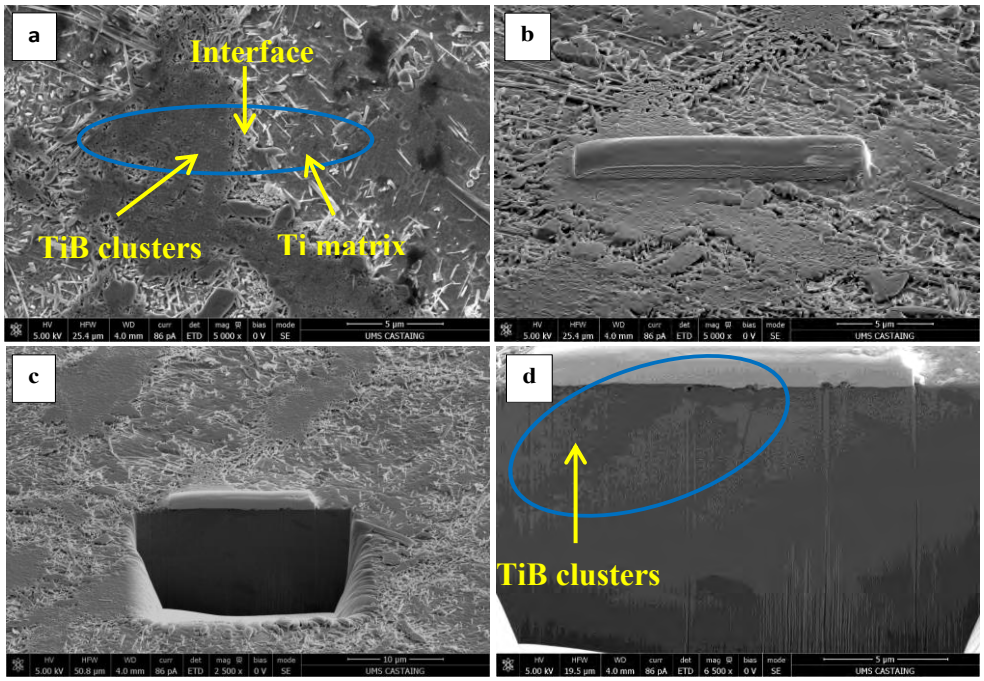

Figure 4.18. FiB lamellae for Ti5wt%B4C(1.67µm) sintered at 1100°C, 3min and 25MPa

Figure 4.19 illustrates the different sections in the lamellae that were analyzed with EELS and STEM in the TEM for Ti5wt%B_4C(1.67µm) TMCs sintered at 800°C. As observed the TEM

bright field micrographs (A1-A3) and (B1-B2) in Figure 4.19 shows the presence of different phases with porosity. In fact what appeared to be a continuous layer at 800°C as observed on the surface (Figure 4.17 (a)) are actually clusters of sub-micron B_4C particles with a reacted perimeter which appeared grey. As shown in the different areas in Figure 4.19 (A2, A3 and B2), there were still some unreacted B_4C particles. These could only be observed on the cross-section of the sintered material. To confirm this, localized point elemental analyses was done by EELS in Figure 4.20. The concentration of the elements indicated higher boron contents in the dark phase, while the grey phase analyzed high contents in titanium as illustrated in the tables corresponding to the images with elemental analysis. Furthermore to clarify the crystal structures in Figure 4.19(a) and (c), FFT pattern were obtained from the HRTEM images and the corresponding lattice planes with d-spacing were identified using CrysTBox software. The measured d-spacing of B_4C were relatively close to the theoretical values with a standard deviation of 0.0015 and 0.0279 as shown in Tables 14 and 15.

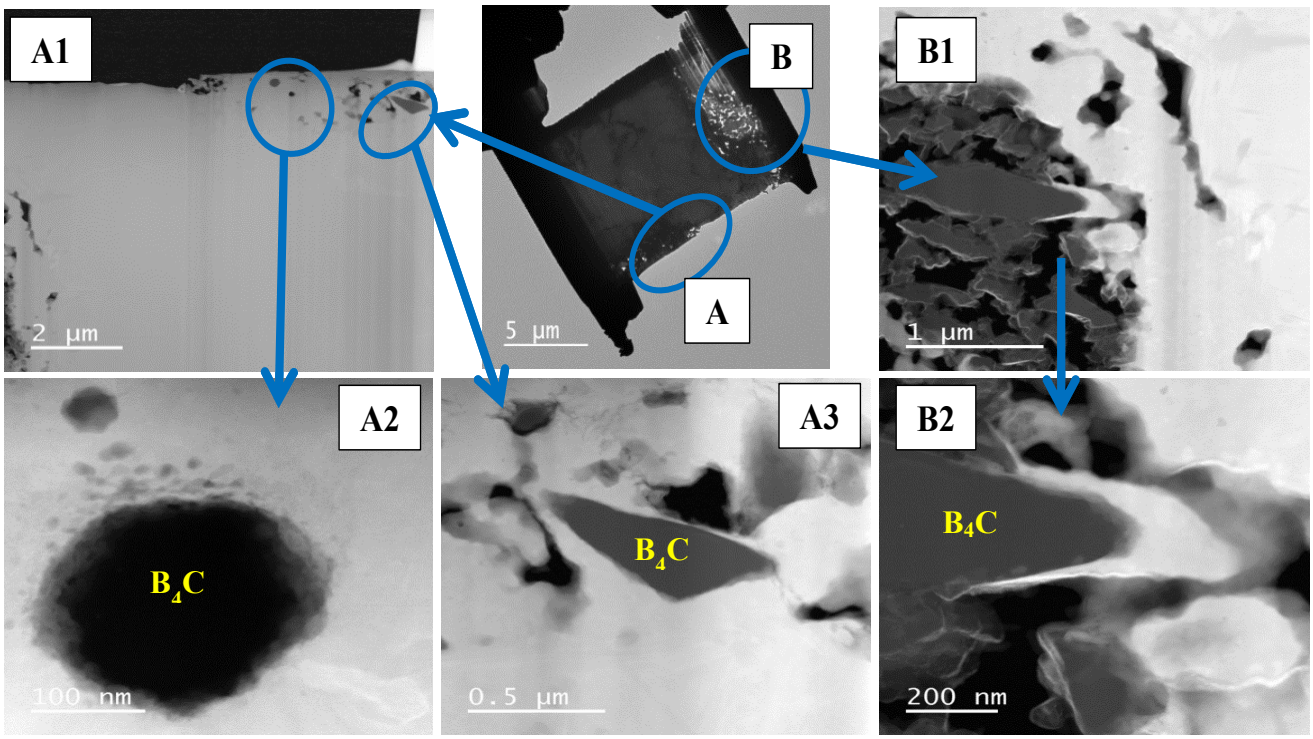

Figure 4.19. TEM micrographs for Ti5wt%B_4C (1.67µm) sintered at 800°C, 3min and 25MPa

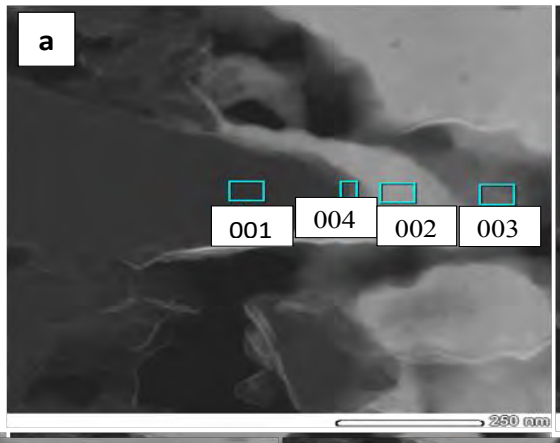

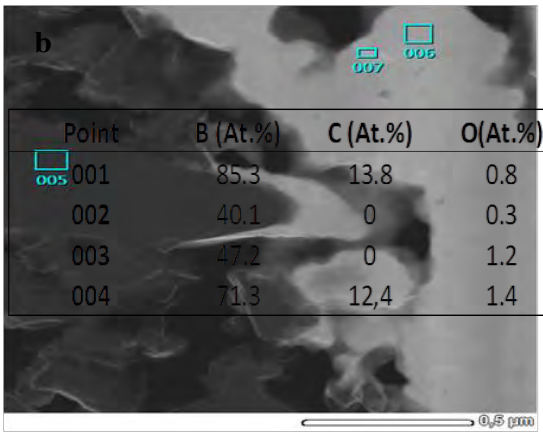

Point	B (At.%)	C (At.%)	O(At.%)	Ti (At.%)
001	85.3	13.8	0.8	0.1
002	40.1	0	0.3	59.6
003	47.2	0	1.2	51.6
004	71.3	12,4	1.4	14.9

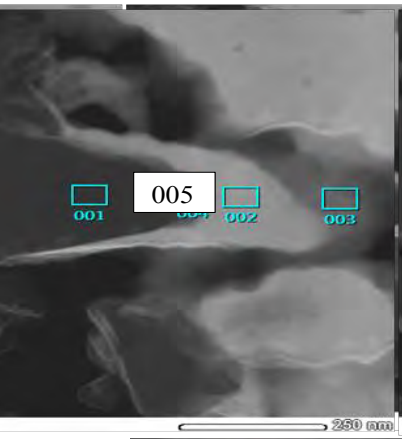

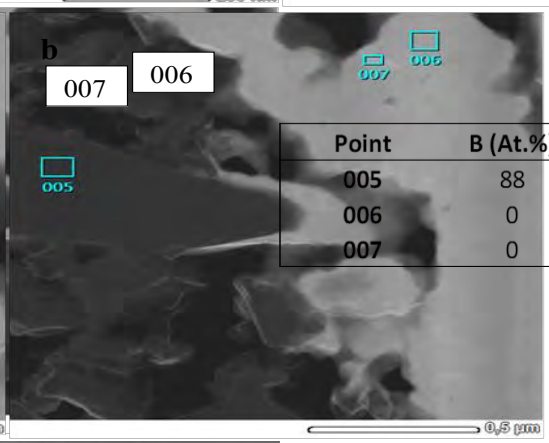

Point	B (At.%)	C (At.%)	O(At.%)	Ti (At.%)
005	88	11.4	0.5	0.1
006	0	0	0	100
007	0	43.5	0	56.5

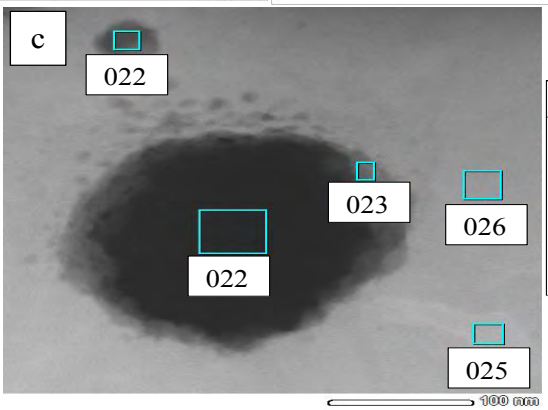

Point	B (At.%)	C (At.%)	O(At.%)	Ti (At.%)
022	86.4	12.9	0.6	0
023	71.8	12.0	0.1	16.1
024	45.9	0	4.3	49.8
025	44.6	0	0.5	54.9
026	57.1	0	0	42.9

Figure 4.20. EELS elemental analysis of particles in Ti5wt%B_4C (a & b) Figure 4.19(B2) and c) Figure 4.19(A2)

Table 14. Experimental and theoretical d-spacing for B_4C in Figure 4.20(a) (Point 001)

B_4C	**A**	**B**	**C**	**D**
Detected planes	0 0 -5	-2 2 -5	-2 2 0	-2 2 5
Experimental d-spacing (nm)	0.232	0.164	0.233	0.165
Experimental d-spacing(1/nm)	4.301	6.097	4.300	6.066
Theoretical d-spacing (nm)	0.242	0.171	0.243	0.171
Theoretical d-spacing(1/nm)	4.139	5.841	4.115	5.847
STDEV: 0.0015				

Table 15. Experimental and theoretical d-spacing for B_4C in Figure 4.20(c) (Point 022)

B_4C	**A**	**B**	**C**	**D**
Detected planes	0 2 1	0 2 4	0 0 3	0 -2 2
Experimental d-spacing (nm)	0.244	0.197	0.414	0.227
Experimental d-spacing(1/nm)	4.101	5.088	2.415	4.407
Theoretical d-spacing (nm)	0.238	0.189	0.403	0.225
Theoretical d-spacing(1/nm)	4.203	5.287	2.484	4.441
STDEV: 0.0279				

Reaction between Ti matrix and B_4C particles occur at their interface, so the atomic contents of B, C and Ti measured in Figure 4.20(a) and (c) were relatively consistent. In point 004 and point 023 the atomic contents were 71.3 B, 12.4 C, 14.9 Ti and 71.8 B, 12.0 C and 16.1 Ti respectively. Presented in Figure 4.21 are FFT patterns showing interfacial products between Ti and B_4C for Ti5wt%B_4C(1.67µm) TMCs sintered at 800°C. The FFT patterns show the detected lattice planes matching theoretical planes. The d-spacing values and the respective lattice planes shown in Table 16 - 18 were that of TiB_2, Ti_3B_4, TiC and Ti_2C phases. Although these phases TiB_2, Ti_3B_4, Ti_2C peaks were not detected in XRD patterns at 800°C, analysis from TEM images revealed their presence. The phases detected are in accordance with those in Ti-B and Ti-C phase diagrams (Baker, 1992).

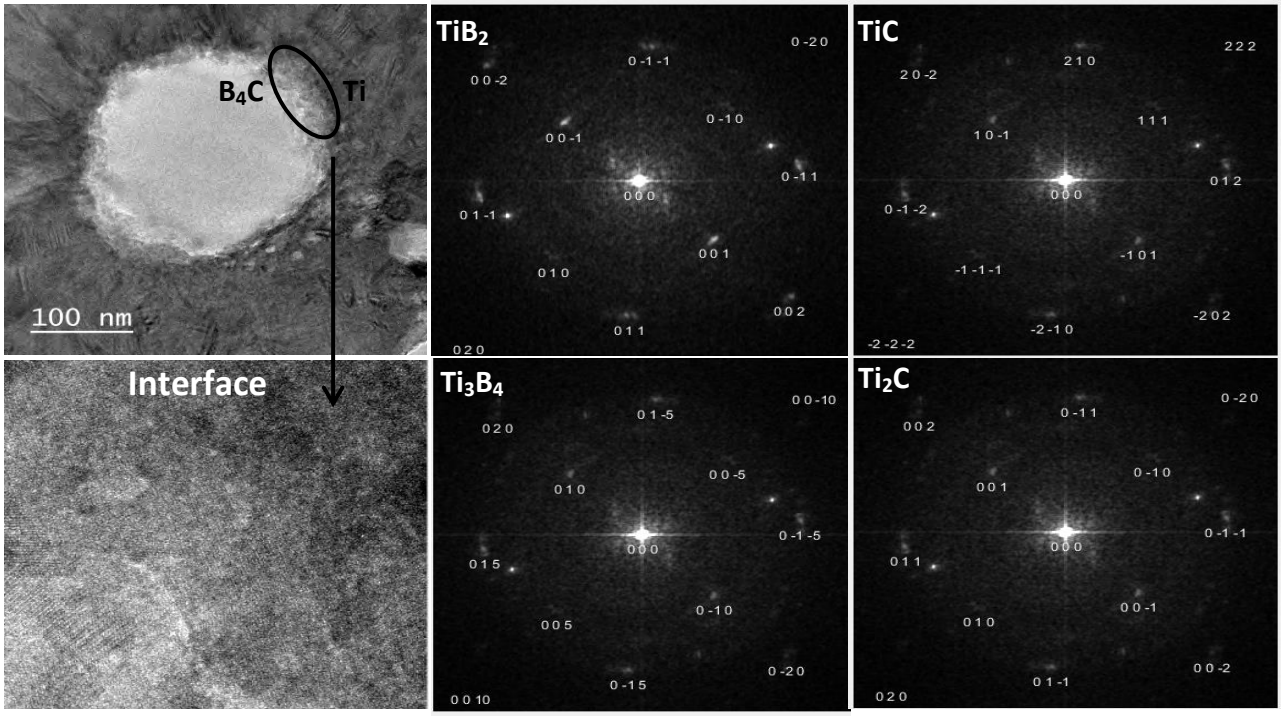

Figure 4.21. FFT patterns of interfacial products between Ti and B_4C for Ti5wt%B_4C(1.67µm) sintered at 800°C

Table 16. Experimental and theoretical d-spacing for TiB_2 phase in Figure 4.21

TiB_2	**A**	**B**	**C**	**D**
Detected planes	0 1 0	0 1 1	0 0 1	0 -1 1
Experimental d-spacing (nm)	0.271	0.211	0.334	0.211
Experimental d-	3.683	4.742	2.993	4.750
Theoretical d-spacing (nm)	0.262	0.203	0.323	0.204
Theoretical d-spacing(1/nm)	3.813	4.902	3.098	4.913
STDEV: 0. 002				

Table 17. Experimental and theoretical d-spacing for Ti_3B_4 in Figure 4.21

Ti_3B_4	**A**	**B**	**C**	**D**
Detected planes	0 0 -5	0 -1 -5	0 -1 0	0 -1 5
Experimental d-spacing (nm)	0.274	0.213	0.333	0.210
Experimental d-	3.643	4.696	3.007	4.752
Theoretical d-spacing (nm)	0.275	0.210	0.326	0.210
Theoretical d-spacing(1/nm)	3.642	4.764	3.068	4.762
STDEV: 0.398				

Table 18. Experimental and theoretical d-spacing for TiC phase in Figure 4.21

TiC	**A**	**B**	**C**	**D**
Detected planes	1 1 1	0 1 2	-1 0 1	-2 -1 1
Experimental d-spacing (nm)	0.274	0.213	0.333	0.210
Experimental d-	3.643	4.696	3.007	4.752
Theoretical d-spacing (nm)	0.249	0.193	0.305	0.176
Theoretical d-spacing(1/nm)	4.016	5.181	3.2786	5.6818
STDEV: 0.004				

Table 19. Experimental and theoretical d-spacing for Ti_2C phase in Figure 4.21

Ti_2C	**A**	**B**	**C**	**D**
Detected planes	0 1 0	0 1 1	0 0 1	0 -1 1
Experimental d-spacing (nm)	0.274	0.213	0.333	0.210
Experimental d-	3.643	4.696	3.007	4.752
Theoretical d-spacing (nm)	0.262	0.204	0.323	0.204
Theoretical d-spacing(1/nm)	3.817	4.902	3.096	4.902
STDEV: 0.002				

At 1100°C as observed in Figure 4.22 (A1 & B1) in the bright field TEM mode there was no particular difference in contrast between the reinforcing phases and Ti matrix. A variety of crystallites in clusters were formed and no B_4C particles were evidenced as shown in Figure 4.22 (A4, B2 and B3), this indicated that complete reaction had occurred between Ti and sub-micron B_4C (1.67μm). The crystallites clusters were segregated at the grain boundaries were the former B_4C (1.67μm) particles were segregated as discussed for 800°C microstructure (Figure 4.19). The elemental composition in the clusters showed mixture of compounds rich

in Ti – B and Ti – C as shown in Figure 4.23. The d-spacing values measured from the FFT patterns revealed the presence of non-stoichiometric phases of Ti_xB_x in Figure 56(B4). The measured d-spacing from the HRTEM images matched theoretical Ti_3B_4 and Ti_2B shown in Table 20 and 21. Analysis revealed TiB whiskers growing within Ti matrix and it was surrounded by smaller fragments of particles high in Ti and B atoms as shown in Figure 4.23(c). Smaller TiC particulates were also present within Ti matrix as shown in Figure 4.24(b).

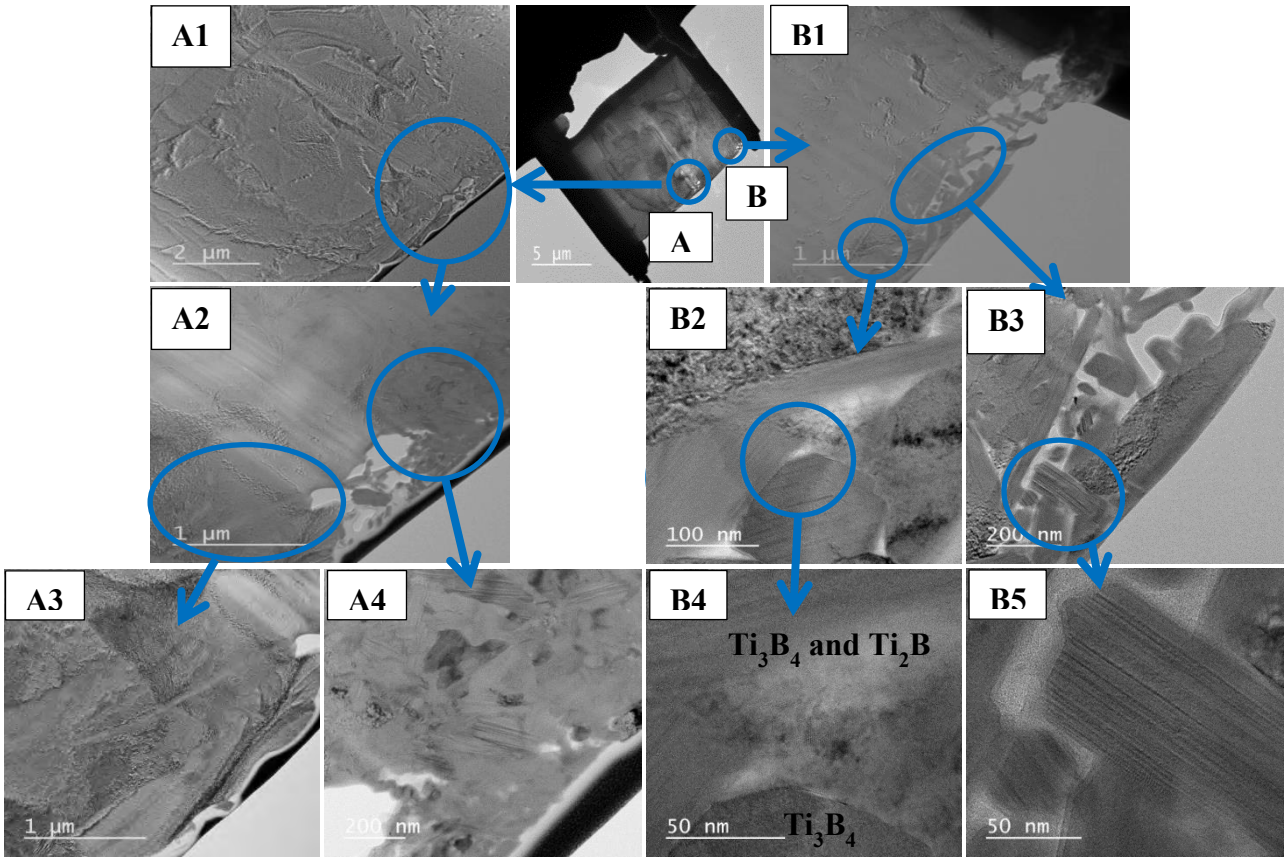

Figure 4.22. TEM micrographs for Ti5wt%B_4C(1.67µm) sintered at 1100°C, 3min and 25MPa

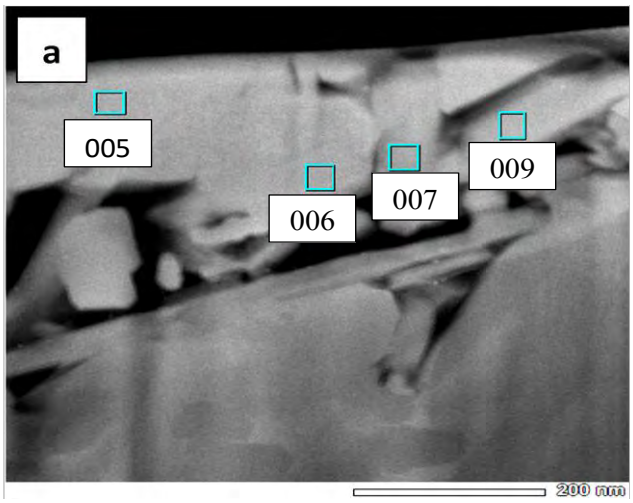

Point	B(At%)	C(At%)	O(At%)	Ti(At%)
005	0	65.1	3.6	31.3
006	0	18.3	5.4	76.2
007	42.0	0	3.7	54.3
008	44.0	0	5.9	50.1

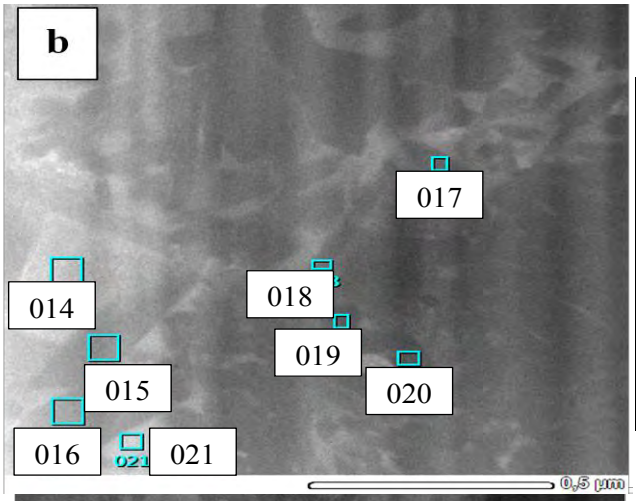

Point	B(At%)	C(At%)	O(At%)	Ti(At%)
014	0	62.1	2.1	35.8
015	40.4	0	9.5	50.1
016	39.9	0	8.1	52.0
017	0	3.0	19.6	77.5
018	30.0	0	12.4	57.6
019	0	0	12.1	87.9
020	0	0	16.1	83.9
021	0	3.5	1.3	95.2

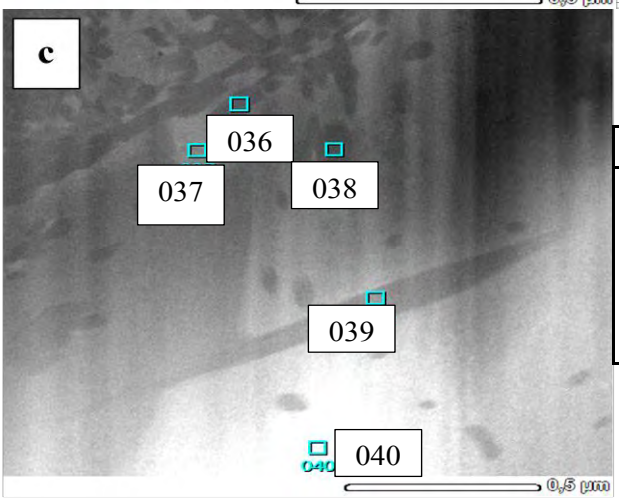

Point	B(At%)	C(At%)	O(At%)	Ti(At%)
36	37.7	0	12.0	50.3
37	0	0	19.1	80.9
38	46.9	0	12.5	40.6
39	18.7	0	12.9	68.4
40	0	0	12.1	87.9

Figure 4.23. EELS elemental analysis of 1100°C Ti5wt%B_4C(1.67µm) a) Figure 4.22(B3), b)Figure 4.22 (A4) and c) Reinforcing phases/ Ti interphase

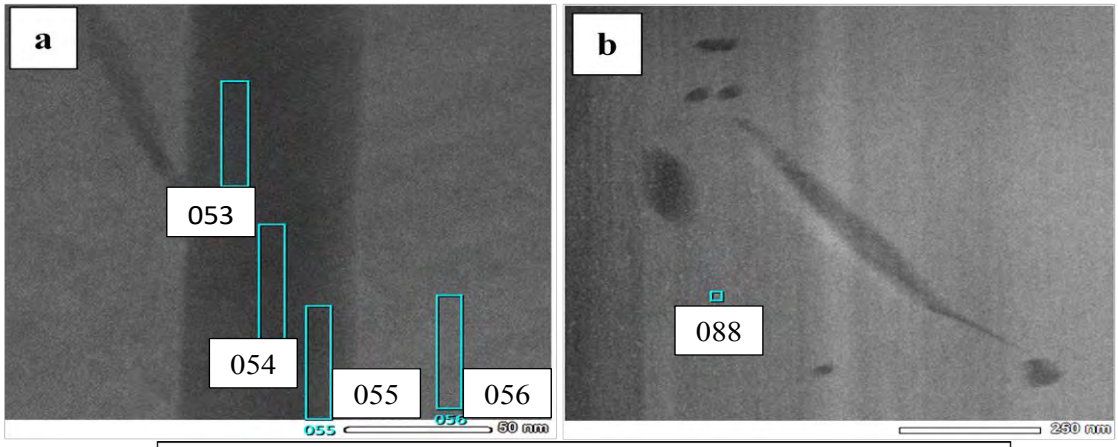

Point	B(At%)	C(At%)	O(At%)	Ti(At%)
053	26.4	0	9.4	64.1
054	31.9	0	6	62.1
055	16.5	0	7.8	75.7
056	0	0	11.5	88.5
088	0	5.7	11.3	83

Figure 4.24. EELS point elemental analysis of 1100°C Ti5wt%B_4C (1.67µm) in matrix region a) TiB whisker and b) TiC particulates

Table 20. Experimental and theoretical d-spacing for Ti_3B_4 phases in Figure 4.22(B4)

Ti_3B_4	**A**	**B**	**C**	**D**
Detected planes	1 0 3	1 -1 1	0 -1 -2	-1 -1 -5
Experimental d-spacing (nm)	0.254	0.219	0.297	0.174
Experimental d-spacing (1/nm)	3.938	4.563	3.368	5.735
Theoretical d-spacing (nm)	0.253	0.220	0.294	0.173
Theoretical d-spacing (1/nm)	3.953	4.545	3.401	5.780
STDEV 0.0011				

Table 21. Experimental and theoretical d-spacing for Ti_2B phases in Figure 4.22(B4)

Ti_2B	**A**	**B**	**C**	**D**
Detected planes	1 -2 0	0 -3 -1	-1 -1 -1	-2 -1 -1
Experimental d-spacing (nm)	0.254	0.174	0.296	0.219
Experimental d-spacing (1/nm)	3.938	5.749	3.379	4.562
Theoretical d-spacing (nm)	0.273	0.186	0.314	0.234
Theoretical d-spacing (1/nm)	3.663	5.376	3.185	4.274
STDEV 0.0028				

Summary

In this section we observed that the TMCs fabricated with finer B_4C(1.67µm) powder at 800°C show unreacted B_4C clusters which transformed into crystallites clusters (Ti-B and Ti-

C compounds) at 1100°C. In literature several authors reported that, in temperature range of 1200-1400°C, the clusters formed were actually nucleation sites for multiple TiB whiskers formed near the previous coarser B_4C particle (3.5-50µm) (Balaji *et al.*, 2014; Ni *et al.*, 2006). Moreover, the TiB clusters were reported to have adverse effect on the mechanical properties. The TiB whiskers within clusters have lower load bearing efficiency in comparison with uniformly distributed ones (Tabrizi *et al.*, 2015) and they can also act as stress initiators especially at lower strains (Gorsse *et al.*, 2003). The TiB clusters have been reported to be completely removed by increasing either temperature, the annealing time (Balaji *et al.*, 2014; Gorsse *et al.*, 2003) or further extrusion of fabricated components (Ni *et al.*, 2006). In section 4.7 the sintering dwelling time is increased from 3min to 30min to homogenize the microstructure by removing the cluster

4.6 Reaction mechanisms for Ti5wt%B_4C with sub-micron B_4C(1.67µm) particles

In considering the phases detected from XRD patterns and microstructural characterization by FIB/SEM and TEM for the reaction between Ti and B_4C, it is quite evident that the reaction took place at 800 and 1100°C. In agreement with literature, it was reported that the reaction between Ti and B_4C took place at temperatures above 800°C (Lu *et al.*, 2008), at 1093°C measured by DTA (Liang *et al.*, 2008) and before 1200°C measured by DSC analysis (Ni *et al.*, 2008a). In addition, the reaction was enhanced by application of increased pressure more especially for TMCs with finer B_4C (1.67µm and 1.79µm) particles. However, we have to consider that in DTA and DSC techniques loose powders are routinely used. So, the reaction sequence for exothermic powders could be misleading since in reactive sintering techniques often the state of compaction (relative density) strongly influence the reaction sequence and the final composition (Brodkin *et al.*, 1996; Dudina *et al.*, 2013). For other reactive sintering processes including the SPS, when new phases are formed, factors such as uniform distribution of reactants in the powder mixtures, the heat release in exothermic reactions, the specific volume change and the by-products formation need to be taken into consideration when microstructure evolution of the synthesized product is traced (Dudina *et al.*, 2013). Moreover, in the SPS the electric current plays a major role in the microstructure development, such that the changes in material electrical conductivity during the reaction and the high temperature reached at the inter-particle contacts serve as reaction initiation zones (Dudina *et al.*, 2013; Tokita, 1999).

In the initial sintering temperature of 800°C at 25MPa we observed Ti, TiB and TiC phases in the XRD pattern and the absence of TiB_2 and B_4C. In the SEM characterization, finer TiB whiskers were more evident than TiC particles (spherical morphology) most likely because of their whisker like morphology. However, cross-sectional analysis of the FIB lamellae by TEM for sample sintered at 800°C revealed partially reacted B_4C particles segregated at the Ti grain boundaries. As reported in literature the TiB_2 layer normally form on the perimeter during consumption of the B_4C particle. According to the elemental atomic composition and the phases detected on FFT patterns at the interface between Ti and B_4C, were TiB_2, Ti_3B_4, TiC and Ti_2C. Brodkin *et al.* (1996) reported the formation of Ti_3B_4 phase at higher temperature ranges of 1450°C - 1600°C for hot pressed Ti-B_4C TMCs. In the present study, we have to note that the temperature in the powder could be higher than that is measured on the graphite die. As reported by Motsi *et al.* (2019), in the SPS the overall temperature measured in the Ti powder was approximately 8% higher than in the graphite die (8 mm inner diameter). The temperature varied with the different stages during sintering, that is from ramping up (±20°C), overshooting (37°C) then stabilizing (±21°C) to reach the set-point temperature of 800°C. So, the actual temperature of Ti5wt%B_4C(1.67µm) was actually higher than the set-point temperature of 800°C. This could be attributed to the pulsed electric current density and the amount of Joule's heat of the Ti powder causing variation in temperature distribution (Matsugi *et al.*, 1996). In addition, it has been reported that during the SPS process higher temperatures are reached on particles surface that lead to melting and vaporization thus enhancing interdiffusion of atoms for densification (Tokita, 1999). As a result, the reaction kinetics involved with sub-micron particles (1.67µm) of the present study in the SPS progressed rapidly (at 800°C), because of the combined effect of larger powder surface area, the effect of current density, Joule's heat and higher interparticle temperatures in contrast to Brodkin *et al.* (1996) who reported reaction kinetics in hot pressing (1450°C - 1600°C).

According to the Gibbs free energy (ΔG) reaction path for Ti-B_4C system the final products should be TiB and TiC at temperatures higher than 800°C. However, experimental results always contradict this conclusion. Therefore it should be considered that, ΔG criterion is not sufficient to predict reaction path of Ti - B_4C system. Nevertheless, the theoretical reactions taking place between Ti and B_4C with their ΔG values are presented in Table 22. According to the ΔG values, the reactions are exothermic and thermodynamically favorable at 800°C, meaning the formation of TiB_2, TiB and TiC are theoretically possible. The most likely phase

to primarily form is TiB_2 (-263KJ.mol^{-1}), followed by TiC (ΔG = -172KJ.mol^{-1}) then lastly TiB whiskers (ΔG = -157 KJ.mol^{-1}) (He *et al.*, 2006). Although the reaction path of the TMC investigated progressed rapidly at 800°C, with the aid of literature the preceding reactions taking place below 800°C can be traced. It was reported that above 600°C formation of TiC is initiated (Mogilevsky *et al.*, 1998), while (Kim *et al.*, 2001) mention that TiC formation from finer and coarse particles take place at 700°C and 800°C, respectively. As for TiB according to the Ti-B phase diagram it forms at much lower temperatures (Baker, 1992).

The proposed reaction paths for Ti and B_4C in the present study which take place at the Ti and B_4C interface, at SPS set-point temperatures of 800°C and 1100°C are as follows;

Table 22. Reactions during reactive SPS of Ti and B_4C particles

Chemical reaction equation	ΔG equation	ΔG/(KJ.mol^{-1})	Reference
$Ti_{(s)} + 2B_{(s)} \rightarrow TiB_{2(s)}$	-284,512 + 20,50T	-263 (800°C)	(He *et al.*, 2006)
$Ti_{(s)} + C_{(s)} \rightarrow TiC_{(s)}$	-183,100 + 10,08T	-172 (800°C)	(He *et al.*, 2006)
$Ti_{(s)} + B_{(s)} \rightarrow TiB_{(s)}$	-163,176 + 5,85T	-157 (800°C)	(He *et al.*, 2006)
$3Ti_{(s)} + B_4C_{(s)} \rightarrow TiB_{2(s)} + TiC_{(s)}$	-762,408 + 17.833T	-743	(Sahoo *et al.*, 2016)
$5Ti_{(s)} + B_4C_{(s)} \rightarrow 4TiB_{(s)} + TiC_{(s)}$	-	-754	(Prakash *et al.*, 2016)

Path 1: Several competitive reactions take place to form the desired phases; the reactions at the Ti/B_4C interface involve simultaneous interdiffusion mechanisms of decomposed B and C atoms into Ti matrix, and Ti into B_4C occupying vacancies left by B and C atoms. The formation of TiB and TiC depends on the diffusion coefficients of B and C in Ti matrix (Jia *et al.*, 2016). Carbon has higher diffusion coefficient than B, thus it rapidly diffuse into the Ti matrix leaving behind higher B concentration close to the Ti/B_4C interface.

Path 2: In the meantime, due to lower diffusion coefficient of B in Ti matrix it would dissolve into the Ti matrix to primarily form TiB phase [Eq.11] (Mogilevsky *et al.*, 1998; Rafiei *et al.*, 2014). Thereafter, some TiC particles form further into the Ti matrix [Eq.12]. Ti then diffuses into vacancies left by B and C in B_4C to form TiB_2 and C substance [Eq.13]

Path 3: Boron further reacts with Ti to form TiB_2 phase according to [Eq.14]. The TiB_2 layer grows and prevents the passage of C from the B_4C, resulting in the growth of carbon layer between B_4C and TiB_2. (Jia *et al.*, 2016) reported path 1 - 3 to take place for Ti-B_4C SPS compact sintered at 1000°C.

Path 4: A stoichiometric Ti_2C phase was also detected, there has been uncertainties in the literature regarding its formation. Especially that, according to the Ti-C phase diagram its existence it's questionable and also the phase diagram at lower carbon concentrations of less than 1 at.% is poorly studied (Aksyonov *et al.*, 2012). Nevertheless, Ti_2C phase [Eq.15] was reported to be an interphase between Ti and TiC, which may exist in temperature ranges of 25 - 1900°C (Aksyonov *et al.*, 2012; Ranganath *et al.*, 1996; Vallauri *et al.*, 2008; Wanjara *et al.*, 2000).

Path 5: B further diffuses into TiB and small Ti_3B_4 platelets nucleate and grow according to [Eq.16]. The formation of Ti_3B_4 platelets was reported to be in temperature ranges of 1450°C - 1600°C in HP, this range is close to Ti melting point 1668°C Brodkin *et al.* (1996). Since in SPS process atoms interdiffusion is enhanced by melting and vaporization on the surface, so it could be assumed that temperature of 1668°C was reached on the surface of Ti particles favouring the formation of Ti_3B_4 at relatively lower set-point temperatures in comparison to HP (Tokita, 1999).

Path 6: Equilibrium is then reached whereby large Ti_3B_4 platelets are formed by TiB reacting with TiB_2 according to [Eq. 17].

SPS set point temperature: 800°C

$$Ti + B \rightarrow TiB \quad \text{[Eq. 11]}$$

$$Ti + C \rightarrow TiC \quad \text{[Eq. 12]}$$

$$2Ti + B_4C \rightarrow TiB_2 + C \quad \text{[Eq. 13]}$$

$$Ti + 2B \rightarrow TiB_2 \quad \text{[Eq. 14]}$$

$$Ti + TiC \rightarrow Ti_2C \quad \text{[Eq. 15]}$$

$$3TiB + B \rightarrow Ti_3B_4 \text{ (small platelets)} \quad \text{[Eq. 16]}$$

SPS set point temperature: 1100°C

$$2TiB + TiB_2 \rightarrow Ti_3B_4 \text{ (large platelets)} \quad \text{[Eq. 17]}$$

4.7 Dwell time effect on the microstructure

The Ti5wt%B_4C(1.67µm) TMCs were characterized with particles clusters consisting of partially reacted B_4C particles at 800°C. Increasing the temperature to 1100°C the reaction between Ti and B_4C was enhanced and clusters of Ti - B with Ti - C compounds were formed (section 4.5). It was reported that the clusters could be efficiently removed by either increasing the processing time (6-100h), heat treatment (1200-1300°C) or hot extrusion (1100°C) (Balaji *et al.*, 2014; Gorsse *et al.*, 2003; Ni *et al.*, 2006). Dwell time during sintering can ensure uniform temperature distribution within the material and so better microstructure homogeneity.

Microstructure evolution at 650 and 800°C and varying dwell times from 0 to 30min for Ti5wt% B_4C TMC with coarser B_4C (17.9µm) is shown in Figure 4.25.

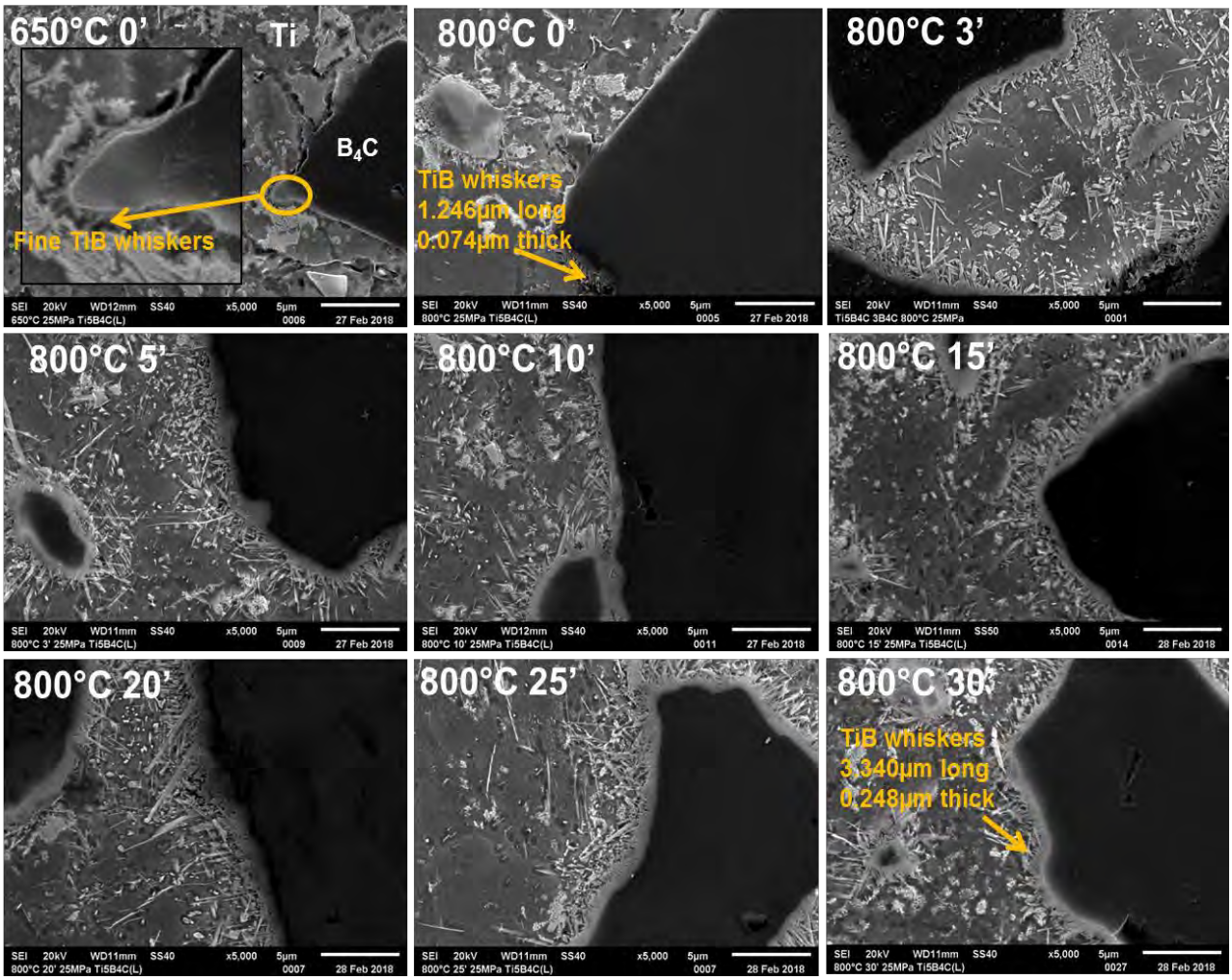

Figure 4.25. Dwell time effect on microstructure evolution of 8mm Ti5wt%B_4C(17.9µm)

The interfacial contact between Ti and B_4C is important as it facilitates the reaction during sintering. If there is no contact between reactants, the reaction will not take place. At 650°C and 0 min seems that the reaction already commenced as very fine TiB whiskers (0.34 µm) were observed, although in some interfacial areas no whiskers were formed due to poor contact between the reactants as a result of low densification. Hence the reaction did not occur on some of interfacial contacts. However, no second phases were detected 650°C by XRD analysis in Figure 4.26 due to XRD detection limit (2-5%). This observation at 650°C co-relates with the results discussed in TEM analysis (section 4.5), wherein the reactions and formation second phases at temperatures below 800°C for TMCs synthesized from finer B_4C (1.67µm) particles was discussed.

With the increase of temperature to 800°C at 0min there was increased densification and the TiB whiskers grew and the TiB peak was visible in Figure 4.26. The increase of dwell time to 3min further improves densification and thus the reactants contact to react and form coarse TiB_2, TiB and TiC phases. With further increase of dwell time (0 to 30min) there was insignificant change of TiB_2 layer but some of TiB whiskers length increased (1.246 to 3.340µm) and were thicker (0.074 to 0.248µm).

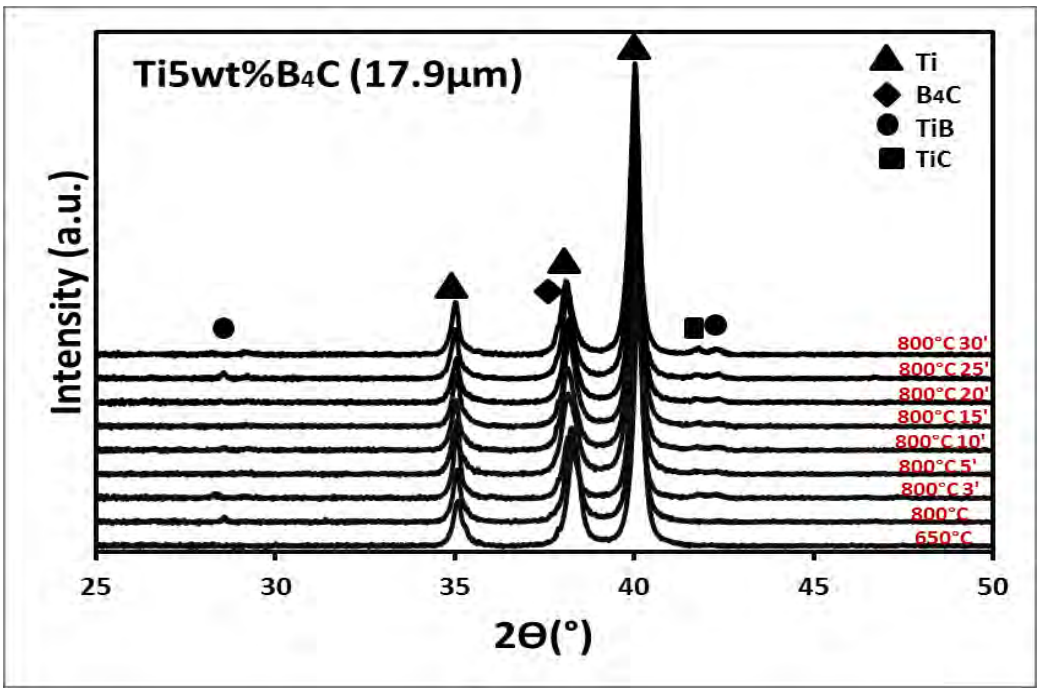

Figure 4.26. XRD phase analysis of 8mm Ti5wt%B4C(17.9µm) sintered at varying dwell time (0 to 30min) at 800°C

Microstructure evolution with dwell time for Ti5wt%B_4C TMC with finer B_4C (1.67µm) is shown in Figure 4.27. At 650°C 0min porosity was observed and densification was improved when temperature was increased to 800°C 0min promoting reactants reaction. Hence, partially reacted B_4C clusters were observed in the Ti grain boundaries with some fine TiB whiskers. The TiC particulates were very small so it was difficult to distinguish them from nucleated secondary alpha Ti within Ti grains, hence they were not identified in the SEM micrographs. However, the XRD analysis in Figure 4.28 revealed small volume fraction TiC particulates already formed at 650°C without any trace of TiB_2 and TiB phases (XRD detection limit 2-5wt%).

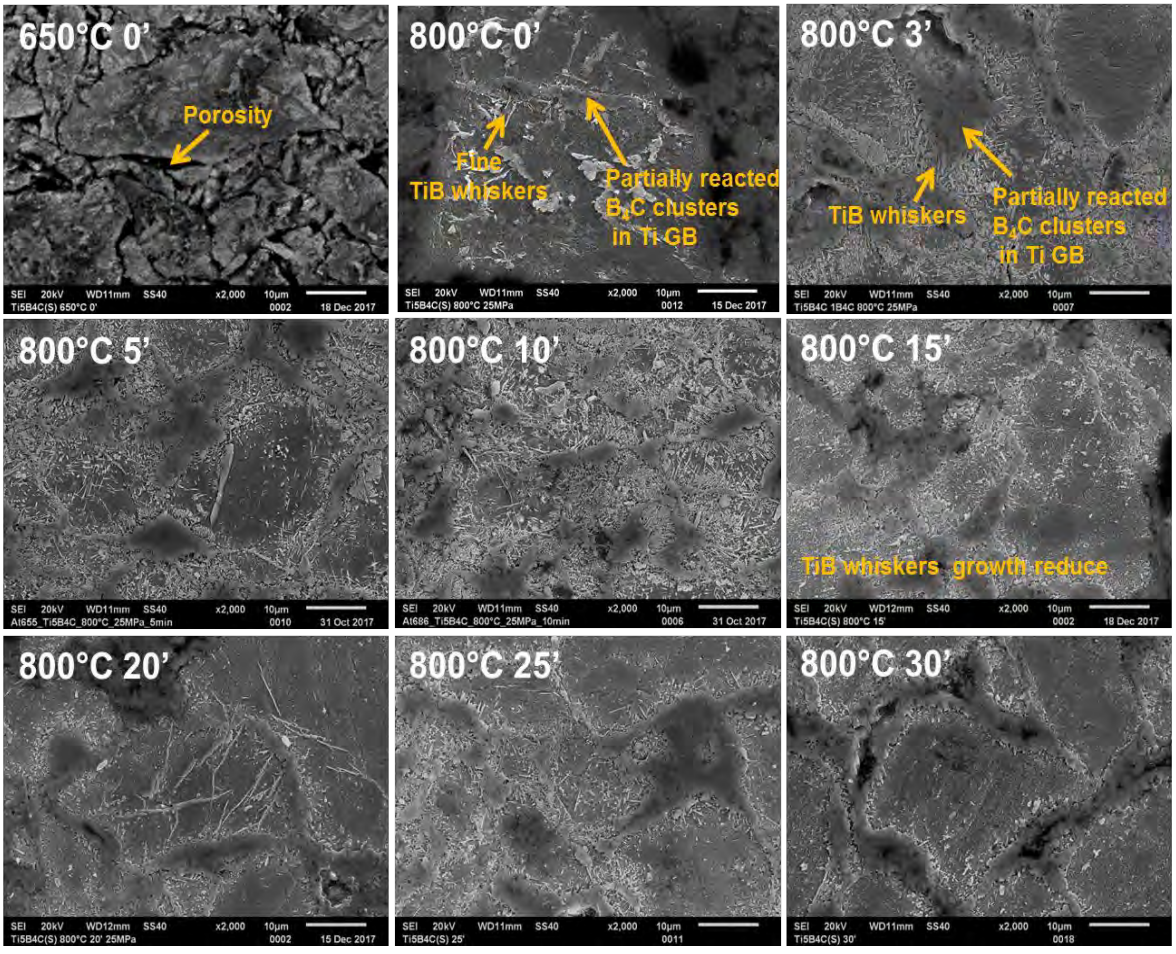

Figure 4.27. SEM observations of dwell time effect on microstructure evolution of 8mm Ti5wt%B_4C(1.67µm)

As dwell time was increased to 3min at 800°C, TiB whiskers were visible and their length increased until 10min. An interesting phenomenon was observed when dwell time was increased to 15min a small fraction of TiB whiskers disappeared although the "grey phase"

was not completely consumed. In agreement with this observation, XRD analysis in Figure 4.28 showed TiB peaks gradually becoming weak after 10min dwell time. Li *et al.* (2018) suggested that diffusion of boron gradually weaken with the increasing processing time and results in the reduction in length of TiB whiskers. Furthermore Fan *et al.* (1997) also stated that after full consumption of TiB_2 coating, the formed long TiB whiskers reduced length to smaller segments with the increased annealing time.

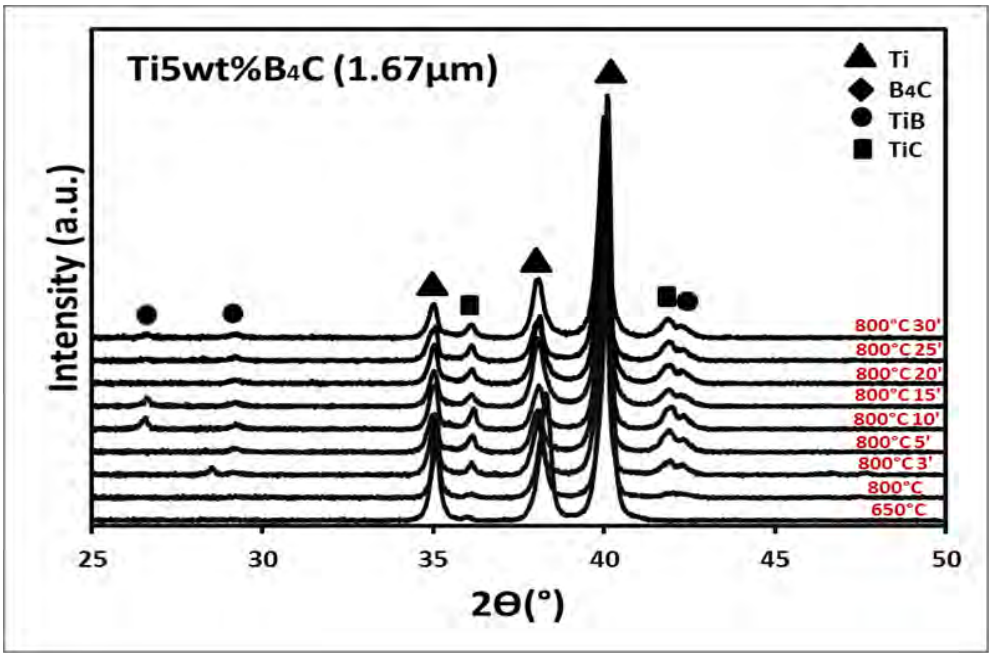

Figure 4.28. XRD phase analysis of 8mm Ti5wt%B_4C(1.67µm) sintered at varying dwell time (0 to 30min) at 800°C

So, combining SEM and XRD results we can say that at 650°C both TiB and TiC phases are formed for TMC with finer B_4C (1.67µm) particles. The results obtained here are similar to those discussed for TMCs with coarser B_4C (17.9 µm) and also in agreement with those discussed in TEM analysis (section 4.5). Suggesting that, in SPS the reaction between Ti and B_4C could be initiated at much lower temperature of 650°C or even lower. This is due to pressure assisting in reactants interfacial contact and the pulsed current density creating higher temperatures in particles surface reaching melting point and evaporation enhancing diffusion of atoms. As such, higher reaction spontaneity in SPS compacted TMCs was achieved at lower temperatures (650°C) in contradiction to DTA(1093°C) and DTA (1200°C) experiments. Whereby, loose powders are normally used reaching exothermic reactions at higher temperatures (Liang *et al.*, 2008; Lu *et al.*, 2008; Ni *et al.*, 2008a).

The results and discussions based on processing TMCs from high contents (10wt%) of B_4C and larger B_4C particle sizes (17.9µm) showed that high temperature (above 1100°C) is required for complete reaction to occur and achieve full densification. Also the dwell time have insignificant change on the TiB_2 layer for Ti5wt%B_4C (17.9µm) TMCs. TMCs based on 1.67µm B_4C have indicated the potential to fully synthesize TiB and TiC phases homogenously dispersed in Ti matrix at lower temperatures, however higher temperatures may be required for complete homogeneity. Therefore, Ti5wt%B_4C TMCs with a diameter of 20mm were prepared using 1.67µm B_4C for mechanical and tribocorrosion properties evaluation. Moreover, TMCs with lower B_4C content Ti1wt%B_4C and Ti2.5wt%B_4C were also prepared to study the effect of reinforcing content on mechanical properties. The TMCs were prepared at temperature of 1000°C and 1100°C, dwell time of 3min to 30min and pressure of 25MPa to 75MPa.

Presented in Figure 4.29 - 4.31 is the effect of dwell time and pressure on the microstructure evolution of 20mm Ti5wt%B_4C(1.67µm) sintered at 1000°C. Figure 4.29 (a-d) shows that, whatever the dwell time and pressure, very fine TiB whiskers and TiC particulates were observed for Ti1wt%B_4C(1.67µm). Figure 4.30(a-d) shows the microstructure of the composite with increased B_4C content in Ti2.5wt%B_4C (1.67µm). As expected, the amount of the reinforcing phases was higher and the tendency of particles to cluster was observed after 3min and 25MPa (Figure 4.30(a)). Further increased B_4C content in Ti5wt%B_4C(1.67µm) TMCs (Figure 4.31(a-d)) leads to also an increase of the amount of reinforcing phases and particles clusters. In contrast to Ti2.5wt%B_4C with lower B_4C content, the particles clusters were formed at 3min, 15min and 3min 75MPa (Figures 4.30 (a, b and d)) completely disappear by increasing the dwell time to 30min as shown in Figure 4.31(c). A complete reaction occurred 1000°C and 30min as coarser TiB whiskers (29.28 µm) and TiC particulates (2.66µm) were formed for Ti5wt%B_4C(1.67µm) .

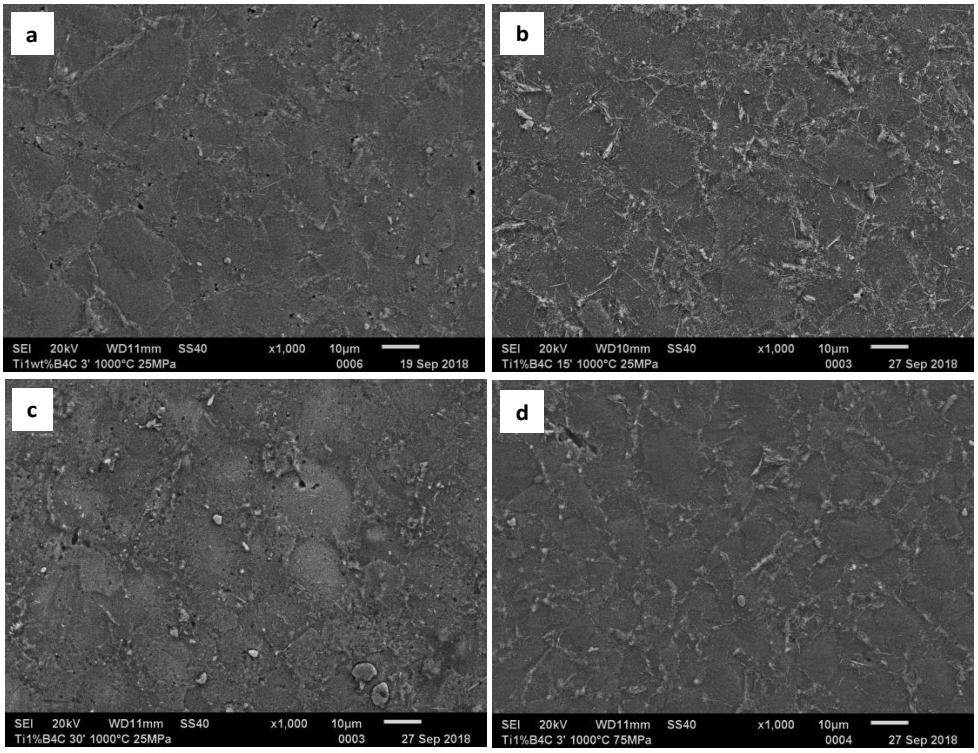

Figure 4.29. SEM micrographs of 20mm Ti1wt% B_4C(1.67 µm) TMCs sintered at 1000°C (a) 3min 25MPa,(b) 15min 25MPa,(c) 30min 25MPa and (d)3min 75MPa

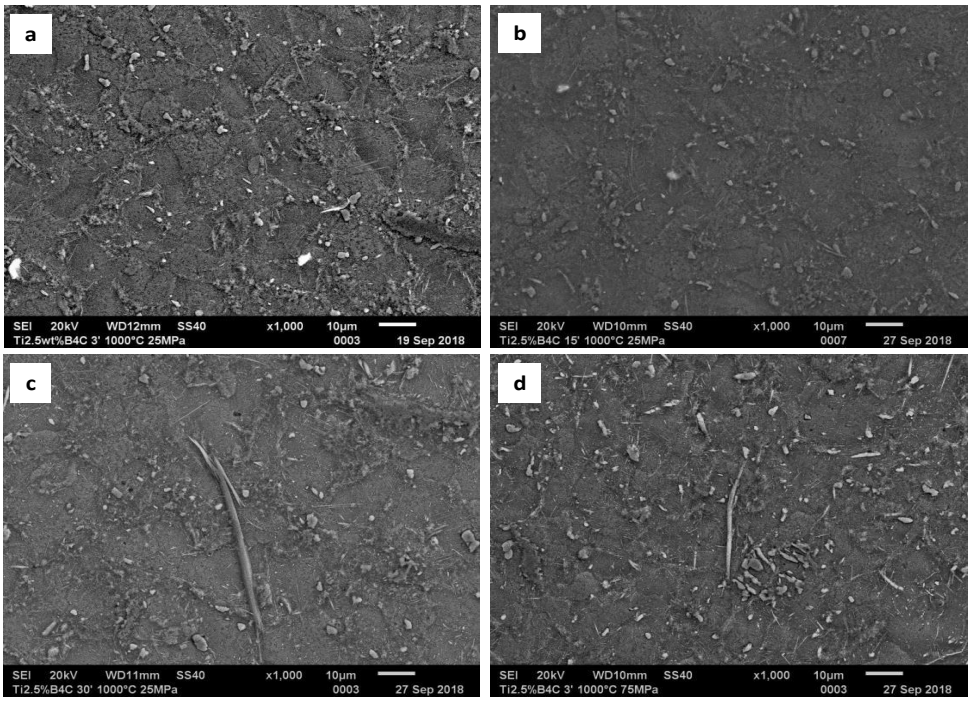

Figure 4.30. SEM micrographs of 20mm Ti2.5wt% B_4C(1.67 µm) TMCs sintered at 1000°C 3min 25MPa,(b) 15min 25MPa,(c) 30min 25MPa and (d)3min 75MPa

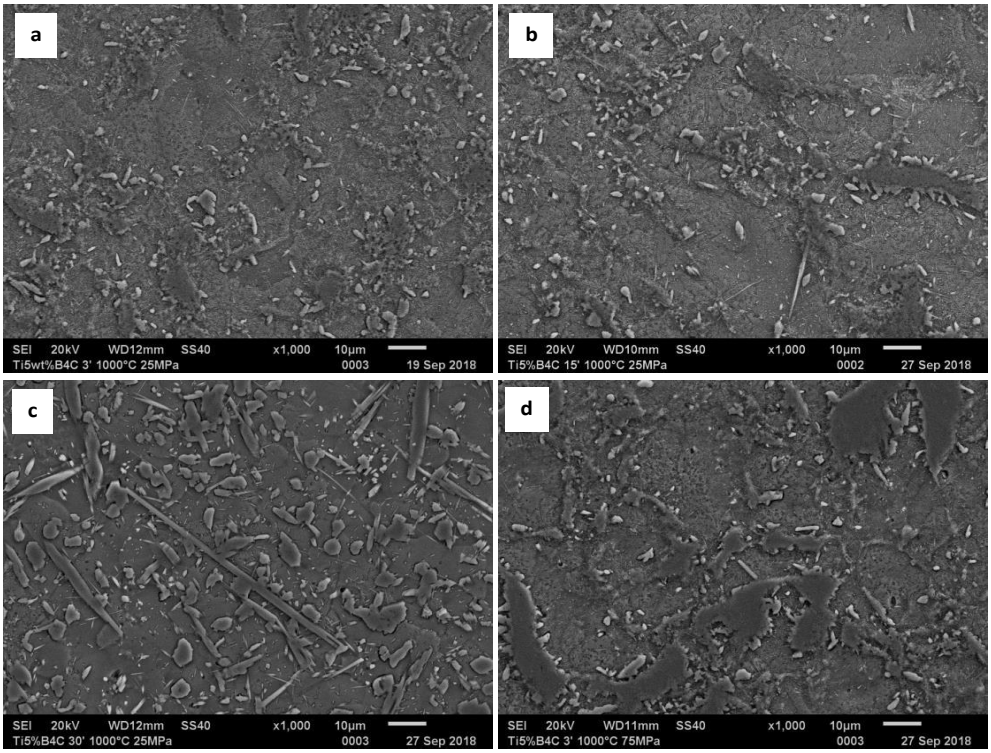

Figure 4.31. SEM micrographs of 20mm Ti5wt% B_4C(1.67µm) TMCs sintered at 1000°C(a) 3min 25MPa,(b) 15min 25MPa,(c) 30min 25MPa and (d)3min 75MPa

The increase of temperature to 1100°C had a significant effect on the reaction and growth of reinforcing phases as observed in Figure 4.32. Already at 3min dwell time as shown in Figure 4.32(a) for Ti1wt%B_4C(1.67µm) reinforcing phases were fine and they became coarser with 15min and 30min dwell times. At 75MPa (Figure 4.32(d)) the microstructure is comparably similar to the one observed at 25MPa (Figure 4.32(a)). Increasing B_4C in Ti2.5wt%B_4C(1.67µm) in Figure 4.33 the reinforcing phases became coarser. Particles clusters were only observed in Ti5wt%B_4C(1.67µm) TMCs at 3min 25MPa and 75MPa as observed in Figure 4.34(a and d). Only prolonged time of sintering from 15 to 30min removed the particles clusters as observed in Figure 4.34 (b and c) were only coarser TiB whiskers and TiC particulates are present. Pressure increase to 75MPa at Figure 4.34d) did not particularly change the microstructure as it was similar to that of 3min and 25MPa in Figure 4.34(a). However, XRD phases analysis for pressure effect shown in Figure 4.35 revealed the presence of Ti_3B_4 phase when pressure was increased to 75MPa especially on TMCs with higher amount of B_4C (Ti5wt%B_4C). In summary, TMCs processed 1100°C with increased dwell time showed absence of particles clusters achieving a homogenous microstructure

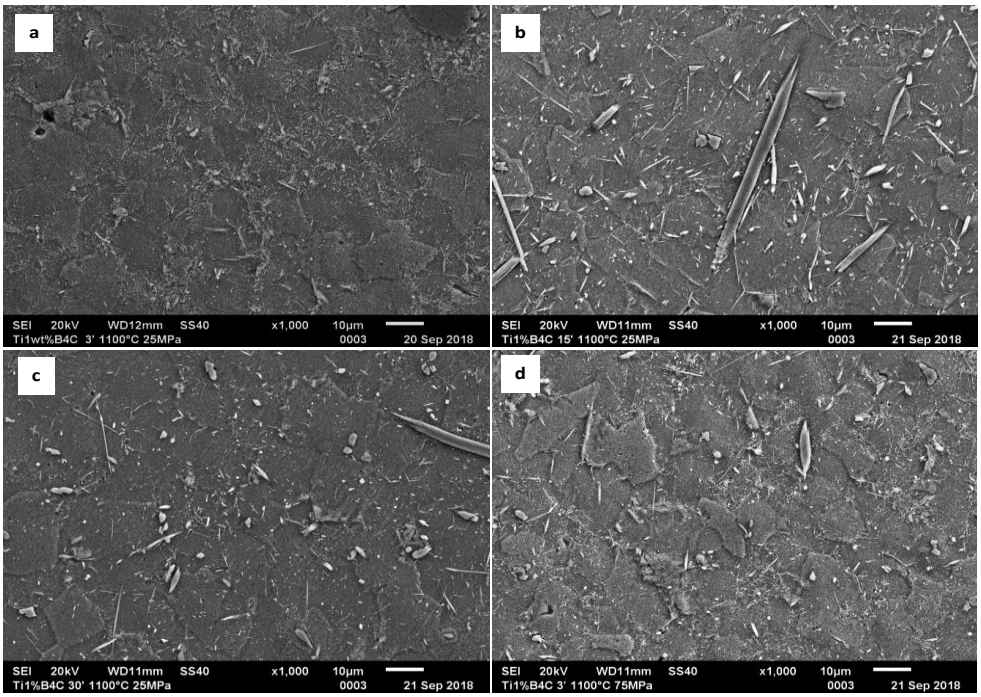

Figure 4.32. SEM micrographs of 20mm Ti1wt% B_4C(1.67µm) TMCs sintered at 1100°C (a) 3min 25MPa,(b) 15min 25MPa,(c) 30min 25MPa and (d)3min 75MPa

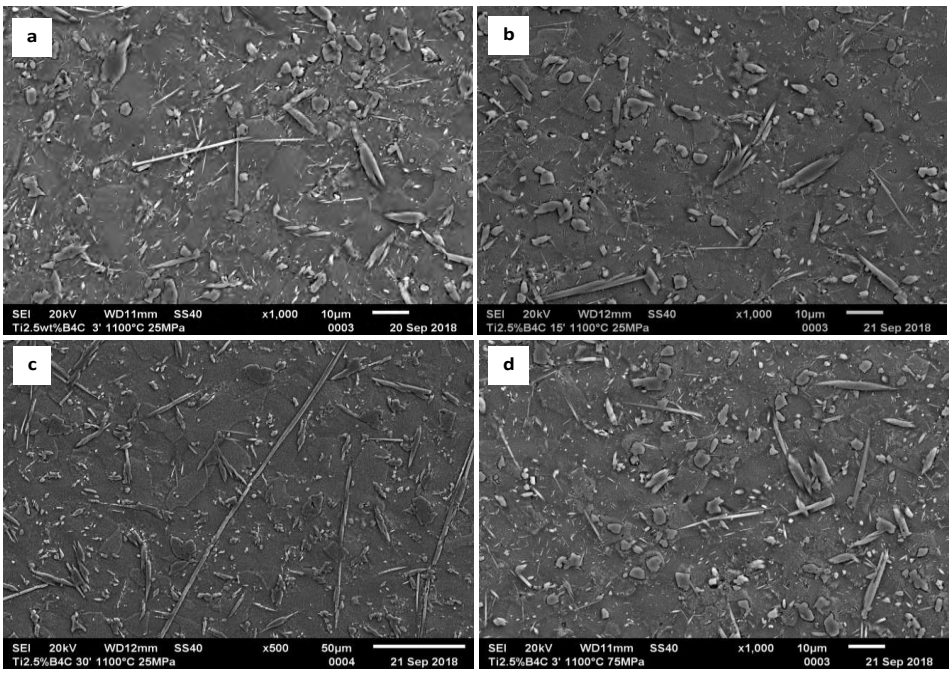

Figure 4.33. SEM micrographs of 20mm Ti2.5wt% B_4C(1.67µm) TMCs sintered at 1100°C (a)3min 25MPa,(b) 15min 25MPa,(c) 30min 25MPa and (d)3min 75MPa

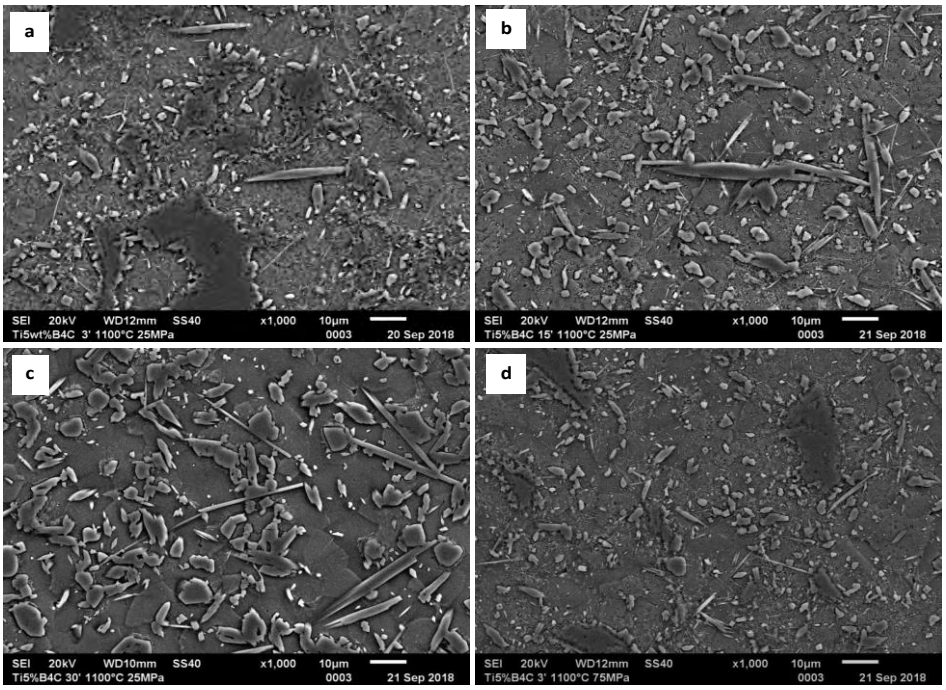

Figure 4.34. SEM micrographs of 20mm Ti5wt% B_4C(1.67µm) TMCs sintered at 1100°C (a)3min 25MPa,(b) 15min 25MPa,(c) 30min 25MPa and (d)3min 75MPa

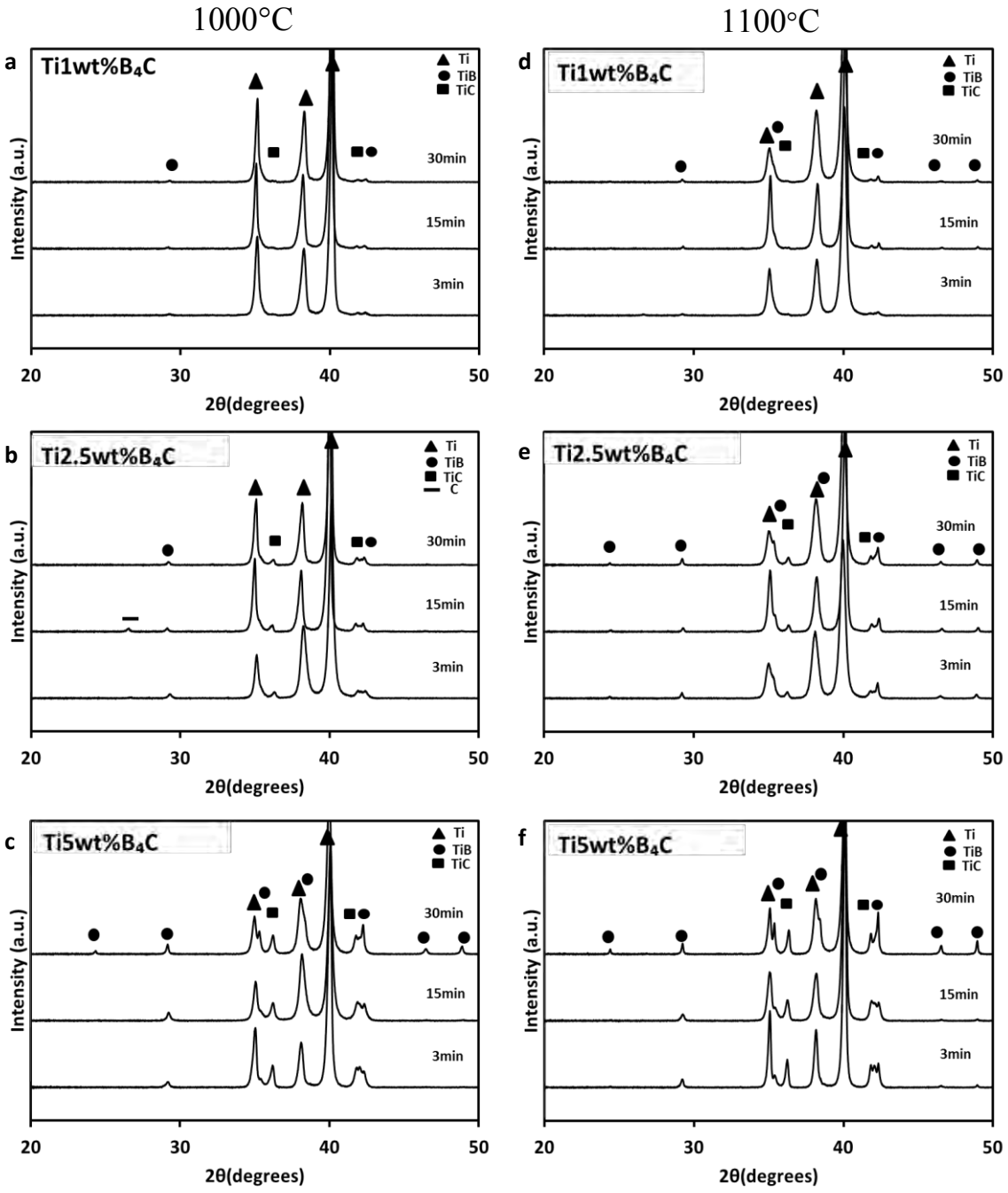

Figure 4.35. XRD phase analysis of 20mm samples (a-c) 1000°C and (d-f) 1100°C

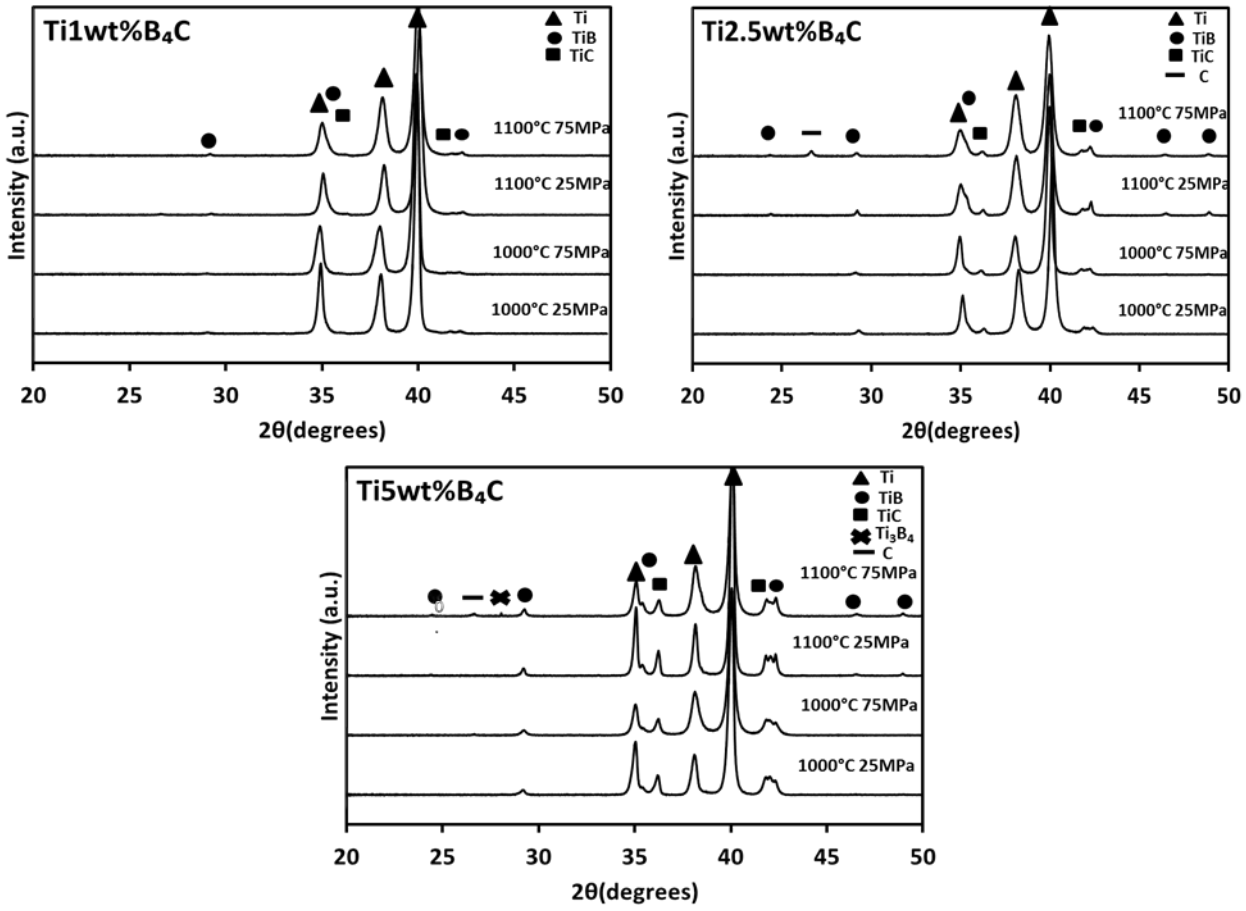

Figure 4.36. XRD phase analysis of pressure effect in D20 TMCs

4.8 Relation between reinforcing phase's content and size to the Vickers hardness

Hardness is a property measure of a material that determines its resistance to plastic deformation, indentation, penetration, abrasion, scratching and wear. Thus its application enables the evaluation of the material's strength, ductility and wears resistance, as such it is possible to determine if the material or the materials processing is suitable for the required application. In this section the relation between process-structure-properties of the synthesized 20mm TMCs are discussed. The Vickers hardness measurements were done using a load of 0.5Kg with a dwelling time of 10s as described in Chapter 2.

Semi-quantitative phase analysis was done, thanks to the XRD analyses (Figure 4.35 & 4.36) by means of RIR method. In all the TMCs at the respective sintering temperature, dwell time and pressure as shown in Table 23 and 24, the amount of TiB whiskers was higher than TiC particulates. The reinforcing phases' weight percent increased with increasing the amount of

B_4C from 1 to 5wt%. The presented experimental density values were obtained by rule of mixtures using the weight percent values of Ti, TiB and TiC obtained by RIR method. The Archimedes density values were in the range of 4.51 - 4.53 g/cm^3 which were relatively close to the calculated theoretical density (Appendix I.II) values of 4.51 - 4.54 g/cm^3. However, the Archimedes densities of Ti1wt%B_4C and Ti2.5wt%B_4C sintered at 1000°C and dwell time of 3min - 30min were much lower, 4.42 - 4.47 g/cm^3, compared with experimental and calculated theoretical density values. This could be attributed to the smaller size and low quantity of the reinforcing phases in the TMCs, as observed in SEM images in section 4.7.

Table 23. Semi- quantitative phase analysis of 20mm Ti and TMCs sintered at 1000°C

	1000°C 3' 25MPa			
	Ti	**Ti1wt%B_4C**	**Ti2.5wt%B_4C**	**Ti5wt%B_4C**
Ti (%)	100	99.50	96.70	92.20
TiB (%)	-	0.30	2.60	5.80
TiC (%)	-	0.10	0.70	2.00
Experimental density (g/cm^3)	4.51	4.51	4.51	4.52
Archimedes density (g/cm^3)	4.50	4.47	4.42	4.48
Theoretical density (g/cm^3)	4.51	4.52	4.53	4.54
	1000°C 15' 25MPa			
	Ti	**Ti1wt%B_4C**	**Ti2.5wt%B_4C**	**Ti5wt%B_4C**
Ti (%)	100	99.50	97.70	90.40
TiB (%)	-	0.40	1.70	7.40
TiC (%)	-	0.10	0.50	2.20
Experimental density (g/cm^3)	4.51	4.51	4.51	4.52
Archimedes density (g/cm^3)	4.50	4.44	4.46	4.50
Theoretical density (g/cm^3)	4.51	4.52	4.53	4.54
	1000°C 30' 25MPa			
	Ti	**Ti1wt%B_4C**	**Ti2.5wt%B_4C**	**Ti5wt%B_4C**
Ti (%)	100	99.50	97.90	90.10
TiB (%)	-	0.40	1.60	6.20
TiC (%)	-	0.10	0.60	3.70
C	-	-	-	-
Experimental density (g/cm^3)	4.51	4.51	4.52	4.53
Archimedes density (g/cm^3)	4.50	4.45	4.47	4.53
Theoretical density (g/cm^3)	4.51	4.52	4.53	4.54
	1000°C 3' 75MPa			
	Ti	**Ti1wt%B_4C**	**Ti2.5wt%B_4C**	**Ti5wt%B_4C**

Ti (%)	100	99.40	97.20	90.00
TiB (%)	-	0.50	2.20	7.10
TiC (%)	-	0.10	0.50	2.10
C	-	-	-	0.80
Ti_3B_4	-	-	-	-
Experimental density (g/cm^3)	4.51	4.51	4.51	4.52
Archimedes density (g/cm^3)	4.50	4.50	4.51	4.53
Theoretical density (g/cm^3)	4.51	4.52	4.53	4.54

Table 24. Semi- quantitative phase analysis of 20mm Ti and TMCs sintered at 1100°C

	1100°C 3' 25MPa			
	Ti	**Ti1wt%B_4C**	**Ti2.5wt%B_4C**	**Ti5wt%B_4C**
Ti (%)	100	98.70	95.80	91.60
TiB (%)	-	1.10	2.70	5.50
TiC (%)	-	0.20	1.50	3.00
Experimental density (g/cm^3)	4.51	4.51	4.52	4.53
Archimedes density (g/cm^3)	4.50	4.50	4.51	4.52
Theoretical density (g/cm^3)	4.51	4.52	4.53	4.54
	1100°C 15' 25MPa			
	Ti	**Ti1wt%B_4C**	**Ti2.5wt%B_4C**	**Ti5wt%B_4C**
Ti (%)	100	98.90	96.60	92.40
TiB (%)	-	0.70	2.10	5.50
TiC (%)	-	0.40	1.30	2.10
Experimental density (g/cm^3)	4.51	4.51	4.52	4.52
Archimedes density (g/cm^3)	4.51	4.51	4.52	4.52
Theoretical density (g/cm^3)	4.51	4.52	4.53	4.54
	1100°C 30' 25MPa			
	Ti	**Ti1wt%B_4C**	**Ti2.5wt%B_4C**	**Ti5wt%B_4C**
Ti (%)	100	97.60	97.50	88.40
TiB (%)	-	2.10	1.70	7.20
TiC (%)	-	0.30	0.50	4.30
C	-	-	0.20	-
Experimental density (g/cm^3)	4.51	4.51	4.50	4.53
Archimedes density (g/cm^3)	4.51	4.50	4.52	4.53
Theoretical density (g/cm^3)	4.51	4.52	4.53	4.54
	1100°C 3' 75MPa			

	Ti	Ti1wt%B_4C	Ti2.5wt%B_4C	Ti5wt%B_4C
Ti (%)	100	99.20	91.50	87.60
TiB (%)	-	0.60	4.50	3.50
TiC (%)	-	0.30	0.70	2.20
C	-	-	3.20	0.80
Ti_3B_4	-	-	-	5.90
Experimental density (g/cm^3)	4.51	4.52	4.42	4.33
Archimedes density (g/cm^3)	4.50	4.50	4.52	4.53
Theoretical density (g/cm^3)	4.51	4.52	4.53	4.54

The hardness values for all the TMCS were obtained using a load of 0.5Kg with a dwell time of 10s and these are presented in Figure 4.37. It was evident that the hardness values of pure titanium were improved by addition of reinforcing phases. The hardness values for the TMCs at both temperatures increases with the increasing content of B_4C. Pure titanium exhibited highest hardness value of 401HV at 1100°C and 30min dwell time, while the highest value for TMCs was 678HV for Ti5wt%B_4C sintered at 3min and 75MPa. The Vickers hardness values of the TMCs were in the range of 428 - 678HV. These values were comparably in the same range with those obtained by pressureless sintering at 1450°C for composites with 10 to 30vol% (TiB + TiC) synthesized from 3µm B_4C (526 and 690HV) were obtained (Kolukuluri, 2013). Also Ni *et al.* (2006) reported a hardness value of 581HV for 0.5µm B_4C 10vol%(TiB + TiC) composite prepared by hot pressing at 1200°C, 30min and 20MPa (Figure 4.38).

Presented in Figure 4.39 is the evolution of reinforcing phase's sizes with the respective SPS sintering conditions. The TiB whiskers length for 8mm TMCs at 800°C increased from 1.264 to 1.461µm, the 20mm increased from 19.343 to 29.567µm at 1100°C with the varied dwell times (3-30min) respectively. Similar observations were made for the width of the TiB. However it has to be noted that, the TiB whiskers growth was inhomogeneous for TMCs sintered at higher temperatures in contrast to those sintered at 800°C. Their length was in the range of 10.628 to 28.284µm at 3min 1100°C (20mm TMCs) higher than those sintered at 3min 800°C (8mm TMCs) with 0.63 to 1.635µm.

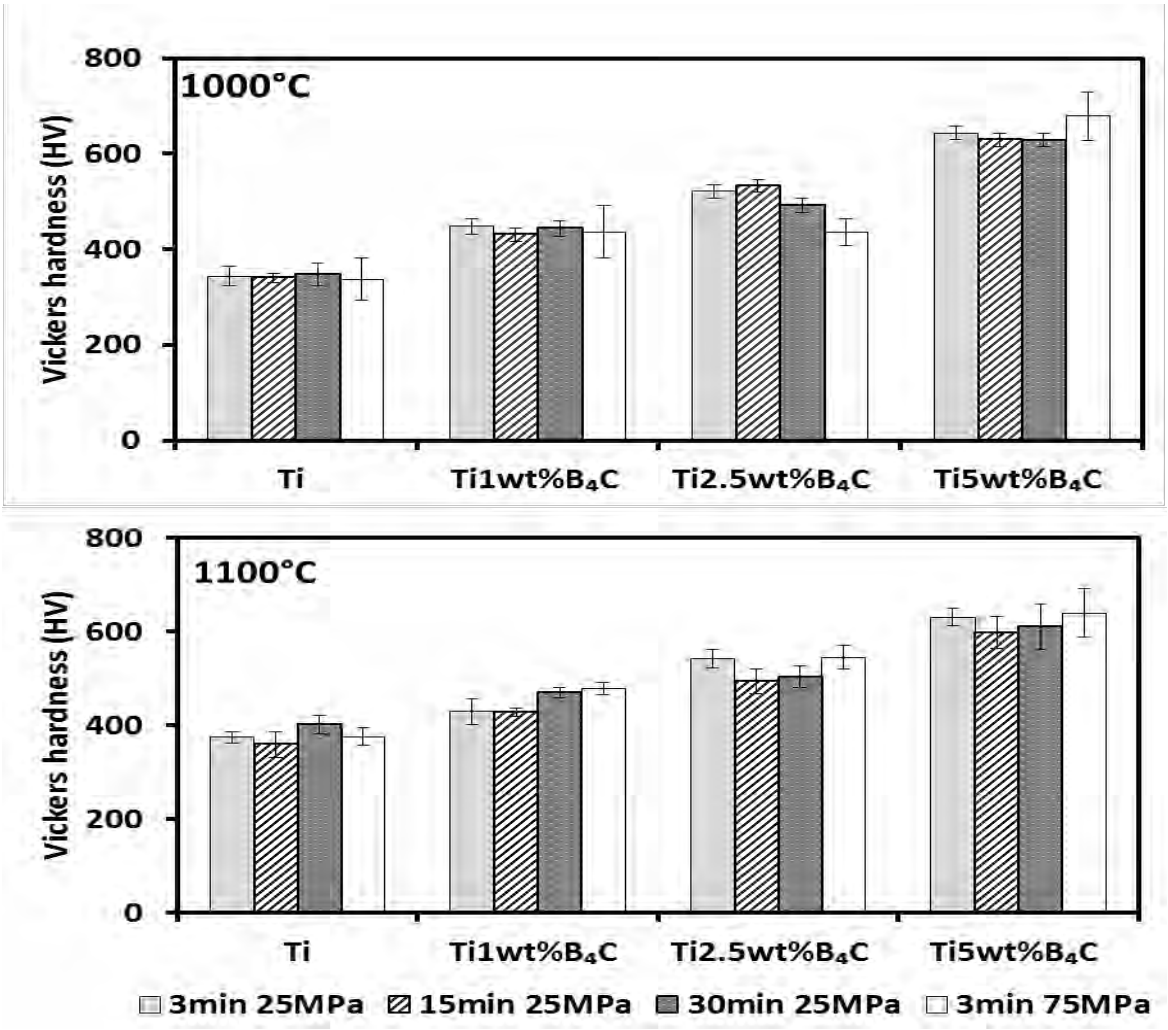

Figure 4.37. Vickers hardness of 20mm TMCs at varying temperature and dwell time

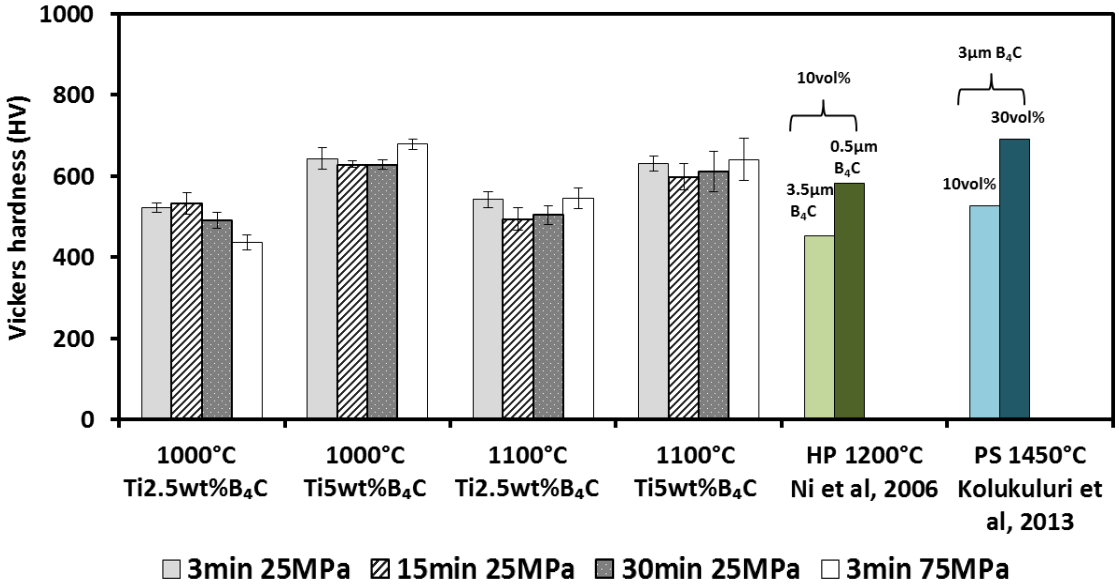

Figure 4.38. Vickers hardness of 20mm TMCs at varying temperature and dwell time

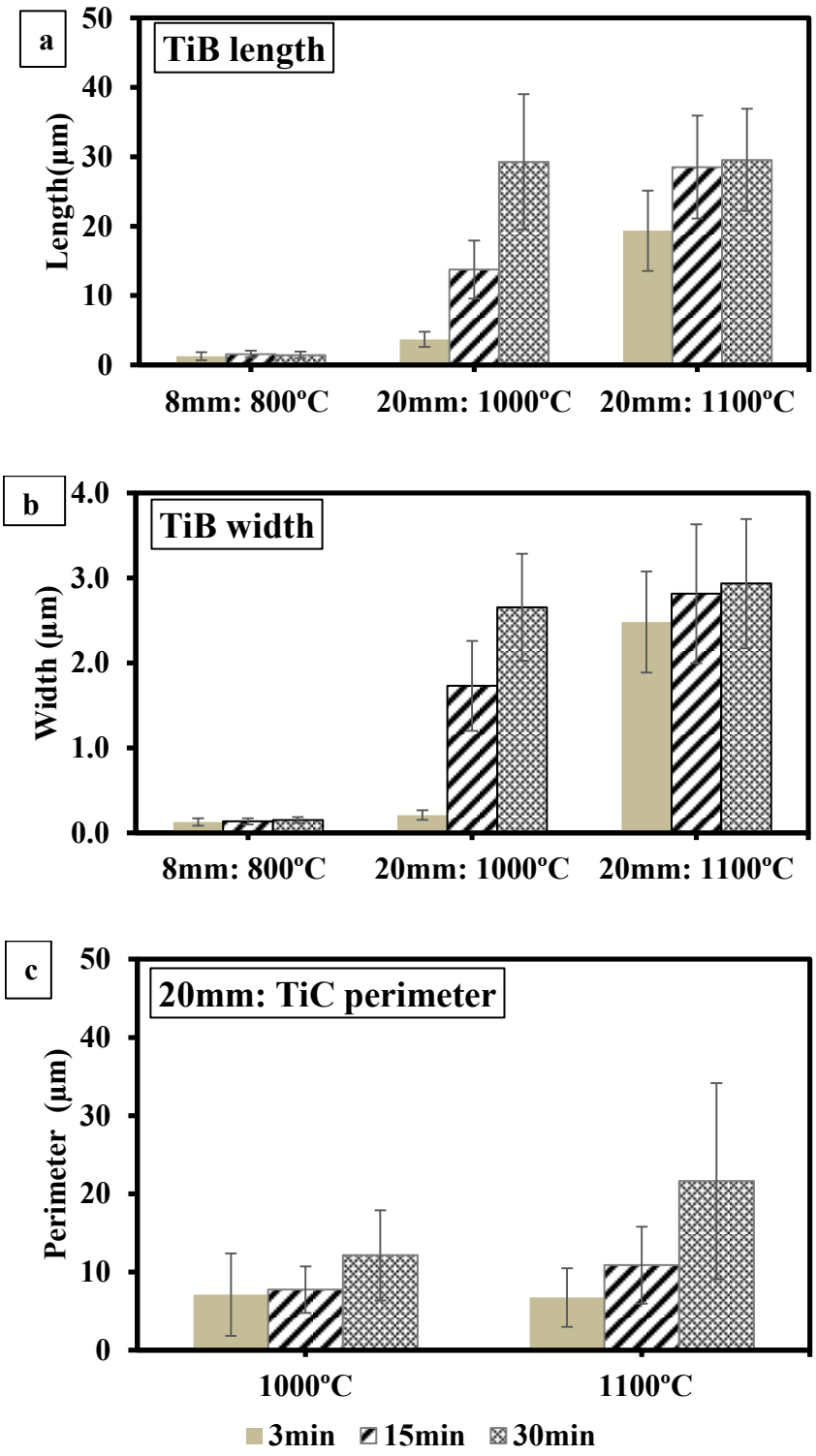

Figure 4.39. Reinforcing phases growth with increasing dwell time, a) TiB length, b) TiB width and c) TiC perimeter

The relationship between the reinforcing phase's content and Vickers hardness for TMCs sintered at 1000°C and 1100°C with the varying dwell time (3-30min) and pressure (25-75MPa) is shown in Figure 4.40. As can be seen the hardness values gradually increased with increasing reinforcement content at the varied sintering temperature, dwell time and pressure. There was a slight variation in hardness values with the respective SPS conditions. Addition of 1 to 5wt%B_4C at 1000°C for the different dwell times (3 - 30min) increased the hardness to about 22 to 46% respectively. Also increasing pressure (25 - 75MPa) at 3min dwell time the hardness values increments with reinforcement were 23 to 48% respectively

However, these hardness variations were comparably in the same range irrespective of coarsening of TiB and TiC. Similar behaviour was observed at 1100°C, hardness variation with dwell time (3 - 30min) was 17 - 38%, with pressure (25 - 75MPa) was 21 - 41% with increasing reinforcement content from 1 to 5wt% respectively. Moreover, comparing the two temperatures, it can be seen that the hardness variations were slightly lowered when temperature increased to 1100°C. This could be attributed to the compacted clusters observed at 1000°C providing higher hardness than homogeneously dispersed TiB and TiC phases formed at 1100°C

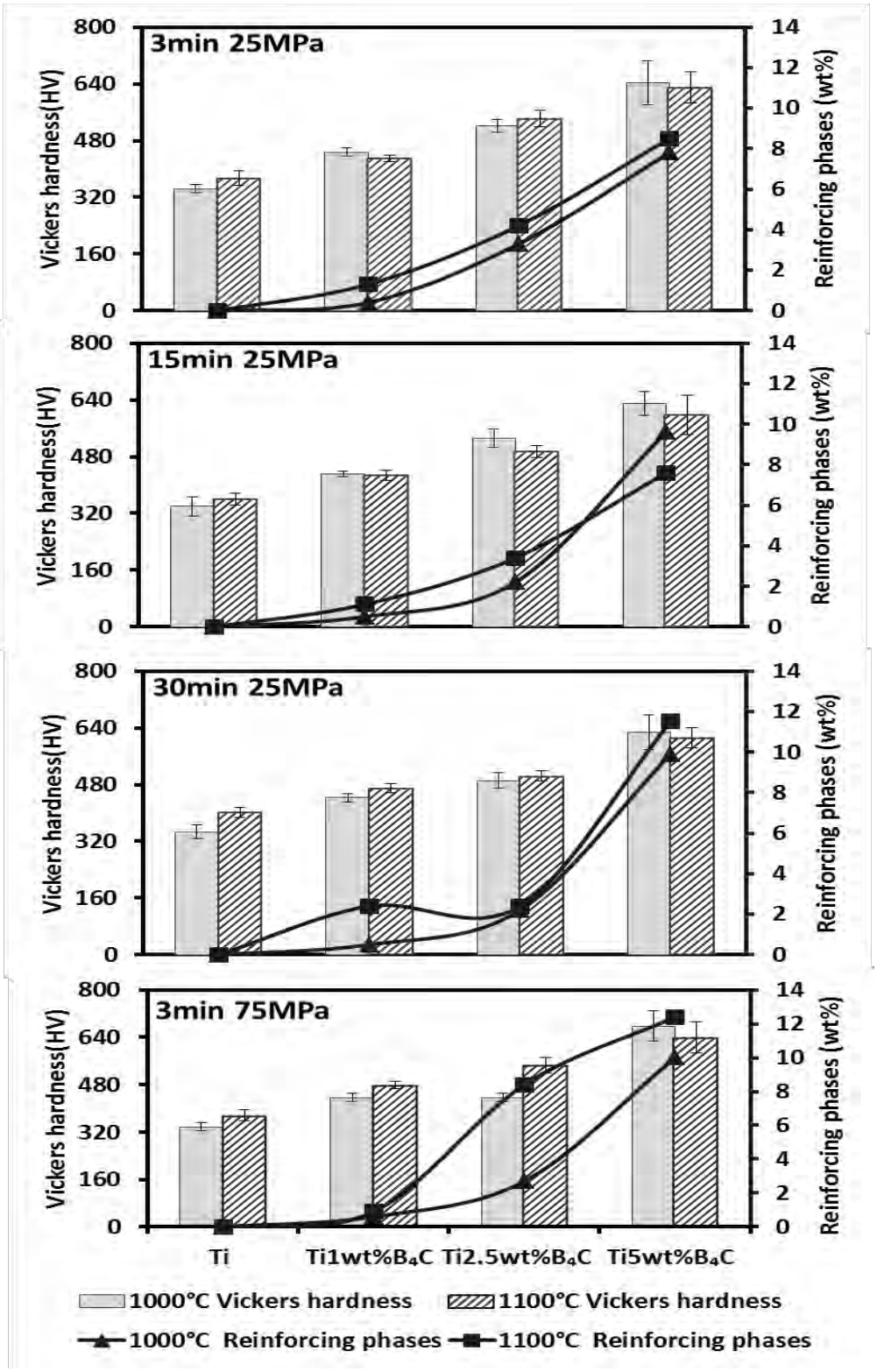

Figure 4.40. Relation between Vickers hardness and reinforcing phases content of 20mm TMCs at varying temperature and dwell time

4.9 Reaction kinetics in TMCs by SPS

Reaction kinetics is widely studied in TiB_2 based hard coatings field including also TiC coatings, than for TMCs prepared by powder metallurgy. In fact, the modeling of reaction kinetics is considered as a suitable tool to select the appropriate process parameters for obtaining adequate boride layer thicknesses in relation with their practical applications (Keddam *et al.*, 2017).

In order to understand the reaction kinetics involved in TMCs prepared by SPS, it is important to study the interphase reaction layer growth (TiB_2 and TiB). The TiB_2 is a transient phase which gives way to formation of TiB whiskers after complete consumption of B_4C particles. However, the stages of reactions and formation of interphases (TiB_2) involved in the microstructure evolution of sub-micron B_4C particles occur rapidly. As such the reaction kinetics at varying temperatures and dwell times (3 to 30min) were quantified for the growth of TiB whiskers and TiC particles for TMCs with 1.67µm B_4C particles shown in Figure 4.41.

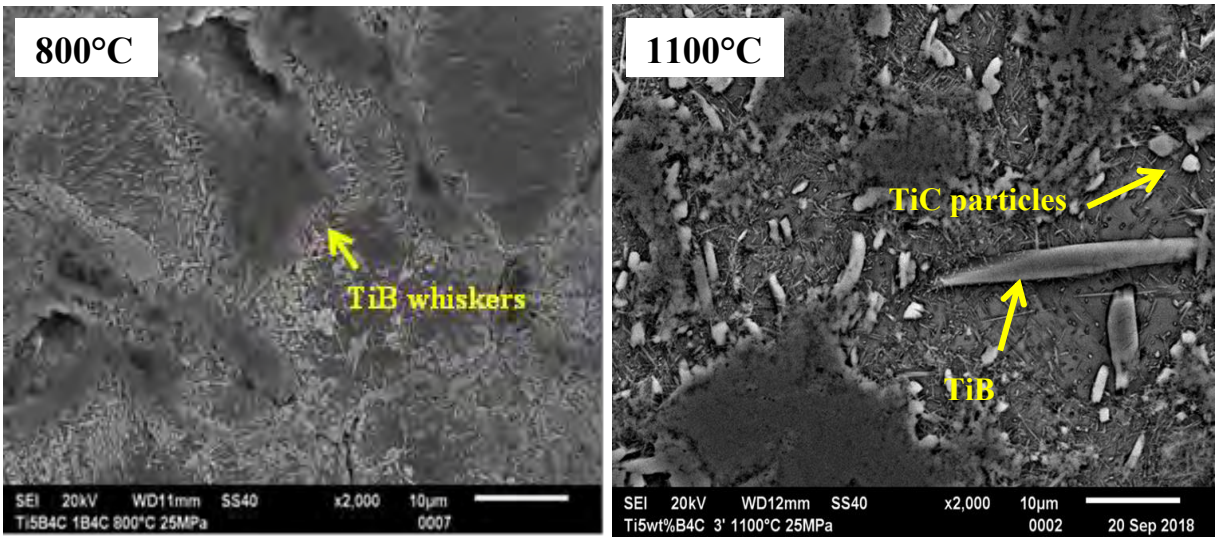

Figure 4.41.TMCs sintered at 800°C and 1100°C showing TiB whiskers

The growth of TiB whiskers and TiC particles are diffusion controlled thus obeys parabolic law mathematically described as follows:

$$x = kt^{1/2} \qquad [Eq.18]$$

Where x represents the length of TiB or perimeter of TiC, k is the growth rate and t is the sintering dwell time.

Presented in Figure 4.42 and 4.43 is the growth in length of TiB whiskers and perimeter of TiC particles increasing gradually with time in the temperature range of 1073-1373°C. The parabolic growth constants were obtained from the slope of the curves. Due to lack of experimental data for TMCs by SPS technique the obtained parabolic growth constants were compared with those obtained by coating techniques in temperature ranges of 973-1123K as shown in Figure 4.44 and 4.45. At low temperatures the TiB values were relatively close to those reported for coating techniques and that of TiC were relatively lower. We have to consider that in coatings the reaction layers are planar so the growth rate may be almost uniform compared with TiB whiskers and TiC particles with inhomogeneous growths. This might have effect on the growth rate determination for the TMC.

In section 4.6 we discuss that diffusion path of atoms involved in the Ti-B_4C TMCs is by interdiffusion mechanisms involving B, C and Ti atoms. The formation of TiB and TiC depends on B and C diffusion coefficients in the Ti matrix. Carbon with higher diffusion coefficient diffuse rapidly further into the Ti matrix and the B is left behind closer to the Ti/B_4C interface, Ti then diffuses into vacancies left by B and C atoms. In agreement with Mogilevsky *et al.* (1998) a complex reaction layer in sequence of Ti-$TiC_{0.5}$-TiB-TiB_2-B_4C was formed at 1000°C and 1300°C for B_4C coating deposited on Ti substrate. This formation was related to the higher diffusivity of carbon in titanium compared to that of boron in titanium and titanium self-diffusion. Vacancy diffusion mechanism of B and C atoms led to the growth of TiB_2, TiB and TiC phases (Fan *et al.*, 1997; Keddam *et al.*, 2016; Martins *et al.*, 2018).

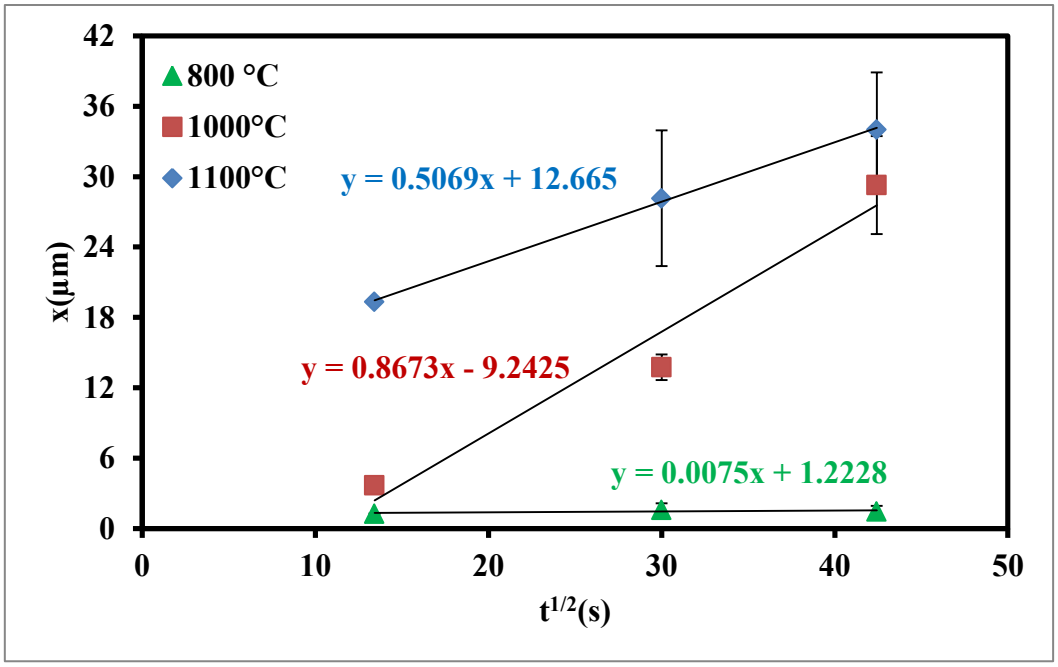

Figure 4.42. Evolution of TiB whiskers length as a function of the square root of time

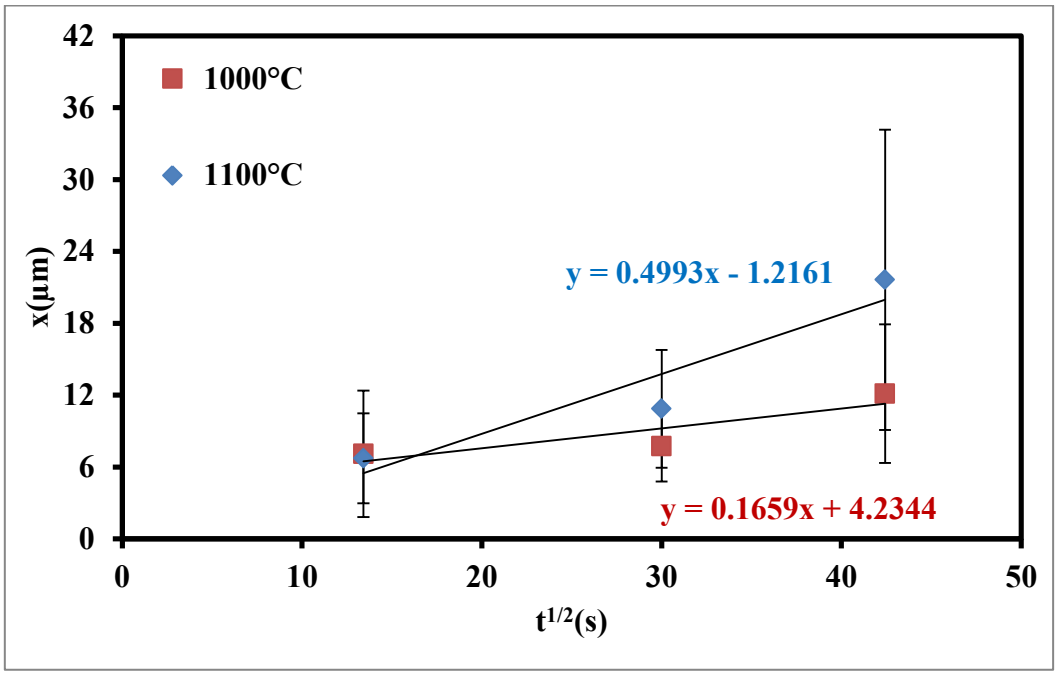

Figure 4.43. Evolution of TiC perimeter as a function of the square root of time

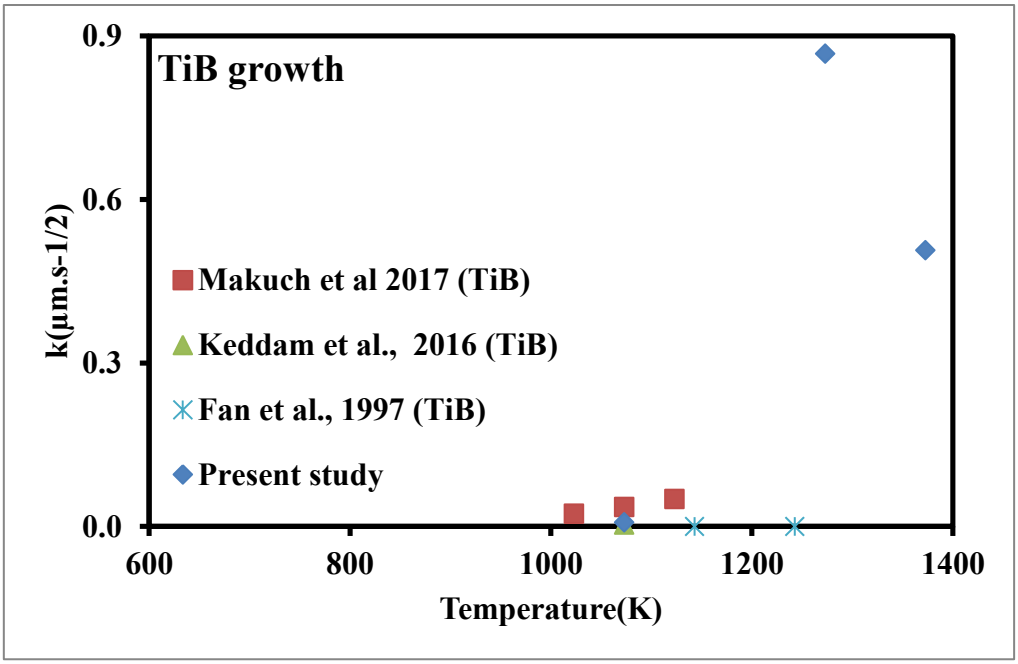

Figure 4.44. Parabolic growth constants for TiB

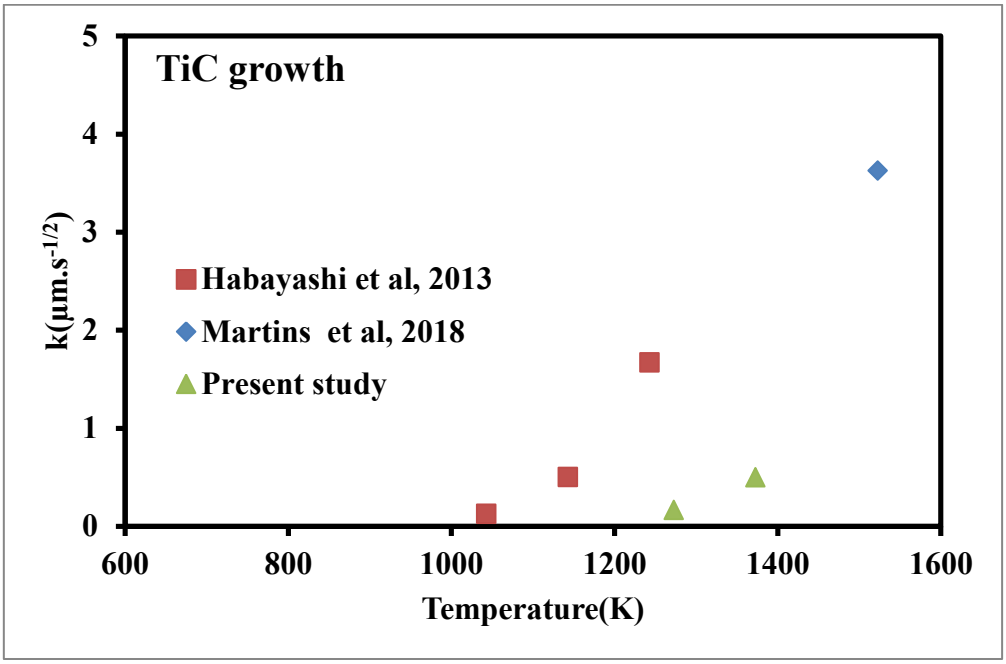

Figure 4.45. Parabolic growth constants for TiC

The growth of TiB whiskers and TiC particles are thermally activated and the growth rate (k) depends on the temperature, using the following equation the activation energy was determined.

$$k = k_0 \exp\left(\frac{E_a}{RT}\right) \qquad [Eq.19]$$

Where k_0 is the frequency constant, E_a is the activation energy, R (8.314J.mol^{-1}.K^{-1}) is the universal gas constant and T is the temperature. The boron and carbon activation energy needed to grow TiB whiskers and TiC particles was determined from the linear slopes in Figure 4.46 and 4.47, it was about 83.09KJ.mol^{-1} and 69.53 KJ.mol^{-1} respectively. These values are compared with those in literature in Table 25 that of TiB is within the range of activation energy values in contrast with TiC which is very low. . As found in literature reaction kinetics are widely investigated for titanium based coatings, so there is a wide gap in literature for titanium matrix composites by SPS. Due to lack of data in the SPS process is difficult to make a good judgement of the activation energies obtained in the present study. Thus more work is needed in this specific research area.

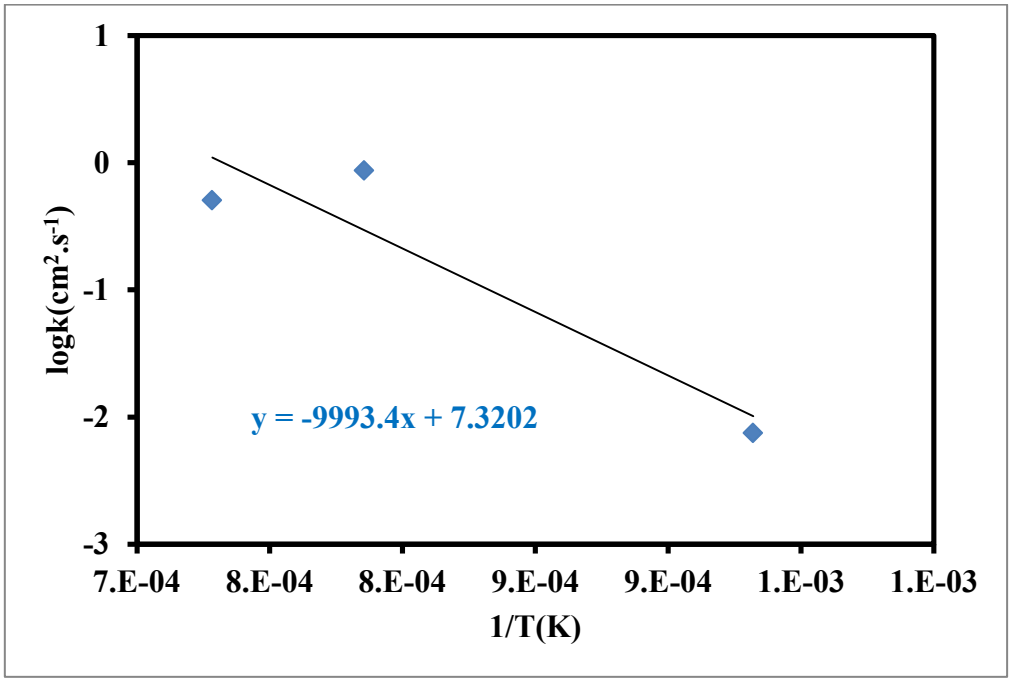

Figure 4.46. Arrhenius relationship between growth rates and sintering temperature for TiB whiskers

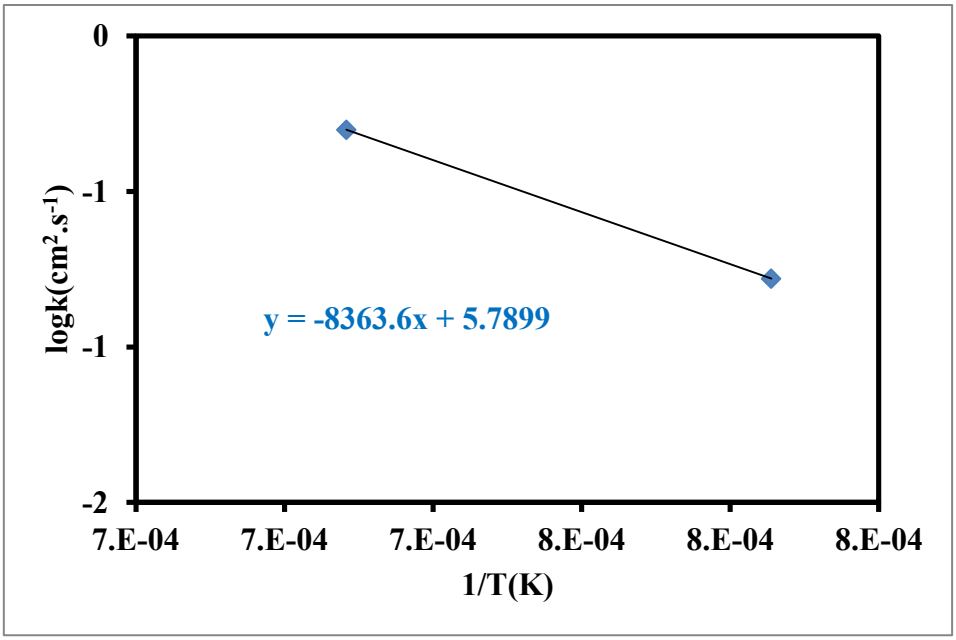

Figure 4.47. Arrhenius relationship between growth rates and sintering temperature for TiC particles

Table 25. Summary of calculated activation energies

Matrix	Process	Temperature range (K)	Activation energy Ea ($KJ.mole^{-1}$)	References
CP-Ti	SPS 25MPa	1073-1373	83.09 (TiB)	Present study
CP-Ti	SPS 25MPa	1073-1373	69.53(TiC)	Present study
CP-Ti	Plasma paste boriding	973–1073	136 (TiB_2), 64(TiB)	(Keddam *et al* .,2017)
CP-Ti	Plasma paste boriding	1023–1123	123(TiB_2), 179(TiB)	(Makuch *et al.*, 2017)
CP-Ti	Plasma paste boriding	973–1073	138 (TiB_2), 55(TiB)	(Keddam *et al.*, 2016)
CP-Ti	Plasma paste boriding	973–1073	94 (TiB_2 + TiB)	(Ataibis *et al.*, 2015)
CP-Ti	CRTD-Bor (electrolyse liquid boriding)	1173–1373	190 (TiB_2)	(Kartal *et al.*, 2013)
CP-Ti	Powder immersion reaction assisted coating method	1273-1473	175($TiC_{0.5}$-TiB-TiB_2)	(Mogilevsky *et al,* 1995)
TB2 alloy	Pack boriding	1223–1373	158(TiB_2), 96 (TiB)	(Li *et al.*, 2018)
Ti6Al4V	Plasmam paste boriding	973–1073	100 (TiB_2 + TiB)	(Ataibis *et al.*, 2015)
Ti6Al4V	Pack boriding	1273–1373	65 (TiB_2 + TiB)	(Fenghua *et al.*, 2010)
Ti6Al4V	Ti6Al4V/Sigma fibre composites	1143–1243	187 (TiB_2),190(TiB)	(Fan *et al.*, 1997)
CP-Ti	SPS 10.5 MPa	1043-1243	218.6 (TiC)	(Hayashi *et al.*, 2013)
Ti-48Al-2Cr-2Nb	SPS 50MPa	1173-1573	232.52 (TiC)	(Martins *et al.*, 2018)
Ti3Al	SHS	-	240 - 460 (TiC)	(Khina *et al.*, 2005)

Summary

Simultaneous synthesis and consolidation of TMCs with homogenously distributed TiB and TiC reinforcing phases in the titanium matrix and detailed analysis of the involved in-situ reaction mechanisms and kinetics was achieved. To achieve this, variety of B_4C powders with different D_{50} particles size (1.67µm, 1.79µm and 17.9 µm) were reactively sintered with CP-Ti (25.9 µm) to simultaneously synthesize and consolidate Ti-(TiB + TiC) TMCs. The relative densities depend on particles size and reaction between the reactants. Relative density of TMCs based on B_4C 1.67µm and 1.79µm was higher and relatively the same at the varied SPS parameters, but that of B_4C 17.9µm was very low. This difference was attributed to the high spontaneity of reaction occurring when smaller particles size were used forming high volume fraction of denser TiB_2(4.52g/cm^3), TiB(4.56g/cm^3) and TiC(4.93 g/cm^3) reinforcing phases at lower temperatures of 800°C. As for TMCs based on coarser B_4C 17.9µm the unreacted B_4C (2.52g/cm^3) contributed to the low relative densities. Relative density of 99% was reached at 800°C for 8mm TMCs Ti5wt%B_4C(1.67µm) and Ti5wt%B_4C(1.79 µm) sintered at pressures of 75MPa and 50MPa respectively. Increasing the amount of B_4C for all the composites led to even lower relative densities due to porosity and unreacted B_4C. Microstructure for B_4C 1.67µm and 1.79µm TMCs were commonly characterized by TiB, TiC and clusters of particles, while that of B_4C 17.9µm TMCs consisted of TiB_2, TiB, TiC and unreacted B_4C. Microstructure analysis on the cross section of the particles clusters for B_4C 1.67µm TMCs revealed unreacted B_4C at 800°C. At 1100°C the B_4C completely reacted to form mixture of phases namely TiB, Ti_3B_4, Ti_2B, TiC, and Ti_2C. On the reaction mechanism, the reaction between the Ti and B_4C was suggested to be initiated at temperatures below the set-point temperature of 800°C. This was due to the higher temperatures reached on the surface of particles reaching the melting point and vaporization which enhanced interdiffusion of atoms. To remove the particles clusters, the dwell time was increased from 3min to 30min and a homogeneous microstructure with TiB and TiC phases was obtained. The Vickers hardness increases with the increasing amount of reinforcing phases (TiB and TiC) and the highest was 678HV obtained at 1000°C 3min 75MPa.

CHAPTER 5: Corrosion and Tribocorrosion of Titanium Matrix Composites (TMCs)

Table of contents

5.0 Introduction

The poor wear resistance of titanium and its alloys limit their application in which the combined effect of wear and corrosion may be encountered. In this regard, the present study was focused on synthesis of ceramic phases in the form of whiskers and particles in titanium based matrix to form advanced TMCs to aid in reducing material loss and prolong the service life. TMCs are alternative material to reduce the overall weight, fuel consumption and harmful emission of combustion products to the environment. Therefore, TMCs find applications in many engineering applications, most importantly in the automotive industry (Mathew *et al.*, 2009). In fact, degradation of materials by corrosion and tribocorrosion is encountered in various harsh technological applications including the automotive industry. In a motor vehicle, the damage in the brake disc is often caused by combination of wear and corrosion especially in humid conditions. As such, TMCs parts would offer both improved corrosion and lightweight properties compared with conventional gray cast iron or the unreinforced titanium based matrix (Blau *et al.*, 2007).

There is vast knowledge in mechanical properties evaluation of TMCs (Geng *et al.*, 2008; Li *et al.*, 2016; Rahoma *et al.*, 2015; Shufeng *et al.*, 2015) while little is known for their tribocorrosion response. Hence, contribution of corrosion and tribocorrosion knowledge in the TMCs research field is very important as it allows better understanding of the overall materials performance and its future potential uses. It was therefore decided to investigate the corrosion and tribocorrosion behaviour titanium reinforced with TiB and TiC phases. In this chapter, the effect of the SPS sintering conditions (i.e. set-point temperature, dwell time, pressure) and TMCs composition on the corrosion and tribocorrosion response of fully consolidated SPS TMCs was investigated. The experiments were carried out in saline conditions to simulate the road deicing conditions whereby salts are usually used as deicing agents. Firstly, the corrosion behaviour was analyzed using the open circuit potential technique to find the equilibrium potential at which the materials show the tendency to corrode. Then the potentiodynamic polarization behaviour was studied to determine to corrosion potential and corrosion current densities. The aforementioned techniques were then performed under applied load in rotating motion to determine the tribocorrosion behaviour, whereby the coefficient of friction was related to corrosion. The depths of the wear tracks were further analyzed by a profilometer to determine the severe surface damage.

5.1 TMCs for corrosion and tribocorrosion studies

In Chapter 4 we observed that TMCs sintered using 1.67μm B_4C particles at 1000 and 1100°C were fully consolidated (99%). These TMCs are of interest to corrosion/tribocorrosion related applications whereby porosity is not desired. Porosity may deteriorate mechanical properties of the materials and can reduce the corrosion resistance of the composites by accelerating corrosion rates. In terms of tribocorrosion, detachment of phases may occur in areas where porosity is concentrated and they may act as third-body abrasives causing severe damage on the surface of the material. Therefore, it was required that porosity is eliminated for the corrosion and tribocorrosion experiments. With the aid of TEM analysis in Chapter 4, we can say that the B_4C particles were completely reacted and the particles clusters were composed of Ti-B and Ti-C compounds in the TMCs of interest. Either further increase of dwell time to 30min or increase of temperature to 1100°C the clusters were completely removed, producing homogenously dispersed TiB and TiC reinforcing phases in Ti matrix. In this Chapter, the focus is on corrosion and tribocorrosion performance of TMCs entirely composed of TiB and TiC reinforcing phases.

The TMC samples for the experiments were sintered at 1000 and 1100°C, at pressure of 25-75MPa and 3-30min dwell time are shown in Figure 5.1 and 5.2 . Increasing dwell time and temperature had a significant effect on the reaction and growth of reinforcing phases. Particles clusters were observed at 1000°C for Ti2.5wt%B_4C and by increasing the temperature to 1100°C they were completely removed. For Ti5wt%B_4C with increased B_4C content, the amount of reinforcing phases and clusters was higher at both temperatures at shorter dwell time (3min) and increased pressure (75MPa). Complete removal of clusters with coarsening of TiB and TiC phases was observed at 30min for 1000°C, while for 1100°C the dwell time was shorten to 15min achieving complete homogeneity. In general, microstructure homogenization by removal of clusters was achieved with increasing dwell time and temperature in contrast to pressure increase.

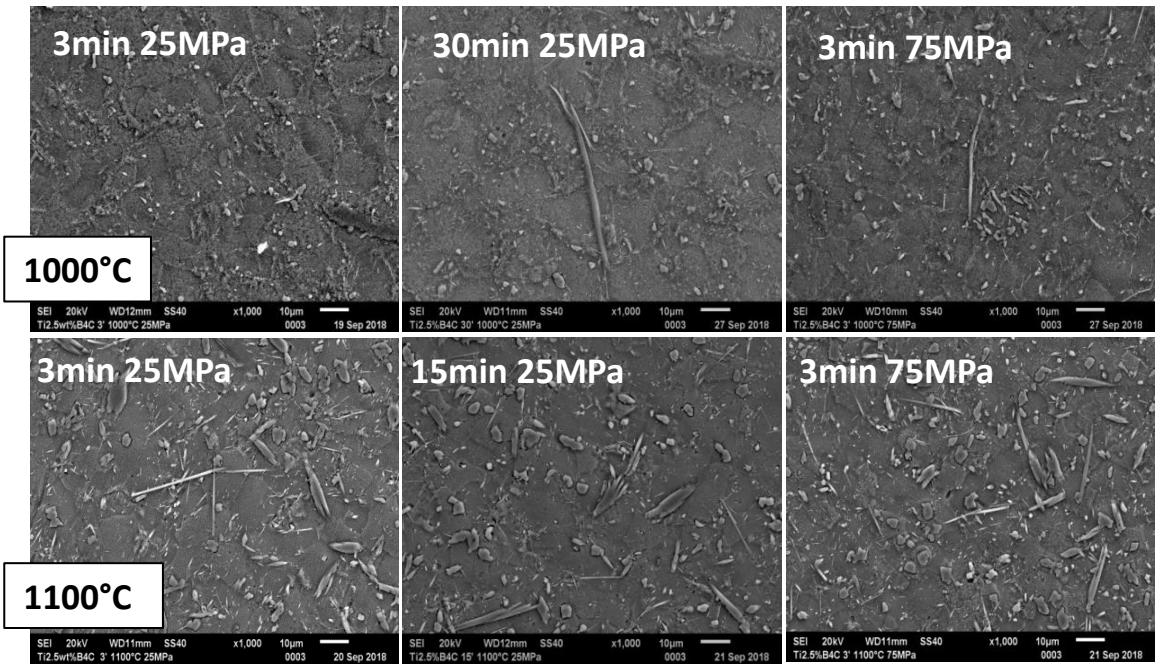

Figure 5.1. SEM micrographs of 20mm Ti2.5wt% B_4C(1.67 μm) TMCs

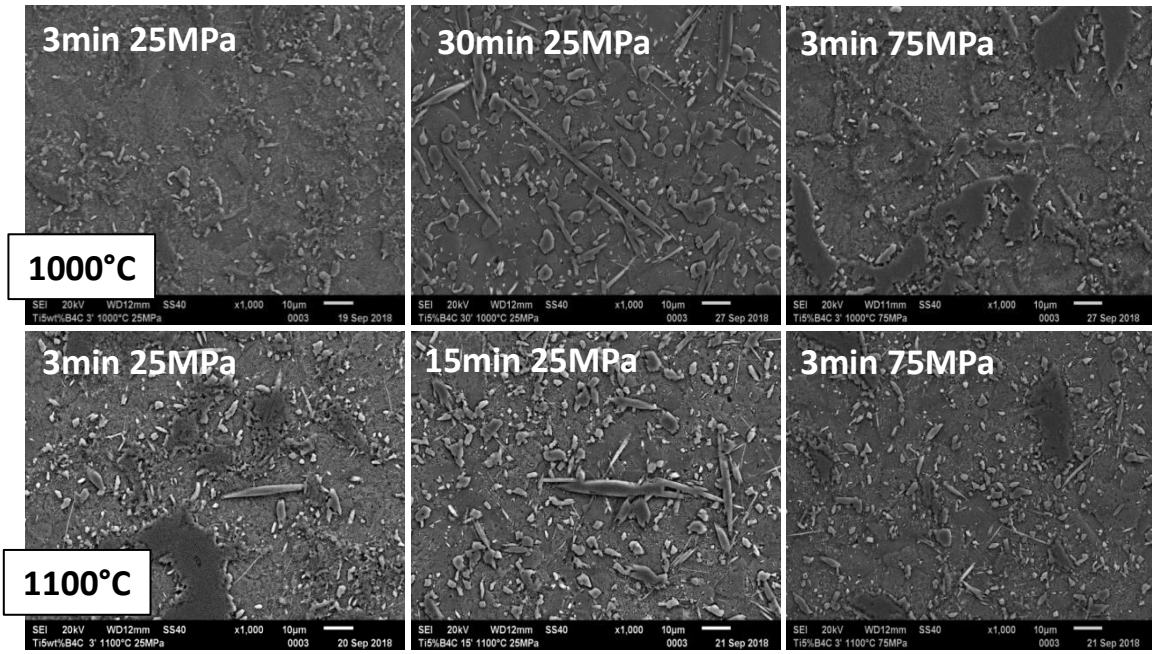

Figure 5.2. SEM micrographs of 20mm Ti5wt% B_4C(1.67 μm) TMCs

5.2 Open circuit potential in 3.5%NaCl for Ti and TMCs sintered at 1000°C and 1100°C

Open circuit potential (OCP) measurement under static conditions at room temperature was carried out for 2h to study the tendency of Ti and TMCs to corrode. Presented in Figure 5.3 and 5.4 is the OCP as a function of time performed in 3.5%NaCl solution for Ti and TMCs sintered at varying dwell time (3min to 30min) and pressure (25MPa to 75MPa) at sintering temperatures of 1000°C and 1100°C respectively. As observed in Figure 5.3 at 1000°C the OCP curves steadily increase with immersion time for the TMCs except for Ti sintered at 3min and 15min showing some fluctuations, which could be due to formation and damage of passive oxide film. The OCP curves positively shifted with addition of B_4C content, showing lower tendencies to corrosion than Ti except at 75MPa for Ti5wt%B_4C.

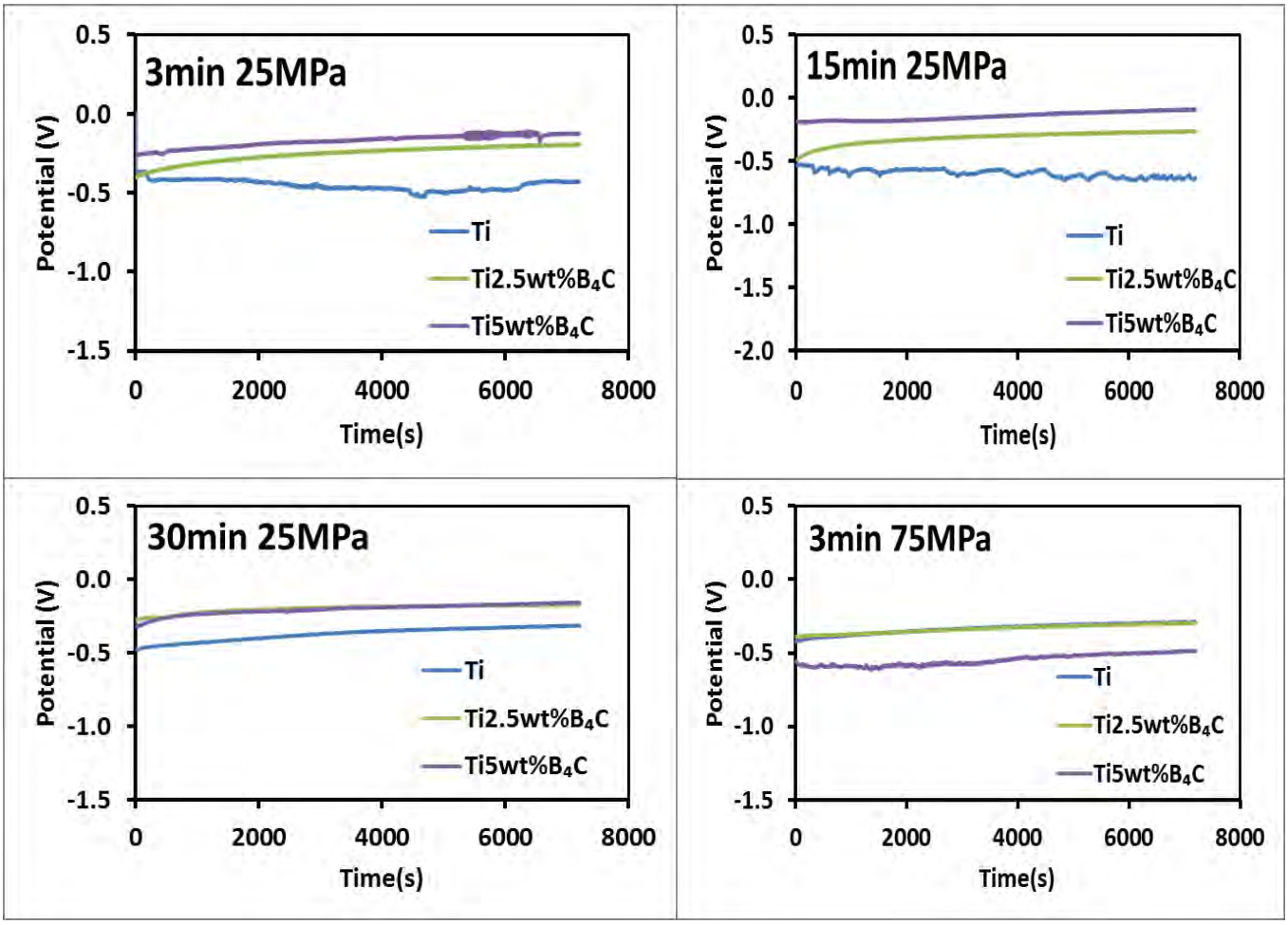

Figure 5.3. Open circuit potential of TMCs sintered at 1000°C with varying dwell times

In Figure 5.4 the OCP curves of Ti and TMCs at 1100°C steadily increases with time without fluctuations showing formation of a stable oxide film. Ti5wt%B_4C showed better

thermodynamic stability to corrosion compared with Ti and Ti2.5wt%B_4C. While at 3min and 30min dwell time Ti2.5wt%B_4C was more prone to corrosion, thus adding 2.5wt% of B_4C did not improve the thermodynamic stability of the material. The OCP values of Ti5wt%B_4C sintered at 1100°C were nobler compared with the one sintered at 1000°C. In summary, increasing amount of reinforcing phases and temperature lowered the susceptibility to corrosion.

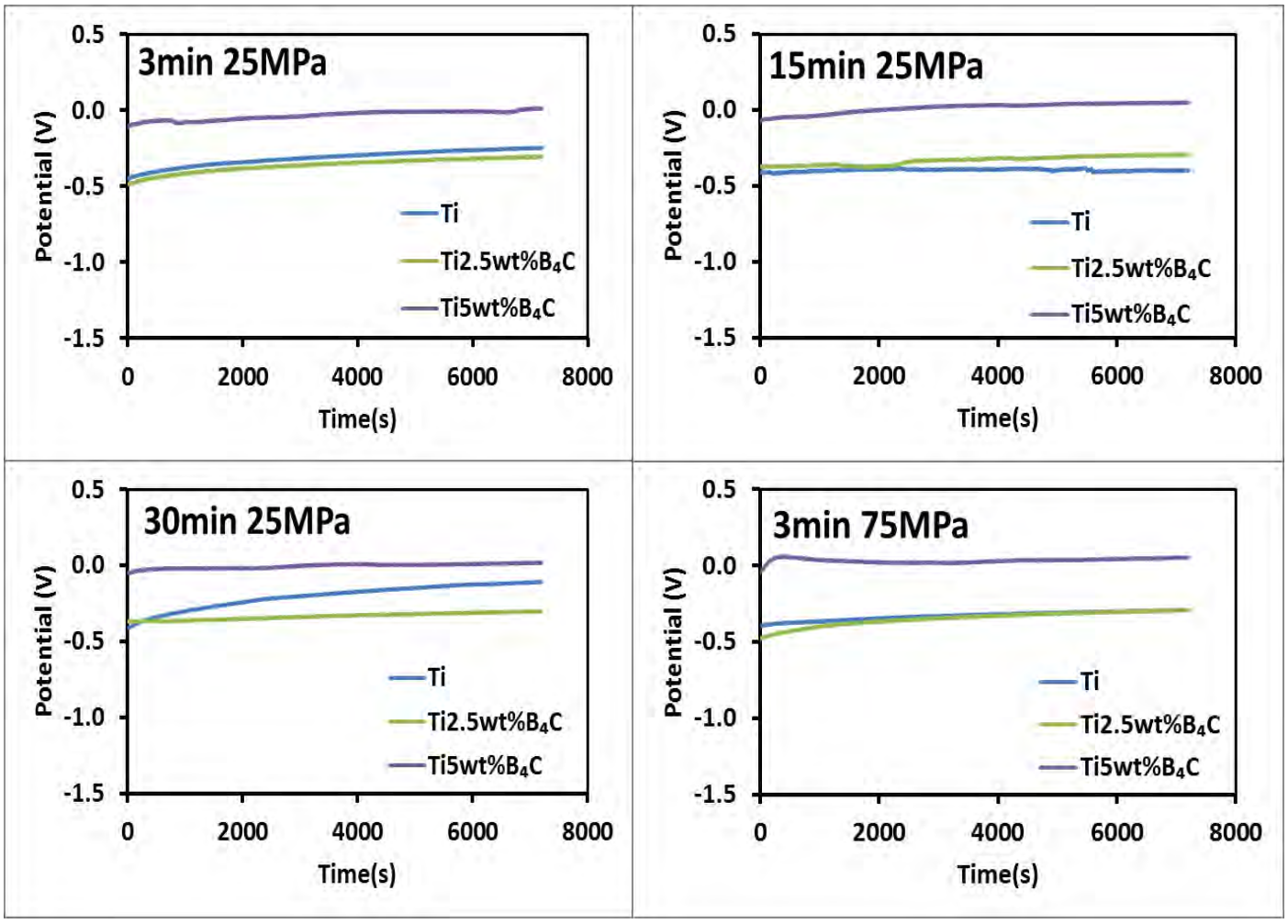

Figure 5.4. Open circuit potential of TMCs sintered at 1100°C with varying dwell times

The microstructure evolution with dwell time, pressure and temperature (Figure 4.30 and 4.31) showed particles clusters (Ti-B and Ti-C compounds) transforming into coarser TiB and TiC phases. In addition, quantification of the phases by RIR method (Chapter 4) showed TiB phase relatively higher than TiC phase at the respective increased sintering conditions and with increase of B_4C content(2-5wt%). Figure 5.5 presents the effect of microstructure variation on the OCP behaviour with increased dwell time and pressure at 1000°C and

1100°C. As observed the OCP values of the TMCs sintered at 1000°C were affected by the varying microstructures obtained with increased dwell time and pressure. In Figure 5.5(a) the OCP values of Ti2.5wt%B_4C sintered at 1000°C positively shifted from 3 to 30min dwell time. This showed that homogenization of microstructure from particles clusters (3min) to well dispersed TiB and TiC reinforcing phases (30min) improves the OCP values of the TMC. While the OCP values of Ti2.5wt%B_4C sintered for 15min were negatively shifted. This could be attributed to the combination of particles clusters with dispersed fine TiB and TiC phases in the microstructure. Similar to the increase of pressure from 25-75MPa, the microstructure was characterized with particles clusters but with coarser TiB and TiC phases this also caused the negative shift of OCP values. This could indicate that particles clusters are not desirable for this types of TMCs as the tendency to corrosion was enhanced by them.

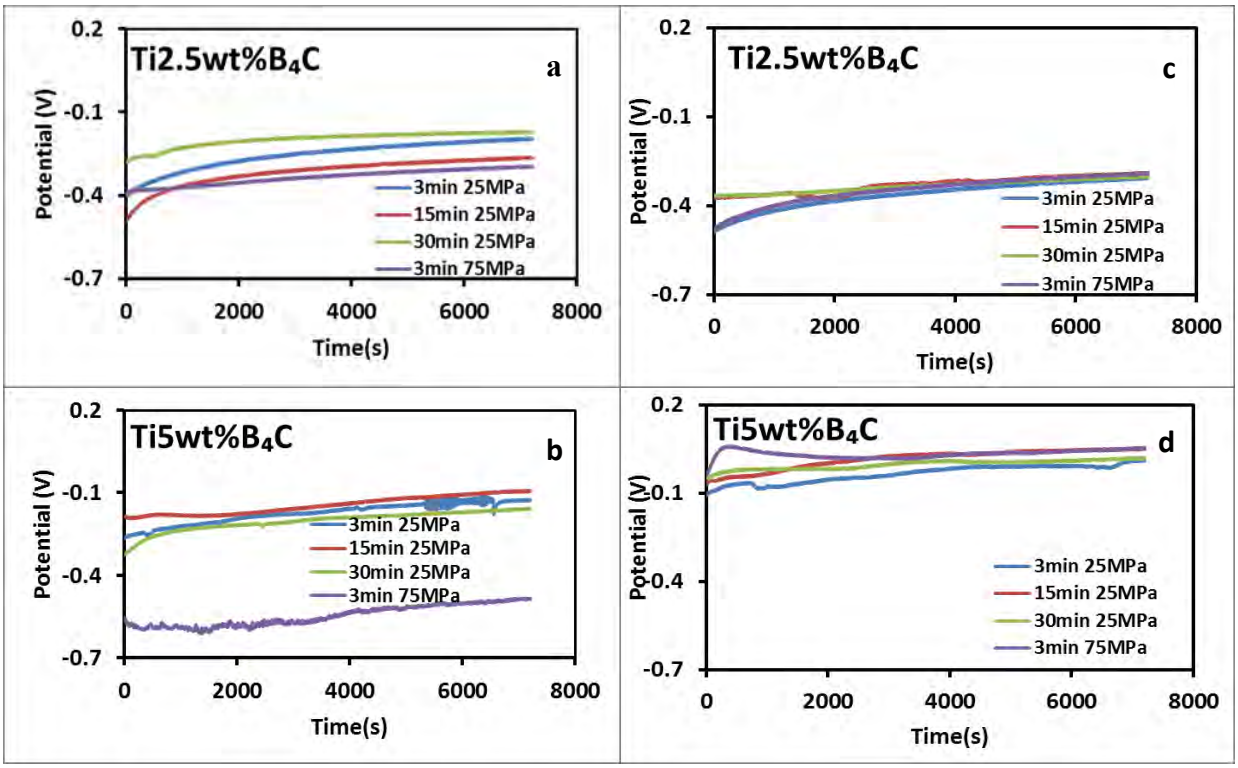

Figure 5.5. Microstructure variation effect at the different dwell times (3-30min) and Pressure (25-75MPa) on the OCP of TMCs sintered at (a & b) 1000°C and (c & d) 1100°C

Similar OCP values behaviour was observed for Ti5wt%B_4C sintered at 1100°C as shown in Figure 5.5(b). The only difference was the OCP values of TMC sintered at 15min were mostly positively shifted. A negative shift of the OCP values was observed when TiB and TiC phases were coarsened with increased dwell time of 30min. Similar to Ti2.5wt%B_4C pressure increase resulted in negative shift of OCP values. Temperature increase to 1100°C as

observed in Figure 5.5(c) for Ti2.5wt%B_4C, in the first 300s the OCP values followed a similar trend to those sintered at 1000°C. OCP values for 15 and 30min dwell time were mostly positively shifted, the microstructure here was characterized with homogenously dispersed TiB and TiC phases. With pressure increase to 75MPa there was insignificant difference with 25MPa, the OCP values were almost the same. Increasing the B_4C content to 5wt% in Figure 5.5(d) resulted in a positive shift of OCP values with increased dwell time and pressure. In quantification of the phases present in Ti5wt%B_4C, Ti_3B_4 phase (5.9wt%) was detected, it could have attributed to the positive shift of OCP values. In contrast to Ti5wt%B_4C sintered at 1000°C Ti_3B_4 phase was present in traces.

5.3 Potentiodynamic polarization in 3.5%NaCl for Ti and TMCs sintered at 1000°C and 1100°C

Potentiodynamic polarization curves of Ti and TMCs sintered at 1000°C, varying dwell times and pressure are presented in Figure 5.6. The polarization curves exhibited similar features, the current density of the cathodic branch decreased when applied potential increased up to the corrosion potential. This was due to hydrogen evolution and, or oxygen reduction on the electrode surface (Ahmad, 2006). Moreover, the anodic branches showed passivation regions at increasing dwell time (30min) and pressure (75MPa), especially Ti5wt%B_4C passivation was observed for all the studied sintering conditions. This indicates that Ti5wt%B_4C may have the highest corrosion protection compared with the other samples. Similar passivation behaviour was observed for Ti-B_4C composites characterized with partially reacted B_4C particles tested in NaCl solution (Toptan *et al.*, 2016). In contrast, active-passive behaviour without a transpassive region for Ti-TiC and Ti-TiB_2 composites until applied potential of 2V in HCl solution has been reported (Covino Jr *et al.*, 2002).

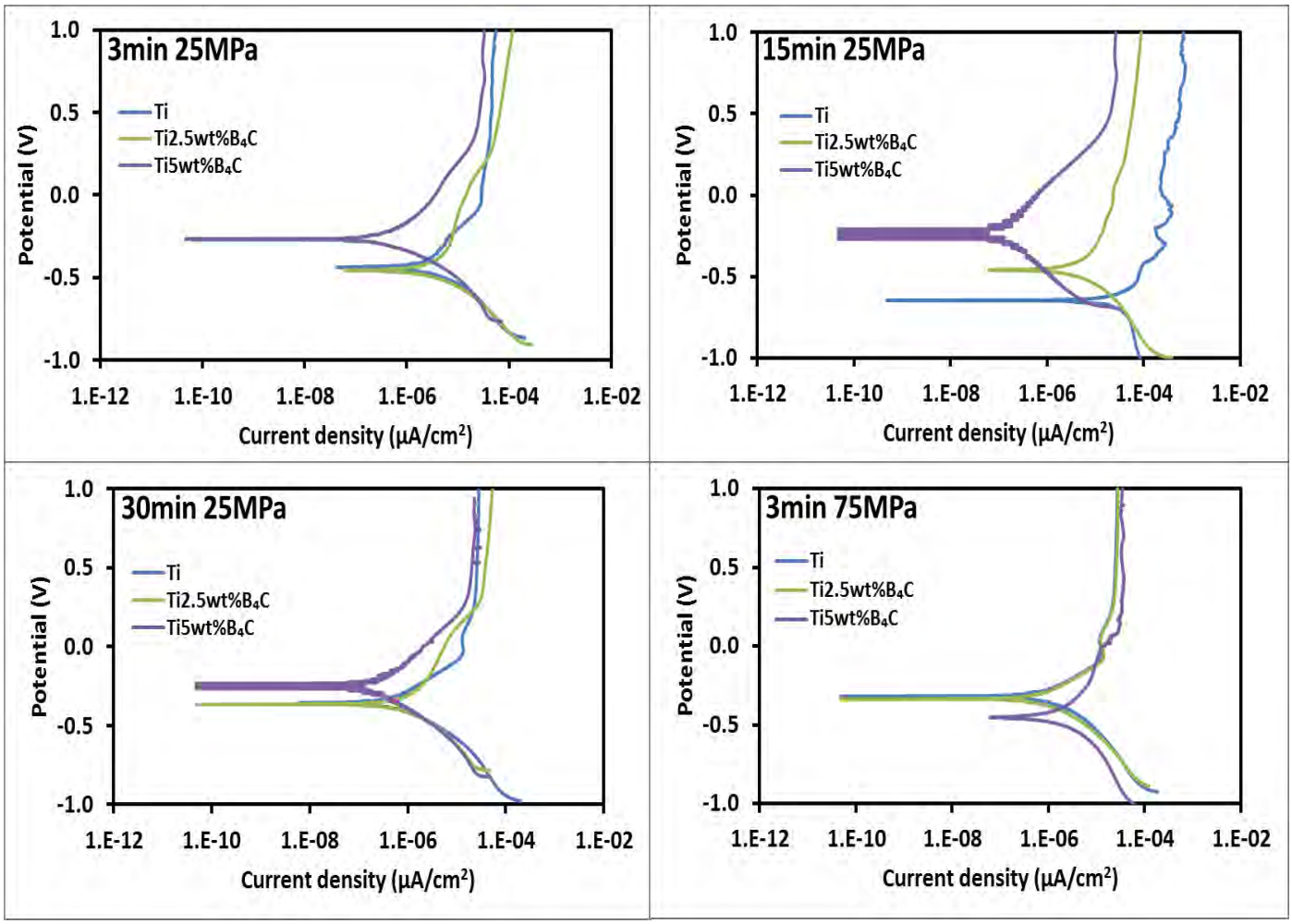

Figure 5.6. Potentiodynamic polarization curves of Ti and TMCs sintered at 1000°C in 3.5%NaCl

On evaluating the corrosion potential (E_{corr}) and corrosion current density (I_{corr}) values reported in Table 25, obtained from the polarization curves (Figure 5.6) using Tafel extrapolation method, there was no specific behaviour trend at the respective varying sintering conditions. The polarization behaviour at the respective dwell times and pressure showed insignificant difference in the E_{corr} values of Ti and Ti2.5wt%B_4C except at 15min. A positive E_{corr} shift was obtained for Ti5wt%B_4C at the respective dwell times, this could be due to the reduced exposed metallic surface area of Ti by the ceramic reinforcing phases (Toptan *et al.*, 2016). Similar results were reported for Ti6Al4V-B_4C (Prakash *et al.*, 2016), addition of ceramic particles may shift the Ecorr value to more noble values. This effect increases the corrosion resistance by the inert physical barrier role of the particles (Han *et al.*, 2015).

The I_{corr} values at 15min (see table 25) were higher for Ti and Ti2.5wt%B_4C, while Ti5wt%B_4C exhibited the lowest I_{corr} values. Further increase of dwell time to 30min the I_{corr}

values were lowered for Ti and Ti2.5wt%B_4C, a slight increase was observed for Ti5wt%B_4C. Increasing pressure to 75MPa resulted in positive E_{corr} shift for Ti and Ti2.5wt%B_4C. Meanwhile, negative E_{corr} shift was observed for Ti5wt%B_4C with the highest I_{corr} value.

Table 26. Corrosion potential (E_{corr}) and corrosion current density (I_{corr}) of Ti and TMCs sintered 1000°C under static conditions

	E_{corr}(V)			
Sample	**3min & 25MPa**	**15min & 25MPa**	**30min & 25MPa**	**3min & 75MPa**
Ti	-0.45	-0.62	-0.36	-0.32
Ti2.5wt%B_4C	-0.46	-0.45	-0.37	-0.34
Ti5wt%B_4C	-0.26	-0.23	-0.24	-0.47
	I_{corr} (A/cm^2) x 10^{-6}			
Sample	**3min & 25MPa**	**15min & 25MPa**	**30min & 25MPa**	**3min & 75MPa**
Ti	4.11	34.06	0.58	0.92
Ti2.5wt%B_4C	3.90	5.82	1.07	1.19
Ti5wt%B_4C	0.45	0.17	0.36	2.94

The effect of TMCs microstructure evolution with dwell time and pressure on the E_{corr} and I_{corr} values it was evident and similar to the OCP values behaviour at 1000°C (Figure 5.5). For Ti2.5wt%B_4C in Table 25 the decreasing E_{corr} values with dwell time showed that formation of homogenized TiB and TiC phases yield a positive E_{corr} shift. This behaviour was in agreement with I_{corr} values which were lowest for 30min dwell time. This showed the improved resistance to corrosion at 30min in contrast to 3 and 15min dwell times. Similar behaviour was observed for Ti5wt%B_4C, the microstructure with particles clusters at 3min exhibited a more negative E_{corr} value and it became positive when TiB and TiC phases were homogenously formed. However, when the phases were coarsened at 30min the E_{corr} value became more negative, showing the lowered corrosion resistance. In agreement, the lowest I_{corr} value was obtained for 15min TMC with finer TiB and TiC phases. On the pressure increase effect for Ti2.5wt%B_4C, an opposite behaviour to OCP values was observed on the E_{ocrr} values which became more positive with reduced I_{corr} value. However, Ti5wt%B_4C still showed a similar trend with the OCP values and pressure increase. The E_{corr} value became more negative with increased I_{corr} values showing reduced corrosion resistance. In summary, addition of reinforcing phases to Ti yielded improved corrosion resistance at 1000°C for Ti5wt%B_4C sintered at 15min.

Presented in Figure 5.7 is the polarization curves of Ti and TMCs sintered at 1100°C, varying dwell times and pressure. Similar to 1000°C, the polarization passivation behaviour was

observed at 1100°C for all the samples. Moreover, on the corrosion values presented in Table 26, E_{corr} values of Ti and Ti2.5wt%B_4C were almost in same range with only I_{corr} values variation at 3min and 30min dwell time. At 15min, dwell time highest I_{corr} values of 2.09 x 10^{-6} A/cm^2 and 1.16 x 10^{-6} A/cm^2 were obtained for Ti and Ti2.5wt%B_4C respectively. Similar to 1000°C, Ti5wt%B_4C sintered at 15min dwell time generally showed higher corrosion resistance. The relationship between the varying microstructures and the E_{corr} and I_{corr} values with the different sintering conditions was also similar to those previously discussed in Table 25. In addition, the presence Ti_3B_4 phase in Ti5wt%B_4C at 75MPa resulted in reduced I_{corr} value and positive OCP value.

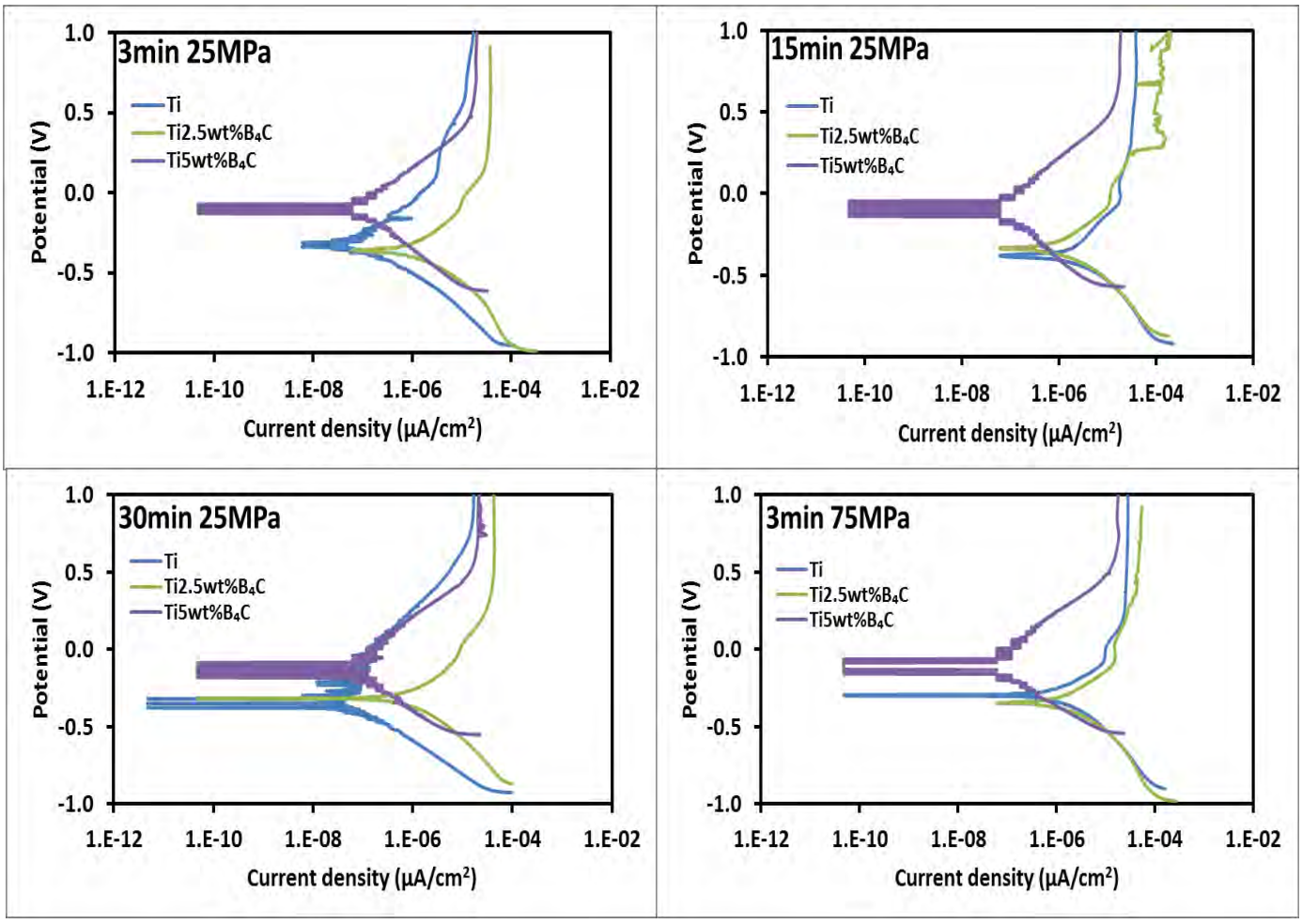

Figure 5.7. Potentiodynamic polarization curves of Ti and TMCs sintered at 1100°C in 3.5%NaCl

Table 27 . Corrosion potential (E_{corr}) and corrosion current density (I_{corr}) of Ti and TMCs sintered 1100°C under static conditions

	E_{corr}(V)			
Sample	**3min & 25MPa**	**15min & 25MPa**	**30min & 25MPa**	**3min & 75MPa**
Ti	-0.32	-0.38	-0.34	-0.30
Ti2.5wt%B_4C	-0.36	-0.34	-0.32	-0.35
Ti5wt%B_4C	-0.08	-0.08	-0.17	-0.09
	I_{corr} (A/cm^2) x 10^{-6}			
Sample	**3min & 25MPa**	**15min & 25MPa**	**30min & 25MPa**	**3min & 75MPa**
Ti	0.01	2.09	0.003	1.02
Ti2.5wt%B_4C	1.12	1.16	1.04	1.56
Ti5wt%B_4C	0.10	0.01	0.10	0.01

In general, sintering at 1100°C improves corrosion resistance of Ti and TMCs than 1000°C, which is in good agreement with the OCP values obtained as presented in Figure 5.4. This was attributed to increased reinforcing phases content, reduced particles clusters and finer TiB and TiC phases resulting in positive OCP and E_{corr} and reduced I_{corr} values. In addition, although the reinforcing phases content increase with dwell time as determined by semi-quantitative analysis, the E_{corr} and I_{corr} values remain insignificantly affected. In the present study the E_{corr} values of Ti - (TiB + TiC) composites were in the range of -0.47V to -0.23V and -0.38V to -0.08V sintered respectively at 1000°C and 1100°C. In comparison to literature for corrosion tests in NaCl based solutions, Toptan *et al.* (2016) reported E_{corr} value of -0.297V for hot pressed Ti-B_4C composites at 1100°C with partially reacted B_4C particles. Other researchers shown in Table 27 have reported E_{corr} values in the range of -0.42V to -0.4V and -0.18 to 0.05V for TiB_2 and TiC single phases fabricated by different methods (Alkhateeb *et al.*, 2011; Coving Jr *et al.*, 1975; Monticelli *et al.*, 2001; Onuoha *et al.*, 2017; Shvets *et al.*, 2016; Verkhoturov *et al.*, 1988). So, depending on the different processing conditions the values of E_{corr} and OCP may vary.

Table 28. Corrosion properties TiB_2 and TiC in NaCl solution in literature

Phase **Process** **Reference**	**Corrosion Conditions**	**RD (%)**	**OCP (V)**	**E_{corr} (V)**	**References**
SPS					
1000°C	3.5wt% NaCl				**Present study**
Ti2.5wt%B_4C		99%	-0.3 to -0.17V	-0.46 to -0.34	
Ti5wt%B_4C		99%	-0.485 to -0.034V	-0.47 to -0.23	
1100°C					
Ti2.5wt%B_4C		99%	-0.307 to -0.29V	-0.36 to -0.32	
Ti5wt%B_4C		99%	0.02 to 0.11V	-0.17 to -0.08	
HP **1100°C** Ti24vol%B_4C	9g/L NaCl	-	-	-0.297	Toptan *et al.* (2016)
Cold compacting and sintering **TiB_2**	Synthetic sea water	66	-	-0.420	(Verkhoturov *et al.*, 1988)
Press and sintered **TiB_2 sinter**	Substitute sea water	-	-	± -0.4	(Coving Jr *et al.*, 1975)
Hot pressing **TiB_2**	3.5wt% NaCl	97		± -0.4	(Monticelli *et al.*, 2001)
TiB_2 Chemical Vapour Deposition	0.5M NaCl	-	@ 0h: -0.457 @ 6h: -0.409	± -0.4	(Alkhateeb *et al.*, 2011)
TiC SPS	3.5wt%NaCl	98	-0.209± 0.035	-0.173 ± 0.094	(Onuoha *et al.*, 2017)
$TiC_{1.0}$ sinter Hot pressing	3wt%NaCl	-	-	0.050	(Shvets *et al.*, 2016)
TiC Cold compacting and sintering	Synthetic sea water	87 55	- -	-0.180 -0.160	(Verkhoturov *et al.*, 1988)

5.4 Open circuit potential under sliding conditions in 3.5%NaCl for Ti and TMCs sintered at 1000°C and 1100°C

This section presents OCP measurements performed to evaluate the tendency of Ti and TMCs to corrode under tribocorrosion conditions. The influence of applied load on the stability of OCP values with relation to induced friction in sliding, the effect of SPS parameters and reinforcing phase's addition to Ti were investigated. The OCP evolution was studied in three sections, the first 1800s presents OCP values without applied load, and secondly the 2N load was applied for 3600s with expected potential drop and lastly the load was removed for 1800s and the OCP values may or not recover. The OCP behaviour of samples sintered at 1000°C at 3min to 30min with pressure ranging from 25 to 75MPa is presented in Figure 5.8.

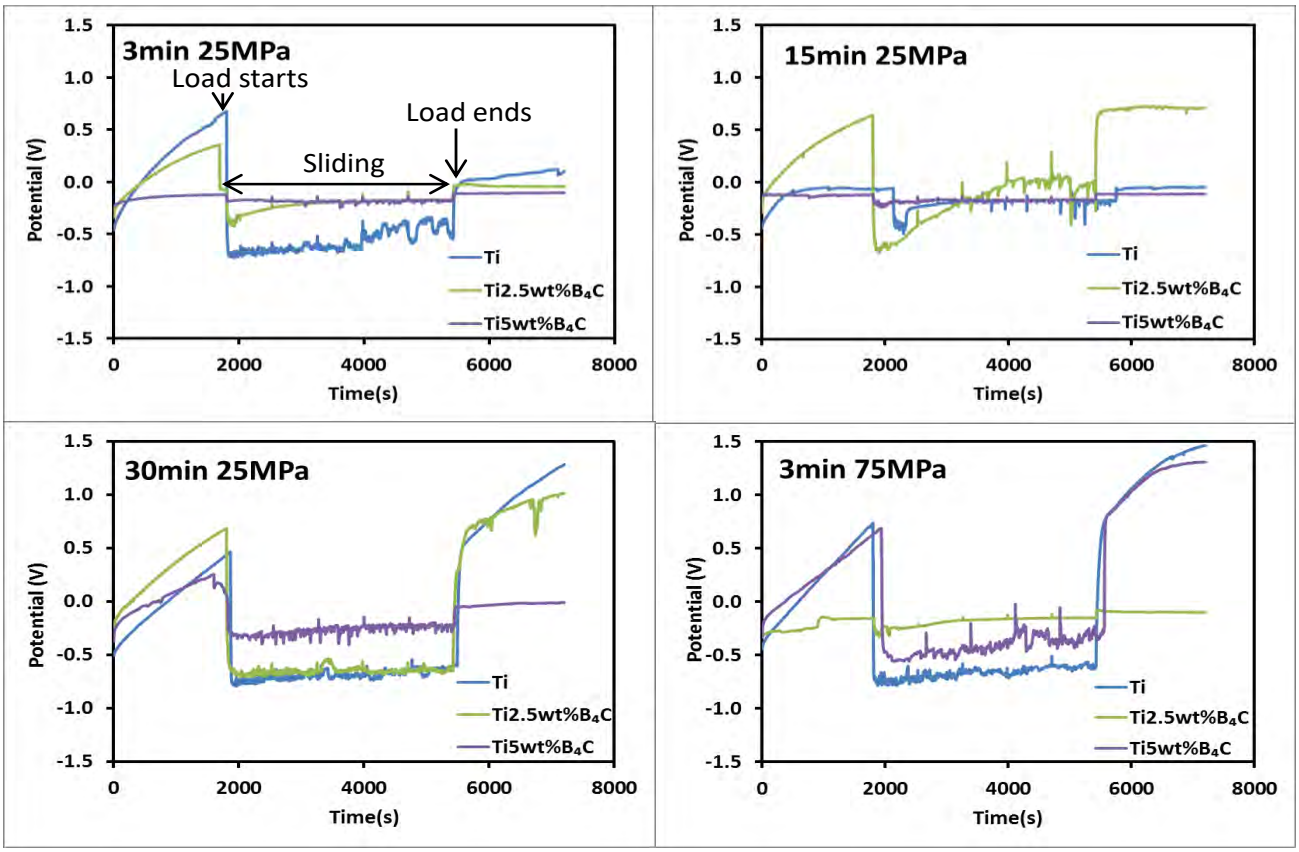

Figure 5.8. Open circuit potential under sliding of Ti and TMCs sintered at 1000°C with varying dwell time

In Figure 5.8 at 1000°C, it was observed that when the load was applied the samples had different potential drops. At 3min 25MPa the largest potential drop being that of Ti with 0.67V to -0.69V, followed by Ti2.5wt%B_4C with 0.35V to -0.36V and smallest drop was obtained for Ti5wt%B_4C with -0.12V to -0.19V. This could clearly indicate that OCP values of Ti5wt%B_4C were slightly affected when load was applied, showing good load carrying ability by the harder reinforcing phases preventing material removal. The potential drop is an indication of electrochemical activity, which is associated with the removal of passive film at the tribological contact area exposing the bare material to the solution and also detachment of materials debris (Mischler *et al.*, 2014). Galvanic coupling is then generated between the unworn (passive) and worn (de-passivated) surface and may result in negative potential shift (López-Ortega *et al.*, 2018).

Under sliding conditions in rotating motion the OCP values of Ti5wt%B_4C were the highest from the beginning of applied load. The OCP values of Ti2.5wt%B_4C after applied load gradually increased reaching those of Ti5wt%B_4C. While the OCP values of Ti were lowest

and showed a gradual increase with some fluctuations. These fluctuations are associated with breakage of passive layer (depassivation) and the re-growth (repassivation) on the worn area (López-Ortega *et al.*, 2018). As the load ends for 3min 25MPa, the OCP values of Ti5wt%B_4C increased reaching values close to pre-sliding figures, however of Ti and Ti2.5wt%B_4C did not recover. This could also indicate good tribocorrosion response of Ti5wt%B_4C compared with Ti and Ti2.5wt%B_4C. The potential increase when the load end was due to formation of passive layer on the depassivated area, known as repassivation. This indicates a restoration process of the potential and it gives information material ability to recover after sliding (López-Ortega *et al.*, 2018).

The dwell time was increased to 15min despite the different potential drops. The data indicate that all the samples potential were restored after sliding. At 30min dwell time under sliding conditions potential drop of Ti5wt%B_4C was high from 0.26V to -0.32V after load was removed the OCP values did not recover in comparison to 3min dwell time. However, the OCP values for Ti5wt%B_4C still remain the highest compared to the rest of samples under sliding conditions. With increase of pressure to 75MPa the potential drop of Ti5wt%B_4C was increased from 0.68V to -0.47V compared to the effect of dwell time. Ti2.5wt%B_4C had the smallest potential drop and highest OCP values under sliding and the OCP values of all the samples recovered when the load ended. Although there was no specific trend with increasing the B_4C content, the results indicate that reinforcing phases significantly improve the tribocorrosion properties of Ti at the respective dwell time and pressure.

Similar OCP trends were observed at 1100°C as shown in Figure 5.9, however the difference was the reduced potential drops after the load was initiated. As observed at 3min for Ti5wt%B_4C the OCP values sharply decreased and quickly increased after load was initiated showing repassivation by the oxide film. In general, increasing the temperature to 1100°C lead to a good OCP restoration at the respective dwell times and pressure for all the samples in contrast to 1000°C. Moreover, Ti5wt%B_4C still exhibits best tribocorrosion properties as the OCP were positively shifted. It seems that when Ti5wt%B_4C was homogenized to coarser TiB and TiC reinforcing phases at 30min the potential drop was increased, similar behaviour was observed at 1000°C. While the potential drops of Ti2.5wt%B_4C which was characterized with homogenized TiB and TiC reinforcing phases at the respective dwell time and pressure were comparably the same.

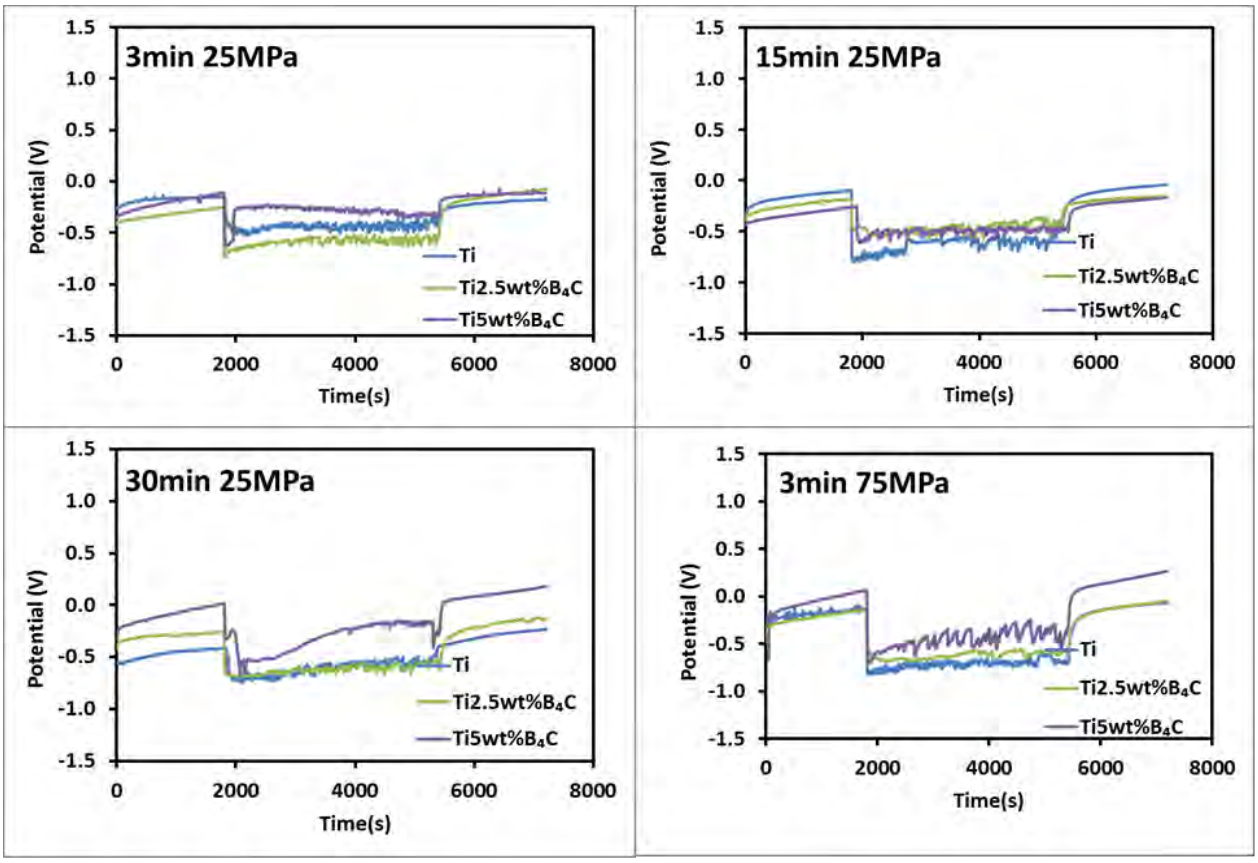

Figure 5.9. Open circuit potential under sliding of Ti and TMCs sintered at 1100°C with varying dwell times

The relationship between the microstructure variation and OCP under tribocorrosion conditions is shown in Figure 5.10. The particles clusters present in Ti2.5wt%B_4C sintered at 3min 25MPa raised the OCP values at the start of sliding at 1000°C as shown in Figure 5.10(a). While particles clusters combined with TiB and TiC phases obtained at 15min resulted in decreased OCP values, which later during sliding increased gradually exceeding those at 3min. Further homogenization to TiB and TiC phases at 30min led to a negative shift of the OCP values. Particles clusters with coarsened TiB and TiC phases obtained at 75MPa did not affect the 25MPa OCP values. This could indicate that the compact particles clusters are able to carry the load in contrast the evenly distributed TiB and TiC phases in lower quantities.

Further increase of B_4C content to 5wt% in Figure 5.10(b) resulted in almost insignificant difference of OCP values under sliding. The three varying microstructures obtained from 3-30min OCP values were in the same range, with a slight decrease at 30min at the start of sliding. The 3min and 15min OCP behaviour was the same, suggesting that the higher volume

fraction of particles clusters and, TiB and TiC phases were able to carry the load imparted. Addition of short fiber (TiB) and hard ceramic particle (TiC) reinforcements (Choi *et al.*, 2013) into titanium matrix significantly improved the wear resistance by direct strengthening effect taking place due to the ability of the reinforcing phases to carry the load (Blau et al, 2017 and Prakash et al, 2016). Also by indirect strengthening taking place by alterations on the Ti matrix structure, such as induced dislocations, Orowan strengthening, grain size refinement and modification of the matrix microstructure as a consequence of the addition of the reinforcing phase (chawla et al, 2006). However, at 75MPa the higher volume fraction of particles clusters with coarsened TiB and TiC phases resulted was undesirable as a negative shift of OCP values was observed. Nevertheless, the influence of the varying microstructures on the OCP values behaviour under sliding conditions co-relates with the OCP values without sliding (*see* Figure 5.9).

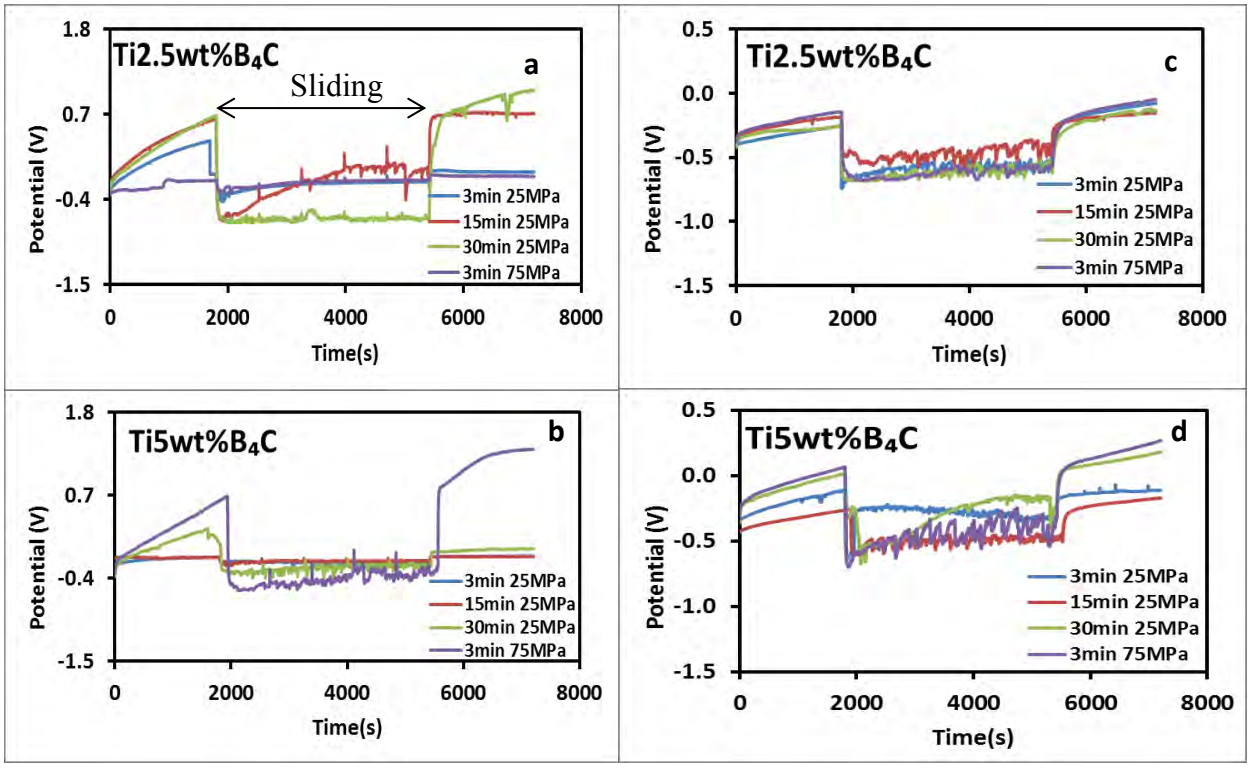

Figure 5.10. Microstructure variation effect at the different dwell times (3-30min) and Pressure (25-75MPa) on the OCP under sliding of TMCs sintered at (a & b) 1000°C and (c & d) 1100°C

Increasing temperature to 1100°C the Ti2.5wt%B_4C clusters transformed into homogeneous TiB and TiC phases at all sintering conditions. In Figure 5.10(C) The 15min TMC OCP

values indicated superior resistance to tribocorrosion in comparison to other sintering conditions. This behaviour is similar to OCP values measured without load (see Figure 5.9). While Ti5w%B_4C characterized with particles clusters (3min 25MPa) showed superior OCP values in the beginning of sliding, the values gradually decreased with time as shown in Figure 5.10(d). The TiB whiskers within clusters have been reported to have lower load bearing efficiency in comparison with the uniformly distributed ones (Tabrizi *et al.*, 2015).

The TMC at 30min with coarser TiB and TiC phases OCP values gradually increased with time exceeding those at 3min (clusters) at the end of sliding. It seems that the coarser TiB and TiC phases (30min) carry the imparted load best than the finer phases (15min). Opposite behaviour was observed under OCP without load the finer phases showed more positive OCP values than the coarser ones. Ti5w%B_4C obtained at 75MPa OCP values were relatively the lowest, the microstructure was characterized with particles clusters combined with coarser TiB, TiC phases and Ti_3B_4 phase.

Figure 5.11 presents the friction coefficient (COF) measured during sliding after 1800s of OCP measurements for samples sintered at 15min dwell time at 1000°C and 1100°C. As observed, generally the COF values for all samples gradually increases as sliding progress under OCP. The COF values of Ti and Ti2.5wt%B_4C at 1000°C were higher than Ti5tw%B_4C. The higher COF values in Ti2.5wt%B_4C could be attributed to pulling out of TiB and TiC clusters due to stresses created in Ti matrix as sliding continues. In turn, the clusters acted as third body abrasive medium inducing higher wear in the larger surface area of Ti thus the higher COF values were reached. The lower COF values obtained for Ti in the beginning of the load in comparison to Ti2.5wt%B_4C could be due to the absence of third body abrasives suggesting that only the counter ball was doing the wear.

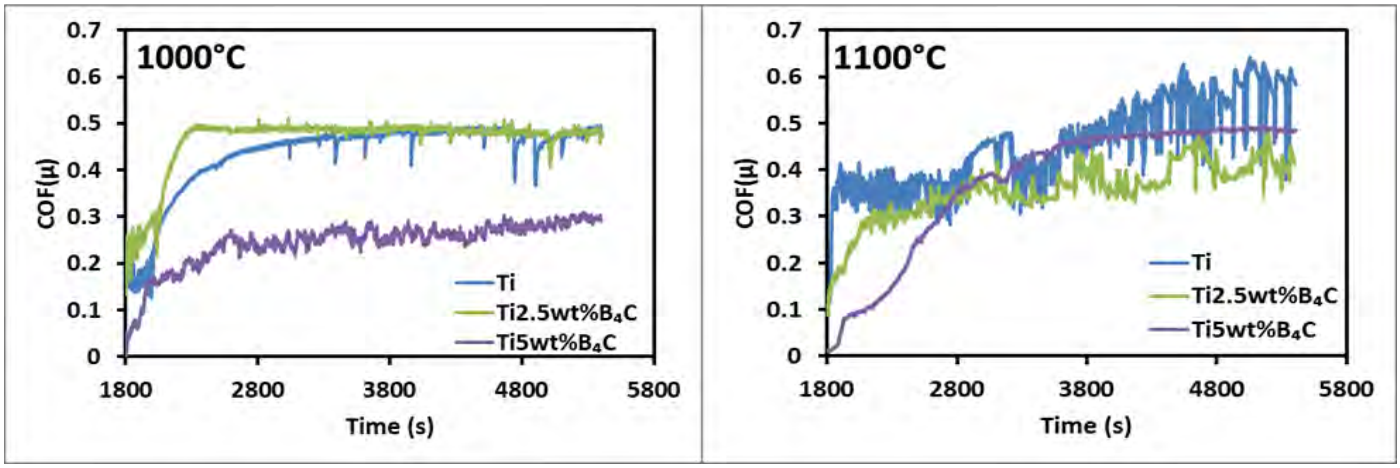

Figure 5.11. Coefficient of friction during OCP as function of time for Ti, Ti2.5wt%B_4C and Ti5wt%B_4C sintered at dwell time of 15min at 1000°C and 1100°C

At 1100°C Ti5wt%B_4C exhibited lower COF values at the the start of sliding and gradually increased but remained lowest in contrast to Ti and Ti2.5wt%B_4C which is an indication of improved wear resistance. This behavior could be attributed to the reduced surface area of Ti matrix by the high amount of compact TiB and TiC clusters that help carry load in Ti5wt%B_4C in contrast to Ti2.5wt%B_4C. Moreover, as the load starts the counter material was in contact with the reinforcing phases hence lower COF values. At 1100°C Ti5wt%B_4C the COF values at the beginning were still lower however they gradually increased exceeding those of Ti2.5wt%B_4C.

5.5. Potentiodynamic polarization behaviour under sliding in 3.5%NaCl for Ti and TMCs sintered at 1000°C and 1100°C

Presented in Figure 5.12 are the polarization curves under sliding in 3.5%NaCl for Ti and TMCs sintered at 1000°C. The E_{corr} and I_{corr} values are shown in Table 28. At 3min dwell time it is evident that increasing the amount of reinforcing phases results in positive E_{corr} shift. The polarization behaviour of Ti showed passivation except at 15min. However, that of Ti2.5wt%B_4C and Ti5wt%B_4C did not show passivation compared with polarization curves without sliding load. The presence of the reinforcing phases may have resulted in weaker protective oxide layer with discontinuities exposing the material to the chloride ions. Under sliding conditions whereby greater material surface alteration was caused by mechanical and electrochemical mechanisms, this weaker oxide layer could not be easily restored (Han *et al.*, 2015).

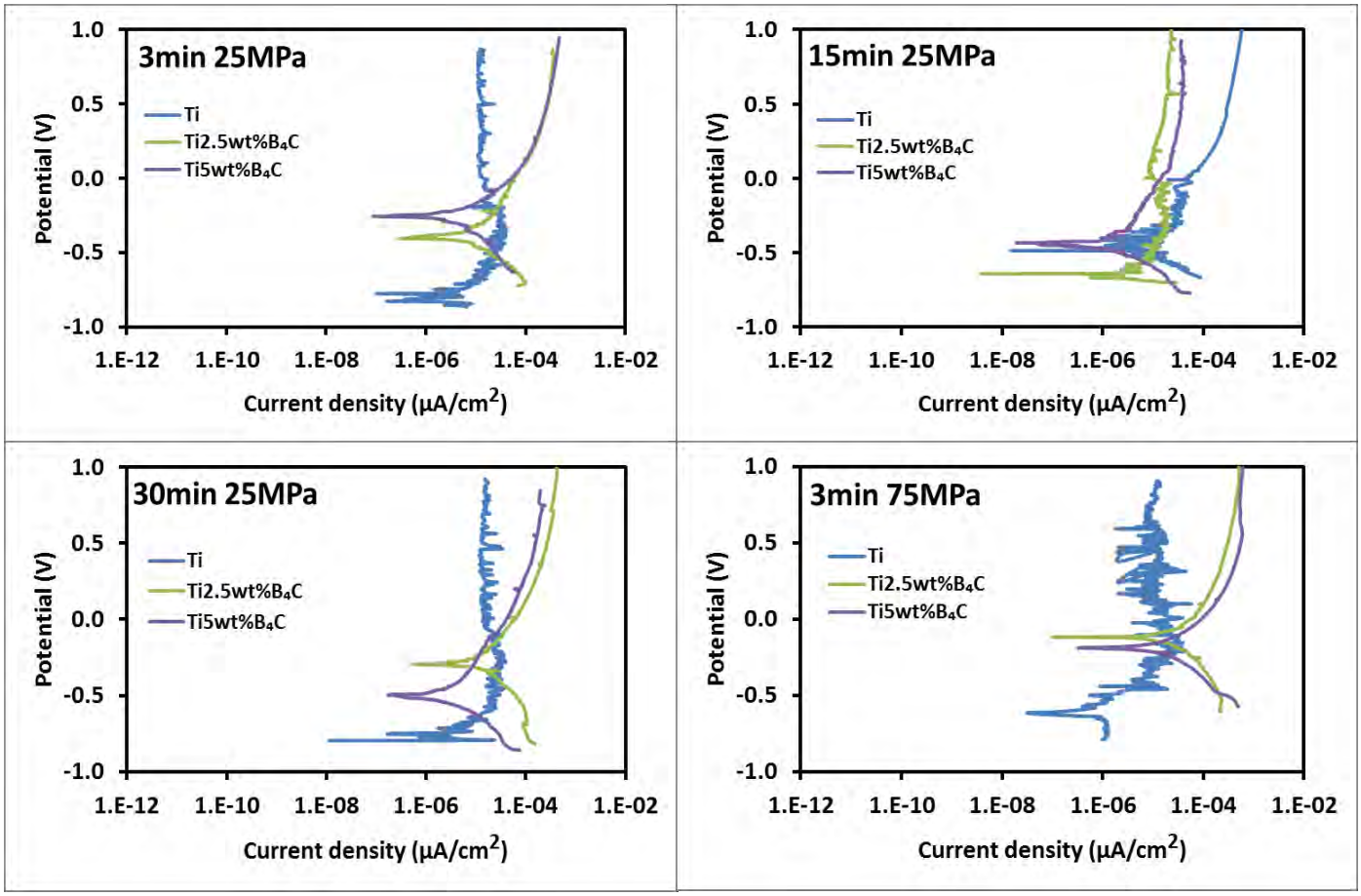

Figure 5.12. Potentiodynamic polarization curves under sliding for Ti and TMCs sintered at 1000°C in 3.5%NaCl

There was no particular order of the E_{corr} values with increasing dwell time from 3min to 30min, but for Ti5wt%B_4C the E_{corr} values became more negative from -0.25V to -0.49V as illustrated in Table 28. The I_{corr} values for Ti5wt%B_4C were much lower reaching 1.41 x 10^{-6} A/cm^2 at 15min then rapidly increased to 4.64 x 10^{-6} A/cm^2 at 30min. Highest I_{corr} values were observed in Ti2.5wt%B_4C with 25.71 x 10^{-6} A/cm^2. This could suggest that when the microstructure was homogenized with increasing dwell time (3min to 30min) from particles clusters to form coarser TiB and TiC in high contents, the I_{corr} values were negatively affected or the TMCs exhibited poor tribocorrosion resistance in contrast to 15min TMCs with finer TiB and TiC.

Table 29. Corrosion potential (E_{corr}) and corrosion current density (I_{corr}) of Ti and TMCs sintered 1000°C under sliding conditions

	E_{corr}(V)			
Sample	**3min & 25MPa**	**15min & 25MPa**	**30min & 25MPa**	**3min & 75MPa**
Ti	-0.79	-0.47	-0.72	-0.59
Ti2.5wt%B_4C	-0.38	-0.63	-0.29	-0.11
Ti5wt%B_4C	-0.25	-0.42	-0.49	-0.19
	I_{corr} (A/cm^2) x 10^{-6}			
Sample	**3min & 25MPa**	**15min & 25MPa**	**30min & 25MPa**	**3min & 75MPa**
Ti	8.25	15.17	7.39	0.68
Ti2.5wt%B_4C	10.20	5.49	25.71	37.13
Ti5wt%B_4C	3.29	1.41	4.64	8.17

These E_{corr} values are consistent with the OCP measurements at 30min (see Figure 5.9) showing large potential drop as load initiates without restoration when the load was removed. Also the OCP values were negatively shifted under applied load when the dwell time was increased to 30min showing higher tendencies to corrosion under sliding in contrast to 15min. When the pressure was increased to 75MPa although the E_{corr} values became more positive, the I_{corr} values were increased to 37.13 x 10^{-6} A/cm^2 and 8.17 x 10^{-6} A/cm^2 for Ti2.5wt%B_4C and Ti5wt%B_4C respectively. So at 1000°C, the TMCs exhibited good tribocorrosion resistance at 15min dwell time and performed very poor at 30min and 75MPa.

Presented in Figure 5.13 are the polarisation curves in tribocorrosion conditions for Ti and TMCs sintered at 1100°C in 3.5%NaCl, the E_{corr} and I_{corr} values are presented in Table 22. Generally similar to 1000°C the E_{corr} values of TMCs were also positively shifted at 1100°C. Polarisation behaviour of Ti at 3min showed unstable passivation region while only at 15min it was stable. Similar to 1000°C, the polarisation behaviour at 1100°C of the TMCs did not show any passivation region in contrast to polarisation behaviour without load (Figure 5.7). However, a diffferent behaviour of E_{corr} values with increasing dwell time was observed compared with 1000°C which showed no particular order. In Table 29 The E_{corr} values of Ti (-0.61V to -0.74V) became more negative with increasing dwell time from 3min to 30min. That of Ti2.5wt%B_4C (-0.52V to -0.47V) and Ti5wt%B_4C(-0.39V to -0.29V) became more positive. This could indicate that Ti will preferentially start to corrode first compared with Ti2.5wt%B_4C and Ti5wt%B_4C.

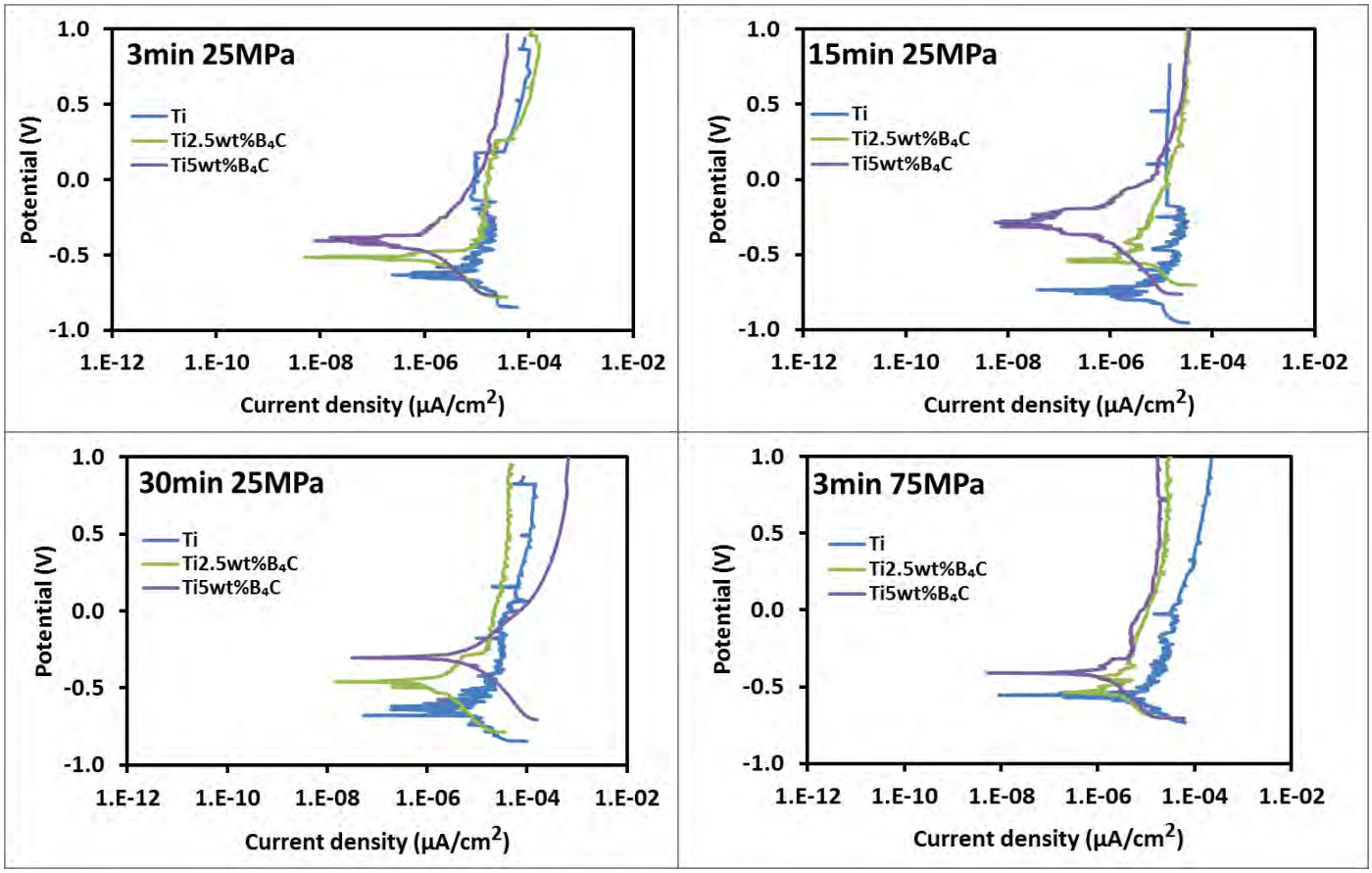

Figure 5.13. Potentiodynamic polarization curves under sliding for Ti and TMCs sintered at 1100°C in 3.5%NaCl

Table 30. Corrosion potential (E_{corr}) and corrosion current density (I_{corr}) of Ti and TMCs sintered 1100°C under sliding conditions

	E_{corr}(V)			
Sample	**3min & 25MPa**	**15min & 25MPa**	**30min & 25MPa**	**3min & 75MPa**
Ti	-0.61	-0.73	-0.74	-0.56
Ti2.5wt%B4C	-0.52	-0.53	-0.47	-0.51
Ti5wt%B4C	-0.39	-0.29	-0.29	-0.41
	I_{corr} (A/cm^2) x 10^{-6}			
Sample	**3min & 25MPa**	**15min & 25MPa**	**30min & 25MPa**	**3min & 75MPa**
Ti	9.57	7.07	6.04	11.91
Ti2.5wt%B4C	1.01	2.05	2.01	2.16
Ti5wt%B4C	0.38	0.05	3.73	1.01

In addition to the positively shifted E_{corr} values of TMCs, the I_{corr} were also reduced with addition of reinforcing phases showing lower material dissolution in contrast to Ti. The I_{corr} values obtained for Ti (9.57 to 6.04 x 10^{-6}A/cm^2) decreased and Ti2.5wt%B_4C (1.01 to

2.01A x 10^{-6}/cm^2) increase with dwell time and that of Ti5wt%B_4C (0.38 to 0.05A x 10^{-6}/cm^2) decreased at 15min. At 75MPa similar to 1000°C, there was a positive E_{corr} shift for all the samples, except Ti5wt%B_4C with only a minor difference (-0.39V to -0.41V). Moreover, the I_{corr} values behaviour at 75MPa was similar to 1000°C, they increased for Ti2.5wt%B_4C and Ti5wt%B_4C. So, similar to 1000°C improved tribocorrosion resistance was obtained for Ti5wt%B_4C with the lowest I_{corr} value of 0.05A x 10^{-6}/cm^2 at 15min. Moreover, the microstructure variations at the different sintering conditions influence on the E_{corr} and I_{corr} values is similar to those discussed without sliding (Table 26). The tribocorrosion perfomance of Ti5wt%B_4C was consistent with results obtained from corrosion without applied load.

It is worth noting that the current density recorded during polarization tests of material subjected to sliding is actually the sum of current in the worn and unworn areas (López-Ortega *et al.*, 2018). As such the current densities induced are normally higher compared with those obtained without sliding, while the E_{corr} values shift negatively as illustrated in Figure 5.14. There is a correlation between the COF induced during sliding with the current density. Figures 5.15 and 5.16 show the COF values measured during polarisation for samples sintered at 15min dwell time at 1000°C and 1100°C respectively. It could be observed that the COF values correlated with polarisation curves and varied with the applied potential in the cathodic and anodic region. In the cathodic region at lower potentials the COF values for most of the samples were lower.

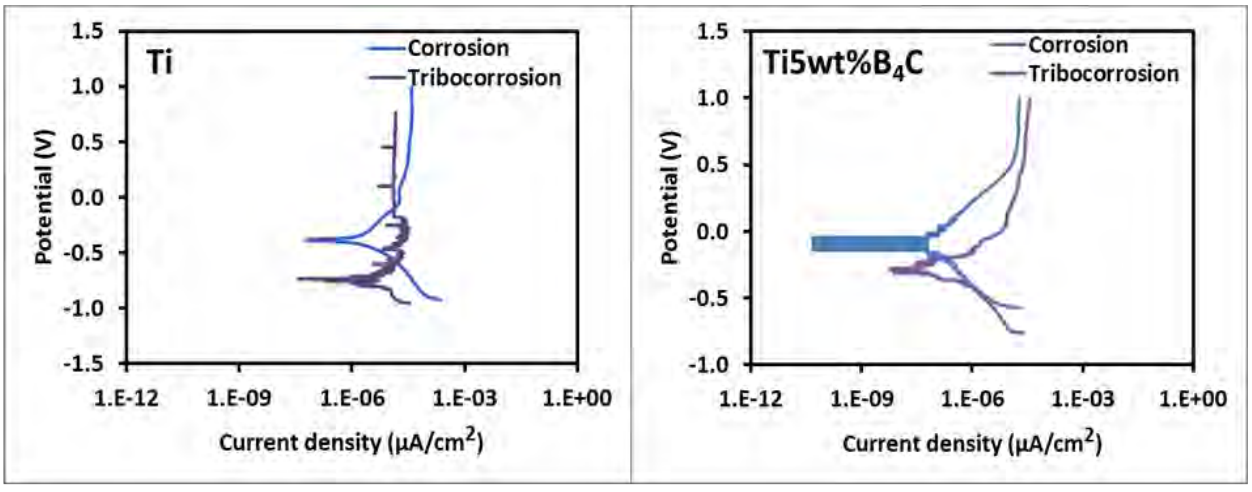

Figure 5.14. Potentiodynamic polarisation curves for corrosion and tribocorrosion for samples sintered at 15min dwell time at 1100°C

With the progression of polarization there was a transition of COF values from cathodic to anodic region especially for Ti and Ti2.5wt%B_4C. The current density fluctuations which could be due to formation of unstable corrosion pits, transitioned into a smoother curve. As a result in the anodic region at higher potentials, the COF values were increased which could be due to the unstable corrosion pits formed without the ability to repassivate (Obadele *et al.*, 2016). In contrast, for Ti5wt%B_4C sintered at 1000°C the COF values were gradually decreased in the anodic region. There are two possibilities for decrease of COF values at higher anodic potentials. Firstly, the formation of a passive oxide film could smoothen and seal of corrosion pits created in the wear track (López-Ortega *et al.*, 2018). Secondly, the surface roughness created by corrosion pits may lead to a reduced surface area in the contact between material and counter ball hence reduction of COF values (Takadoum, 1996). The COF values are summarized in Figure 5.17. Their behaviour was similar to those measured during OCP (*see* Figure 5.11). In both conditions, at the beginning of sliding, COF values were higher for Ti and Ti2.5wt%B_4C, and lower for Ti5wt%B_4C.

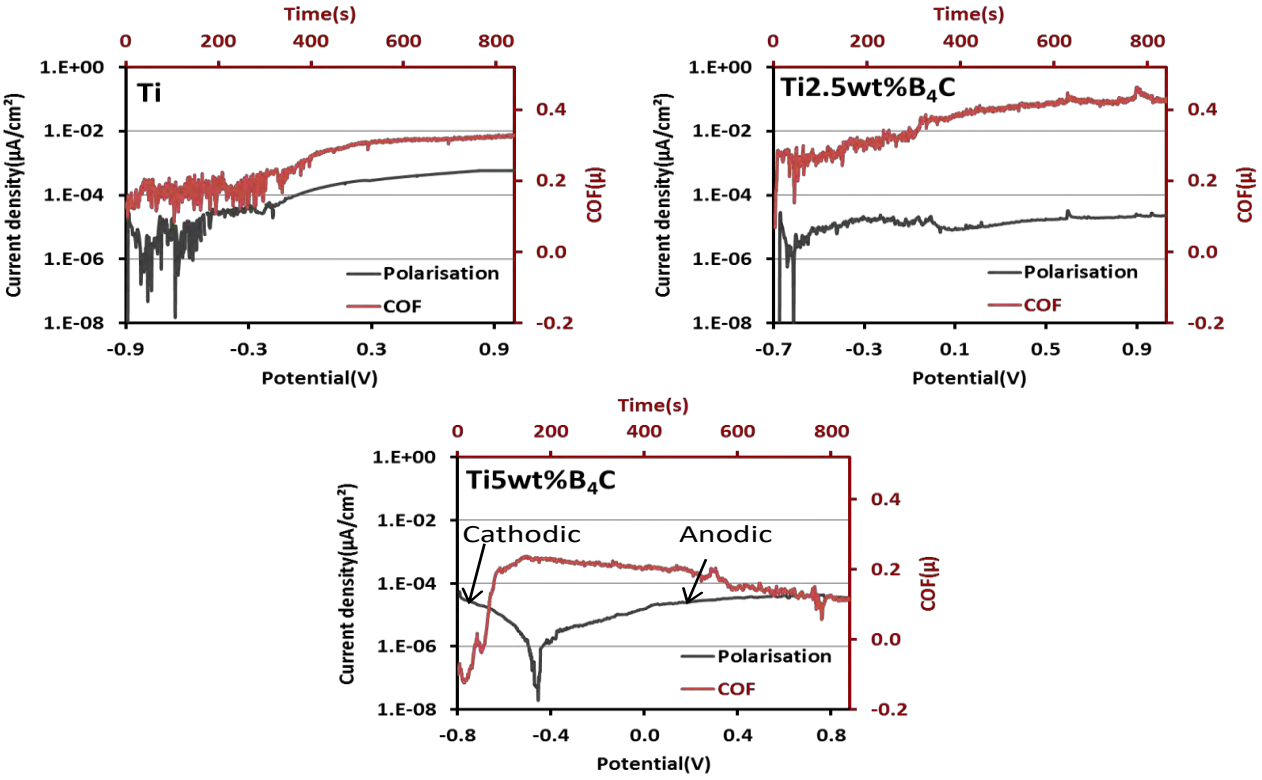

Figure 5.15. Potentiodynamic polarization curves relation to evolution of coefficient of friction for Ti and TMCs sintered at 15min dwell time and 1000°C

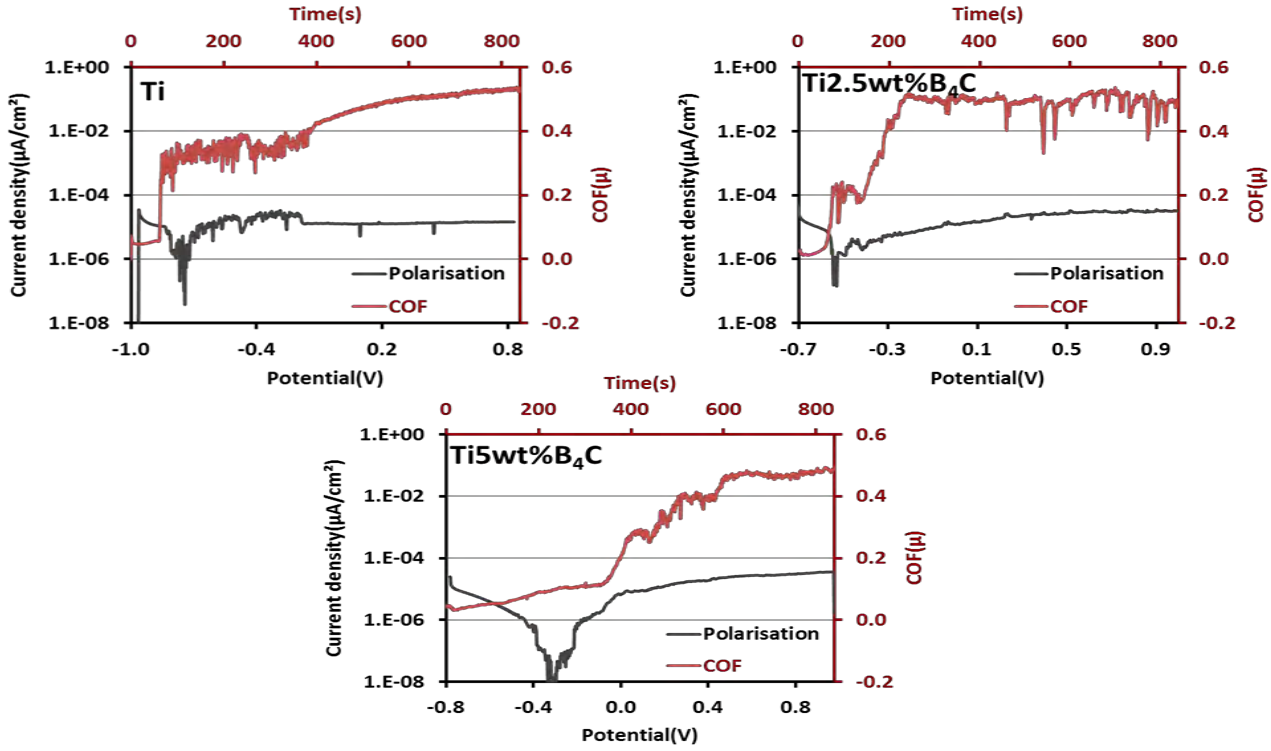

Figure 5.16. Potentiodynamic polarization curves relation to evolution of coefficient of friction for Ti and TMCs sintered at 15min dwell time and 1100°C

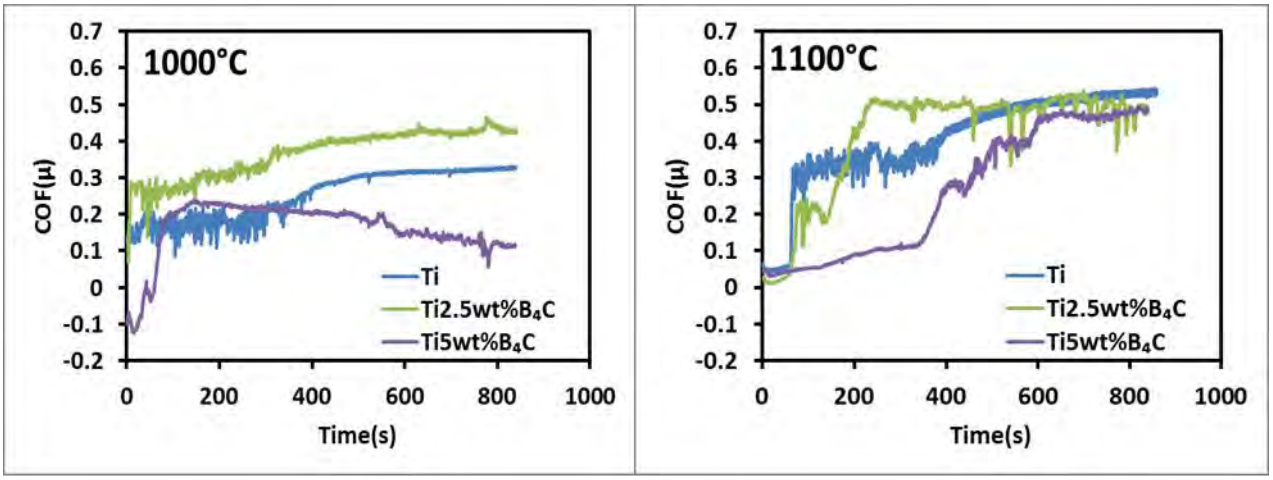

Figure 5.17 Overall coefficient of friction during potentiodynamic polarisation as function of time for Ti and TMCs sintered at dwell time of 15min at 1000°C and 1100°C

5.6 Wear tracks morphology

Figure 5.18 shows SEM images of worn tracks of the samples after tribocorrosion polarization tests for Ti and TMCs sintered at 15min dwell time at 1000°C and 1100°C. Figure 5.18 (a) presents worn track for Ti sintered at 1000°C with a larger width. In this case, a combination of plastic deformation, smearing, deep grooves and debris deposition on the

sides on the wear track are results in severe damage. Addition of reinforcing phase to 2.5wt% as shown in Figure 5.18 (b) reduced the worn track width and the shallow grooves with debris deposition on both sides of the track indicated improved wear resistance. Further increase of reinforcing phases to 5wt% (Figure 5.18 (c)) leads to a slight deposition of debris on the sides of track and the grooves were fading. Increasing the temperature to 1100°C generally reduced surface damage. In Figure 5.18 (d) debris compacts were observed in Ti and the wear track width was reduced with minor grooves. In Figure 5.18 (e) the damage morphology changed for Ti2.5wt%B_4C. Pits/holes were observed showing detachment of reinforcing phases which could have acted as third body abrasive inducing more wear. Figure 5.18 (f) shows wear morphology of Ti5wt%B_4C. As observed, there was less surface damage on the TMC, which validates the improved tribocorrosion resistance of the TMC. So at 1100°C, the surface of Ti5wt%B_4C was insignificantly affected. In addition, the wear tracks profiles shown in Figure 5.19 support this assumption. The wear depth reduces generally with increasing amount of reinforcing phases.

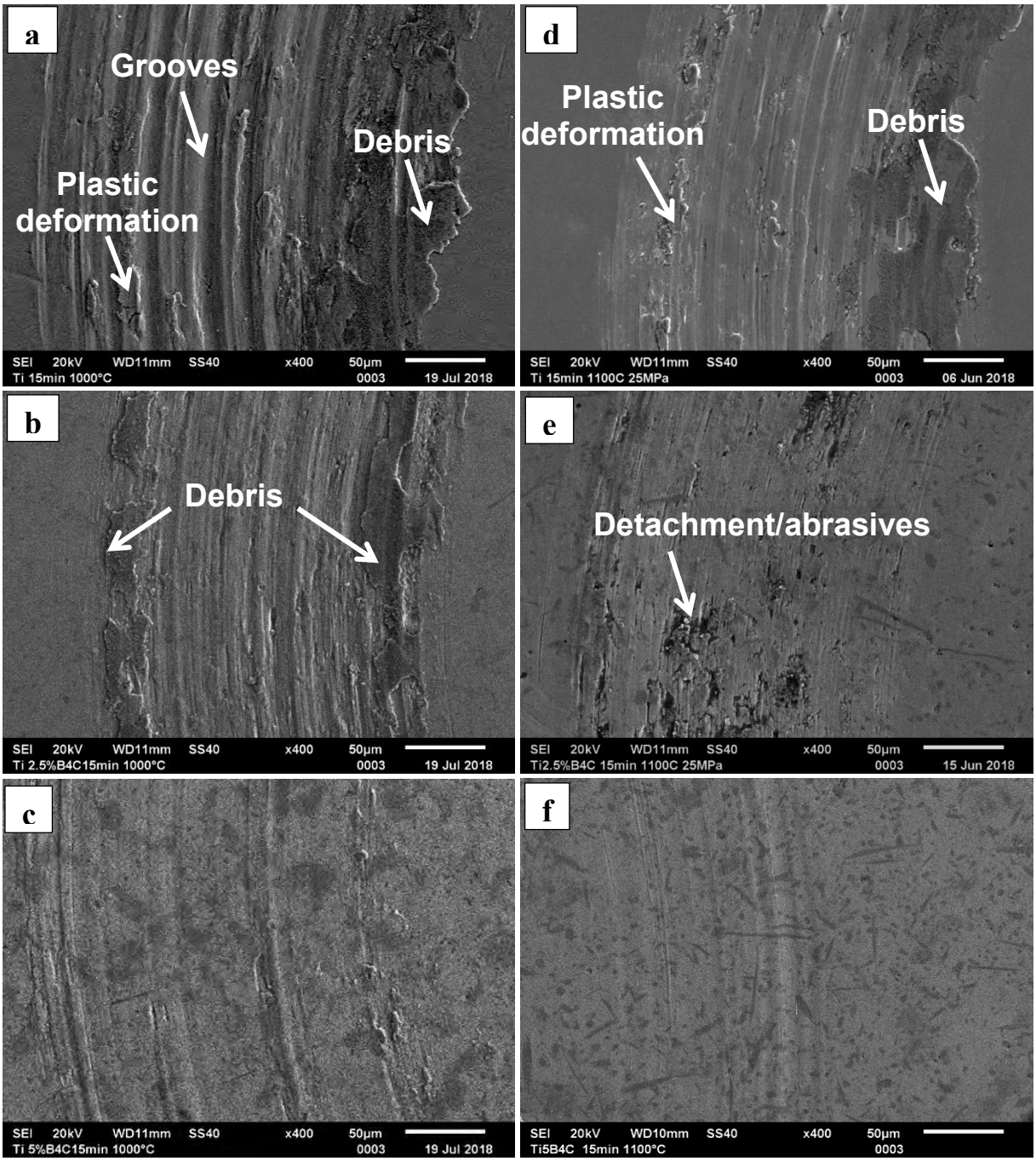

Figure 5.18. SEM images of worn surfaces after potentiodynamic polarization for Ti, Ti2.5wt%B_4C and Ti5wt%B_4C sintered at dwell time of 15min at (a-c) 1000°C and (d-f) 1100°C

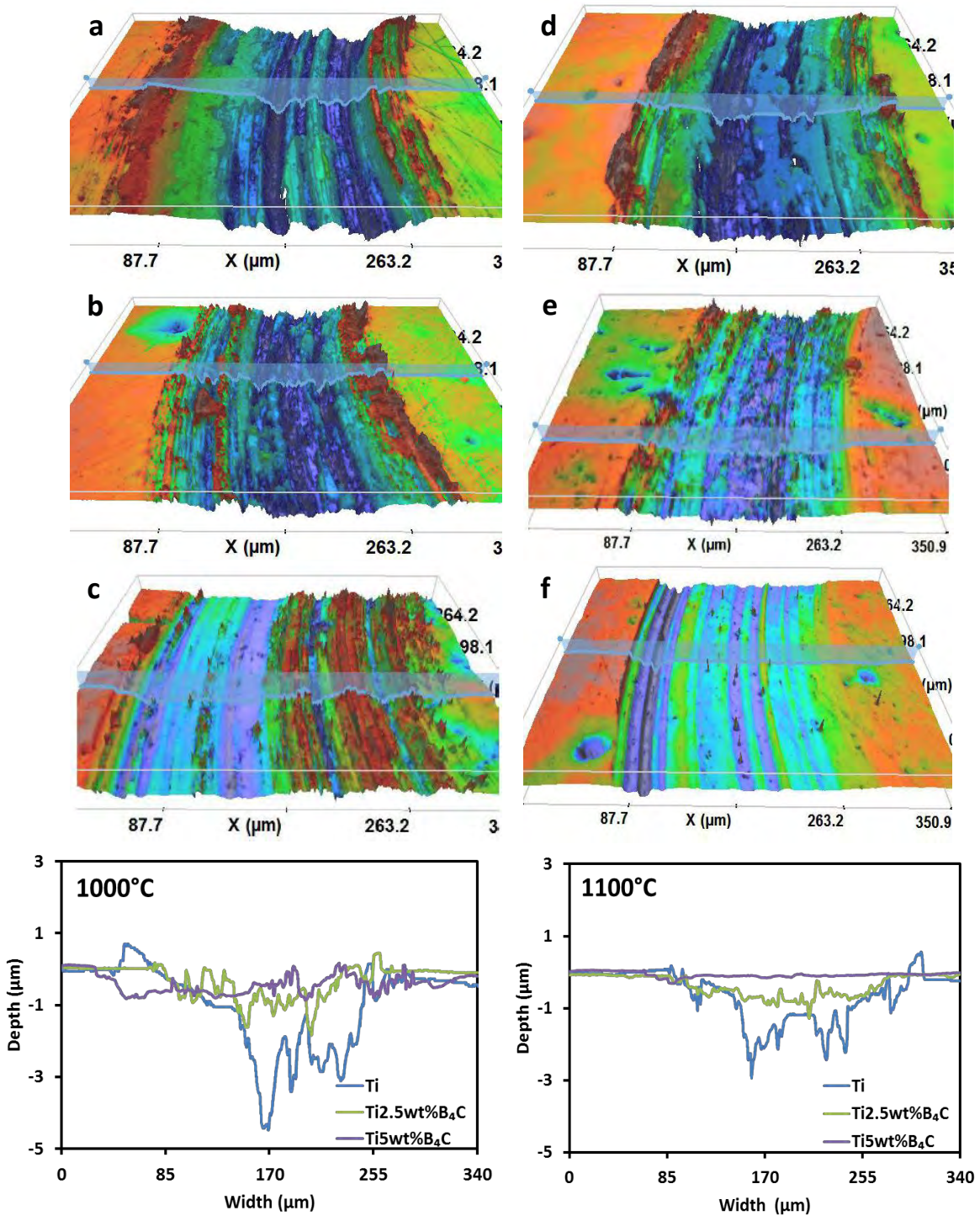

Figure 5.19. Surface profiles of Ti, Ti2.5wt%B_4C and Ti5wt%B_4C samples sintered at 15min dwell time subjected to potentiodynamic polarisation (a-c) 1000°C and (d-f) 1100°C

The wear tracks became wider and shallow when dwell time was increased to 30min (Figure 5.20) and this is supported by wear profiles (Figure 5.21), in contrast to those sintered at 15min, which were deeper and narrow. This could indicate that the surface area in the tribological contact between the samples and counter material was increased due to material

softening at higher dwell time. As a result, the anodic/wear track area was also increased resulting in higher I_{corr} values than with samples sintered at 15min dwell time. Similar to 15min dwell time there was less damage on the Ti5wt%B_4C TMCs which were fully transformed into finer TiB and TiC reinforcing phases. As observed in Figure 5.20 (c) the TiB whisker that was perpendicular to the imparted sliding load broke without any signs of detachment showing the strong bond with Ti matrix. In contrast to Toptan *et al.* (2016) who reported detachment of partially reacted B_4C particles, as sliding continued, stresses were created around the particles and were later pulled out causing more surface damage. This could indicate that TiB and TiC reinforcing phases would offer improved reinforcement compared with partially reacted B_4C.

Furthermore, it has to be noted that on the unworn area where no mechanical degradation is observed, normal corrosion took place. Presented in Figure 5.22 is the pitting and galvanic corrosion mechanism observed on Ti and TiB whiskers respectively. We have to consider that in the present system of Ti - (TiB + TiC) there are mixed corrosion potentials involved with different reactions taking place. On the TMC it was observed that galvanic corrosion took place on the Ti/TiB interface. This resulted in preferential dissolution of TiB whisker, suggesting that the corrosion potential of the TiB was more negative than Ti making it less noble (Sivakumar *et al.*, 2015). This type of corrosion is common in metal matrix composites it has been reported that selective corrosion usually take place at the matrix/reinforcement interface and results in dissolution of the reinforcement (Doni *et al.*, 2014).

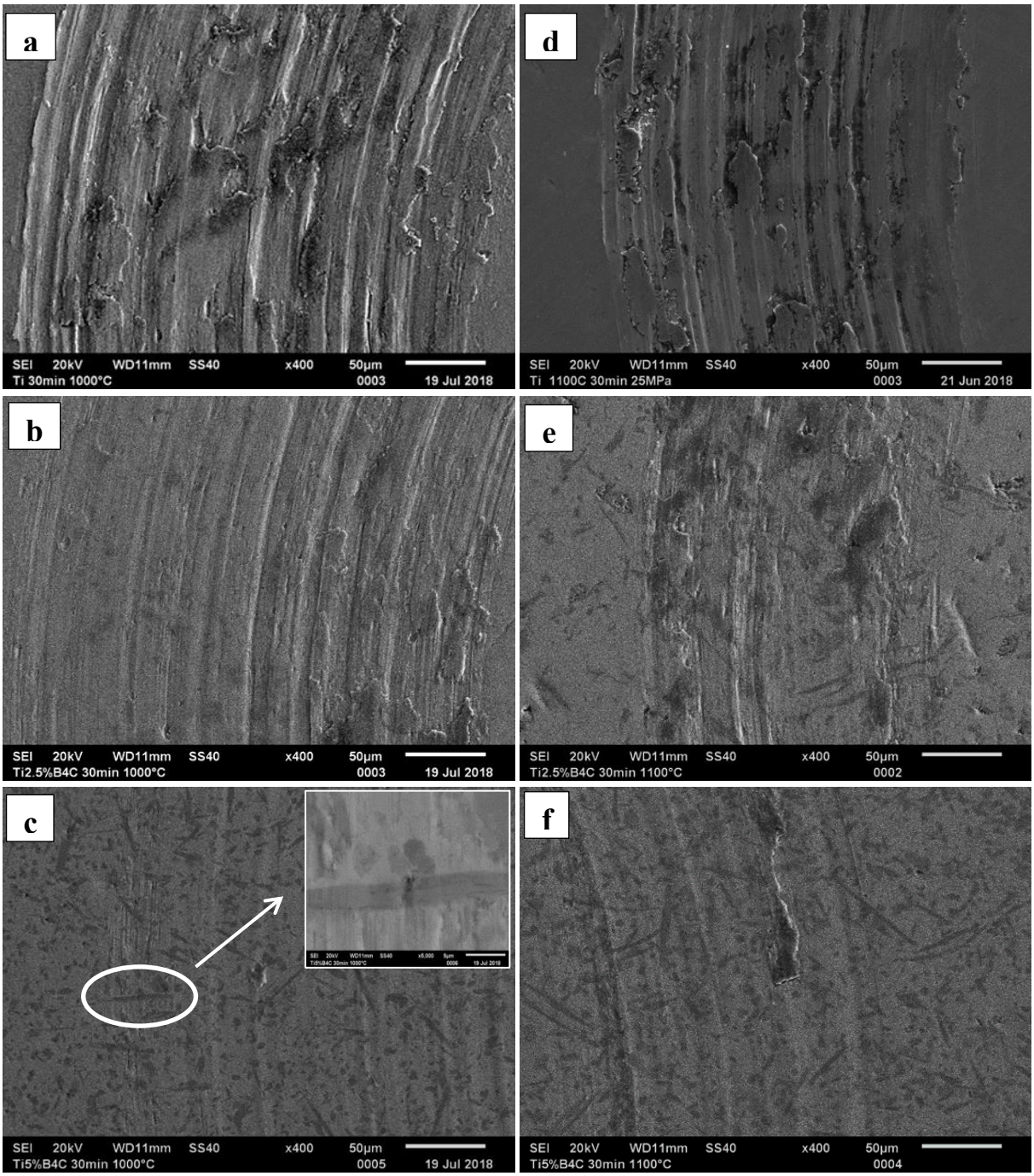

Figure 5.20. SEM images of worn surfaces after potentiodynamic polarisation for Ti, Ti2.5wt%B_4C and Ti5wt%B_4C sintered at dwell time of 15min at (a-c) 1000°C and (d-f) 1100°C

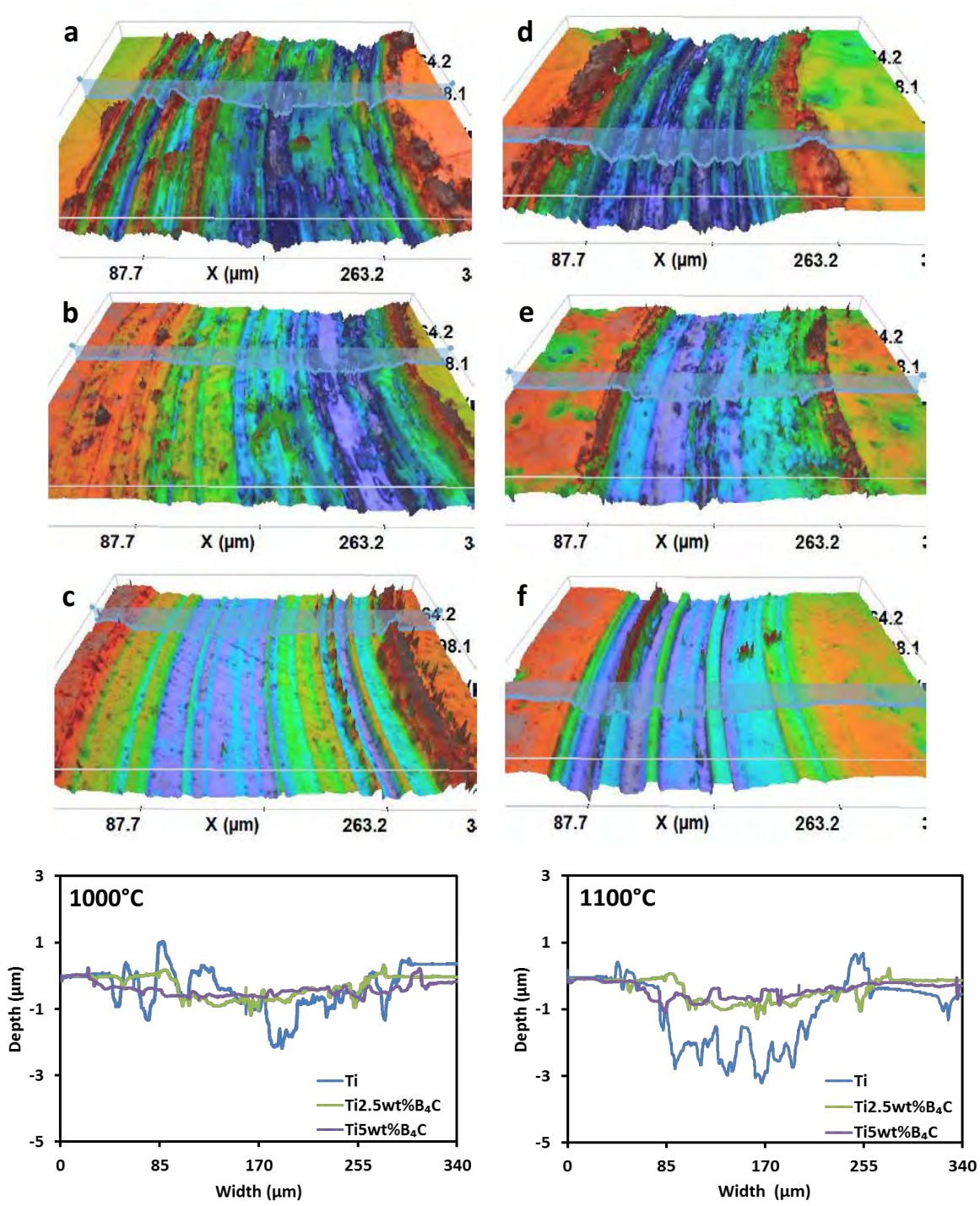

Figure 5.21. Surface profiles of Ti, Ti2.5wt%B_4C and Ti5wt%B_4C samples sintered at 30min dwell time subjected to potentiodynamic polarisation (a-c) 1000°C and (d-f) 1100°C

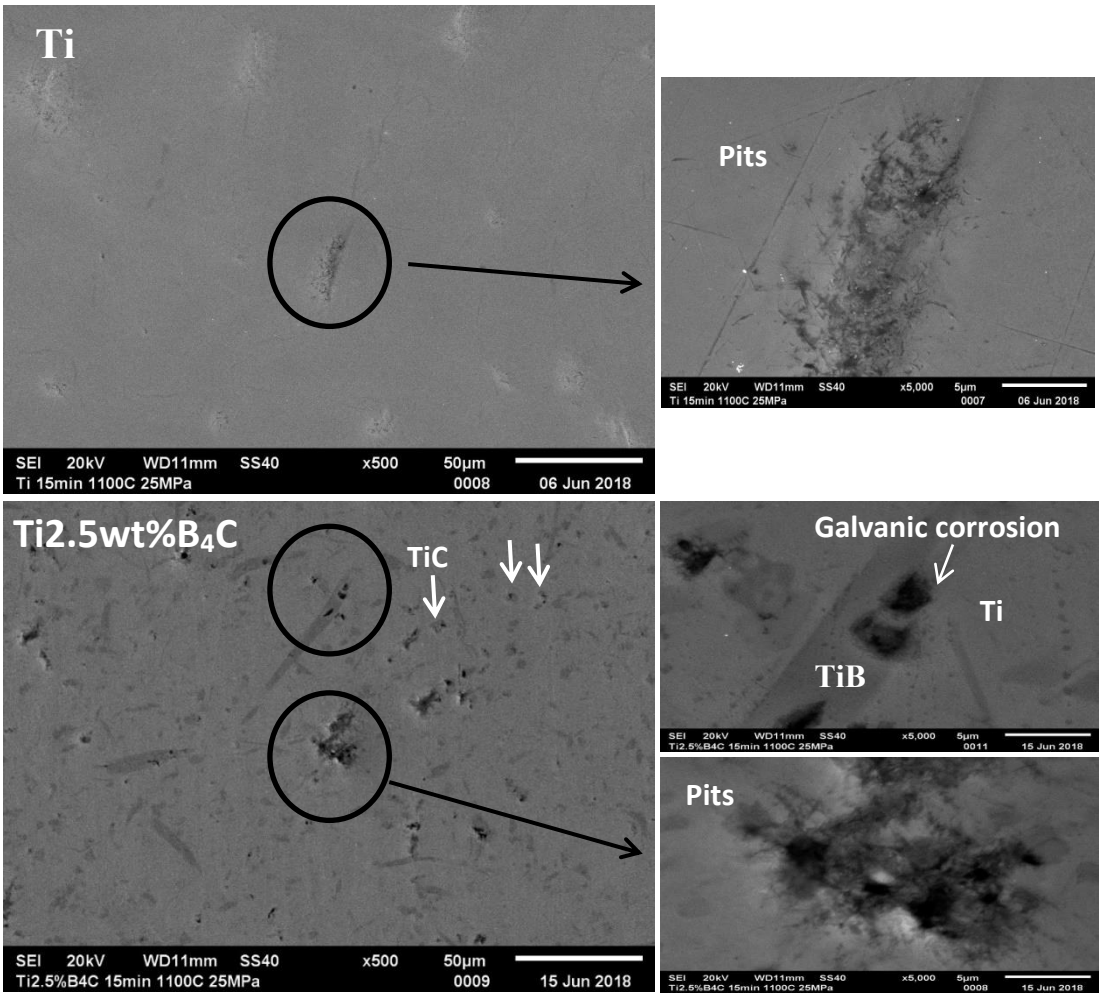

Figure 5.22. Corrosion morphology on Ti and TMC

To compare the wear data for all the samples under sliding polarisation, the volume loss was calculated considering the depth and width of the worn tracks measured using Sensofar Interferometric and Confocal Microscope. As observed in Figure 5.23 at both tempeartures there was no specific trend with increasing the dwell time and pressure to volume loss. However, it can be seen that the volume loss of CP-Ti is reduced with addition of reinforcing phases. It was suggested that the poor tribological properties of titanium and its alloys are attributed to their low work-hardening and low plastic shearing resistance (Molinari *et al.*, 1997). The addition of reinforcing phases improves the hardness of CP-Ti hence the lower volume loss of the TMCs. The particles clusters formed at 1000°C have low strength, are centers for stress concentration and crack nucleation sites. As a result they may breakout and be pulled out during sliding causing severe damage resulting in higher material loss(Ni *et al.*, 2006; Tabrizi *et al.*, 2015). Generally homogenized TiB and TiC at 1100°C provided better strengthening as the TMCs yielded lower material loss.

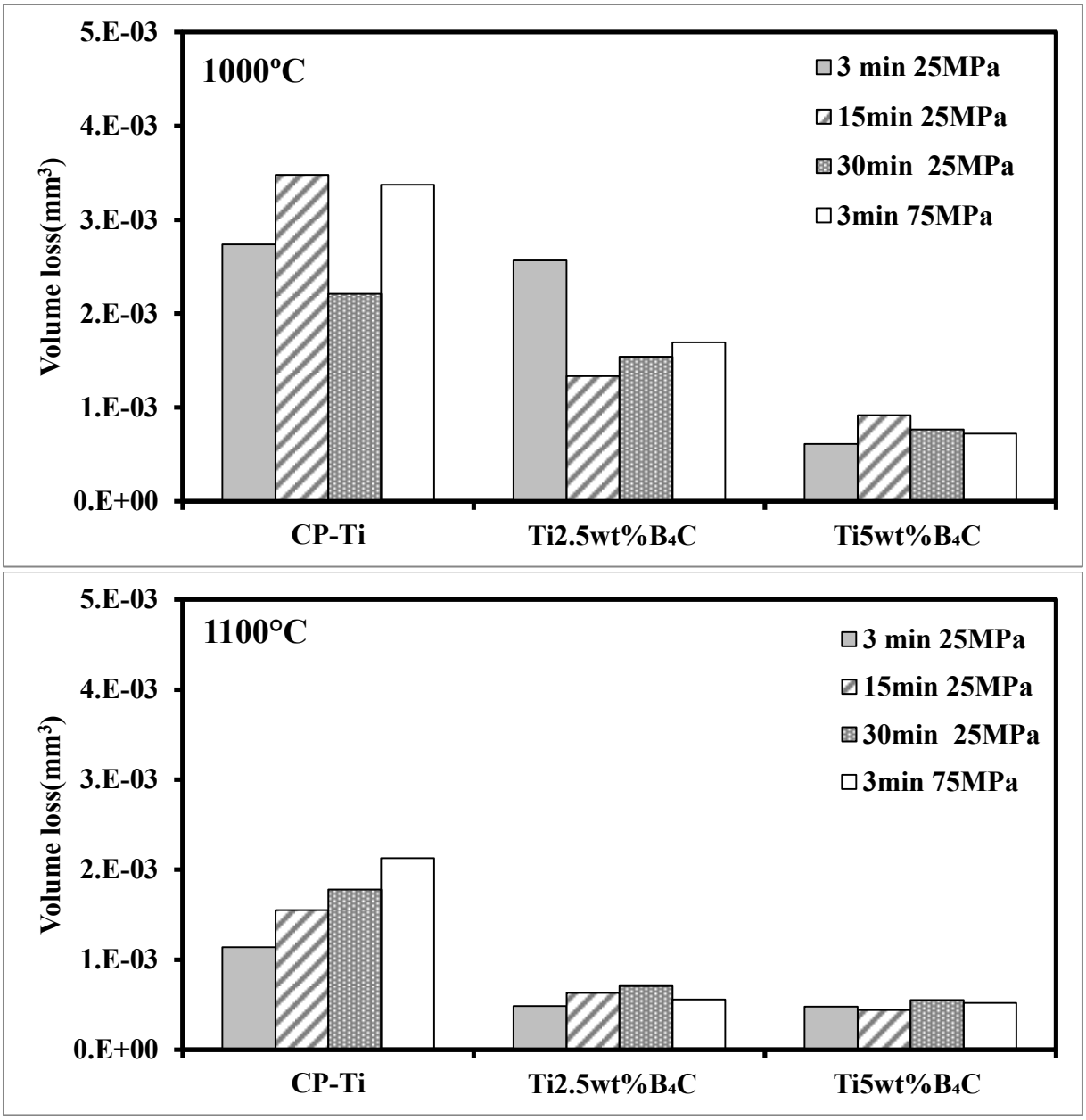

Figure 5.23 Volume loss of CP-Ti and TMCs subjected to polarisation during sliding

Summary

The corrosion and tribocorrosion behaviour of Ti in 3.5%NaCl solution was improved by addition of TiB and TiC reinforcing phases. The E_{corr} values were positively shifted with increasing amount of reinforcing phases. Under corrosion conditions, the corrosion resistance was improved by the inert physical barrier role of the reinforcing phases. While in tribocorrosion conditions, the load carrying capacity of the reinforcing phases contributed to the lower wear loss. In general, the OCP, E_{corr} and I_{corr} values obtained under corrosion and

tribocorrosion conditions correlated due to the same microstructural features observed. The particles clusters and coarser reinforcing phases contributed to more negative OCP and E_{corr} values with higher I_{corr} values. In essence they reduced the corrosion resistance of the TMCs and they are not a desirable microstructural feature. Increasing the temperature to 1100°C at 15min dwell time the microstructure was homogenized to finer TiB and TiC reinforcing phases compared with 30min, the I_{corr} values and the surface damage was reduced. Further increase of dwell time to 30min led to coarsening of TiB and TiC reinforcing phases and matrix softening, which resulted in higher I_{corr} values and severe surface damage. Ti5wt%B_4C sintered at 1100°C and 15min yielded overall improved corrosion and tribocorrosion performance compared with other samples. In the present study the mechanism of material degradation is by mechanical and chemical. The reinforcing phases under study enhanced the composites properties differently. Predominantly the TiC phase showed to be corrosion resistant while the TiB phase with a whisker morphology was wear resistant.

General conclusion

This research focused on improving the corrosion and tribocorrosion properties of CP-Ti by incorporating Titanium boride (TiB) and Carbide (TiC) reinforcing phases during reactive sintering in the SPS of mixtures of pure titanium with differeny grades of Boron Carbide (B_4C) powders. The relationship between microstructure evolution at varying SPS sintering conditions and corrosion and tribocorrosion behaviour of TMCs was investigated.

Microstructure evolutions of two CP-Ti materials with varying interstitial content, revealed a delayed transformation for the material with high content of oxygen (α-phase stabiliser) and that with high hydrogen content (β-phase stabiliser) it was promoted at lower temperatures and pressures. Due to the detrimental effect of hydrogen content in CP-Ti properties, the powder with lower hydrogen content was chosen for synthesis of TMCs. Incomplete reaction resulted from using coarser B_4C particles which in turn lowered the relative densities. These TMCs were not suitable for further characterizations due to unreacted B_4C which required high temperatures for complete consumption. The reaction for TMCs with finer B_4C particles was highly spontaneous and higher amount of denser reinforcing phases were formed at lower temperatures resulting in higher relative densities. The TMCs were characterized with particles clusters which emerged from the former finer B_4C particles segregated in the grain boundaries of Ti.

As such, further microstructure characterization and mechanical properties evaluation were performed on TMCs with finer B_4C particles. TEM characterization of the FIB lamellae extracted from the interface of Ti and particles clusters revealed partially reacted B_4C particles at 800°C. On evaluating the phases detected at 800°C, it could be suggested that in the SPS the reaction progressed rapidly at set-point temperature. This was attributed to the large surface area of fine B_4C powder and the high temperatures reached on the surface of particles reaching melting point and vaporization thus enhancing atoms interdiffusion thanks to the pulsed electric current in the SPS. At 1100°C the particles clusters with unreacted B_4C observed at 800°C transformed into Ti-B and Ti-C compounds. Depending on the amount of reinforcing phases content in the TMCs the particles clusters were homogenized to TiB and TiC phases with increase of dwell time and temperature.

On the effect of microstructure on the mechanical properties, the hardness values increased with increasing reinforcing phase's content, the presence of particles clusters and coarsening of TiB and TiC reinforcing phases. The corrosion and tribocorrosion behaviour relation to

microstructure of TMCs was consistent with TMCs sintered at 1000 and 1100°C. Increasing reinforcing phase's content and homogenized finer TiB and TiC reinforcing phases increased corrosion and tribocorrosion resistance. While the particles clusters and coarse TiB and TiC lowered the resistance to corrosion and tribocorrosion. The COF values of Ti5wt%B_4C under polarisation were lower at higher potentials in comparison to CP-Ti. This showed the capacity of reinforcing phases to carry the applied load and thus improving the wear resistance of CP-Ti. In addition the material loss was reduced with increasing amount of reinsforcing phases by also lowering the material loss. In general, Ti5wt%B_4C characterized with homogenized TiB and TiC reinforcing phases exhibited the best corrosion and tribocorrosion resistance.

Perspectives

The findings of this study indicate that Ti based TiB and TiC composites can be actively used in engineering applications whereby corrosion and tribocorrosion properties are of utmost importance. Such applications include the automotive industry whereby the demand for lightweight parts required for reducing the weight and emission of harmful exhaust gases to the atmosphere is very crucial. However, before up scaling such materials processed by powder metallurgy technique for industrial use, thorough investigation on the material tribocorrosion properties on this research topic is required.

References

ABEDI, M., MOSKOVSKIKH, D. O., ROGACHEV, A. S. & MUKASYAN, A. S. 2016. Spark Plasma Sintering of Titanium Spherical Particles. *Metallurgical and Materials Transactions B,* 47(5):2725-2731.

AHMAD, Z. 2006. *Principles of corrosion engineering and corrosion control*. Elsevier.

AJAYAN, P. M., SCHADLER, L. S. & BRAUN, P. V. 2006. *Nanocomposite science and technology*. John Wiley & Sons.

AKSYONOV, D. A., LIPNITSKII, A. G. & KOLOBOV, Y. R. 2012. Ab initio study of Ti–C precipitates in hcp titanium: Formation energies, elastic moduli and theoretical diffraction patterns. *Computational Materials Science,* 652012/12/01/:434-441.

ALI, R., ALKHATEEB, E., KELLNER, F., VIRTANEN, S. & POPOVSKA-LEIPERTZ, N. 2011. Chemical vapor deposition of titanium based ceramic coatings on low carbon steel: Characterization and electrochemical evaluation. *Surface and Coatings Technology,* 205(23-24):5454-5463.

ALKHATEEB, E., ALI, R., VIRTANEN, S. & POPOVSKA, N. 2011. Electrochemical evaluation of the corrosion behavior of steel coated with titanium-based ceramic layers. *Surface and Coatings Technology,* 205(8-9):3006-3011.

ALMAN, D. E. & HAWK, J. A. 1999. The abrasive wear of sintered titanium matrix–ceramic particle reinforced composites. *Wear,* 225:629-639.

ANDREEV, Y., LEVASHOV, E. A., SHEVEIKO, A., KOSIANIN, V. I., MOORE, J. J. & OLSON, D. L. 1997. Electrochemical corrosion behavior of SHS-synthesized dc magnetron composite TiC-based targets and sputtered thin films. *Surface and Coatings Technology,* 90(1-2):42-52.

ANSELMI-TAMBURINI, U., GENNARI, S., GARAY, J. E. & MUNIR, Z. A. 2005. Fundamental investigations on the spark plasma sintering/synthesis process II. Modeling of current and temperature distributions. *Materials Science and Engineering: A,* 394(1-2):139-148.

ARIZA GALVÁN, E., MONTEALEGRE-MELÉNDEZ, I., ARÉVALO, C., KITZMANTEL, M. & NEUBAUER, E. 2017. Ti/B4C Composites Prepared by In Situ Reaction Using Inductive Hot Pressing. Paper presented at the *Key Engineering Materials*.

ATAIBIS, V. & TAKTAK, S. 2015. Characteristics and growth kinetics of plasma paste borided Cp–Ti and Ti6Al4V alloy. *Surface and Coatings Technology,* 279:65-71.

BAILLIEUX, J., POQUILLON, D. & MALARD, B. 2015. Observation using synchrotron X-ray diffraction of the crystallographic evolution of α-titanium after oxygen diffusion. *Philosophical Magazine Letters,* 95(5):245-252.

BAKER, H. 1992. *ASM handbook: alloy phase diagrams*. (3). ASM international.

BALAJI, V. & KUMARAN, S. 2013. Development of Titanium/TiC-TiB Hybrid Composite by in-situ Reaction during Spark Plasma Sintering.

BALAJI, V. & KUMARAN, S. 2015. Dry Sliding Wear Behavior of Titanium–(TiB+ TiC) in situ Composite Developed by Spark Plasma Sintering. *Tribology Transactions,* 58(4):698-703.

BALAJI, V. S. & KUMARAN, S. 2014. Densification and microstructural studies of titanium–boron carbide (B4C) powder mixture during spark plasma sintering. *Powder Technology,* 264:536-540.

BARSOUM, M. W. & HOUNG, B. 1993. Transient plastic phase processing of titanium–boron–carbon composites. *Journal of the American Ceramic Society,* 76(6):1445-1451.

BAS, A. D., GHALI, E. & CHOI, Y. 2017. A review on electrochemical dissolution and passivation of gold during cyanidation in presence of sulphides and oxides. *Hydrometallurgy,* 172:30-44.

BASU, B., RAJU, G. & SURI, A. 2006. Processing and properties of monolithic TiB2 based materials. *International materials reviews,* 51(6):352-374.

BATRAEV, I., CHAITANYA, S., CHENG, X., DUDINA, D. V., KRISHNARAJ, V., KUMAR, R., et al. 2014. *Metal Matrix Composites: Materials, Manufacturing and Engineering*. (3). Walter de Gruyter GmbH & Co KG.

BEVERSKOG, B., CARLSSON, J.-O., BAUER, A. D., DESHPANDEY, C., DOERR, H., BUNSHAH, R., et al. 1990. Corrosion properties of TiC films prepared by activated reactive evaporation. *Surface and Coatings Technology,* 41(2):221-229.

BHAUMIK, S., DIVAKAR, C., SINGH, A. K. & UPADHYAYA, G. 2000. Synthesis and sintering of TiB2 and TiB2–TiC composite under high pressure. *Materials Science and Engineering: A,* 279(1-2):275-281.

BLAU, P. J., JOLLY, B. C., QU, J., PETER, W. H. & BLUE, C. A. 2007. Tribological investigation of titanium-based materials for brakes. *Wear,* 263(7–12), 9/10/:1202-1211.

BOLZONI, L., RUIZ-NAVAS, E. M. & GORDO, E. 2013. Processing of elemental titanium by powder metallurgy techniques. Paper presented at the *Materials Science Forum*.

BRODKIN, D., KALIDINDI, S. R., BARSOUM, M. W. & ZAVALIANGOS, A. 1996. Microstructural evolution during transient plastic phase processing of titanium carbide-titanium boride composites. *Journal of the American Ceramic Society,* 79(7):1945-1952.

CALLISTER, W. D. & RETHWISCH, D. G. 2007. *Materials science and engineering: an introduction*. (7). Wiley New York.

CALLISTER, W. D. & RETHWISCH, D. G. 2011. *Materials science and engineering*. (5). John wiley & sons NY.

CAMPBELL, F. C. 2010. *Structural composite materials*. ASM international.

CAO, Y., ZENG, F., LU, J., LIU, B., LIU, Y. & LI, Y. 2015. In Situ Synthesis of TiB/Ti6Al4V Composites Reinforced with Nano TiB through SPS. *MATERIALS TRANSACTIONS,* 56(2):259-263.

CASATI, R. & VEDANI, M. 2014. Metal Matrix Composites Reinforced by Nano-Particles—A Review. *Metals,* 4(1):65-83.

CHAIM, R., LEVIN, M., SHLAYER, A. & ESTOURNÈS, C. 2008. Sintering and densification of nanocrystalline ceramic oxide powders: a review. *Advances in Applied Ceramics,* 107(3):159-169.

CHAIM, R., MARDER, R., ESTOURNÉS, C. & SHEN, Z. 2012. Densification and preservation of ceramic nanocrystalline character by spark plasma sintering. *Advances in Applied Ceramics,* 111(5&6):280-285.

CHANDRAN, K. R., PANDA, K. & SAHAY, S. 2004. TiB w-reinforced Ti composites: processing, properties, application prospects, and research needs. *Jom,* 56(5):42-48.

CHAUDHARI, R. & BAURI, R. 2013. Reaction mechanism, microstructure and properties of Ti–TiB insitu composite processed by spark plasma sintering. *Materials Science and Engineering: A,* 587:161-167.

CHAWLA, N. & CHAWLA, K. 2006. Metal-matrix composites in ground transportation. *Jom,* 58(11):67-70.

CHEN, L. & YAO, Y. 2014. Processing, microstructures, and mechanical properties of magnesium matrix composites: a review. *Acta Metallurgica Sinica (English Letters),* 27(5):762-774.

CHENG, L., XIE, Z., LIU, G., LIU, W. & XUE, W. 2012. Densification and mechanical properties of TiC by SPS-effects of holding time, sintering temperature and pressure condition. *Journal of the European Ceramic society,* 32(12):3399-3406.

CHOI, B.-J. & KIM, Y.-J. 2013. In-Situ (TiB+ TiC) particulate reinforced titanium matrix composites: Effect of B4C size and content. *Metals and Materials International,* 19(6):1301-1307.

CHOI, Y. & RHEE, S.-W. 1994. Equilibrium in the reaction of Ti and C to form substoichiometric TiC x. *Journal of Materials Science Letters,* 13(5):323-325.

CLYNE, T., WITHERS, P. & WARD, L. 1995. An introduction to metal matrix composites', Cambridge Solid State Science Series; 1993. Cambridge, Cambridge University Press.

CONRAD, H. 1981. Effect of interstitial solutes on the strength and ductility of titanium. *Progress in Materials Science,* 26(2-4):123-403.

CORDERO, B., GÓMEZ, V., PLATERO-PRATS, A. E., REVÉS, M., ECHEVERRÍA, J., CREMADES, E., et al. 2008. Covalent radii revisited. *Dalton Transactions,* 0(21):2832-2838.

COURET, A., MOLÉNAT, G., GALY, J. & THOMAS, M. 2008. Microstructures and mechanical properties of TiAl alloys consolidated by spark plasma sintering. *Intermetallics,* 16(9):1134-1141.

COVING JR, B., CRAMER, S., CARTER, J. & SCHLAIN, D. 1975. Corrosion of titanium diboride. *Journal of the Less Common Metals,* 41(2):211-224.

COVINO JR, B. S. & ALMAN, D. E. 2002. *Corrosion of titanium matrix composites*. Albany Research Center (ARC), Albany, OR.

CROSBY, K., SHAW, L. L., ESTOURNES, C., CHEVALLIER, G., FLIFLET, A. W. & IMAM, M. A. 2014. Enhancement in Ti–6Al–4V sintering via nanostructured powder and spark plasma sintering. *Powder Metallurgy,* 57(2):147-154.

DEGNAN, C. & SHIPWAY, P. 2002. A comparison of the reciprocating sliding wear behaviour of steel based metal matrix composites processed from self-propagating high-temperature synthesised Fe–TiC and Fe–TiB2 masteralloys. *Wear,* 252(9-10):832-841.

DIOUF, S., DUROWOJU, M. O., SHONGWE, M. B. & OLUBAMBI, P. A. 2017. Processing of pure titanium containing titanium-based reinforcing ceramics additives using spark plasma sintering. *Leonardo Electronic Journal of Practices and Technologies*(30):269-286.

DJELLOULI, B. & AOURAG, H. 2001. Theoretical studies of stoichiometric TiC. *physica status solidi (b),* 225(2):265-270.

DOMNICH, V., REYNAUD, S., HABER, R. A. & CHHOWALLA, M. 2011. Boron carbide: structure, properties, and stability under stress. *Journal of the American Ceramic Society,* 94(11):3605-3628.

DONACHIE, M. J. 2000. *Titanium: a technical guide*. ASM international.

DONI, Z., ALVES, A., TOPTAN, F., PINTO, A., ROCHA, L., BUCIUMEANU, M., et al. 2014. Tribocorrosion behaviour of hot pressed CoCrMo− Al2O3 composites for biomedical applications. *Tribology-Materials, Surfaces & Interfaces,* 8(4):201-208.

DUDINA, D. V. & MUKHERJEE, A. K. 2013. Reactive spark plasma sintering: successes and challenges of nanomaterial synthesis. *Journal of Nanomaterials,* 2013:5.

ERIKSSON, M., SALAMON, D., NYGREN, M. & SHEN, Z. 2008. Spark plasma sintering and deformation of Ti–TiB2 composites. *Materials Science and Engineering: A,* 475(1-2):101-104.

ERIKSSON, M., SHEN, Z. & NYGREN, M. 2005. Fast densification and deformation of titanium powder. *Powder Metallurgy,* 48(3):231-236.

FAN, Z., GUO, Z. & CANTOR, B. 1997. The kinetics and mechanism of interfacial reaction in sigma fibre-reinforced Ti MMCs. *Composites Part A: Applied Science and Manufacturing,* 28(2):131-140.

FAZAL, M., HASEEB, A. & MASJUKI, H. 2014. A critical review on the tribological compatibility of automotive materials in palm biodiesel. *Energy Conversion and Management,* 79:180-186.

FEDRIZZI, L., ROSSI, S., BELLEI, F. & DEFLORIAN, F. 2002. Wear–corrosion mechanism of hard chromium coatings. *Wear,* 253(11-12):1173-1181.

FENG, H., ZHOU, Y., JIA, D., MENG, Q. & RAO, J. 2006. Growth Mechanism of In Situ TiB Whiskers in Spark Plasma Sintered TiB/Ti Metal Matrix Composites. *Crystal Growth & Design,* 6(7):1626-1630.

FENGHUA, L., XIAOHONG, Y., JINGLEI ZHANG, Z. F., DIANTING, G. & ZHENGPING, X. 2010. Growth kinetics of titanium boride layers on the surface of Ti6Al4V. *Acta Metallurgica Sinica (English Letters),* 23(4):293-300.

FRAGE, N., FROUMIN, N. & DARIEL, M. 2002. Wetting of TiC by non-reactive liquid metals. *Acta Materialia,* 50(2):237-245.

FU, Z. & KOC, R. 2016. Sintering and mechanical properties of TiB 2-TiC-Ni using submicron borides and carbides. *Materials Science and Engineering: A,* 676:278-288.

FU, Z. & KOC, R. 2017. Pressureless sintering of submicron titanium carbide powders. *Ceramics International,* 43(18):17233-17237.

FUKAI, Y. 2006. *The metal-hydrogen system: basic bulk properties*. (21). Springer Science & Business Media.

FUKUSHIMA, A., FUJIWARA, C., KAGAWA, Y. & MASUDA, C. 2000. Effect of interfacial properties on tensile strength in SiC/Ti–15–3 composites. *Materials Science and Engineering: A,* 276(1-2):243-249.

GALVANETTO, E., GALLIANO, F., BORGIOLI, F., BARDI, U. & LAVACCHI, A. 2001. XRD and XPS study on reactive plasma sprayed titanium–titanium nitride coatings. *Thin Solid Films,* 384(2):223-229.

GARBIEC, D., SIWAK, P. & MRÓZ, A. 2016. Effect of compaction pressure and heating rate on microstructure and mechanical properties of spark plasma sintered Ti6Al4V alloy. *Archives of Civil and Mechanical Engineering,* 16(4):702-707.

GARCÍA, I., CONDE, A., LANGELAAN, G., FRANSAER, J. & CELIS, J.-P. 2003. Improved corrosion resistance through microstructural modifications induced by codepositing SiC-particles with electrolytic nickel. *Corrosion science,* 45(6):1173-1189.

GENG, L., NI, D. R., ZHANG, J. & ZHENG, Z. Z. 2008. Hybrid effect of TiBw and TiCp on tensile properties of in situ titanium matrix composites. *Journal of Alloys and Compounds,* 463(1-2):488-492.

GEORGIOU, E., DREES, D., DOSTA, S., MATTEAZZI, P., KUSINSKI, J. & CELIS, J.-P. 2017. Wear evaluation of nanostructured Ti cermets for joint reconstruction. *Biotribology,* 11:44-50.

GONZÁLEZ, C. & LLORCA, J. 2001. Micromechanical modelling of deformation and failure in Ti–6Al–4V/SiC composites. *Acta Materialia,* 49(17):3505-3519.

GORSSE, S. & MIRACLE, D. 2003. Mechanical properties of Ti-6Al-4V/TiB composites with randomly oriented and aligned TiB reinforcements. *Acta Materialia,* 51(9):2427-2442.

GU, D., MENG, G., LI, C., MEINERS, W. & POPRAWE, R. 2012. Selective laser melting of TiC/Ti bulk nanocomposites: Influence of nanoscale reinforcement. *Scripta Materialia,* 67(2):185-188.

GU, Y., LIU, J.-X., XU, F. & ZHANG, G.-J. 2017. Pressureless sintering of titanium carbide doped with boron or boron carbide. *Journal of the European Ceramic society,* 37(2):539-547.

GUIDERDONI, C., PAVLENKO, E., TURQ, V., WEIBEL, A., PUECH, P., ESTOURNÈS, C., et al. 2013. The preparation of carbon nanotube (CNT)/copper composites and the effect of the number of CNT walls on their hardness, friction and wear properties. *Carbon,* 58:185-197.

GÜLSOY, H. Ö., GÜLSOY, N. & CALIŞICI, R. 2014. Particle morphology influence on mechanical and biocompatibility properties of injection molded Ti alloy powder. *Bio-medical materials and engineering,* 24(5):1861-1873.

GUNDEL, D. & WAWNER, F. 1991. Interfacial reaction kinetics of coated SiC fibers with various titanium alloys. *Scripta metallurgica et materialia,* 25(2):437-441.

HAN, Y.-M. & CHEN, X. 2015. Electrochemical Behavior of Al-B4C metal matrix composites in NaCl solution. *Materials,* 8(9):6455-6470.

HAO, Y., LIU, J., LI, J., LI, S., ZOU, Q. & CHEN, X. 2015. Rapid preparation of TiC reinforced Ti6Al4V based composites by carburizing method through spark plasma sintering technique. *Materials & Design (1980-2015),* 65:94-97.

HAYASHI, T., MATSUURA, K. & OHNO, M. 2013. TiC coating on titanium by carbonization reaction using spark plasma sintering. *MATERIALS TRANSACTIONS*:L-M2013829.

HE, L., ZHANG, X. & TONG, C. 2006. Surface modification of pure titanium treated with B4C at high temperature. *Surface and Coatings Technology,* 200(9):3016-3020.

HOLT, J. B. & MUNIR, Z. A. 1986. Combustion synthesis of titanium carbide: Theory and experiment. *Journal of Materials Science,* 21(1):251-259.

HUANG, B., LI, M., CHEN, Y., LUO, X. & YANG, Y. 2015. Interfacial reaction in SiCf/Ti-6Al-4V composite by using transmission electron microscopy. *Materials Characterization,* 109:206-215.

HUANG, L. J., GENG, L., LI, A., YANG, F. & PENG, H. 2009. In situ TiBw/Ti–6Al–4V composites with novel reinforcement architecture fabricated by reaction hot pressing. *Scripta Materialia,* 60(11):996-999.

HUSSAINOVA, I. 2003. Effect of microstructure on the erosive wear of titanium carbide-based cermets. *Wear,* 255(1-6):121-128.

IZUI, H., TOEN, K., KAMEGAWA, S. & KOMIYA, Y. 2018. Dry sliding wear behavior of TiB/Ti and TiC/Ti composites. *Mechanical Engineering Journal,* 5(4):17-00523-00517-00523.

JAYALAKSHMI, S. & GUPTA, M. 2015. Light Metal Matrix Composites. In: *Metallic Amorphous Alloy Reinforcements in Light Metal Matrices*. Springer:7-58

JIA, L., CHEN, B., LI, S.-F., IMAI, H., TAKAHASHI, M. & KONDOH, K. 2014a. Stability of strengthening effect of in situ formed TiCp and TiBw on the elevated temperature strength of (TiCp+TiBw)/Ti composites. *Journal of Alloys and Compounds,* 614:29-34.

JIA, L., LI, S.-F., IMAI, H., CHEN, B. & KONDOH, K. 2014b. Size effect of B4C powders on metallurgical reaction and resulting tensile properties of Ti matrix composites by in-situ reaction from Ti–B4C system under a relatively low temperature. *Materials Science and Engineering: A,* 614:129-135.

JIA, L., WANG, X., CHEN, B., IMAI, H., LI, S., LU, Z., et al. 2016. Microstructural evolution and competitive reaction behavior of Ti-B 4 C system under solid-state sintering. *Journal of Alloys and Compounds,* 687:1004-1011.

JIMOH, A., SIGALAS, I. & HERMANN, M. 2012. In situ synthesis of titanium matrix composite (Ti-TiB-TiC) through sintering of TiH2-B4C. *Mater. Sci. Appl,* 3:30-35.

JIN, Y., WNAG, H., ZENG, S. & ZHANGE, E. 2002. Formation and growth mechanism of TiC srystal in TiCp/Ti composites. *Transactions of Nonferrous Metals Society of China,* 12(6):1158-1163.

JOHANSSON, L. I. 1995. Electronic and structural properties of transition-metal carbide and nitride surfaces. *Surface science reports,* 21(5-6):177-250.

KAINER, K. U. 2006. *Metal matrix composites: custom-made materials for automotive and aerospace engineering*. John Wiley & Sons.

KARTAL, G. & TIMUR, S. 2013. Growth kinetics of titanium borides produced by CRTD-Bor method. *Surface and Coatings Technology,* 215:440-446.

KEDDAM, M. & TAKTAK, S. 2017. Characterization and diffusion model for the titanium boride layers formed on the Ti6Al4V alloy by plasma paste boriding. *Applied Surface Science,* 399:229-236.

KEDDAM, M., TAKTAK, S. & TASGETIREN, S. 2016. A diffusion model for the titanium borides on pure titanium. *Surface Engineering,* 32(11):802-808.

KELLY, A. & ZWEBEN, C. H. 2000. *Comprehensive composite materials*. Elsevier.

KHINA, B., FORMANEK, B. & SOLPAN, I. 2005. Limits of applicability of the "diffusion-controlled product growth" kinetic approach to modeling SHS. *Physica B: Condensed Matter,* 355(1-4):14-31.

KIESCHKE, R. R. & CLYNE, T. W. 1991. Development of a diffusion barrier for SiC monofilaments in titanium. *Materials Science and Engineering: A,* 135:145-149.

KIM, I. Y., CHOI, B. J., KIM, Y. J. & LEE, Y. Z. 2011. Friction and wear behavior of titanium matrix (TiB+TiC) composites. *Wear,* 271(9-10):1962-1965.

KIM, Y.-J., CHUNG, H. & KANG, S.-J. 2001. In situ formation of titanium carbide in titanium powder compacts by gas–solid reaction. *Composites Part A: Applied Science and Manufacturing,* 32(5):731-738.

KLINGER, M. & JÄGER, A. 2015. Crystallographic Tool Box (CrysTBox): automated tools for transmission electron microscopists and crystallographers. *Journal of applied crystallography,* 48(6):2012-2018.

KOLUKULURI, S. V. 2013. Structure Property Correlation in Discontinuously Reinforced Titanium matrix Composites.

KONITZER, D. & LORETTO, M. 1989. Microstructural assessment of Ti6A14V-TiC metal-matrix composite. *Acta Metallurgica,* 37(2):397-406.

KÜBARSEPP, J., KLAASEN, H. & PIRSO, J. 2001. Behaviour of TiC-base cermets in different wear conditions. *Wear,* 249(3-4):229-234.

KUMAR, M. S., CHANDRASEKAR, P., CHANDRAMOHAN, P. & MOHANRAJ, M. 2012. Characterisation of titanium–titanium boride composites processed by powder metallurgy techniques. *Materials Characterization,* 73:43-51.

KUS, U. 2017. ETUDE DE LA CONTRIBUTION DE LA TECHNIQUE SPARK PLASMA SINTERING A L'OPTIMISATION DES PROPRIETES MECANIQUES DE L'ALLIAGE DE TITANE TA6V. PhD, Toulouse, France, Université Toulouse III - Paul Sabatier.

KUS, U., HUEZ, J., DELAGNES, D., CHEVALLIER, G. & ESTOURNÈS, C. 2016. Proceedings of the 13th World Conference on Titanium. *Proceedings of the 13th World Conference on Titanium*:651-656.

KWASNIAK, P., MUZYK, M., GARBACZ, H. & KURZYDLOWSKI, K. J. 2014. Influence of oxygen content on the mechanical properties of hexagonal Ti—First principles calculations. *Materials Science and Engineering: A,* 590:74-79.

LAGOS, M. A., AGOTE, I., ATXAGA, G., ADARRAGA, O. & PAMBAGUIAN, L. 2016. Fabrication and characterisation of Titanium Matrix Composites obtained using a combination of Self propagating High temperature Synthesis and Spark Plasma Sintering. *Materials Science and Engineering: A,* 655:44-49.

LAMPKE, T., LEOPOLD, A., DIETRICH, D., ALISCH, G. & WIELAGE, B. 2006. Correlation between structure and corrosion behaviour of nickel dispersion coatings containing ceramic particles of different sizes. *Surface and Coatings Technology,* 201(6):3510-3517.

LANDOLT, D., MISCHLER, S. & STEMP, M. 2001. Electrochemical methods in tribocorrosion: a critical appraisal. *Electrochimica acta,* 46(24-25):3913-3929.

LEYENS, C. & PETERS, M. 2003. *Titanium and titanium alloys: fundamentals and applications*. John Wiley & Sons.

LI, B., LIU, Y., CAO, H., HE, L. & LI, J. 2009. Rapid fabrication of in situ TiC particulates reinforced Fe-based composites by spark plasma sintering. *Materials Letters,* 63(23):2010-2012.

LI, D., PING, D., LU, Y. & YE, H. 1993. Characterization of the microstructure in TiB-whisker reinforced Ti alloy matrix composite. *Materials Letters,* 16(6):322-326.

LI, P., LIU, D., BAO, W., MA, L. & DUAN, Y. 2018. Surface characterization and diffusion model of pack borided TB2 titanium alloy. *Ceramics International,* 44(15):18429-18437.

LI, S., KONDOH, K., IMAI, H., CHEN, B., JIA, L., UMEDA, J., et al. 2016. Strengthening behavior of in situ-synthesized (TiC–TiB)/Ti composites by powder metallurgy and hot extrusion. *Materials & Design,* 95:127-132.

LIANG, C. P. & GONG, H. R. 2010. Fundamental influence of hydrogen on various properties of α-titanium. *International Journal of Hydrogen Energy,* 35(8):3812-3816.

LIANG, Y., WANG, H., YANG, Y., DU, Y. & JIANG, Q. 2008. Reaction path of the synthesis of TiC–TiB2 in Cu–Ti–B4C system. *International Journal of Refractory Metals and Hard Materials,* 26(4):383-388.

LOCCI, A. M., ORRÙ, R., CAO, G. & MUNIR, Z. A. 2006. Simultaneous Spark Plasma Synthesis and Densification of TiC–TiB2 Composites. *Journal of the American Ceramic Society,* 89(3):848-855.

LÓPEZ-ORTEGA, A., ARANA, J. & BAYÓN, R. 2018. Tribocorrosion of Passive Materials: A Review on Test Procedures and Standards. *International Journal of Corrosion,* 2018.

LU, C. & LI, Z. 2008. Structural evolution of TiH2–B4C during ball milling and subsequent heat treatment. *Journal of Alloys and Compounds,* 448(1-2):198-201.

LUO, X., YANG, Y., YU, Y., WANG, X., HUANG, B. & CHEN, Y. 2012. Effect of Mo coating on the interface and mechanical properties of SiC fiber reinforced Ti6Al4V composites. *Materials Science and Engineering: A,* 550:286-292.

LÜTJERING, G. & WILLIAMS, J. C. 2003. *Titanium*. (2). Springer.

LÜTJERING, G. & WILLIAMS, J. C. 2007a. Engineering materials and processes: Titanium. 8:1-16.

LÜTJERING, G. & WILLIAMS, J. C. 2007b. Titanium. *Titanium*.

MAKUCH, N., KULKA, M., KEDDAM, M., TAKTAK, S., ATAIBIS, V. & DZIARSKI, P. 2017. Growth kinetics and some mechanical properties of two-phase boride layers produced on commercially pure titanium during plasma paste boriding. *Thin Solid Films,* 626:25-37.

MANIÈRE, C., NIGITO, E., DURAND, L., WEIBEL, A., BEYNET, Y. & ESTOURNÈS, C. 2017. Spark plasma sintering and complex shapes: The deformed interfaces approach. *Powder Technology,* 3202017/10/01/:340-345.

MAO, Y., YU, S., ZHANG, Y., GUO, B., MA, Z. & DENG, Q. 2015. Microstructure analysis of graphite/Cu joints brazed with (Cu-50TiH2)+B composite filler. *Fusion Engineering and Design,* 1002015/11/01/:152-158.

MARTINS, D., GRUMBACH, F., MANIÈRE, C., SALLOT, P., MOCELLIN, K., BELLET, M., et al. 2017. In-situ creep law determination for modeling Spark Plasma Sintering of TiAl 48-2-2 powder. *Intermetallics,* 86:147-155.

MARTINS, D., GRUMBACH, F., SIMOULIN, A., SALLOT, P., MOCELLIN, K., BELLET, M., et al. 2018. Spark plasma sintering of a commercial TiAl 48-2-2 powder: Densification and creep analysis. *Materials Science and Engineering: A,* 711:313-316.

MASIKANE, M. A. 2016. Investigation into the microstructure and tensile properties of unalloyed titanium and Ti-6Al-4V alloy produced by powder metallurgy, casting and layered …. *Investigation into the microstructure and tensile properties of unalloyed titanium and Ti-6Al-4V alloy produced by powder metallurgy, casting and layered ….*

MATHEW, M., SRINIVASA PAI, P., POURZAL, R., FISCHER, A. & WIMMER, M. 2009. Significance of tribocorrosion in biomedical applications: overview and current status. *Advances in tribology,* 2009.

MATSUGI, K., ISHIBASHI, N., HATAYAMA, T. & YANAGISAWA, O. 1996. Microstructure of spark sintered titanium-aluminide compacts. *Intermetallics,* 4(6):457-467.

MATSUGI, K., KURAMOTO, H., YANAGISAWA, O. & KIRITANI, M. 2003. A case study for production of perfectly sintered complex compacts in rapid consolidation by spark sintering. *Materials Science and Engineering: A,* 354(1-2):234-242.

MIKLASZEWSKI, A., GARBIEC, D. & NIESPODZIANA, K. 2018. Sintering behavior and microstructure evolution in cp-titanium processed by spark plasma sintering. *Advanced Powder Technology,* 29(1):50-57.

MISCHLER, P., ESPALLARGAS, N. & IGUAL MUÑOZ, A. 2014. Bio-Tribocorrosion fundamentals to orthopaedic surgeon and researcher. New Horizon Workshop 10, Bio-Tribocorrosion: Fundamentals and Advances in Orthopaedics, New Orleans, 1–10.

MISCHLER, S. 2008. Triboelectrochemical techniques and interpretation methods in tribocorrosion: a comparative evaluation. *Tribology International,* 41(7):573-583.

MOGILEVSKY, P., WERNER, A. & DUDEK, H. 1998. Application of diffusion barriers in composite materials. *Materials Science and Engineering: A,* 242(1-2):235-247.

MOHANTY, M. & SMITH, R. 1995. Lightweight TiC/Ti wear-resistant coatings for lightweight structural applications. *Journal of Thermal Spray Technology,* 4(4):384-394.

MOLINARI, A., STRAFFELINI, G., TESI, B. & BACCI, T. 1997. Dry sliding wear mechanisms of the Ti6Al4V alloy. *Wear,* 208(1-2):105-112.

MONTICELLI, C., FRIGNANI, A., BELLOSI, A., BRUNORO, G. & TRABANELLI, G. 2001. The corrosion behaviour of titanium diboride in neutral chloride solution. *Corrosion science,* 43(5):979-992.

MORSI, K. & PATEL, V. V. 2007. Processing and properties of titanium–titanium boride (TiBw) matrix composites—a review. *Journal of Materials Science,* 42(6):2037-2047.

MOTSI, G. T., GUILLEMET-FRITSCH, S., CHEVALLIER, G., SHONGWE, M. B., OLUBAMBI, P. A. & ESTOURNES, C. 2019. Microstructural evolution and mechanical properties of pure titanium powders processed by spark plasma sintering. *Powder Technology,* 345:415-424.

MUNIR, Z. A., ANSELMI-TAMBURINI, U. & OHYANAGI, M. 2006. The effect of electric field and pressure on the synthesis and consolidation of materials: A review of the spark plasma sintering method. *Journal of Materials Science,* 41(3):763-777.

MUNOZ, A. I. & ESPALLARGAS, N. 2011. Tribocorrosion mechanisms in sliding contacts. In: *Tribocorrosion of Passive Metals and Coatings*. Elsevier:118-152

MUNRO, R. G. 2000. Material properties of titanium diboride. *Journal of Research of the National Institute of Standards and Technology,* 105(5):709.

NALWA, H. S. 1999. *Handbook of nanostructured materials and nanotechnology, five-volume set*. Academic Press.

NAMINI, A. S., AZADBEH, M. & ASL, M. S. 2017. Effect of TiB2 content on the characteristics of spark plasma sintered Ti–TiBw composites. *Advanced Powder Technology,* 28(6):1564-1572.

NI, D. R., GENG, L., ZHANG, J. & ZHENG, Z. Z. 2006. Effect of B4C particle size on microstructure of in situ titanium matrix composites prepared by reactive processing of Ti–B4C system. *Scripta Materialia,* 55(5):429-432.

NI, D. R., GENG, L., ZHANG, J. & ZHENG, Z. Z. 2008a. Fabrication and tensile properties of in situ TiBw and TiCp hybrid-reinforced titanium matrix composites based on Ti–B4C–C. *Materials Science and Engineering: A,* 478(1-2):291-296.

NI, D. R., GENG, L., ZHANG, J. & ZHENG, Z. Z. 2008b. TEM characterization of symbiosis structure of in situ TiC and TiB prepared by reactive processing of Ti–B4C. *Materials Letters,* 62(4-5):686-688.

NIE, J., WU, Y., LI, P., LI, H. & LIU, X. 2012. Morphological evolution of TiC from octahedron to cube induced by elemental nickel. *CrystEngComm,* 14(6):2213-2221.

OBADELE, B. A., ANDREWS, A., SHONGWE, M. B. & OLUBAMBI, P. A. 2016. Tribocorrosion behaviours of AISI 310 and AISI 316 austenitic stainless steels in 3.5% NaCl solution. *Materials Chemistry and Physics,* 171:239-246.

OGWU, A. & DAVIES, T. 1996. The densification and mechanical properties of a TiC and TiB2 hardmetal sintered with a reactive alloy binder. *physica status solidi (a),* 153(1):101-116.

OKSIUTA, Z., DABROWSKI, J. & OLSZYNA, A. 2009. Co–Cr–Mo-based composite reinforced with bioactive glass. *Journal of Materials Processing Technology,* 209(2):978-985.

ONUOHA, C. C., MEMARRASHIDI, Z., KIPOUROS, G. J., FARHAT, Z. N. & PLUCKNETT, K. P. 2017. Aqueous corrosion behaviour of TiC-304L stainless steel cermets in a 3.5 wt% NaCl solution. *International Journal of Refractory Metals and Hard Materials,* 66:234-243.

ORRU, R., LICHERI, R., LOCCI, A. M., CINCOTTI, A. & CAO, G. 2009. Consolidation/synthesis of materials by electric current activated/assisted sintering. *Materials Science and Engineering: R: Reports,* 63(4-6):127-287.

PANDA, K. B. & CHANDRAN, K. S. 2006. First principles determination of elastic constants and chemical bonding of titanium boride (TiB) on the basis of density functional theory. *Acta Materialia,* 54(6):1641-1657.

PONTHIAUX, P., WENGER, F., DREES, D. & CELIS, J.-P. 2004. Electrochemical techniques for studying tribocorrosion processes. *Wear,* 256(5):459-468.

PRAKASH, K. S., GOPAL, P., ANBUROSE, D. & KAVIMANI, V. 2016. Mechanical, corrosion and wear characteristics of powder metallurgy processed Ti-6Al-4V/B4C metal matrix composites. *Ain Shams Engineering Journal*.

PRASAD, S. & ASTHANA, R. 2004. Aluminum metal-matrix composites for automotive applications: tribological considerations. *Tribology letters,* 17(3):445-453.

QIAN, M., YANG, Y. F., LUO, S. D. & TANG, H. P. 2015. Titanium Powder Metallurgy. *Titanium Powder Metallurgy*:201-218.

QIN, Y., GENG, L. & NI, D. 2012. Dry sliding wear behavior of titanium matrix composites hybrid-reinforced by in situ TiBw and TiCp. *Journal of Composite Materials,* 46(21):2637-2645.

QUINN, C. & KOHLSTEDT, D. 1984. Solid-State Reaction Between Titanium Carbide and Titanium Metal. *Journal of the American Ceramic Society,* 67(5):305-310.

RAFIEI, M., SALEHI, M. & SHAMANIAN, M. 2014. Formation mechanism of B4C–TiB2–TiC ceramic composite produced by mechanical alloying of Ti–B4C powders. *Advanced Powder Technology,* 25(6):1754-1760.

RAHOMA, H. K. S., CHEN, Y. Y., WANG, X. P. & XIAO, S. L. 2015. Influence of (TiC+TiB) on the microstructure and tensile properties of Ti-B20 matrix alloy. *Journal of Alloys and Compounds,* 627:415-422.

RANGANATH, S. & SUBRAHMANYAM, J. 1996. On the in situ formation of tic and ti 2 c reinforcements in combustion-assisted synthesis of titanium matrix composites. *Metallurgical and Materials Transactions A,* 27(1):237-240.

RAVI CHANDRAN, K. S., PANDA, K. B. & SAHAY, S. S. 2004. TiBw-reinforced Ti composites: Processing, properties, application prospects, and research needs. *Jom,* 56(5), 2004/05/01:42-48.

REVATHI, A., MAGESH, S., BALLA, V. K., DAS, M. & MANIVASAGAM, G. 2016. Current advances in enhancement of wear and corrosion resistance of titanium alloys-a review. *Materials Technology,* 31(12):696-704.

ROSSO, M. 2006. Ceramic and metal matrix composites: Routes and properties. *Journal of Materials Processing Technology,* 175(1-3):364-375.

SAHAY, S., RAVICHANDRAN, K., ATRI, R., CHEN, B. & RUBIN, J. 1999. Evolution of microstructure and phases in in situ processed Ti–TiB composites containing high volume fractions of TiB whiskers. *Journal of materials research,* 14(11):4214-4223.

SAHOO, B. & PANIGRAHI, S. 2016. Synthesis, characterization and mechanical properties of in-situ (TiC-TiB2) reinforced magnesium matrix composite. *Materials & Design,* 109:300-313.

SAIRAM, K., SONBER, J., MURTHY, T. C., SUBRAMANIAN, C., FOTEDAR, R., NANEKAR, P., et al. 2014. Influence of spark plasma sintering parameters on densification and mechanical properties of boron carbide. *International Journal of Refractory Metals and Hard Materials,* 42:185-192.

SEAH, K., THAMPURAN, R. & TEOH, S. 1998. The influence of pore morphology on corrosion. *Corrosion science,* 40(4-5):547-556.

SHEN, X., ZHANG, Z., WEI, S., WANG, F. & LEE, S. 2011. Microstructures and mechanical properties of the in situ TiB–Ti metal–matrix composites synthesized by spark plasma sintering process. *Journal of Alloys and Compounds,* 509(29):7692-7696.

SHON, J.-H., PARK, J.-M., CHO, K.-S., HONG, J.-K., PARK, N.-K. & MYUNG-HOON, O. H. 2014a. Effects of various sintering methods on microstructure and mechanical properties of CP-Ti powder consolidations. *Transactions of Nonferrous Metals Society of China,* 24.

SHON, J., SONG, I.-B., CHO, K.-S., PARK, Y.-I., HONG, J.-K., PARK, N.-K., et al. 2014b. Effect of particle size distribution on microstructure and mechanical properties of spark-plasma-sintered titanium from CP-Ti powders. *International Journal of Precision Engineering and Manufacturing,* 15(4):643-647.

SHUFENG, L. I., KONDOH, K., IMAI, H., CHEN, B., JIA, L. & UMEDA, J. 2015. Microstructure and mechanical properties of P/M titanium matrix composites reinforced by in-situ synthesized TiC–TiB. *Materials Science and Engineering: A,* 628:75-83.

SHVETS, V., LAVRENKO, V., TALASH, V., PANASYUK, A. & RUDENKO, Y. B. 2016. Anodic Polarization of Titanium Carbide TiC x in 3% NaCl Solution in the Homogeneity Range. *Powder Metallurgy and Metal Ceramics,* 55(7-8):469-476.

SIVAKUMAR, B., SINGH, R. & PATHAK, L. C. 2015. Corrosion behavior of titanium boride composite coating fabricated on commercially pure titanium in Ringer's solution for bioimplant applications. *Materials Science and Engineering: C,* 48:243-255.

SOLONINA, O. & ULYAKOVA, N. 1974. Effect of carbon on the mechanical properties and structure of titanium alloys. *Metal Science and Heat Treatment,* 16(4):310-312.

SONG, G., CAO, C.-N. & CHEN, S.-H. 2005. A study on transition of iron from active into passive state. *Corrosion science,* 47(2):323-339.

SONG, W., NING, J., MAO, X. & TANG, H. 2013. A modified Johnson–Cook model for titanium matrix composites reinforced with titanium carbide particles at elevated temperatures. *Materials Science and Engineering: A,* 5768/1/:280-289.

STACHOWIAK, G. W. & BATCHELOR, A. W. 2006. Engineering Tribology (Third Edition). *Engineering Tribology (Third Edition)*:595-619.

STACK, M. 2002. Mapping tribo-corrosion processes in dry and in aqueous conditions: some new directions for the new millennium. *Tribology International,* 35(10):681-689.

TABRIZI, S. G., SAJJADI, S. A., BABAKHANI, A. & LU, W. 2015. Influence of spark plasma sintering and subsequent hot rolling on microstructure and flexural behavior of in-situ TiB and TiC reinforced Ti6Al4V composite. *Materials Science and Engineering: A,* 624:271-278.

TAKADOUM, J. 1996. The influence of potential on the tribocorrosion of nickel and iron in sulfuric acid solution. *Corrosion science,* 38(4):643-654.

TAL-GUTELMACHER, E. & ELIEZER, D. 2005. The hydrogen embrittlement of titanium-based alloys. *Jom,* 57(9):46-49.

TANG, J.-X., CHENG, J.-H., ZENG, Z.-Q. & MIAO, H.-Z. 2000. Diffusion Path and Reaction Mechanism between Ti and B~ 4C. *JOURNAL OF INORGANIC MATERIALS-BEIJING-,* 15(5):884-888.

TEBER, A., SCHOENSTEIN, F., ABDELLAOUI, M. & JOUINI, N. 2012. Fabrication, microstructure and mechanical properties of novel bulk binderless (Ti0. 8Zr0. 2) C carbides prepared by mechanical alloying and spark plasma sintering. *Ceramics International,* 38(6):4929-4933.

TJONG, S. C. & MAI, Y.-W. 2008. Processing-structure-property aspects of particulate-and whisker-reinforced titanium matrix composites. *Composites Science and Technology,* 68(3-4):583-601.

TOKITA, M. 1999. Mechanism of spark plasma sintering. Paper presented at the *Proceeding of NEDO International Symposium on Functionally Graded Materials*.

TOPTAN, F., REGO, A., ALVES, A. C. & GUEDES, A. 2016. Corrosion and tribocorrosion behavior of Ti–B4C composite intended for orthopaedic implants. *Journal of the Mechanical Behavior of Biomedical Materials,* 61:152-163.

TOPTAN, F. & ROCHA, L. A. 2017. Tribocorrosion in metal matrix composites. In: *Materials Science and Engineering: Concepts, Methodologies, Tools, and Applications*. IGI Global:825-844

TRZASKA, Z., COURET, A. & MONCHOUX, J.-P. 2016. Spark plasma sintering mechanisms at the necks between TiAl powder particles. *Acta Materialia,* 118:100-108.

UPADHYAYA, G. 1997. *Powder metallurgy technology*. Cambridge Int Science Publishing.

VALLAURI, D., ADRIÁN, I. C. & CHRYSANTHOU, A. 2008. TiC–TiB2 composites: A review of phase relationships, processing and properties. *Journal of the European Ceramic society,* 28(8):1697-1713.

VASANTHAKUMAR, K. & BAKSHI, S. R. 2018. Effect of C/Ti ratio on densification, microstructure and mechanical properties of TiCx prepared by reactive spark plasma sintering. *Ceramics International,* 44(1), 2018/01/01/:484-494.

VASANTHAKUMAR, K., KARTHISELVA, N., CHAWAKE, N. M. & BAKSHI, S. R. 2017. Formation of TiCx during reactive spark plasma sintering of mechanically milled Ti/carbon nanotube mixtures. *Journal of Alloys and Compounds,* 709:829-841.

VERKHOTUROV, A., KUZENKOVA, M., LEBUKHOVA, N. & PODCHERNYAEVA, I. 1988. Electrochemical behavior of transition metals and refractory compounds of titanium in synthetic sea water. *Soviet Powder Metallurgy and Metal Ceramics,* 27(2):162-166.

WANG, D., YUAN, H. & QIANG, J. 2017. The Microstructure Evolution, Mechanical Properties and Densification Mechanism of TiAl-Based Alloys Prepared by Spark Plasma Sintering. *Metals,* 7(6):201.

WANG, H., SUN, S., WANG, D. & TU, G. 2012. Characterization of the structure of TiB2/TiC composites prepared via mechanical alloying and subsequent pressureless sintering. *Powder Technology,* 217:340-346.

WANJARA, P., DREW, R., ROOT, J. & YUE, S. 2000. Evidence for stable stoichiometric Ti2C at the interface in TiC particulate reinforced Ti alloy composites. *Acta Materialia,* 48(7):1443-1450.

WASZ, M., BROTZEN, F., MCLELLAN, R. & GRIFFIN, A. 1996. Effect of oxygen and hydrogen on mechanical properties of commercial purity titanium. *International materials reviews,* 41(1):1-12.

WELSCH, G., BOYER, R. & COLLINGS, E. 1993. *Materials properties handbook: titanium alloys*. ASM international.

WEN, G., LI, S., ZHANG, B. & GUO, Z. 2001. Reaction synthesis of TiB2–TiC composites with enhanced toughness. *Acta Materialia,* 49(8):1463-1470.

WESTON, N. S., DERGUTI, F., TUDBALL, A. & JACKSON, M. 2015. Spark plasma sintering of commercial and development titanium alloy powders. *Journal of Materials Science,* 50(14):4860-4878.

WILL, G. 2004. Electron deformation density in titanium diboride chemical bonding in TiB2. *Journal of Solid State Chemistry,* 177(2):628-631.

WOOD, R. J. 2017. Marine wear and tribocorrosion. *Wear,* 376:893-910.

WRIEDT, H. A. & MURRAY, J. L. 1987. The N-Ti (Nitrogen-Titanium) system. *Bulletin of Alloy Phase Diagrams,* 8(4):378-388.

WU, Q., YANG, C., XUE, F. & SUN, Y. 2011. Effect of Mo addition on the microstructure and wear resistance of in situ TiC/Al composite. *Materials & Design,* 32(10):4999-5003.

XUE, J.-X., LIU, J.-X., ZHANG, G.-J., ZHANG, H.-B., LIU, T., ZHOU, X.-S., et al. 2016. Improvement in mechanical/physical properties of TiC-based ceramics sintered at 1500° C for inert matrix fuels. *Scripta Materialia,* 114:5-8.

YAN, M., XU, W., DARGUSCH, M. S., TANG, H. P., BRANDT, M. & QIAN, M. 2014. Review of effect of oxygen on room temperature ductility of titanium and titanium alloys. *Powder Metallurgy,* 57(4):251-257.

YANG, Y. & QIAN, M. 2015. Spark plasma sintering and hot pressing of titanium and titanium alloys. In: *Titanium Powder Metallurgy: Science, Technology and Applications* (Vol. 219). Butterworth-Heinemann

YANG, Y. F., JIN, S. B. & JIANG, Q. C. 2013. Effect of reactant C/Ti ratio on the stoichiometry, morphology of TiCx and mechanical properties of TiCx-Ni composite. *CrystEngComm,* 15(5):852-855.

YU, H., ZHANG, W., WANG, H., JI, X., SONG, Z., LI, X., et al. 2017. In-situ synthesis of TiC/Ti composite coating by high frequency induction cladding. *Journal of Alloys and Compounds,* 701:244-255.

ZADRA, M., CASARI, F., GIRARDINI, L. & MOLINARI, A. 2008. Microstructure and mechanical properties of cp-titanium produced by spark plasma sintering. *Powder Metallurgy,* 51(1):59-65.

ZADRA, M., CASARI, F., GIRARDINI, L. & MOLINARI, A. 2013. Microstructure and mechanical properties of cp-titanium produced by spark plasma sintering. *Powder Metallurgy,* 51(1):59-65.

ZARRINFAR, N., SHIPWAY, P., KENNEDY, A. & SAIDI, A. 2002. Carbide stoichiometry in TiC x and Cu–TiC x produced by self-propagating high-temperature synthesis. *Scripta Materialia,* 46(2):121-126.

ZHANG, E., ZENG, G. & ZENG, S. 2002. Effect of in situ TiB short fibre on oxidation behavior of Ti–6Al–1.2B alloy. *Scripta Materialia,* 46(11), 2002/06/07/:811-816.

ZHANG, W., YANG, Y. Q., ZHAO, G. M., FENG, Z. Q., HUANG, B., LUO, X., et al. 2014. Interfacial reaction studies of B4C-coated and C-coated SiC fiber reinforced Ti–43Al–9V composites. *Intermetallics,* 50:14-19.

ZHANG, X., SONG, F., WEI, Z., YANG, W. & DAI, Z. 2017. Microstructural and mechanical characterization of in-situ TiC/Ti titanium matrix composites fabricated by graphene/Ti sintering reaction. *Materials Science and Engineering: A,* 705:153-159.

ZHECHEVA, A., SHA, W., MALINOV, S. & LONG, A. 2005. Enhancing the microstructure and properties of titanium alloys through nitriding and other surface engineering methods. *Surface and Coatings Technology,* 200(7):2192-2207.

Appendix I

I.I Mass required for sintering Ti5wt%B_4C composites

$$\rho_{\text{composite}} = x_{Ti}\,\rho_{Ti} \times x_{B_4C}\;\rho_{B_4C}$$

$$= (0.95 \times 4.51) + (0.05 \times 2.52)$$

$$= 4.2845 + 0.126$$

$$= 4.4105 \text{g/cm}^3$$

$$m = \rho V$$

$$= 4.4105 \times 0.1$$

$$= 0.441\text{g (Ø8mm and 2mm in thickness pellets)}$$

I.II Theoretical density of sintered Ti5wt%B_4C composites

$$m_{Ti} = 0.95 \text{ x } 0.441$$

$$= 0.41895\text{g}$$

$$n_{Ti} = \frac{m}{M}$$

$$= \frac{0.41895}{47.88}$$

$$= 0.00875\text{mol}$$

$$m_{B_4C} = 0.05 \text{ x } 0.441$$

$$= 0.02205\text{g}$$

$$x_{B_4C} = \frac{m}{M}$$

$$= \frac{0.02205}{55.25}$$

$$= 0.000399095\text{mol}$$

$5Ti + B_4C \rightarrow TiC + 4TiB$ (assuming a complete reaction)

B_4C is a limiting reactant therefore:

1mol B_4C = 1mol TiC

0.000399095mol B_4C = xmol TiC

Therefore: xmol TiC = 0.000399095mol

$$m_{TiC} = nM$$
$$= 0.000399095 \text{ X } 59.89$$
$$= 0.0239017995g$$

1mol B_4C = 4mol TiB

0.000399095mol B_4C = xmol TiB

Therefore: xmol TiB = 0.00159638mol

$$m_{TiB} = nM$$
$$= 0.00159638 \text{ x } 58.69$$
$$= 0.0936915422g$$

$$m_{Ti(unreacted)} = m_{reactants} - m_{products}$$
$$= (m_{Ti} + m_{B_4C}) - (m_{TiC} + m_{TiB})$$
$$= (0.41895 + 0.02205) - (0.0239017995 + 0.0936915422)$$
$$= 0.441 - 0.1178172215$$
$$= 0.323182778g$$

$$m_{products} = m_{TiC} + m_{TiB} + m_{Ti(unreacted)}$$
$$= 0.0239017995 + 0.0936915422 + 0.323182778$$
$$= 0.441g$$

$$x_{TiC} = \frac{0.0239017995}{0.441}$$

$$= 0.0541990918$$

$$x_{TiB} = \frac{0.0936915422}{0.441}$$

$$= 0.2124524766$$

$$x_{Ti} = \frac{0.323182778}{0.441}$$

$$= 0.7328407664$$

$$\rho_{\text{product}} = x_{Tic}\,\rho_{Tic} + x_{TiB}\,\rho_{TiB} + x_{Ti}\,\rho_{Ti}$$

$$= (0.0541990918 \times 4.93) + (0.2124524766 \times 4.56) + (0.7328407664 \times 4.51)$$

$$= 0.2672015226 + 0.9687832933 + 3.305111856$$

$$= 4.54 g/cm^3$$

I.III Theoretical volume percentage of reinforcing phases in Ti5wt%B_4C

$$V_{TiB} = \frac{\frac{w_{TiB}}{\rho_{TiB}}}{\frac{w_{TiB}}{\rho_{TiB}} + \frac{w_{TiC}}{\rho_{TiC}} + \frac{w_{Ti}}{\rho_{Ti}}} \times 100\%$$

$$V_{TiB} = \frac{\frac{0.2124524766}{4.56}}{\frac{0.2124524766}{4.56} + \frac{0.0541990918}{4.93} + \frac{0.7328407664}{4.51}} \times 100\%$$

$$V_{TiB} = 21\%$$

Table 31. Theoretical volume percentage of reinforcing phases in complete chemical reaction

	Ti	Ti1wt%B_4C	Ti2.5wt%B_4C	Ti5wt%B_4C	Ti10wt%B_4C
Ti (vol%)	100	95	87	74	47
TiB (vol%)	0	4	11	21	43
TiC (vol%)	0	1	2	5	10

Resumé
La faible résistance à l'usure du titane et de ses alliages limite leur application dans laquelle l'effet combiné de l'usure et de la corrosion peut être rencontré. À cet égard, l'ajout de phases céramiques sous forme de whiskers (TiB) ou de particules (TiB_2 et TiC) dans une matrice à base de titane pour former des composites avancés à matrice de titane (TMC), peut aider à réduire les pertes de matériau et à prolonger la durée de vie. Dans cette étude, les composites de titane à base de TiB_2, TiB et TiC ont été produits par Spark Plasma Sintering (SPS) réactif de titane pur commercial (CP-Ti) et de poudres B_4C de différentes tailles de particules. On s'est rendu compte qu'à une température de consigne de 800°C, la réaction avait commencé en raison des avantages du courant pulsé dans le SPS. L'analyse SEM / FIB / TEM sur le matériau fritté à 800°C a montré une phase grise continue, constituée d'amas de particules de B_4C partiellement réagies ségrégés aux joints des grains de la matrice Ti. À 1100°C, les réactifs ont complètement réagi et se sont transformés en clusters de divers composés riches en B et C (Ti-B et Ti-C). L'homogénéisation de la microstructure a été obtenue à des temps de séjour de 0 à 30 min pour éliminer les amas formés. Le comportement en corrosion et en tribocorrosion du CP-Ti et des TMC a été étudié dans des solutions 3,5% molaire de NaCl. Les résultats ont montré qu'une quantité croissante des phases de renforcement à 5% en poids réduisait la sensibilité à la corrosion et à la tribocorrosion des TMC frittés à 1100°C, car les valeurs de potentiel en circuit ouvert étaient positivement décalées pour Ti5wt% B_4C. De graves dommages à la surface avec des rainures profondes dans CP-Ti ont été observés dans les pistes usées indiquant une usure adhésive. Aucun retrait des phases de renforcement TiB et TiC n'a été observé pour Ti5wt% B_4C, en raison de la forte force de liaison interfaciale avec la matrice Ti.
Mots-clés: CP-Ti, composites à matrice de titane, SPS, propriétés mécaniques, tribocorrosion

Abstract
The poor wear resistance of titanium and its alloys limit their application in which the combined effect of wear and corrosion may be encountered. In this regard, addition of ceramic phases in the form of whiskers (TiB) or particles (TiB_2 and TiC) in titanium based matrix to form advanced titanium matrix composites (TMCs), can aid reduce material loss and prolong the service life. In this study TiB_2, TiB and TiC based titanium composites were produced by reactive Spark Plasma Sintering (SPS) of commercial pure titanium (CP-Ti) and B_4C powders of varying particles sizes. It was realized that at 800°C set-point temperature the reaction had initiated due to the benefits of pulsed current in the SPS. SEM/FIB/TEM analysis on the material sintered at 800°C showed a continuous grey phase, constituted of clusters of partially reacted B_4C particles segregated at Ti matrix grain boundaries. While at 1100°C, the reactants completely reacted and transformed into clusters of various compounds high in B and C (Ti-B and Ti-C). Microstructure homogenization was achieved at dwell times of 0-30 min to remove the formed clusters. Corrosion and tribocorrosion behaviour of CP-Ti and TMCs was investigated in solutions 3.5% molar of NaCl. The results showed that increasing amount of the reinforcing phases to 5wt% reduced the corrosion and tribocorrosion susceptibility of the TMCs sintered at 1100°C, as the open circuit potential values were positively shifted for Ti5wt%B_4C. Severe surface damage with deep grooves in CP-Ti was observed in worn tracks indicating adhesive wear. No pulling out of TiB and TiC reinforcing phases was observed for Ti5wt%B_4C, due to the strong interfacial bond strength with the Ti matrix.
Keywords: CP-Ti, Titanium matrix composites, SPS, mechanical properties, tribocorrosion